Structure, Properties and Formation Histories

of S0 Galaxies

by

Kaustubh Vaghmare

Thesis Supervisor

Prof. Ajit K. Kembhavi

A thesis presented for the degree of
Doctor of Philosophy
to

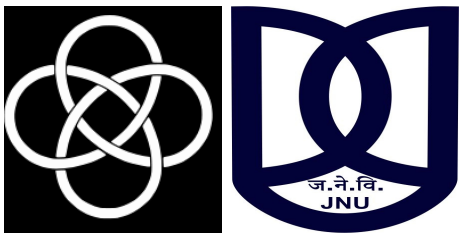

IUCAA &
Jawaharlal Nehru University
India

July, 2015

Structure, Properties and Formation Histories of S0 Galaxies

by

Kaustubh Vaghmare

Certificate

This is to certify that the thesis entitled **Structure, Properties and Formation Histories of S0 Galaxies** submitted by **Mr. Kaustubh Vaghmare** for the award of the degree of Doctor of Philosophy to Jawaharlal Nehru University, New Delhi is his original work. This has not been published or submitted to any other University for any other Degree or Diploma.

Pune
July 30th, 2015

Prof. Ajit K. Kembhavi
(Thesis Advisor & Director, IUCAA)

Declaration

I hereby declare that the work reported in this thesis is entirely original. This thesis is composed independently by me at the Inter-University Centre for Astronomy and Astrophysics, Pune under the supervision of Prof. Ajit K. Kembhavi. I further declare that the subject matter presented in the thesis has not previously formed the basis for the award of any degree, diploma, associateship, fellowship or any other similar title of any University or Institution.

Pune
July 30th, 2015

Prof. Ajit K. Kembhavi
(Thesis Advisor)

Mr. Kaustubh Vaghmare
(Ph.D. Candidate)

Dedicated to ...

Prathama &
Prakash
(my parents, my Gods)

Rahul
(my brother, whose ever presence with my parents and unquestioning support allowed me to work in peace)

&
Sneha
(my beloved)

Acknowledgements

For all students and regular visitors, it is clear that Prof. Ajit Kembhavi is one of the busiest people with frequent meetings, visits abroad, directorial duties and several other responsibilities. A testament to this is the simple fact that parts of this thesis have actually been corrected by him while waiting in South Block, New Delhi. A question I have been asked often is - *how has it been to work with him? How did you manage? Do you wish you had worked with someone else?* And my answer has been the same always. Yes, it has been difficult no doubt but when I compare myself with what I was when I got started and what I am today, I see so much growth. The growth has not just been academic. I have grown as a teacher, a mentor, a manager, a team member etc. In every single interaction with him, there was a lot I could learn in a short time. And even when I was not interacting with him, I found myself busy wrapping my head around his method of work and management. And I find myself privileged to have had the chance to work with him. Thanks to him, I had a chance to be a part of many committees and projects. I have had the chance to do work beyond my main thesis topic and grow in several directions.

The general difficulty of working with a supervisor as busy as Prof. Kembhavi was manageable greatly because of Sudhanshu Barway's guidance. Sudhanshu has been a great mentor, the *co-brainstormer* behind all the projects in this thesis. His general advice on surviving graduate school days has also proved valuable. He has generously hosted me at the South African Astronomical Observatory in Cape Town on multiple occassions. During my trips to Cape Town, his wife Anjali and daughter Nihira opened their doors for me and gave me a home away from home for which I remain ever grateful.

In the initial days of my PhD, I drew a lot of wisdom and help from Yogesh Wadadekar. His course on Astronomical Techniques was probably what cemented my decision that I wanted to work on Observational Astronomy. Through his course I was introduced to the Python programming language, a skill which has remained the corner stone of all my analysis done for the work in this thesis and beyond. During the later days of my graduate school, Varun Bhalerao joined as a postdoctoral fellow and Ashish Mahabal became a frequent visitor to IUCAA. With Varun, I had

the chance of doing a project that allowed me a glimpse of transient astronomy and with Ashish, I found myself expanding my skill set to large databases by working on the Catalina Real-time Transient Survey Virtual Observatory project. I can safely say that my growth in management skills and use of computational machinery grew exponentially thanks to my interactions with them.

In the early days of learning photometry and IRAF, Vijay Mohan, one of the most patient teachers I know of, groomed me into using all the tools. And later when I took it on myself to master the fine art of spectroscopic analysis, I received a lot of help from Hadi Rahmani, Vivek and Anand. Finally, I learned most of the SALT data analysis and spectral modelling from Petri Vaisanen (SAAO) and his student Rajin Ramphul (UCT). I also had the privilege of interacting with Steve Crawford, Alexei Kniazev, Christian Hettlage, Kevin Hainline and David Buckley during my visits to Cape Town and learned a lot through discussions with them.

A good deal of my time in graduate school was spent working for the Virtual Observatory India project. I had the chance of working with a fine team comprising of software engineers from both IUCAA and Persistent Systems Pvt Ltd. My thanks to Santosh Jagade, Ajay Vibhute, Sharmad Navalkar, Prerak Garg, and Snehal Valame. To Santosh and Ajay, along with Sagar and Prafull, I also thank them for the significant amount of improvement in my skill at playing badminton, all their help in lab workshops conducted by me at IUCAA and the tea table fun with Neelam and Praveen.

And what is graduate school without your batch mates, your partners in crime? My gratitude to Luke Chamandy for his constant support and advice, my thanks to Rosy, Tina and Tori - you guys are great! And for bearing witness to my dare devil acts on the IUCAA terrace, the constant mimicry, for bearing my loud music, my very bad guitar playing, my annoying use of whistles as replacement to door knocking etc. I owe one (oops, many) to Suprit, my good friend and *balcony mate* (a phrase that the younger generation of students have replaced with the more disgusting phrase *bathroom mate*). And hey, you do need one senior student to keep warning you of the pot holes ahead and advise you both when needed and otherwise - Sibashish played this role perfectly.

One of the things that kept me sane during my time in IUCAA was my participation in public outreach. There was something about speaking to school & college children, and the general audience which was refreshing to do. And for the opportunities provided to me to do this, I am very thankful to Arvind Paranjpye and Samir Dhurde. The inspiration to look at science outreach as an important undertaking came from the inspiring works of Prof. Jayant Narlikar and the late Carl Sagan. My thanks to all members of the science outreach team for having supported me in all these activities. My thanks also to Ranjeev, Durgesh and Kanak for advices on

various aspects of academia.

Having travelled abroad as well as around India, having seen events small and big, if there is one conclusion I can say I have reached without any doubt, is this - IUCAA has the best administrative team (period). Everything in IUCAA is taken care of and I cannot ask for more. I have been helped by all of them with no questions asked and I would like to thank all of them. With many, I have developed strong personal rapports and will carry them always in my heart. I especially miss Susan Kuriakose, whose untimely passing away was perhaps the most shocking thing to happen. My special thanks to Sandeep for always squeezing me into Prof. Kembhavi's schedule, Samak for all the superb PJs, Chella for his confident and reassuring nods, Santosh Khadilkar for his *we'll manage it* attitude, Samuel for the ever present gesture inviting me in his office, Deepika, for making travel itineraries look easy (they are not!), Mukund Sahasrabuddhe for making accounting look trivial (again, it's not), Rajesh Pardeshi for all the *of course, it's our job* statements and Goswamiji for all the *fikar na karo, ho jayega*s. My thanks to every single person in the administration and the support staff.

How often do you get to talk to people who have braved the enemy when it tried to enter your country? For me, it was a singular privilege that I was protected on all four directions by people with such experience. And to add to it, these security personnels of IUCAA were always willing to share their experiences, their war time stories and what not! And what to say about the cosmetic staff, the folks manning the receptions, the engineers - ever alert - all making everything go like clockwork!

One of the central aspects about IUCAA is the visitor programme which allows one to meet an amazing diversity of people across the globe. I have met many people during the course of last several years, all of whom had a lot to teach me - George Djorgovski, George Helou, Poshak Gandhi, Smita Mathur, Sajeeth Phillip, C D Ravikumar, Asis & Tanuka Chattopadhaya, Amit Pathak, Shantanu Rastogi, Gazi Ahmed, Changbom Park, and Devraj Pawar.

I now step back in time and recollect the people who inspired me to do science in general. I especially recollect the time back in ninth grade (or standard), a time where a series of low scores in Mathematics and Science convinced me that I was not meant to do science. It was then I met Bhaskara Reddy, the mathematics and science teacher in St. Paul's High School, where I spent a great fraction of my life. He taught me a whole new way of looking at the subject and my scores have never dropped since. When I was doing my B.Sc. in Physics, I met with a chance encounter Prof. Najam-ul Hasan and Priya Hasan who inspired me to appreciate the field of astronomy and contributed immensely to my landing in the IUCAA VSP programme and getting preselected for the IUCAA PhD Programmme. My immense thanks also goes to Mrs. Kamala Lata and Mr. T. S. Balakrishna, who

kept immense faith in me while I struggled in a war against a society who saw no meaning in scientific inquiry.

In a world where a degree is meant to be nothing more than a ticket to enter a room where a job interview is held, I met some inspiring people who helped make sense of what pursuit of knowledge was really about. Umesh Vijayshankar, Chandrasekharudu and Kalyan Sunkara offered me the single most valuable thing during my B.Sc. days - the assurance of the sense of immortality that the pursuit of knowledge provides. For their companionship, care and mentorship, I shall always be thankful. My thanks also to Ramya, Ronak and Jitender for ever believing in me. Through thick and thin, Shivkumar, Pratik and Zoheb remained my ever loyal friends right from the early days of schooling - thanks guys!

I strongly feel that in our education system, the value of experiments and observations in science is under-rated. It was my privilege to be able to do a Master's degree from the University of Hyderabad where my teachers showed the joy as well as the importance of dedicated and patient observations in science. I recollect the days where I'd spent nights in the lab all alone but for one brilliant person Jais Tom who shared with me, the importance of understanding an experiment inside out. Jais was inspirational in many ways. A son of a low wage construction worker who used the prize money he won in Chess tournaments to sponsor his education. By passing away in a tragic drowning accident, he taught me one last lesson - to accept the unfairness of Universe as is!

For a very brief moment, between my Bachelor's and Master's programmes, I had the chance of working at the Hong Kong and Shanghai Banking Corporation's (HSBC) Electronic Data Processing Centre. Here, I was exposed to an entirely different culture, one aimed at running a large organization in the smoothest possible manner. While I value the relative freedom and peace academia provides, I believe a lot of my learning and growth happened here.

During my PhD, at all times when I felt home sick and wanted to find a place to feel at home my Uncle and Aunt Shirish and Bharati Kaku, along with their daughter Shreeya, provided unconditional support hence playing a vital role in preserving me during all these years. Special thanks to Parimal, Ameya & Kaustubh for the fun weekends and Anand, Seema, Mona & Alka *atya* for making me one of their own.

I also thank the Council of Scientific and Industrial Research (CSIR) for financial support.

A hundred times every day I remind myself that my inner and outer life are based on the labors of other men, living and dead, and that I must exert myself in order to give in the same measure as I have received and am still receiving. In the spirit of this quote by Einstein, let me conclude by thanking every one else who has through the chain of causality, action-reaction, known and unknown, allowed me to

be where I am and wherever I will be.

List of Publications

The thesis is largely based on the following publications.

- "Luminosity dependent star-formation history of S0 galaxies: evidence from GALEX-SDSS-2MASS-WISE colours" by Sudhanshu Barway, Yogesh Wadadekar, Kaustubh Vaghmare and Ajit Kembhavi (**2013 MNRAS 432 430B**)
- "A Spitzer Study of Pseudobulges in S0 Galaxies - Secular Evolution of Disks" by Kaustubh Vaghmare, Sudhanshu Barway, Ajit Kembhavi (**2013 ApJL 767L 33V**)
- "Spiral Galaxies as Progenitors for Pseudobulge Hosting S0s" by Kaustubh Vaghmare, Sudhanshu Barway, Smita Mathur and Ajit Kembhavi (**2015 MNRAS 450 873V**)

Other publications by me not included in the thesis are

- "Reflection-dominated Nuclear X-Ray Emission in the Early-type Galaxy ESO 565-G019" by Gandhi P., et al. (**2013 ApJ 773 51G**)
- "AstroStat: A VO Tool for Statistical Analysis" by Ajit Kembhavi, Kaustubh Vaghmare, et al. (**2015 A&C 11 126K**)

Abstract

Galaxies are the basic building blocks of the large scale structure of the Universe. They comprise a large number (10^{6-12}) of stars, gas, dust and dark matter and present themselves in a variety of morphologies. The first attempt at classification of galaxies was the famous tuning fork diagram proposed by Hubble (1936). In this scheme, the elliptical shaped galaxies are placed on the left hand side and comprise a single component of stars. The spiral galaxies, both barred and unbarred are placed on the right, arranged in the decreasing order of the bulge size and winding of the spiral arms. These galaxies, at minimum, are made of two basic stellar components namely the central bulge and the outer disk. Apart from these two classes, there are also galaxies which have a bulge and a disk but contain no spiral arms. These are known as S0 galaxies. As a large fraction of these are found to contain a lens-like structure in their disk, they are also known as lenticular galaxies.

Any classification scheme in any branch of science cannot be a random collection of objects. The scheme should capture the inter-relationships between the various classes and their broad properties. Hubble originally placed the S0 galaxies in between the ellipticals and spirals as a single class. Several decades later, the tuning fork continues to remain a starting point for any introductory treatment on galaxies. However, the implication of this position given to S0 galaxies can be debated. The Hubble tuning fork suggests that the S0 galaxies are all alike, have properties intermediate to ellipticals & spirals, and are a transition class. In recent decades, observational evidence suggests that this class encompasses a diverse range of objects with vastly different properties and hence formation histories.

When S0s are taken as a single class of objects and the correlations between their structural properties are investigated, they show a large scatter. In other words, they don't follow the trends otherwise followed by ellipticals or by spiral galaxies. However, Barway et al. (2007, 2009) show that it is possible to divide S0 galaxies into two bins of luminosity. The *bright* S0s and *faint* S0s behave differently indicating a different formation process at work. In particular, the bright S0s are more like elliptical galaxies and have likely formed in a similar manner viz. by hierarchical clustering and through mergers at an early epoch. The faint S0s on the other hand show signs of having formed through secular processes over a much larger

period of time. In Barway et al. (2011), they find that bar fraction in S0 galaxies is also a function of luminosity. In all these studies, environment i.e. whether a galaxy is isolated or lives in a group / cluster, also plays an important role.

If it is indeed true that the formation mechanisms of bright and faint S0 galaxies are different, this difference should be reflected in the star formation histories as well. The signatures of the star formation history can be found in the spectral energy distribution of these galaxies. As a part of this thesis, we have used multiwavelength data from ultravoilet through mid-infrared from surveys such as the Galaxy Evolution Explorer (GALEX), the Sloan Digital Sky Survey (SDSS), the Two Micron All Sky Survey (2MASS) and the Wide-field Infrared Survey Explorer (WISE) to check the luminosity dependence of star formation histories. The sample of galaxies used for the study is derived from the Uppsala General Catalog (UGC). We use various diagnostics such as the $FUV - NUV$ vs $NUV - K$ color-color diagram, the $NUV - r$ color and the $D_n(4000)$ index to compare the stellar populations as a function of luminosity and environment. We find that indeed bright S0 galaxies are consistent with a single coeval population of stars with age $\sim 10^{9-10}$ yr. The faint S0s however have a more complicated star formation history. The environment is found to have a secondary effect.

While in the first part of the thesis, the properties studied are of galaxies taken as a whole, the second part of the thesis focusses on individual properties of the bulges and disks. In particular, the dichotomy of bulges in the context of S0 galaxies is studied. By this we refer to the known existence of at least two types of bulges - the classical bulges which can be viewed as ellipticals surrounded by a disk (Renzini, 1999), and the pseudo-bulges which are currently understood to be inner disk-like components formed through secular evolution (Kormendy and Kennicutt, 2004). For this study, the surface brightness profiles of a sample of S0s and spirals, as captured in the 3.6 micron imaging provided by the Spitzer Space Telescope's Infrared Array Camera, are decomposed into the bulge, disk (and bar) components using the technique of 2-d image decomposition. The properties of the bulges are used to classify them on the basis of criteria established in literature by, for example, Fisher and Drory (2008) and Gadotti (2009). However, the data obtained by the Spitzer Space Telescope requires significant amount of preprocessing before the standard technique of 2-d image decomposition can be employed. Before presenting the results based on the obtained structural parameters, the thesis covers in great detail the steps needed for this preprocessing and their importance.

A comparison of the disk properties of classical and pseudo-bulge hosting S0s reveals differences depending on the type of bulge hosted. In particular, the scale length of the disk is on average smaller for pseudobulge hosting S0s compared to that of classical bulge hosting S0s. The S0s hosting these two types of bulges are

also found to obey an offset relation between the central surface brightness of the disk and its scale length. Pseudobulges evolve through secular processes in which the disk gas and stellar matter fall inwards as a result of instabilities within the disk, like a bar for example, leading to the formation of an inner disk like component. One can interpret the differences in the disk properties as signatures of the process that lead to the formation of the pseudobulges. An alternate interpretation can also be that there is a bimodality of disks in the Universe and at least for S0 galaxies, disks with lower scale length have a higher probability of hosting pseudobulges.

Another possible hypothesis to explain the differences in the disk properties of pseudobulge hosting S0s is that they are a signature of the processes responsible for transforming the spiral galaxies into S0s. For example, if a spiral galaxy is subjected to gas stripping, it will extinguish the star formation leading to the fading of spiral arms. This will cause the spiral to transform and appear like an S0 galaxy. In order to verify if this is possible, we compare our sample of pseudobulge hosting S0 galaxies with a sample of pseudobulge hosting spiral galaxies. We find that among them, the early-type galaxies are consistent with being the progenitors of pseudobulge hosting S0s in the gas stripping scenario while the late-type galaxies cannot transform into present day pseudobulge hosting S0s in the same manner unless aided by additional processes such as accretion of dwarf galaxies through minor mergers.

The first two parts of the thesis are statistical studies carried out using detailed analysis of imaging data for various samples of S0 galaxies. However, a true understanding of the formation history and properties of S0 galaxies requires detailed modelling and analysis of their spectrum. In the third part of the thesis, we review the methods by which long-slit spectra of the galaxies can be used to comment on their properties and describe an ongoing project with the Southern African Large Telescope (SALT). The thesis describes the pipelines developed for the basic data reduction, the determination of rotation curves and the modelling of spectra using Starlight (Cid Fernandes et al., 2005). Results for a subset of galaxies in the form of age gradients, change in population abundances as a function of the position along the major axis of the galaxy are presented. The consistency of the results with currently accepted formation mechanisms for these objects is discussed.

The thesis concludes with a summary of all the studies and a description of the potential work that can be done to further the understanding of S0 galaxies and galaxies in general.

Contents

List of Figures

List of Tables

List of Abbreviations

2MASS Two Micron All Sky Survey

ADC Analog-Digital Converter

ADU Analog-Digital Unit

AGB Asymptotic Giant Branch

ASCII American Standard Code for Information Interchange

BCD Basic Calibrated Data

BVIT Berkeley Visible Imaging Tube

CBCD Corrected Basic Calibrated Data

CB Classical bulge

CCD Charge Coupled Device

CDS Centre de Données astronomiques de Strasbourg

COBE COsmic Background Explorer

DIRBE Diffuse Infrared Background Experiment

DN Digital Number

DR7 Data Release 7

DSS Digitized Sky Survey

FFT Fast Fourier Transform

FIF Fiducial Image Frame

FITS Flexible Image Transport System

FP Fabry-Perot

FSPS Flexible Stellar Population Synthesis

FUV Far Ultraviolet

FWHM Full Width at Half Maximum

GALEX Galaxy Evolution Explorer

HET Hobby Eberly Telescope

HRS High Resolution Spectrograph

HST Hubble Space Telescope

ICM Intracluster Medium

IMF Initial Mass Function

IRAC Infrared Array Camera

IRAF Image Reduction and Analysis Facility

IR Infrared

IRS Infrared Spectrograph

JPEG Joint Photographic Experts Group

LR Low Resolution

MIPS Multiband Imaging Photometer

MJy Mega Jansky

M/L Mass-to-Light Ratio

MOPEX MOsaicking and Point EXtraction

MOS Multi Object Spectrograph

MR Medium Resolution

NASA National Aeronautics and Space Administration

NED NASA Extragalactic Database

NUV Near Ultraviolet

PAH Polycyclic Aromatic Hydrocarbons

PBCD Post Basic Calibrated Data

PB Pseudobulge

PSF Point Spread Function

RC3 Revised Third Catalogue

RSS Robert Stobie Spectrograph

SALT Southern African Large Telescope

SDSS Sloan Digital Sky Survey

SHA Spitzer Heritage Archive

SMA Semi Major Axis

SNR Signal to Noise Ratio

SSP Simple Stellar Population

TF Tunable Filter

TP Thermally Pulsating

UGC Uppsala General Catalogue

ULySS University of Lyons Spectroscopic analysis Software

UV Ultraviolet

VPH Volume Phase Holographic

WISE Wide-field Infrared Survey Explorer

Chapter 1

Introduction

Galaxies serve as the basic building blocks of the large scale structure of the Universe just as atoms serve as building blocks of our everyday lives' gross material. It is therefore essential to study the properties of galaxies and to understand their formation and evolution in order to grasp the overall workings of Nature when it comes to forming large scale structure. Galaxies are a conglomeration of 10^{6-12} stars and also contain gas, dust and dark matter. Much progress has been made since the times of Shapley and Curtis when astronomers were not even sure whether the first discovered galaxies, the spiral nebulae, were actually a part of the Milky Way or separate *island universes*. Thanks to powerful telescopes capable of seeing objects at unimaginable distances and powerful computers that not only enable the extraction of the last bit of useful science from data gathered by these telescopes but also the simulation of the the complex physics, there is much we now know about galaxies. And as is the case with the general pursuit of science, there are many voids in our knowledge and the thirst to try and fill as many as possible exists. The work done in this thesis is an attempt to try and fill one such void. The first section of this chapter focusses on a general introduction to galaxy morphology while the next section discusses a special class of galaxies known as S0 and its importance in understanding galaxy evolution in general. We then end with a discussion of the bulges of galaxies and a summary of what we know about their formation.

1.1 Galaxy Morphology

The morphology of a galaxy refers to its physical structure and form which in turn are products of how they formed, the nature of their interactions with the environment, internal processes responsible for their long term evolution, the effects of the elusive dark matter and their general star formation history. When a class of objects presents itself with a variety of forms, a logical starting point in understanding its members is to come up with a classification scheme. Ideally, such a classification

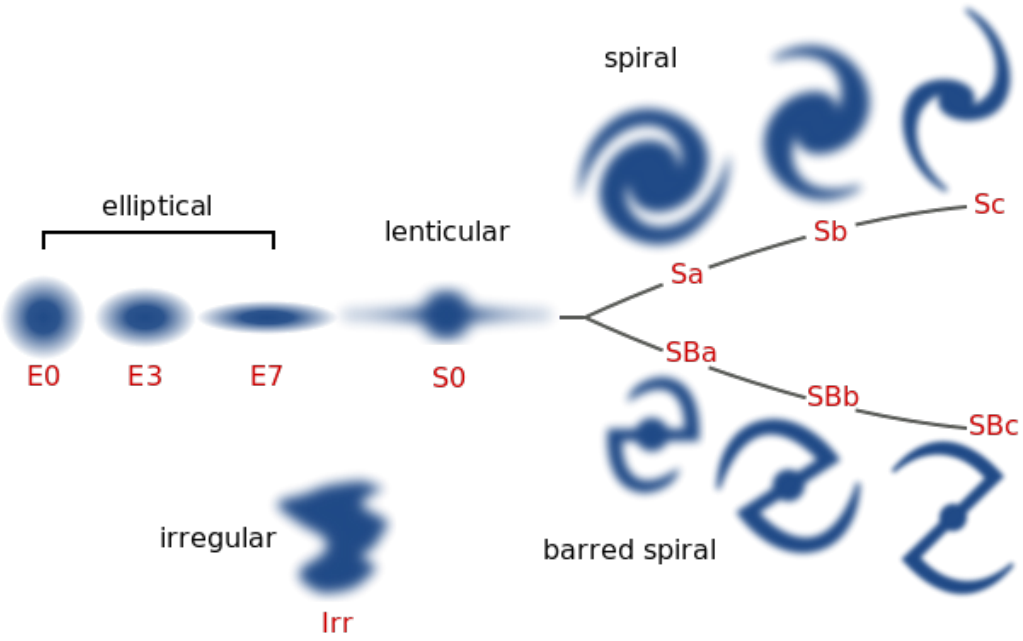

Figure 1.1: The Hubble tuning fork diagram of galaxy classification.

scheme arranges the various types in a manner that the arrangement itself speaks volumes of their commonalities and inter-relationships. The earliest attempt at classifying galaxies was made by Hubble (1936) who, in his book *The Realm of the Nebulae*, proposed a tuning fork diagram of galaxy classification, which even today remains a starting point for any introductory academic treatise on this subject.

A version of this famous tuning fork diagram is shown in Figure 1.1. On the left are galaxies that appear to have an elliptical shape and are arranged in increasing order of their ellipticity. Intrinsically, these are three dimensional ellipsoids and largely comprise an old and evolved stellar population as made evident by their *red and dead* appearance. To the right are two prongs of the tuning fork, with one prong reserved for galaxies containing a bar-like structure while the other prong for those without. On each prong, galaxies are arranged in decreasing order of the prominence of the nuclear region and the winding of the spiral arms. These galaxies have a more complicated structure than the ellipticals with at least two components - a bulge (explained in detail in the next section) and a disk. The disk in turn has spiral arms which show knots of star formation. Typical examples of an elliptical, a spiral and a barred spiral galaxy are shown in Figure 1.2. At the junction of the tuning fork are a class of galaxies that in appearance at least are somewhere in between - the S0 galaxies. These galaxies have a well defined central bulge and a disk but the disk has no spiral arms. They may or may not contain a bar like structure. These galaxies are often referred to as lenticular galaxies due to the presence of a lens-like structure in the disks of a vast majority of them.

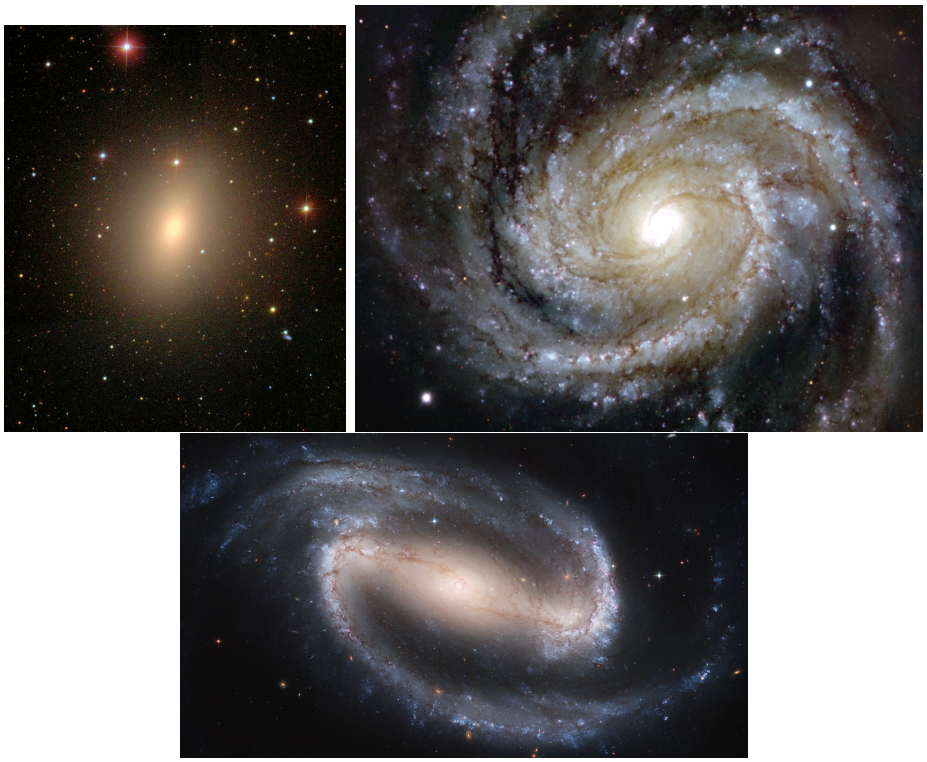

Figure 1.2: Examples of an elliptical galaxy (NGC 4621), a spiral galaxy (M100) and a barred spiral galaxy (NGC 1300). Images, from WikiSky/SDSS, ESA/VLT and NASA/ESA/HST respectively.

The ellipticals together with the S0s are known as early-type galaxies while the spirals, both barred and unbarred, are known as late-type galaxies. This terminology seems to suggest a hypothesis that elliptical galaxies represent a very early phase in the evolution of the galaxies and somehow ellipticals evolve into spirals. We now know beyond reasonable doubt that this view is not true but astronomers, living up to the reputation of devising eccentric and often confusing terminology, continue to use these terms even today. There are of course a lot of galaxies which have shapes so different from ellipticals and spirals that they cannot be placed anywhere on the tuning fork - they are called *irregular galaxies*.

Increasing observational data soon revealed the limitations of the original Hubble classification scheme and led to several attempts to either revise it or to propose a completely different formation scheme altogether. For example, Sandage (1961) using the incomplete notes of Hubble released *The Hubble Atlas of Galaxies* and proposed another dimension, that of the presence or absence of a ring in a galaxy. de Vaucouleurs (1959) introduced a concept known as a *classification volume*, where the classification scheme became more complicated with ellipticals being split to stages such as E^+, E^-, same with S0s etc. In 1976, van den Bergh introduced a trident classification scheme to overcome what he argues are severe limitations of the Hubble scheme. In the last decade or so, authors such as Cappellari et al. (2011) and

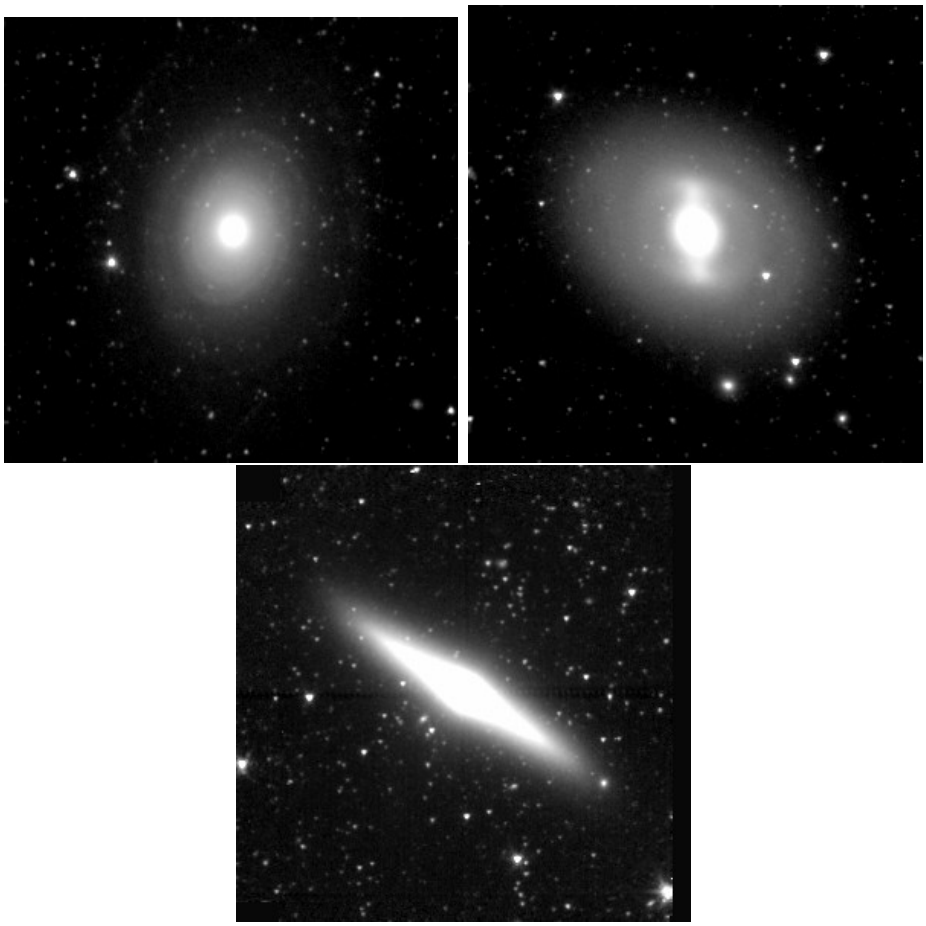

Figure 1.3: Example images of S0 galaxies. The galaxies are IC 5267, NGC 0936 and NGC 4026. All images are taken at 3.6 micron by the Spitzer Space Telescope.

Kormendy and Bender (2012) have in turn used modern data, both photometric and kinematic (spectroscopic) to try and come up with an ideal classification scheme.

Many of these changes made to the original Hubble tuning fork are in part due to the large body of observational and simulation studies done to understand the S0 class of galaxies. The present thesis also focusses on various aspects of these galaxies. A brief review of this class is provided in the next section.

1.2 Lenticular or S0 Galaxies

As defined earlier, these are galaxies which have a central bulge component and a disk without any apparent spiral structure. Galaxies classified as such can have other structures such as bars, rings or ovals (see Figure 1.3 for examples). Let us consider the position given to these galaxies on the Hubble tuning fork as shown in Figure 1.1. As argued earlier, a classification scheme cannot be a random arrangement of objects but should capture as much information as possible about the classes and their inter-relationships. The position given to S0 galaxies, implies three important

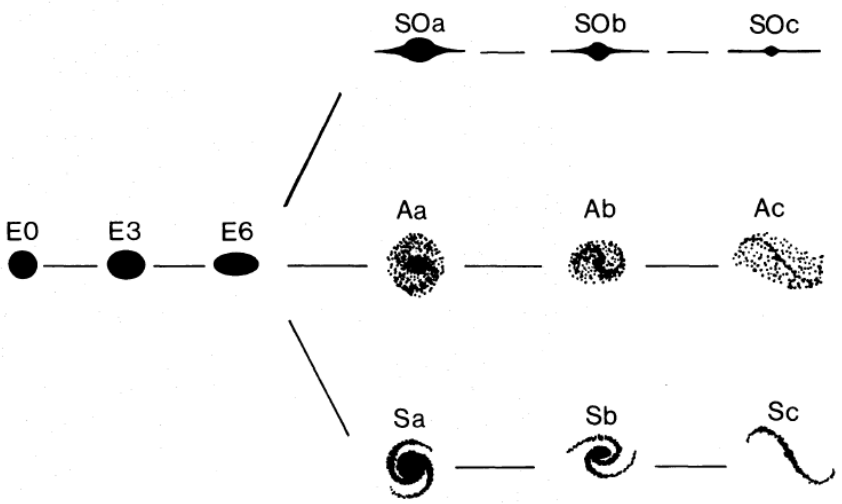

Figure 1.4: The trident classification scheme proposed by van den Bergh (1976).

points about this class of objects:

- They are a transition class. Processes responsible for transforming galaxies from one side of the fork to the other produce objects in the intermediate stage that resemble S0 galaxies.
- The properties of S0 galaxies are intermediate to those of the ellipticals and spirals. For several years, the observational data supported this - statistically, the average properties of S0s such as bulge-to-total luminosity ratios B/T, abundance of dust, star formation rates, amount of molecular gas etc were found to be intermediate to those of ellipticals and spirals.
- All S0 galaxies, as defined above are homologous to each other. In the words, they are all alike except for scale and share a common evolutionary process.

The beginning of the realization that the above picture painted by the Hubble tuning fork for S0 galaxies may not be correct can be traced back to van den Bergh (1976). He proposed an alternate classification scheme - *a trident*, shown in Figure 1.4 in which S0 galaxies were removed from their position at the junction and given a separate *third prong*. van den Bergh hypothesized that all S0 galaxies cannot be alike simply because the bulge-total ratio spanned a large range of values and it was unlikely that a single common formation mechanism could be responsible. He also created a class known as *anaemic spirals*, spiral galaxies whose arms are fading or have faded away. One of the motivations in creating the three prongs was to account for possible effects of environment such as gas stripping via ram pressure or galaxy harassment which could transform galaxies along the vertical direction. That such a transformation from a spiral to an S0 galaxy can occur is often said to be responsible for the morphology-density relation found by Dressler

(1980). According to this relation, the abundance of S0s in a cluster increases and that of spirals decreases with decreasing redshift.

Barway et al. (2007, 2009) showed that with respect to various well known correlations between structural parameters of the galaxies (refer to Chapter 2 for further details on how correlations can be used for commenting on the underlying formation mechanisms) S0 galaxies exhibit a large scatter. As these correlations are expected to arise in specific formation scenarios, this large scatter in turn implies a diversity in the formation mechanisms at work. The authors further show that the process dominantly responsible for the formation of the galaxy depends on the luminosity with the environment playing a lesser role. They divide S0 galaxies into bright and faint bins based on the K-band near-infrared luminosity and show that properties of bright S0s are consistent with having formed through major merger like events, as in the case of ellipticals, while the fainter S0 galaxies have likely formed through secular processes. If this is true, one expects the star formation histories, which are captured in the spectral energy distribution of the galaxies, to be markedly different for the bright and faint S0 galaxies. Investigating this possibility using multiwavelength photometry data was the goal of one the studies carried out as a part of this thesis. The results and techniques of this investigation have been explained in Chapters 3 and 4.

1.3 Bulges of Galaxies

What are bulges? While a large number of studies exist which comment on bulges, their properties and formation mechanisms, there is no clear consensus among astronomers as to how one can define them. Below we present a few ways in which bulges can be defined and provide the definition adopted in this thesis with justification.

The simplest method to define a bulge, although vague and subjective, is based on visual classification. In many galaxies, one can, by eye, see a central component of stars looking more concentrated and standing apart from the outer regions of the disk. However, defining a bulge this way has various issues. Firstly, it is a subjective process which means that the process of identification of bulges is not a reproducible one. Secondly, it does not allow to quantify the properties of the bulge. For example, to what radial distance the bulge dominates in terms of stellar light, is not well defined. This does not allow us to study bulge and disk properties in isolation, in a well defined manner.

Another method involves a study of isophotes, which are contours of equal intensity. One can choose to mark contours on the images using a utility like ds9[1] or one

[1] *ds9* is a program designed by the Smithsonian Astronomical Observatory which enables a user

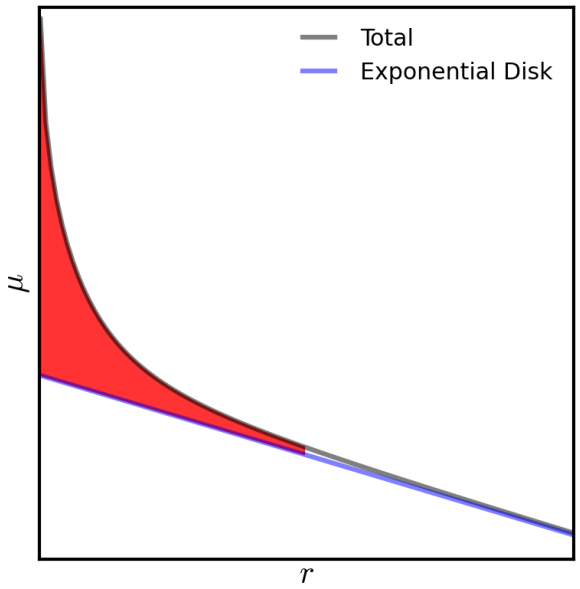

Figure 1.5: The photometric definition of a bulge. The red shade marks the excess light towards the centre of the galaxy which cannot be explained as an inward extrapolation of the exponential profile obeyed by the outer disk. (This figure is a reproduction of a similar figure by Gadotti.)

can actually fit ellipses to them using a suitable tool such as the *ellipse* program, which is a part of the Image Reduction and Analysis Facility (IRAF). The isophotes in the central region form a different family from those of the outer regions indicating physically distinct components. This definiton is physicallly well motivated but still lacks certain objectivity. The difference in isophotes is with respect to the position angle and ellipticity. How much change in these is *enough* to mark out the bulge component as separate from disk is where the subjectivity arises.

If the galaxy is edge-on, one can see the disk clearly and often a central component which is thicker or extends well above the plane of the disk. This component can be defined as the bulge. But this method will work only for edge-on galaxies which are rarer as can be deduced using a simple probability argument. This leads us to the photometric definition of a bulge, which despite some limitations, is the most commonly adopted definition in current astronomical literature.

Freeman (1970) showed that the light distributions of disks can be described using an exponential profile. Most of the light from the outer parts of late type galaxies is from the disk and thus can be modeled using an exponential profile (the details of modeling are covered in Chapters 2 and 5). However, when one extrapolates the disk profile inwards, one sometimes finds an excess of light. This is illustrated in Figure 1.5. The region where the excess of light arises can be defined as the bulge. This definition has two major advantages - it is objective and allows us to clearly define regions whose light is dominated by bulge and that by the disk.

to both view and analyze astronomical images

Thus this definition is adopted for the rest of the thesis.

Types of Bulges. Observational studies carried out before the mid-90s, showed that bulges of most late-type galaxies exhibit the following common trends:

- They are smooth and featureless, even when examined in high resolution imaging data of the kind provided by the Hubble Space Telescope (HST).

- They are kinematically hot components, i.e., they are random rotational velocity supported rather than rotationally supported systems. A mathematical definition of being kinematically hot is to say that $V/\sigma \ll 1$, where V is the stellar circular rotational velocity while σ is the velocity dispersion, a measure of the random motion of stars about the galaxy centre.

- They have a brightness profile close to the de Vaucouleurs $r^{1/4}$ profile which is known to describe the profile of elliptical galaxies.

- They contain a largely *red and dead* stellar population. Most of the stars have likely formed in a single burst of star formation at a very early epoch.

- They obey various correlations obeyed by elliptical galaxies. (Details of the correlations and their physical significance can be found in Chapter 2)

However, as better and more sensitive observational data became available, it became clear that some bulges in late-type galaxies exhibit properties quite different from those mentioned above.

- A close examination of the bulges in high resolution imaging revealed the presence of rich structure such as nuclear spirals, rings, and bars (Erwin and Sparke, 2002; Carollo et al., 1997).

- They are rotationally supported i.e kinematically cold systems. Mathematically, in such systems, $V/\sigma \gg 1$ (Kormendy, 1993).

- Their brightness profile is better described using an exponential profile as opposed to an $r^{1/4}$ profile (Andredakis and Sanders, 1994).

- They exhibit signs of recent and ongoing star formation. The stellar population is almost as young or perhaps even younger than that of the outer disk (Fisher, 2006).

- They do not obey some correlations which otherwise hold true for elliptical galaxies (Khosroshahi et al., 2000).

The bulges obeying the latter set of properties are clearly different from those obeying the first set of properties. It is reasonable to assume that the processes governing the formation of the two types of bulges should be different. Based on simulation studies, it is expected that the first type of bulges have likely formed through mergers - major and minor. These are known as *classical bulges* (Kormendy and Kennicutt, 2004) and can be described as ellipticals surrounded by a disk (Renzini, 1999). Bulges of the second type have likely formed through secular processes i.e. processes taking place slowly due to the build up of instabilities within the disk. A bar, for example, due to its non-axisymmetric potential leads to an orbital structure that causes gas to lose angular momentum and fall inwards, thus building up central gas density (Debattista et al., 2004) This can lead to the rise of a second component of stars which we would call a bulge. Such bulges are referred to as *pseudobulges*.

In current literature there is a certain ambiguity about the term *pseudobulges*. Boxy / peanut shaped bulges are also sometimes referred to as pseudobulges. These are inner parts of a bar that have buckled away due to vertical instabilities produced within it (Athanassoula, 2005). However, the process of formation is entirely different from the secular evolution scenario described above. In brief, boxy/peanut bulges are different from pseudobulges, which evolve secularly through material infall. In the current thesis, whenever the term pseudobulge is used, it refers to products of secular evolution satisfying the properties described above.

Many studies have been carried out in last few years by various researchers to study the differences in the properties of the pseudobulges and classical bulges. Fisher and Drory (2008) used high resolution imaging data obtained from HST to classify bulges and a follow up study, Fisher and Drory (2010), tried to explore the consistency of pseudobulges having formed through secular processes. Gadotti (2009) made detailed comparisons between ellipticals, classical and pseudobulges using a sample of $\sim$ 1000 galaxies from the Sloan Digital Sky Survey (SDSS). A common theme in these studies was to study the bulge dichotomy without any emphasis on the global morphology of the host galaxies. Given the peculiarity of the S0 class of galaxies, we thought that the bulge dichotomy in the context of S0 galaxies and a comparison with spirals would be interesting. Chapter 5 describes the sample and analysis techniques used for such a study while Chapters 6 and 7 describe the findings.

1.4 Outline of the Thesis

The thesis is broadly divided into three main parts following the introduction in Chapters 1 and 2. In Part 1, we study the dependence of the star formation histories

of S0 galaxies based on a sample derived from the Upsalla General Catalogue (UGC) with available multiwavelength photometry. Chapter 3 describe the sample itself and an outline of the kind of techniques and diagnostics used in this study. Chapter 4 describes the results and their implications for the formation of S0 galaxies in general.

The second part of thesis describes a quantitative morphology based study of S0 galaxies using deep mid-infrared imaging obtained with the Spitzer Space Telescope. Chapter 5 describes in the detail both the sample and the analysis while Chapter 6 describes possibly the first systematic study of S0 galaxies aimed at bulge classification and exploration of disk properties as a function of bulge type. Chapter 7 compares the pseudobulges of S0 galaxies with the bulges of spiral galaxies to unravel an evolutionary link between the two classes.

In the third part of the thesis, the study of S0 galaxies based on spectroscopic analysis done using long-slit data obtained from the Southern African Large Telescope (SALT) is described. Chapter 8 provides a general overview of spectroscopy, Chapter 9 describes SALT and its instruments while Chapter 10 presents detailed spectroscopic analysis of a sample of pseudobulge hosting S0 galaxies.

Chapter 2

Photometric Studies of Galaxy Morphology

"You can't do astrophysics by just taking pictures with little colored pieces of glass"

from "Astronomical Spectroscopy" by Phil Massey

The above quote stresses the importance of spectroscopy for gaining information about the properties of an astronomical source. This quote, however, downplays (intentionally or unintentionally) the power of image analysis and what it can tell us about the properties and the formation of the galaxies. In this chapter, we review quantitative methods of studying galaxy morphology and the nature of astrophysical insights that have been possible as a result of such image analysis.

2.1 Parametric Methods

Given an image of the galaxy one can construct a 1-d surface brightness profile - a plot of the surface light intensity or the brightness as a function of the distance from the centre of the galaxy. There are multiple methods to achieve this - the simplest being that one can take a slice along the major axis. Independent of the method used, what is important is that such a profile can be obtained and its behavior can be described using a simple mathematical function. de Vaucouleur found that in case of elliptical galaxies, the brightness varied as a function of $R^{1/4}$, with R being the distance from the centre. Figure 2.1 shows the surface brightness profile of a galaxy obeying such a law. The X-axis is deliberately chosen to be $R^{1/4}$ so that the plot appears as a simple straight line and brings out in a better way, the validity of $R^{1/4}$ profile.

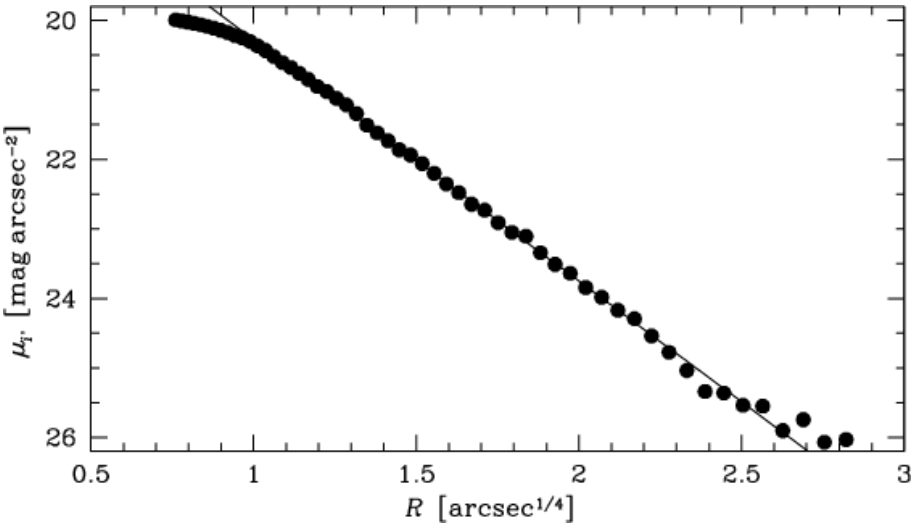

Figure 2.1: A surface brightness profile of a elliptical galaxy in a cluster. The X-axis is deliberately chosen as $R^{1/4}$ so that any galaxy obeying a $R^{1/4}$ profile results in a simply straight line on this plot. Courtesy: Lopes de Oliveira et al. (2006)

The de Vaucouleur profile can be written as:

$$I(R) = I_e \; e^{-b\left[\left(\frac{R}{R_e}\right)^{1/4}-1\right]} \tag{2.1}$$

I_e represents the intensity at *the effective radius* R_e. The quantity b can be chosen such that R_e represents the radius containing half the total integrated intensity. It can be shown that $b = 7.669$ if R_e is defined this way. It was later found that several elliptical galaxies do not obey this law and deviate systematically from it. Sersic (1968) generalized de Vaucouleur's law so that it could explain the brightness profiles for a wider sample of elliptical galaxies. This profile, referred in modern astronomy literature as the Sérsic law, can be written as:

$$I(R) = I_e \; e^{-b_n\left[\left(\frac{R}{R_e}\right)^{1/n}-1\right]} \tag{2.2}$$

Here, n is referred to as the Sérsic index. The quantity b_n is not an independent parameter defining the profile but is a function of n, again chosen such that R_e contains half the total light. The exact expression of b_n is quite complicated but it can be approximated using a simple polynomial $b_n = 1.9992n - 0.3271$ (Capaccioli, 1989). Thus the elliptical galaxy's structure can be quantified using the following parameters,

- R_e, a measure of the size.
- n, a measure of the concentration of light towards the centre. (To understand this better, refer to Figure 2.2 which shows the profile for a given effective radius but different values of n.)

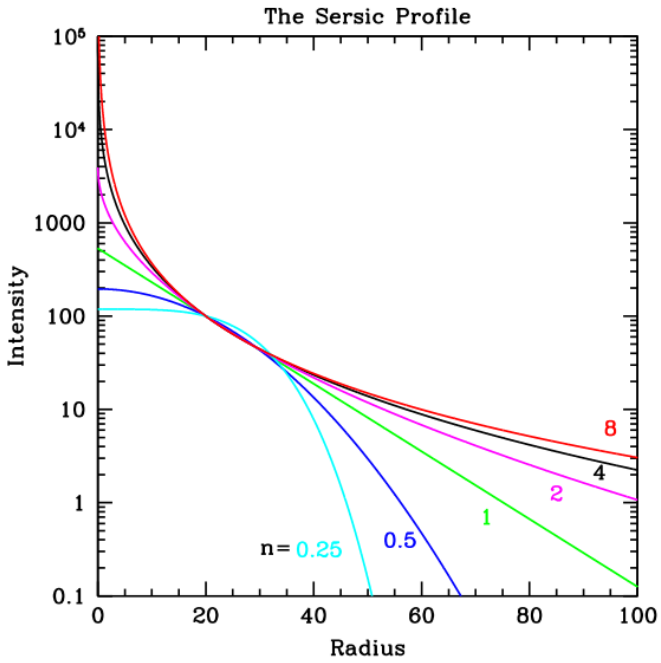

Figure 2.2: Sérsic profiles for a fixed effective radius but with varying values of n. Courtesy: Peng et al. (2002)

- I_e, a measure of the overall surface brightness of the galaxy. Generally, astronomers prefer to use the equivalent quantity μ_e, the surface brightness in mag per square arcseconds. I_e and the distance are independent quantities so long as one works in nearby Universe.

The technical difficulties associated with the exercise of deriving these parameters are deferred to Chapter 5.

The parameters derived for a single galaxy by themselves do not reveal much about it. But if a statistically signifcant and meaningful sample of galaxies is assembled and parameters are derived for all the galaxies, one finds various correlations between them which provide some insight on the common underlying astrophysics behind these objects. For example, Kormendy (1977) discovered a correlation between the surface brightness at effective radius and the effective radius of bright elliptical galaxies. This correlation implies that large galaxies have lower surface densities and which has implications for how galaxies formed. In modern literature, instead of plotting the brightness at effective radius, astronomers prefer to use the average surface brightness within the effective radius since it can be determined with a lower level of uncertainty.

By invoking relatively simple astrophysical arguments, it is possible to explain the physics behind the formation of elliptical galaxies knowing that the above correlation is valid and specifically the value of the slope of the relation. The Kormendy relation implies $R \sim I^{-0.8}$. Assuming the virial theorem and a constant mass-to-

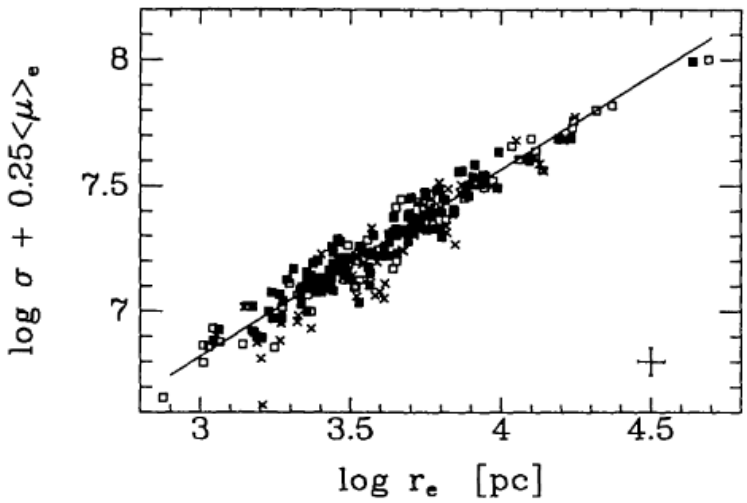

Figure 2.3: The fundamental plane as studied in Jorgensen et al. (1995).

light ratio, it can be shown that if elliptical galaxies form via dissipationless (dry) merging of two galaxies, $R \sim I^{-1}$ while if they form through rapid dissipative collapse of gas, via $R \sim I^{-0.5}$. That elliptical galaxies obey $R \sim I^{-0.8}$ implies that a combination of the two processes is at work.

Later, it was shown that the Kormendy relation is actually a 2-d projection of a higher dimensional relation, today known as the Fundamental Plane (Djorgovski and Davis, 1987; Dressler et al., 1987). This is a 3-d relationship between the velocity dispersion of the stars about the galaxy centre and the two quantities involved in the Kormendy relation. Mathematically, this relationship can be written as follows.

$$\log r_e = A \log \sigma + B \langle \mu \rangle_e + C \tag{2.3}$$

The relation as studied by Jorgensen et al. (1995) is shown in Figure 2.3. The Fundamental Plane serves several purposes:

- From a practical standpoint, the relation offers a method to estimate the distance of these objects. One can measure the average brightness and the velocity dispersion, which are distance independent quantities, to deduce the effective radius. Knowing the effective radius in units of kiloparsec in this manner and angular units from observations allows one to estimate the angular distance to the object.

- From a physical perspective, the relation tells us about the underlying physics governing the formation of elliptical galaxies. For example, by assuming the virial theorem, a smooth functional dependence of the mass-to-light ratio M/L on luminosity and that ellipticals form a homologous family, we can derive the fundamental plane and show that $M/L \sim L^{\sim 0.25}$. That elliptical galaxies obey

this correlation over a wide range of luminosities and other properties is a testament to common underlying formation processes.

Another example of a correlation is the photometric plane (Khosroshahi et al., 2000) which involves purely photometric parameters namely n, r_e and $\mu(0)$ (the central surface brightness). Studies such as Lima Neto et al. (1999) have interpreted this and other correlations from the point of view of systems attaining a local maximum in specific entropy.

Thus far, we have looked at the concept of quantitative morphology for elliptical galaxies. Freeman (1970) showed that the brightness profile of late-type galaxies on the Hubble tuning form which contain very little contribution from a bulge-like component, can be described using an exponential profile.

$$I(R) = I(0)\ e^{-r/r_d} \tag{2.4}$$

r_d here is the disk scale length and defines the distance from the centre at which the intensity falls to 1/e times the intensity at the centre, represented by $I(0)$. Thus the two key parameters describing the morphology of a disk are its central brightness and the scale length. For most late-type galaxies, the total surface brightness profile can be described by a combination of Sérsic and exponential profile. The process of fitting such a combination allows us to decompose the brightness distribution into the bulge and disk contributions.

So far, we have looked at examples of correlations involving parameters, all of which describe an elliptical galaxy or bulges of late-type galaxies, which earlier were thought to be ellipticals surrounded by disks. Courteau et al. (1996), however, found a strong correlation between the bulge effective radius and the scale length of the disk. This $r_e - r_d$ correlation offers insight into the dominant formation processes at work. Several studies have shown through simulations, that mergers of two disk galaxies or a series of mergers can form elliptical galaxies. These simulations can also reproduce the correlations described above. In the most extreme case, such a merger will lead to a pure bulge galaxy i.e. an elliptical. However, when sufficient amount of gas is present, bulge + disk systems can also form. This was considered as a viable mechanism for formation of a bulge+disk system for several years. However, in this process, the bulge forms first and later, the disk forms through accretion of cold gas under the gravitational potential of the dark matter halo and the bulge. In such a scenario, one does not expect the bulge and the disk parameters to correlate as the processes that form them are independent. Several authors have argued that the presence of the $r_e - r_d$ correlation rules out mergers as a possible mechanism to form a galaxy comprising a bulge and disk.

The alternate mechanism of formation invoked to explain this coupling between

the bulge and disk parameters is that of secular evolution. In this scenario, the disk forms first and later, instabilities in the disk such as a bar cause gas to fall inwards leading to a building up of central density viz. bulges. This way, the bulge formation is directly coupled with the disk and hence one expects bulge and disk parameters to be well correlated.

2.2 Non-parametric Methods

In the parametric approach, summarized in the previous section, the quantities used to describe the structure of the galaxy are free parameters of analytical functions used to describe a component of the galaxy. This assumes that a given model fully describes the target component. However, this need not be true. Cases in which this assumption breaks down are unrelaxed systems which have recently undergone a merger. Such galaxies exhibit a disturbed morphology and their light distribution cannot be fully described using conventional analytical models. Other cases are that of high redshift galaxies ($z \geq 1$) which are still forming and have not attained the structures as seen on the Hubble tuning fork. Another problem with the parametric approach to galaxy morphology is that (as explained in Chapter 5) it is not straightforward to implement automatically though pipelines such as PyMorph (Vikram et al., 2010) make a good attempt to to achieve this.

To overcome these limitations, a few researchers (Conselice, 2003; Lotz et al., 2004) have tried to develop alternate ways of describing the quantitative morpholgy of a galaxy, in a manner where no or minimal assumptions are made about the brightness distribution. These methods will be briefly mentioned for completeness but they have not been used in this thesis. In such a scheme the quantities used to describe the galaxies are

- Concentration. A ratio of radii containing specific fractions of the total galaxy light. This will be larger for elliptical galaxies and classical bulges while lower for late-type galaxies.

- Asymmetry. A difference of the original image and its version rotated by 180 degrees. This brings out global distortions in the shape of the galaxy and hence can comment on whether a galaxy is an unrelaxed merger remnant, for example.

- Clumpiness. The difference between the original image and a smoothened version of the same - highlights the high spatial frequency structure. This brings out star formation regions, spirals etc.

- Gini Coefficient. A measure of how unequally the light is distributed in a galaxy. This is similar to the Gini coefficient used in economics to estimate the inequality of wealth distribution.

- The M_{20} coefficient. The moment of 20% brightest pixels in a galaxy.

Using these coefficients, one can construct parametric spaces in which galaxies can be separated into various classes such as star bursts, ellipticals etc.

2.3 Summary

In this section, a review of quantitative methods of studying galaxy morphology have been presented with emphasis on the parametric approach. The parametric approach is a very powerful method by which the behavior of a sample of galaxies with respect to various correlations can be studied to unravel various aspects of the formation mechanisms at work.

Chapter 5 explains the details of the use of this technique. Chapter 6 explains the use of correlations for classification of bulges while Chapter 7 demonstrates the use of correlation studies in uncovering the connection between S0s and spirals.

Part I

Dependence of Star Formation Histories of S0 Galaxies on Their Luminosity and Environment

Chapter 3

The UGC S0 Sample; Study of Stellar Populations

As we have seen in Chapter 1, there is strong observational evidence for the existence of sub-populations within the S0 class of galaxies, with rather different properties and formation histories (Barway et al., 2007, 2009). The conclusion reached by these studies is based on the difference in behavior of the S0 galaxies with respect to well known correlations among the structural parameters of the galaxy, depending on their luminosity and environment.

Barway et al. (2007) plot the correlation between the bulge effective radius r_e and the scale length of the disk r_d for a sample of S0 galaxies. This correlation, first studied by Courteau et al. (1996) is important to constrain the dominant formation mechanism at work in building up a galaxy. In order to build a bulge-disk system, one can invoke two commonly discussed scenarios in galaxy formation. In the first scenario, two disk galaxies undergo a major merger and form a central bulge component; later, as the system settles down, conditions become suitable for the surrounding gas to get accreted under the gravitational influence of the dark matter halo and form a disk. In this case, the processes responsible for the formation of the bulge and the disk are independent and thus one does not expect the parameters describing bulge and disk properties to correlate strongly. In the second scenario, the disk forms first and later the instabilities in the disk cause gas to fall inwards leading to a bulge-like component forming at the centre. In this secular evolution scenario, one expects the parameters of the bulge and disk to correlate strongly.

Barway et al. (2007) find that S0 galaxies, considered as a single population, do not obey such a correlation. But when they divide the galaxies based on luminosity, clear trends emerge - bright galaxies are responsible for the large scatter in the relationship and obey a weak anti-correlation while faint galaxies obey a tight positive correlation. A figure from Barway et al. (2007), showing this correlation, has been reproduced in Figure 3.1. This clearly implies that the S0s can have diverse

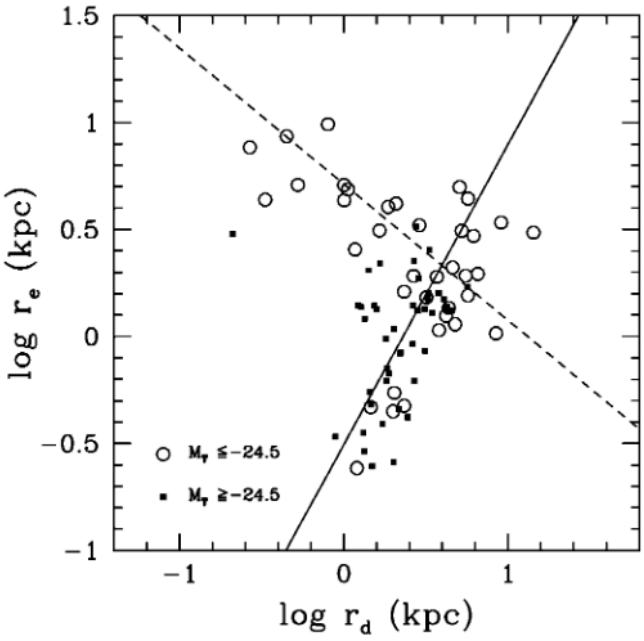

Figure 3.1: Figure 3 of Barway et al. (2007) showing S0 galaxies on $r_e - r_d$ diagram. The empty circles and filled circles indicate bright and faint S0 galaxies respectively.

processes at work in shaping them and which process is responsible seems to be strongly dependent on the luminosity. In subsequent work reported in Barway et al. (2009), other correlations such as the Kormendy relation etc were studied and again the differences for bright and faint S0s were found to hold true. Environment does play a role as well but as a second order effect. Barway et al. (2011) find that even bar fraction appears to be a function of luminosity and environment with fainter S0 galaxies more likely to host a bar than their bright counterparts.

If it is indeed true that different formation processes are at work for the bright and faint S0 galaxies, this must reflect in the star formation histories as well. The signature of whether a galaxy has formed its stars in one catacylsmic event at very early epochs or whether through slow/secular processes, will be embedded in its spectral energy distribution. The aim of the current study is to verify and study these differences using population synthesis techniques. This involves modelling the evolution of the integrated spectrum of the galaxy as a function of time. As obtaining spectra for a statistically significant sample of galaxies is uneconomical in terms of telescope time, we aim to use broadband photometry from wavebands ranging from ultraviolet (UV) to mid-infrared (mid-IR). The current Chapter focusses on a description of the process of sample construction and the techniques used while Chapter 4 explains the results and the significance of these results for the evolution of S0 galaxies.

3.1 Description of the Sample

3.1.1 Considerations in assembling the sample

Light from different wavelength regions brings with it information about different physical phenomena, conditions etc of the astrophysical source from which it emenates. Consider a galaxy which has experienced a recent burst of star formation - its population has a component of young and hot, blue stars which contribute significant amount of light in the UV region. These stars, being very massive, live for relatively short time. The low mass stars in the burst which emit most of their light in the infrared, live for a longer time. Thus, by using a color[1] based on photometric measurements in the UV and infrared, it is possible to distinguish between galaxies which have experienced recent star formation and those with the bulk of stars formed at an early epoch. This provides insight on the star formation history of the galaxies, which is the aim of the current study.

The Sloan Digital Sky Survey (SDSS) is an important and influential sky survey carried out since 2000 which collects information, both photometric and spectroscopic, of all astronomical sources within its detection limit. The data are distributed through a series of data releases. The photometry is done in five bands namely u, g, r, i and z. Using the spectra collected through a $3''$ fiber placed on the center of the objects, various quantities such as the redshift or the $D_n(4000)$ index (to be described later) are also determined and made available to astronomers. Using the data from SDSS, studies such as by Tago et al. (2010) determine the environments of these galaxies. Thus, the SDSS presents itself as an invaluable resource to any study such as ours requiring multi-wavelength photometry as well as environment information. Note that the SDSS is not an all-sky survey but is constrained to a specific region largely in the northern celestial hemisphere.

Photometric measurements from other wavebands can be acquired through various surveys. The Two Micron All Sky Survey (2MASS) (Skrutskie et al., 2006) is an all sky survey conducted in the J, H and K_s[2] near-infrared wavebands. The Galaxy Evolution Explorer (GALEX) has conducted surveys of the sky and measured the near ultraviolet (NUV) and far ultraviolet (FUV)[3] magnitudes of sources. The Wide-field Infrared Survey Explorer (WISE) (Wright et al., 2010) has conducted an all-sky survey in mid-infrared wavebands centered at 3.4, 4.6, 12 and 22 microns. Data from these surveys combined with those from the SDSS are ideal for our intended study.

[1] A difference in magnitudes measured in two wavebands/filters for the same source.

[2] The K_s band is similar to the K-band except that it has a more abrupt cut-off at a shorter wavelength.

[3] NUV and FUV bands have effective wavelengths of 2267 and 1516 angstroms.

3.1.2 Sample Construction

Since the study was intended to be carried out on S0 galaxies, a catalogue with detailed visual classification was needed. We used the Uppsalla General Catalogue (UGC) (Nilson, 1973) which is essentially complete to a limiting major-axis diameter of 1 arcmin or to a limiting apparent magnitude of 14.5 on the blue prints of the Palomar Observatory Sky Survey for the sky north of declination −2.5 degrees. Detailed visual classification has been done by expert astronomers for all the galaxies in this catalogue.

All galaxies classified as S0 in the UGC and having a total integrated B-band magnitude greater than 14.0 form our parent sample, comprising 635 galaxies. This sample was cross-matched with the SDSS DR7 (Abazajian et al., 2009) - 387 galaxies were found having imaging data in all the five bands. Of these 387 galaxies, all but two galaxies have imaging in the near-infrared bands of 2MASS. The images of the remaining two galaxies are affected by artifacts rendering them useless. Further, redshift information was not available for four galaxies plus another ten galaxies were found to be classified as ellipticals or spirals, according to the homogenized classification available on the NASA Extragalactic Database (NED)[4] and HyperLeda[5]. These databases, operated and maintained by the National Aeronautics and Space Administration (NASA) of USA and the University of Lyons of France respectively, collate information on objects from a variety of sources and use various methods to homogenise the information, which is thus likely to be more accurate than that in the UGC, which is based on the relatively shallow images from the Palomar Observatory Sky Survey. As a result of the filtration, the sample at this stage consists of 371 S0 galaxies.

In the next stage, these 371 galaxies were cross matched with the GALEX GR6 (the sixth major GALEX data release) and FUV and NUV data were found for 243 galaxies. The galaxy UGC 9094 has a very noisy image in both the bands and was thus excluded from the sample.

3.1.3 Verification of Morphological Classification

The morphological types listed in the UGC catalogue were determined visually using blue photographic plates obtained from the Palomar Observatory Sky Survey. It is possible that spiral features may not be seen without deeper imaging and thus a galaxy is classified as S0 despite having spiral arms. To reduce the possibility of contamination of the sample of S0s from spirals or ellipticals, we visually inspected images of all galaxies classified as S0 in the UGC.

[4]http://nedwww.ipac.caltech.edu/
[5]http://leda.univ-lyon1.fr/

For this purpose, two sets of images were used.

- The coloured JPEG images provided by the SDSS website.

- High signal-to-noise ratio images produced by combining images from g-, r- and i- bands using a prescription provided by Lisker et al. (2006).[6]

In the first set of images, any spiral features can be easily discernable by the eye while the overall depth of the second set of images reveals any underlying faint features. These sets of images were inspected independently by two researchers involved in the study and it was found that

- The five galaxies UGC 1157, UGC 4596, UGC 4963, UGC 5638, UGC 8204 were misclassified as S0. They contain spiral arms as revealed in the images used for visual inspection and were removed from the sample. These images are shown in Figure 3.2.

- A few galaxies show very weak asymmetries and traces of possibly faded spiral arms. These have been kept in the sample.

- Five objects were found which resembled elliptical galaxies. However, it is not possible for visual inspection alone to be able to differentiate between ellipticals and S0s, especially when they are face-on. As the number of such ambiguous cases relative to the total number of objects present in the sample is low, these objects were retained.

The final sample comprises 237 objects, classified as S0 and with broadband imaging data in the bands - FUV & NUV from GALEX; u, g, r, i & z from SDSS; H, J & K from 2MASS and 3.4, 4.6, 12 and 22 micron from WISE.

[6] In this prescription, the following steps are carried out:

- Smoothen the image by convolving it with a Gaussian kernel. This can be done using the Image Reduction and Analysis Facility (IRAF).
- Run SExtractor and produce a segmentation image - this marks all the pixels occupied by the sky as zero and those occupied by the objects as non-zero.
- Use the *imstat* task in IRAF to estimate the background in each image and subtract it.
- Use the *imshift* task in IRAF to shift the g-band and i-band images to match the r-band image.
- Apply a weight of $w_{g,i} = S_{g,i}\sigma_r^2/S_{r,i}\sigma_{g,i}^2$ to the g- and i-band images.
- Co-add the weighed, shifted and background subtracted images.

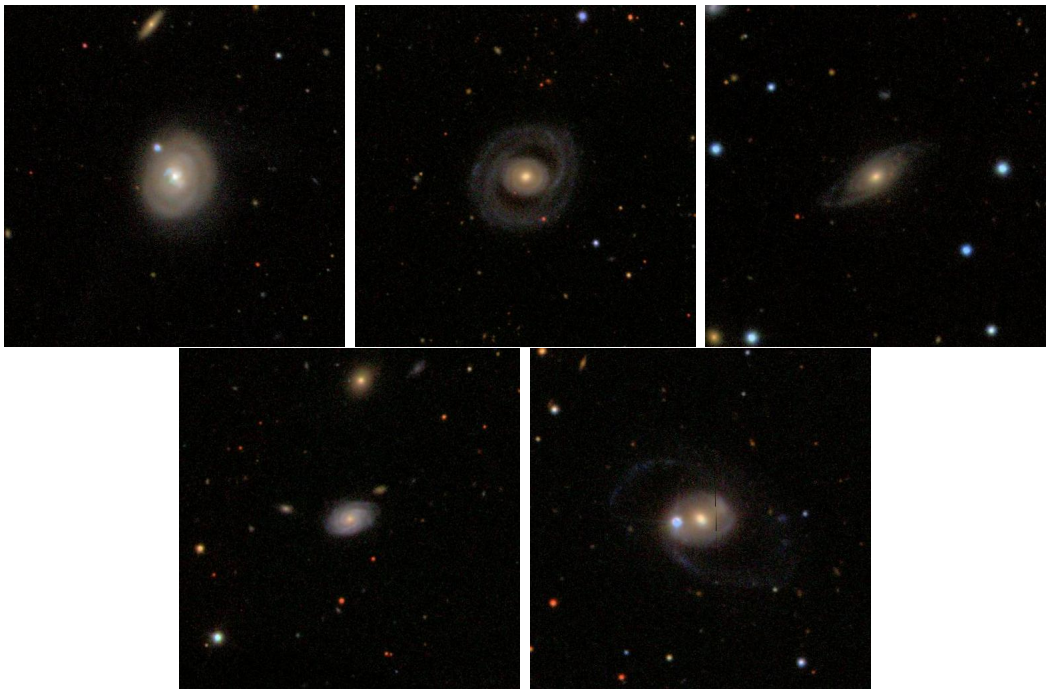

Figure 3.2: The SDSS color images of five galaxies, originally classified as S0 but found to contain spiral arms. From top-bottom, left-right, there are UGC 1157, UGC 4596, UGC 4963, UGC 5638, UGC 8204.

3.2 Basic Corrections to Photometry

Magnitude System The AB magnitude system[7] (Oke and Gunn, 1983) was adopted for the current study. The magnitudes reported in the data releases of GALEX, SDSS and WISE are already in the AB magnitude system while those in the 2MASS are in the Vega system. To convert the K-band Vega magnitudes of 2MASS to the AB system, we add 1.84 as suggested by Cohen et al. (2003) and Muñoz-Mateos et al. (2009). The J and H-band magnitudes have not been utilized in the study and thus no conversions were applied to them.

Foreground Extinction The light from any galaxy is affected by the dust present in our Galaxy - the Milky Way. This is known as foreground extinction and in order to correct the photometry measurements for it, we require two pieces of information - (i) a redenning map which, based on data collected from observational studies, determines how much dust the light from a given source located at a certain point

[7]Unlike the Vega magnitude system where magnitudes are assigned relative to the energy flux received from the Vega star, the AB system is directly defined in terms of absolute flux. If f_ν is the flux measured in units of Jansky ($10^{-26}\mathrm{WHz}^{-1}\mathrm{m}^{-2}$), then the AB system magnitude is given by

$$m_{AB} = -2.5 \log f_\nu + 8.90$$

in the sky will pass through, and (ii) an extinction law which describes the intensity of light attenuation due to dust as a function of wavelength. For (i), the redenning maps from Schlegel et al. (1998) were used while for (ii) the extinction law described in Cardelli et al. (1989) and Wyder et al. (2005) was used. All photometric measurements were corrected for foreground extinction in this manner.

K-correction The median redshift of the sample is ~ 0.01. Thus, one does not need to perform any K-corrections to the photometric measurements.

3.3 Sample Subdivision Based on Luminosity and Environment

In the introduction to the current chapter we reviewed in detail the dependence of the dominant formation histories of S0 galaxies on their luminosity as established by Barway et al. (2007, 2009). The authors used the technique of 2-d image decomposition (descibed in Chapter 5) and measured the bulge effective radius r_e and the disk scale length r_d. They found that S0s did not obey such a correlation i.e. there was a large scatter. But when the S0s were divided into *bright* and *faint* groups using the K-band absolute magnitude of -24.5 (Vega system), they found that the bright S0s were responsible for the scatter while the faint S0s obeyed a tight correlation. This division line of -24.5 is somewhat arbitrary i.e. there is no physical reason why this boundary must be used. But its use results in the sample being divided into roughly equal halves and also distinguishes their behavior on other correlations. A small shift (0.5-1 magnitude) in this boundary does not result in any appreciable change in the results.

For the current sample, we adopt the same K-band absolute magnitude limit to divide our sample into bright and faint luminosity bins. Since the original division line was derived in the Vega system while the current study uses the AB system, we first transform the boundary by adding 1.84 (following Munoz-Mateos et al. 2009). A galaxy is then classified as bright if $M_K < -22.66$ and faint if $M_K > -22.66$. The distribution of absolute K-band magnitudes along with this division line are shown in Figure 3.3.

To obtain the environment information for these galaxies, we use the results from Tago et al. (2010) who use a friends-of-friends algorithm on the entire SDSS DR7 data set to identify groups of galaxies. In the catalogue by Tago et al. (2010), only those galaxies which are members of a group are present along with group IDs and number of members in the group. Using this information, the galaxies are classified as either *field* galaxies (absent in the catalogue of groups) and *group/cluster*

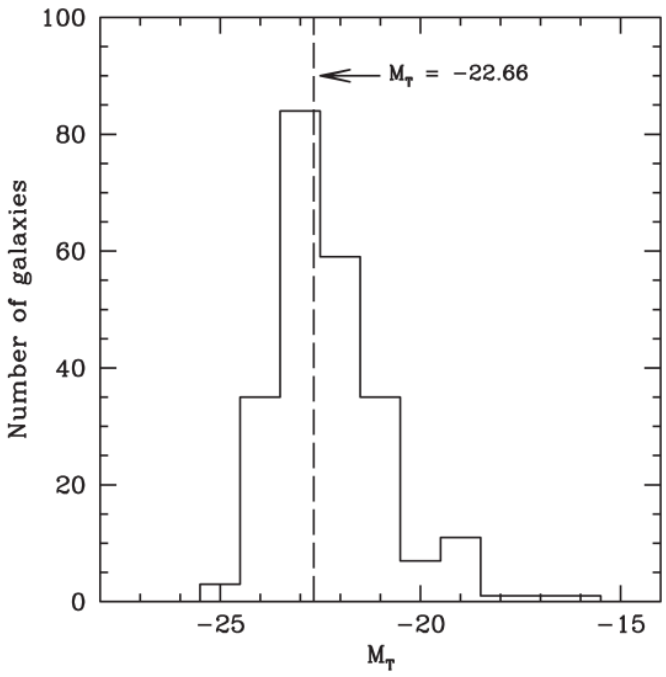

Figure 3.3: Distribution of total K-band absolute magnitudes for the current sample.

galaxies (present in the catalogue of groups). The Tago et al. (2010) catalog does not offer any information about whether a galaxy belongs to a group (a relatively loose but bound collection of galaxies) or a cluster (a tightly bound collection of galaxies). The information about whether a galaxy belongs to a cluster comes from literature survey done using NED as a starting point. For convenience, galaxies from either a group or cluster will be simply referred to as *group galaxies*. Of the 237 galaxies being used in the final sample, 64 are in the field while 173 are in a group environment. This low fraction of S0 galaxies in the field environment is consistent with the morphology-density relation found by Dressler (1980), according to which the relative fraction of the S0s present in groups/cluster environment increases with cosmic time i.e. towards smaller redshift while the fraction of spirals decreases. This finding has often been interpreted as lending strong support to the hypothesis that spiral galaxies transform into S0s through various intra-cluster processes.

In Figure 3.4 is shown the break-up of the number of galaxies in different luminosity and/or environment bins.

3.4 Tracing the Evolution of a Galaxy on a Color-Color Diagram

As mentioned earlier, the regions in galaxies which have experienced recent star formation dominate in the UV light and are thus well traced by images obtained

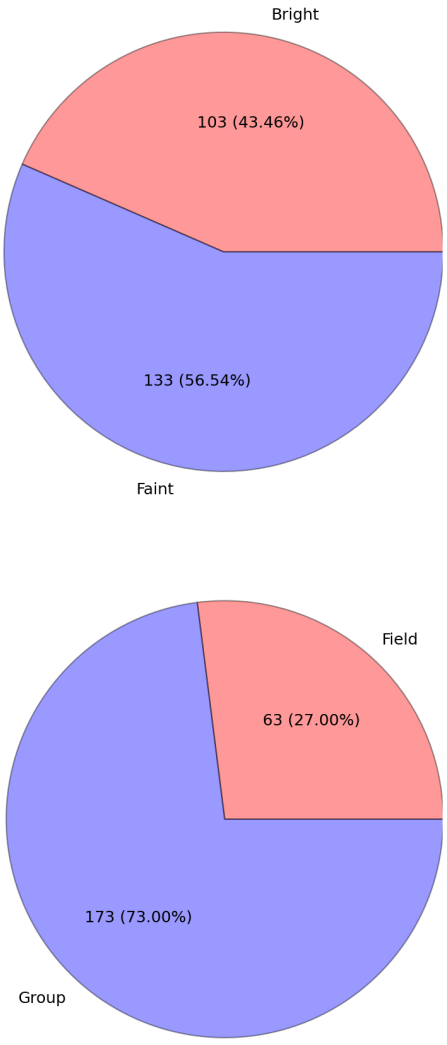

Figure 3.4: The distribution of the final sample of 237 S0 galaxies into luminosity and environment bins. The pie chart on the top shows that more or less equal fraction of S0s reside in both bright and faint bins. However, as the pie chart on the bottom shows, a very small fraction of S0s are found in field environments - this high fraction of S0s in group environments is consistent with studies such as Dressler (1980).

from GALEX. On the other hand, the near-IR images obtained from 2MASS trace the older stellar population of the galaxies which are dominated by low mass stars. The NUV detector on the GALEX is very sensitive to the presence of a young stellar population enabling us to detect very small fractions (1-3%) of young stars formed in the last few billion years (Schawinski et al., 2006). Thus one can separate out galaxies with dominantly old and dominantly young stars by making a color-color diagram with NUV as a common filter.

On such a plot, we would like to draw a curve which traces out the galaxy's position as a function of age. At low ages, the young & hot stars dominate the stellar light budget but since these stars are massive, they consume their fuel rapidly and die out. So, at later times, the galaxy is dominated by the longer-lived, cooler low mass stars. In order to draw such a curve, one needs the following information

- a library of stellar spectra; how the spectrum of a star with given mass, metallicity and temperature looks like at any given point in its lifetime
- evolutionary tracks or models; how the stars move along the Hertzsprung-Russel[8] diagram as a function of time
- an initial mass function; when the star burst occurs, what is the distribution of stellar masses?
- a growth function which describes the star formation rate as a function of time.

S0 galaxies have traditionally been believed to form at an early epoch via a major merger or rapid collapse and so a single instantaneous burst of star formation is a good approximation to its star formation history (called SSP, a Simple Stellar Population). Using a variety of tools such as GALAXEV (from Bruzual & Charlot 2003), FSPS or Flexible Stellar Population Synthesis (Conroy et al., 2009) or EzGal (Mancone and Gonzalez, 2012), it is possible to evolve the integrated spectra as a function of time. These tools are able to construct the spectra using a simple procedure outlined below:

- Use the initial mass function (IMF) to find the relative contributions of stars of various masses.
- Locate the spectra corresponding to each consitituent star from the stellar library.
- Add these spectra weighed by their relative contribution as determined above to find the integrated spectrum at $t = 0$.

[8] A plot between luminosity and temperature of stars which is used for studying stellar evolution

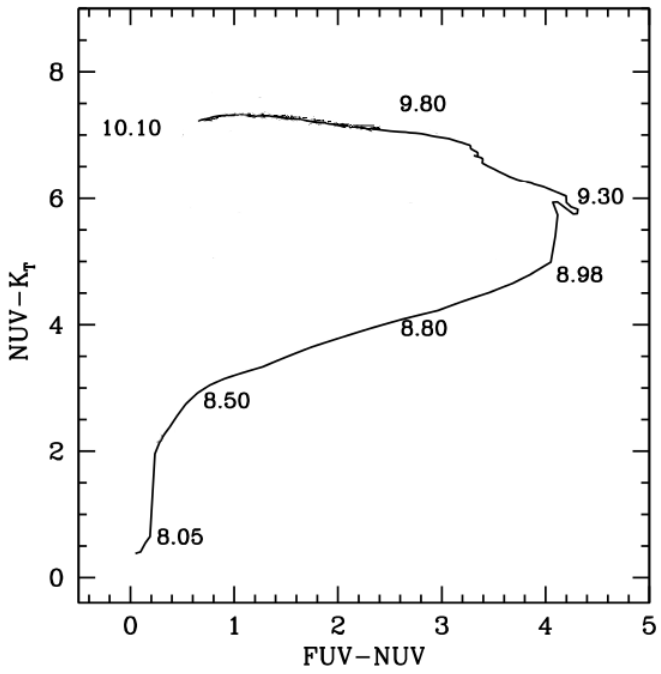

Figure 3.5: A plot of NUV − K_T against FUV − NUV with a line marking the evolution of an SSP as a function of age. The numbers along the curve denote the logarithm of the age of the SSP.

- Using evolutionary tracks, one can find where on the Hertzsprung-Russel diagram, the initial population has evolved to.
- Construct the integrated spectrum by adding appropriate spectra with appropriate weights.
- Repeat the process for subsequent ages.

At any given time in the life of a stellar population, the integrated spectra can be convolved with a filter response function[9] to obtain the broadband magnitude of the object. This in turn allows one to construct colors and thus see how an SSP evolves on a color-color diagram. We model an SSP using stellar library and evolution tracks from Charlot & Bruzual (2007), which are an improved but unpublished version of those described in Bruzual and Charlot (2003), along with a Salpeter IMF. This is shown in Figure 3.5. The numbers along the curve are logarithms of the age.

How sensitive are the trends in Figure 3.5 to the choice of the IMF and the libraries? The libraries and the evolution tracks are a result of several researchers creating radiative transfer and atmospheric opacity models and evolving them as a function of stellar age. These models are well determined for stars in the main sequence and several other branches *but* a lot remains unclear about certain specific

[9] A function which describes the fraction of light allowed to pass through by a filter as a function of the wavelength.

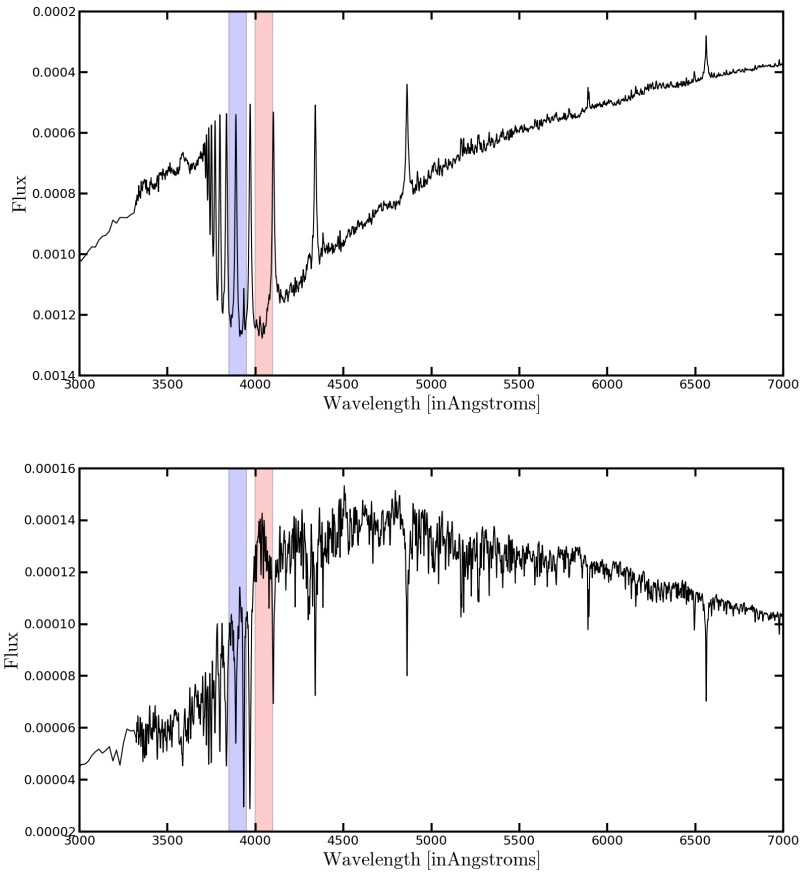

Figure 3.6: The integrated spectrum of a Simple Stellar Population at ages 100 million years (top) and 1 Gigayear (bottom). The blue and red strips mark the regions in which flux is integrated to measure the $D_n(4000)$ index. These spectra have been constructing using a suite of tools called GALAXEV made available by Bruzual & Charlot at the URL http://www2.iap.fr/users/charlot/bc2003/.

phases of evolution. For example, the Asymptotic Giant Branch (AGB) or the Thermally Pulsating (TP) stars are not well understood. Different libraries and evolution tracks differ with regards to these phases. For studies aimed at star burst galaxies or those whose populations are of the order of few million years old, the choice of tracks and libraries can make significant difference. However, when dealing with S0 galaxies, such a choice is unlikely to make a difference since S0s formed at early epochs as well as those which have assembled their mass recently would have a majority of stars whose properties are well understood. Thus the choice of stellar libraries or even the IMF are not expected to affect the broad trends explored in this study.

3.5 The $D_n(4000)$ break

Consider a galaxy whose stars have formed in a single instantaneous burst of star formation. At an age of 100 million years, it will have an integrated spectrum as shown in the top panel of Figure 3.6. The stars in such a galaxy are allowed to evolve for about a Gyr. During this time, several changes take place - the very massive blue stars evolve off the main sequence and die away in a display of cosmic fireworks known as supernovae. The older, low mass stars synthesize heavier elements or metals which generally exist in ionized state. Their presence in the atmospheres cause absorption at several closely spaced wavelength in the < 4000 angstrom part of the spectrum. As a result, there is a sudden break in the flux at the 4000 angstrom wavelength. This can be seen in the second panel of the Figure 3.6.

This break can be quantified in a number of ways. For the present study, the definition provided by Balogh et al. (1999) is adopted. The total fluxes in the blue continuum in the wavelength range of 3850-3950 angstroms and that in the red continuum with wavelength range 4000-4100 angstroms are measured. The ratio of the flux in red continuum to the blue continuum is defined as the $D_n(4000)$ index. Referring again to Figure 3.6, it can be clearly seen that the value of the index will be larger for a dominantly older stellar population while smaller for a recently formed stellar population. Another virtue of this index is that it very insensitive to redenning effects of dust owing to the very closely spaced red and blue continuums used for determing it.

In the SDSS DR9 (Ahn et al., 2012), spectra of galaxies as measured by a $3''$ fiber have also been provided. The SDSS pipeline automatically determines the $D_n(4000)$ index and makes it available in the *galspecindx* table. However, this index is not available for all the 371 galaxies available in the SDSS. Owing to the design of the instrument, there is a cut-off at the bright magnitude end beyond which the detector saturates and experiences cross-talk. So, data for only 180 galaxies are available. Thus, when exploring the behavior of the S0 galaxies in the current sample with respect to this index, only this subset will be utilized.

In the next chapter, the behavior of S0 galaxies on these and other diagnostic plots, as a function of luminosity and environment is described, along with implications of these results.

Chapter 4

Dependence of Star Formation History of S0s on Luminosity and Environment

4.1 Nature of Stellar Populations in S0s

4.1.1 Examining the $FUV - NUV$ vs $NUV - K$ Color-Color Diagram

A detailed description of how the $FUV-NUV$ vs $NUV-K$ color-color diagram can be used to get a quick overview of the nature of the stellar population in a galaxy, has been presented in section 3.4. The sample of S0s, the construction and properties of which were described in the previous chapter is plotted on such a diagram as shown in Figure 4.1. The bright S0 galaxies are denoted as empty circles on this diagram while the faint S0s are denoted by filled circles. A close inspection of this figure reveals that the bulk of the bright S0s sit in a region corresponding to an SSP of age $\sim 10^{9-10}$ years. Thus the dominant population of stars in these galaxies is of the old, low mass type. These stars could have all formed in the same galaxy by a rapid collapse-like mechanism or it is also possible that a series of dry major mergers between ellipticals or disk galaxies at a very early epoch is responsible for such a stellar population.

This result means that these bright S0s resemble ellipticals both in terms of the dominant stellar population as well as possible formation mechanisms. This result is not surprising because in several earlier studies, the S0 galaxies have indeed been found to resemble elliptical galaxies in their 'red and dead' appearance except that they are surrounded by a disk. Even the place of the S0s on the Hubble tuning fork was motivated by the close similarities in the optical colors of the ellipticals and

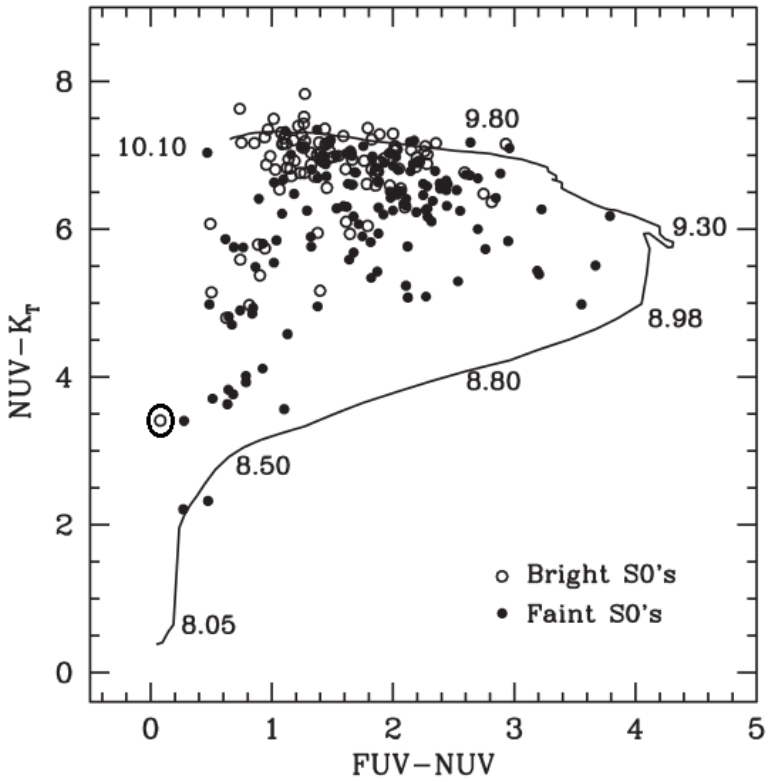

Figure 4.1: A plot of $NUV-K$ color plotted against the $FUV-NUV$ GALEX color with empty and filled circles respectively denoting the bright and faint S0 galaxies. The contour traces the evolution of a Simple Stellar Population as a function of time. The numbers denote the logarithm of the age in years. A bright S0 galaxy which is removed from the region occupied by most has been marked with a black circle.

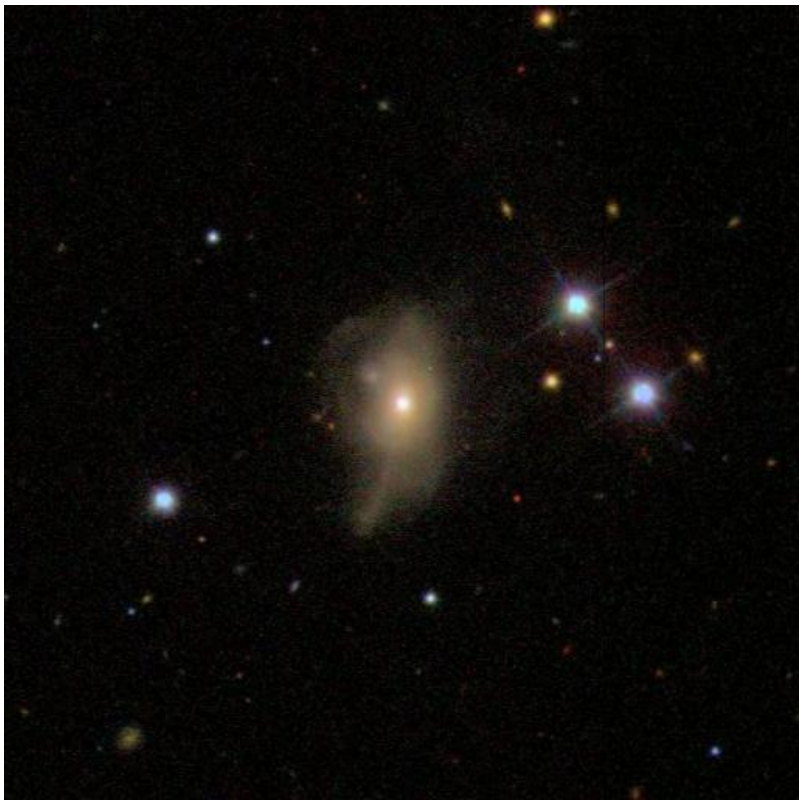

Figure 4.2: The SDSS color image of the galaxy UGC 1597. This galaxy is a strong outlier in the plot shown in Figure 4.1. Inspection shows a disturbed appearance which in turn implies a recent merger.

S0s. This result is also consistent with the those of Barway et al. (2007, 2009) who find that bright S0 galaxies obey similar correlations as their elliptical counterparts. That the ellipticals obey these correlations indicate they are virialized, pressure supported and dynamically hot systems, known to form through major merger as various simulations studies have demonstrated. So it is likely that bright S0s formed in a similar manner.

A close inspection of the empty cirlces on Figure 4.1 reveals one which is removed from the rest - towards the lower left - implying extreme blue colors known to be quite uncharacteristic of elliptical galaxies. This galaxy is UGC 1597. A close inspection of the SDSS image, shown in Figure 4.2, of this galaxy reveals a disturbed appearance, indicating a recent merger. The spectrum obtained from the SDSS fibre shows a strong H_α emission line, a sign of strong star formation. Further, the galaxy is known to be a Seyfert galaxy. All these properties can explain why this galaxy breaks away from the trend shown by other bright S0 galaxies. For subsequent analysis, this galaxy is removed from the sample.

The faint S0 galaxies, indicated as filled circles, show a much larger scatter in Figure 4.1. More than half of these galaxies are well away from the contour expected to be followed by an SSP. This means that the stellar population in these galaxies

cannot be explained as having formed in a single episodic burst of star formation - the star formation history is more complicated. If we consider a scenario where disk instabilities cause gas infall leading to slow star formation sustained over a long period of time, the spectrum and hence colors of such galaxies would look significantly different from those formed in a single episodic burst. The bulges of such galaxies would not be expected to follow the trends of elliptical galaxies and hence one would expect them to deviate from the tight correlations obeyed by the ellipticals. This is precisely what was found by Barway et al. (2009). It should be noted that not all faint S0s exhibit this trend, a good fraction of them in fact are consistent with an SSP.

4.1.2 UV-Optical Colors

It's been shown by various studies such as Schawinski et al. (2006) that UV-optical colors can be used to differentiate between younger and older stellar populations. In particular, Schawinski et al. (2006) show that galaxies with recent star formation will have NUV − r < 5.4. Having both NUV measurements from GALEX and r-band photometry from SDSS, we plot in Figure 4.3 a color-color diagram between $FUV - NUV$ and NUV − r. The division line proposed by Schawinski et al. (2006) has also been marked. The symbols of empty and filled circles are used to denote the bright and faint S0s.

Out of 237 galaxies plotted on this diagram, 135 are above this division line, indicating a dominantly old stellar population while 102 galaxies are below the division line, indicating recent star formation. Of the 135 galaxies with older stellar populations, 83 (61%) are bright. This number of bright galaxies drops to 17 (17%) for the galaxies with recent star formation. This trend can also be seen in Figure 4.4 which shows the distribution of the NUV − r color, with bright and faint S0 populations indicated by solid and dotted lines respecitvely. Thus, the fainter S0s show clear signs of recent star formation.

4.1.3 Comparison with an Earlier Study

In Donas et al. (2007), star forming S0 galaxies were identified by the authors through similar techniques involving color-color diagrams. The sample used by them comprised both elliptical galaxies as well as S0 galaxies, commonly considered together as *early-type* galaxies in the literature. The sample is based on the RC3 (de Vaucouleurs et al., 1991) catalogue. They plotted a color-color diagram using $B-V$ from the RC3 and FUV-NUV and found a large scatter in case of S0 galaxies. Their interpretation of this result was that some S0s were exhibiting low-level star formation thereby causing the scatter.

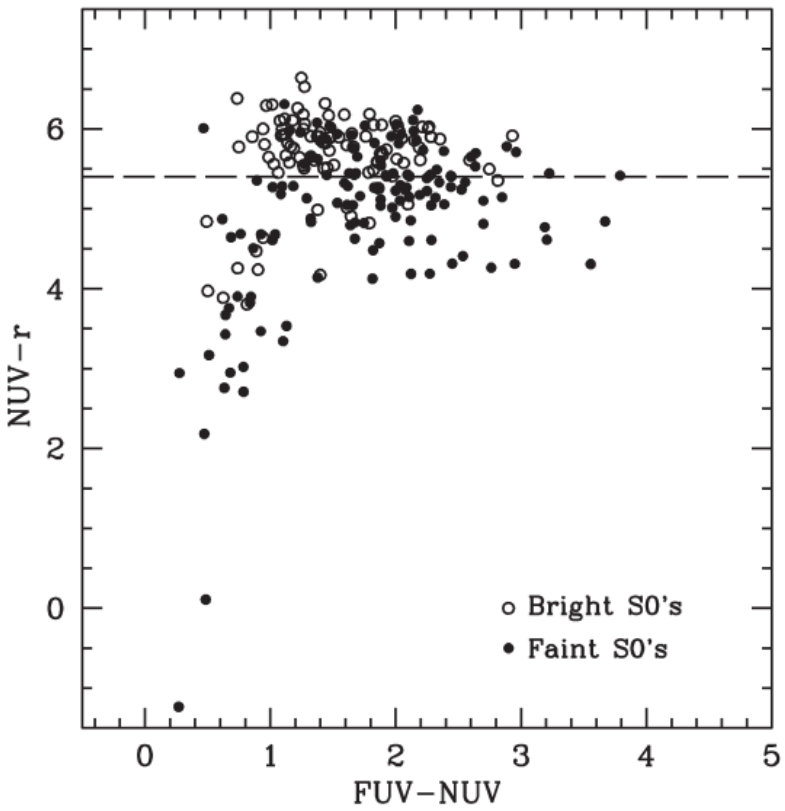

Figure 4.3: A plot of $NUV - r$ color against the $FUV - NUV$ GALEX color with empty and filled circles representing bright and faint S0s respectively. The line marks $NUV - r = 5.4$, which can be used to identify recently formed stars.

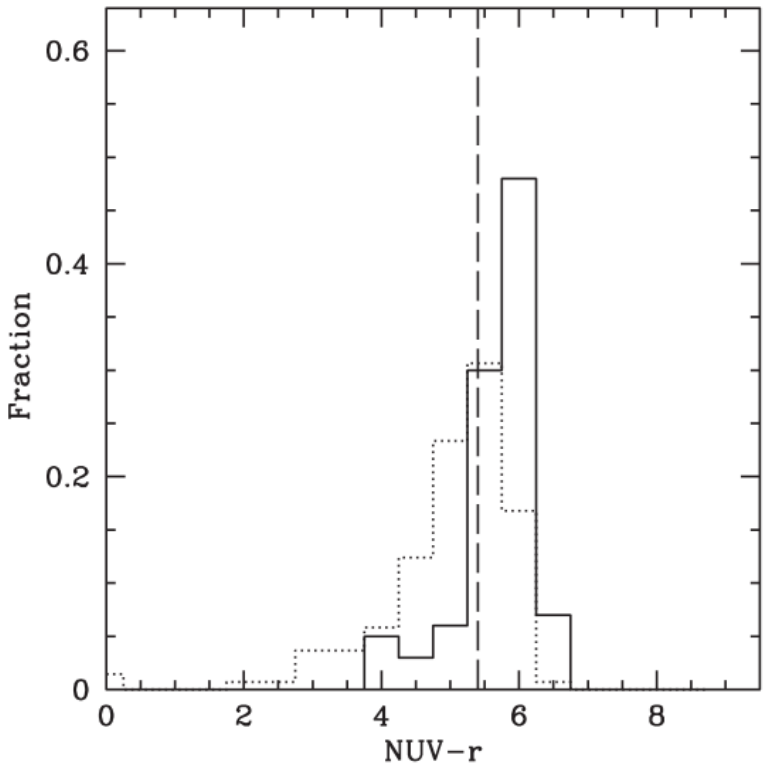

Figure 4.4: Distribution of the $NUV - r$ colors for the current sample of S0 galaxies with solid and dotted lines respectively denoting bright and faint S0 galaxies. The vertical dashed line marks $NUV - r = 5.4$, used to identify a recently formed stellar population.

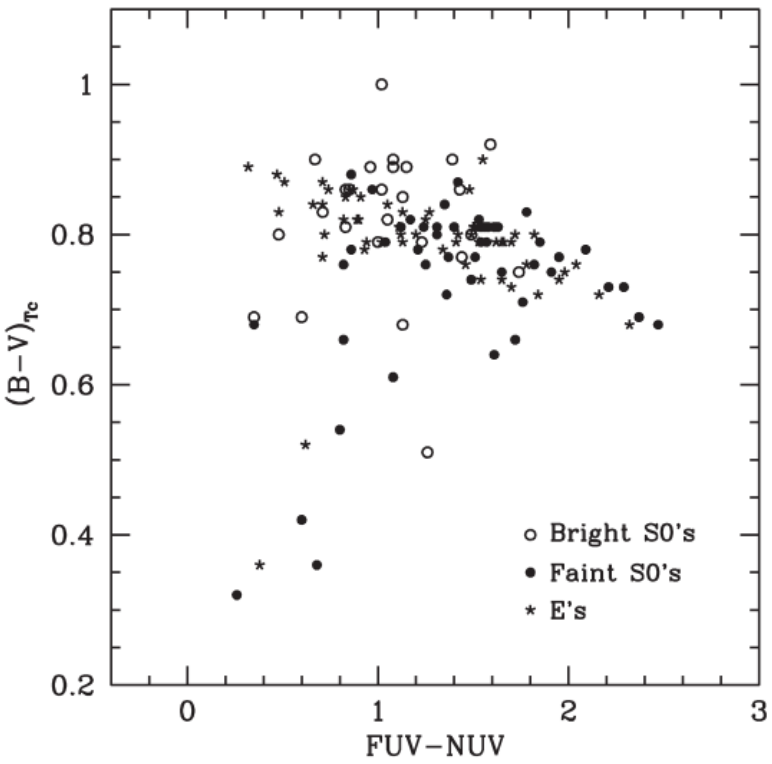

Figure 4.5: The Figure from Donas et al. (2007) but with S0 galaxies separated into bright and faint.

We have replotted the figure of Donas et al. (2007) with their sample. The ellipticals are marked by an asterisk but instead of treating all S0s alike, as done by Donas et al. (2007), our plot distinguishes between bright and faint S0s (using K-band luminosities obtained from 2MASS measurements). The S0s noted by them as causing a large scatter and speculated to be star forming, are all faint S0s. The two ellipticals with extremely blue colors are star forming and were explained as such by Donas et al. (2007).

4.1.4 Environmental Dependence

The environment in which a galaxy resides can play a major role in its evolution. Perhaps the strongest evidence for this is the morphology-density relation first pointed out by Dressler (1980). This relation shows that the relative abundance of S0s and spirals in clusters of galaxies changes with redshift. This means that there are processes at work in these environments which change the morphology of the galaxies from spiral-like to lenticular-like. One example of such a process is ram-pressure stripping. A galaxy with abundant gas moves through the intra-cluster medium (ICM) which in turn exerts a pressure on the gas causing it to be expelled. The loss of gas in the galaxy extinguishes star formation regions in the galaxy leading to an overall change in both the global structure as well as population abundances.

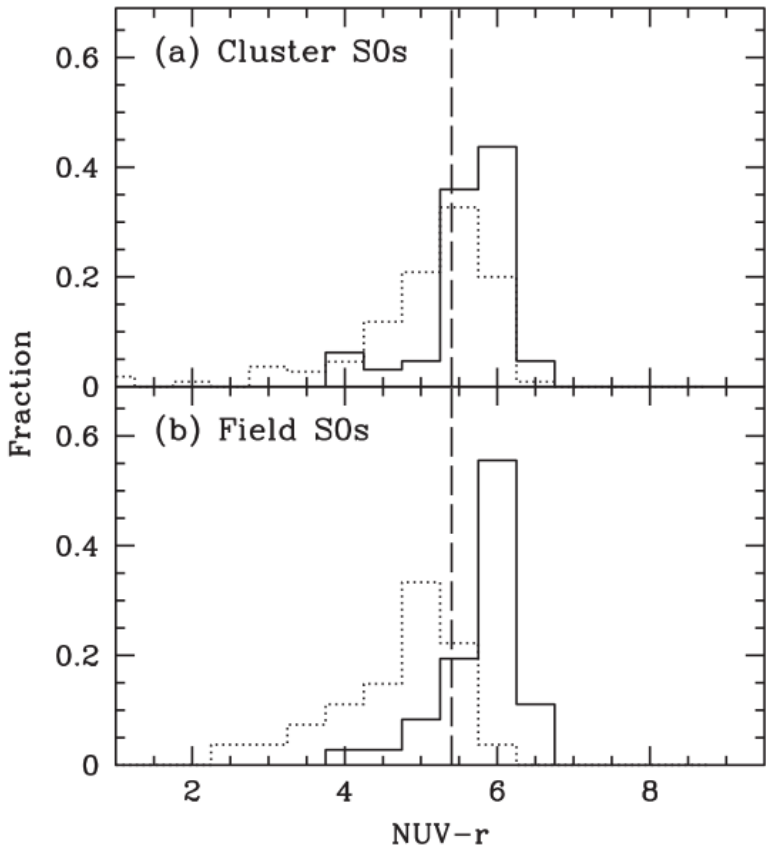

Figure 4.6: Distribution of $NUV - r$ for S0 galaxies in groups (top panel) and in fields (lower panel). In both panels, the solid and dotted lines denote bright and faint S0s respectively while the dashed line marks the $NUV - r = 5.4$ boundary used to identify recently formed stellar population.

Ram pressure stripping is only one of many rich processes possibly at work inside clusters and groups. The key point here is that the environment is expected to be important.

As pointed out in the earlier chapter, the S0s in the current sample have been divided into field and group[1]. The distribution of $NUV - r$ is shown in Figure 4.6 for bright and faint S0s in groups (top-panel) and for those in fields (bottom-panel). The trend found in Figure 4.4 that in galaxies with no recent star formation bright galaxies outnumber faint ones, is found in both the cases in Figure 4.6 but is stronger in the field environemt. But it should be noted that the overall number of S0s in the field environment is much smaller. So, the stronger separation seen in the case of field environment is less statistically robust - the separation may not be as significant as it appears to be in lower panel of Figure 4.6. Overall, it is evident that luminosity is the primary differentiator in case of S0s with the environment playing a second order but significant effect.

[1]As pointed in Chapter 3 galaxies, group here means both group and/or cluster

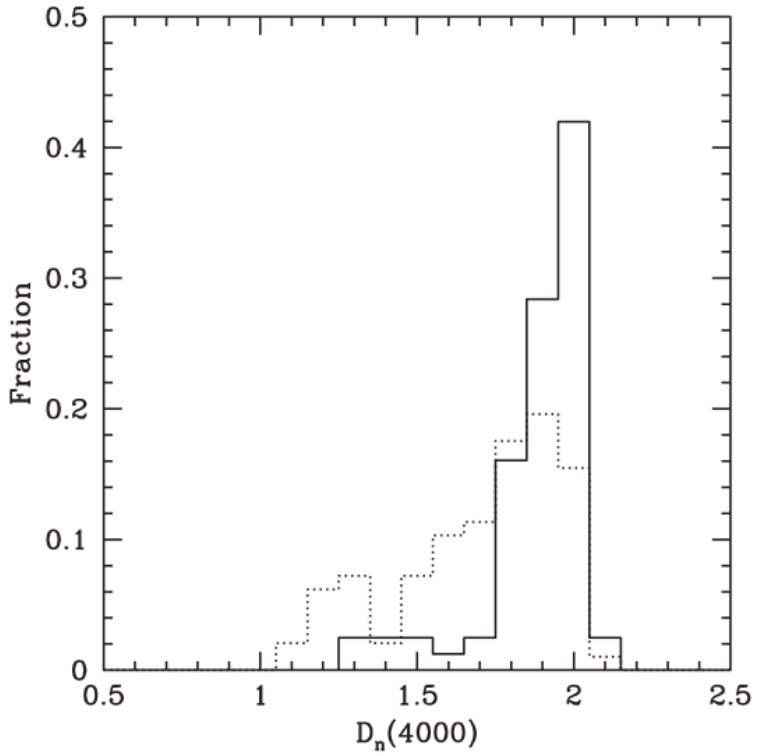

Figure 4.7: Distribution of the $D_n(4000)$ index for the subset of 180 S0 galaxies (for which the index measurements were available). The solid and dotted lines respectively denote the bright and faint S0 galaxies.

There are a few caveats in studying effects of environment that deserve attention. Consider a galaxy currently found to be in a group. It is not necessary that this galaxy has always been there, it is possible for the galaxy to have evolved in a field and under the gravitational influence of group, fallen into it. On the other hand, it's also possible that the galaxy we see as isolated, underwent interactions with a group in the past. In other words, the environment we find a galaxy in today may be very different for the environments the galaxy has experienced in its past. Another caveat is that when we decide to compare bright and faint S0s in different environments, we implicitly assume a homology between the two classes; the key finding of this study is that two classes are sufficiently different.

4.1.5 $D_n(4000)$

For reasons explained in the previous chapter, the $D_n(4000)$ index measurements are only available for a subset of 180 galaxies. The distribution of the $D_n(4000)$ index is plotted in Figure 4.7. The distribution for the bright S0s (solid line) is sharply peaked around $D_n(4000) = 2$ which indicates that most of these objects are similar in their stellar population to the elliptical galaxies. The fainter S0s, on the other hand show a much wider distribution indicating a mixed population of both

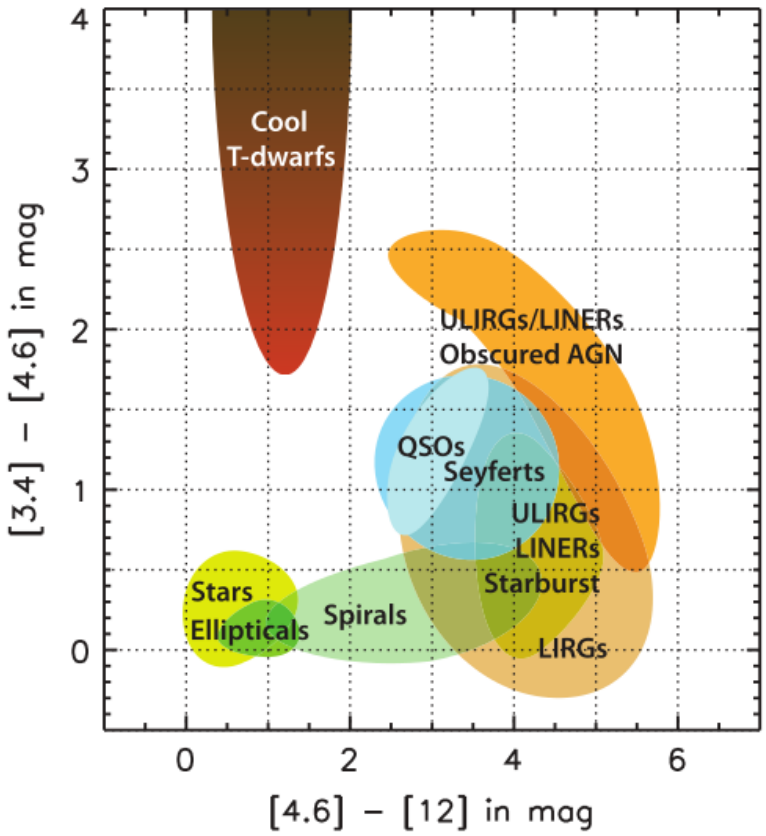

Figure 4.8: Figure 12 from Wright et al. (2010) which shows a color-color diagram plotted between [3.4] = [4.6] and [4.6]-[12.0]. The utility of this diagram lies in its ability to differentiate between various interesting astrophysical objects based on their location.

old and young stars.

4.1.6 The WISE Mid-IR Color-Color Diagram

Photometry in the 3.4, 4.6, 12 and 22 micron wavebands is available for the current sample of S0s through the Wide-field Infrared Survey Explorer (WISE). Using data from three of these bands, Wright et al. (2010) have plotted a color-color diagram as shown in Figure 4.8. Different bands probe different components of the astrophysical source. For example, the polycyclic aromatic hydrocarbons (PAHs) have a signature that contributes to the 3.4 micron band. Different astrophsical sources have different abundances of these components under different conditions and thus can be differentiated based on their position on such a color-color diagram. This figure plots the [3.4]-[4.6] color against the [4.6]-[12.0] color and marks the regions occupied by different classes of astronomical sources.

A similar diagram for the current sample of S0s has been plotted in Figure 4.9. The dark shaded ellipse marks the region of elliptical galaxies. The lighter ellipse marks the region of spiral galaxies which have ongoing star formation in them and

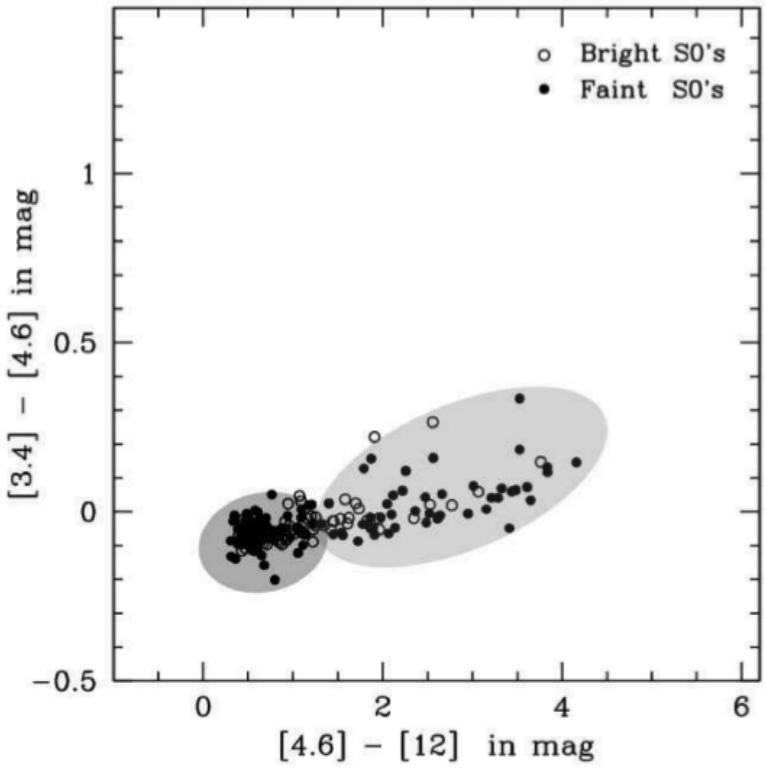

Figure 4.9: The WISE color-color diagram plotted between [3.4] - [4.6] and [4.6]-[12.0] showing the S0s in the current sample with bright and faint S0s denoted by empty and filled circles respectively. The darker and lighter shaded ellipses mark regions typically occupied by elliptical and spiral galaxies respectively.

much of their stars have formed recently. Again, we see that the bright S0s dominate in the region of elliptical galaxies while the faint S0s dominate in the region of spiral galaxies. This result shows that there is a group of S0s (bright) which are similar to ellipticals and another group (faint) which show stronger similarity to the spirals.

4.2 Conclusions and Summary

The work done by Barway et al. (2007, 2009, 2011) shows that S0 galaxies exhibit vastly different properties depending on their luminosity and environment. The bright S0 galaxies show tell-tale signs of having formed in a manner similar to the ellipticals while the faint S0 galaxies show signs of having formed secularly with a possible connection with spiral galaxies. The implication of this finding is expected to be evident in the star formation histories of these galaxies as can be traced using their spectral energy distributions and exploiting the technique of stellar population synthesis. The primary goal of this study is to investigate whether this implication holds true.

The current study shows, using multiwavelength broadband photometry from UV to mid-IR wavelengths that in particular, bright S0 galaxies predominantly contain a coeval stellar population with a large age ($\sim 10^{10}$ years) with very little or no sign of recent star formation, while a good fraction of faint S0s show a mixed population and signs of recent star formation. These faint S0s are likely to have a complicated star formation history with multiple episodes of star formation. There are multiple scenarios which can be invoked that are consistent with such a history. For example, if a galaxy's evolution is largely secular in which disk instabilities drive gas inwards, the star formation will occur over extended times and thus will not be explainable as a single burst. Other processes that can lead to a complicated history include those experienced in rich environments such as minor mergers, ram pressure stripping or galaxy harassment. It is speculated that S0s were once spiral galaxies whose spiral arms faded because of ceased star formation due to gas stripping.

The study, consistent with earlier studies, reveals luminosity to be the prime factor governing the evolution with the environment playing a secondary role. It should be noted that near-IR luminosity is a reasonable proxy for stellar mass and it is therefore possible that it is stellar mass which is the primary factor governing the dominant formation mechanism. Any attempt at using the spectral energy distribution to arrive directly at the mass in order to confirm this will involve assuming some models.

From the point of view of understanding broad trends for a statistically significant sample, the use of broad band photometry is justified. However, the ideal investigation will involve using detailed 2-dimensional or long slit spectroscopy or

maybe even 3-dimensional spectroscopy to study detailed kinematics and star formation histories of these objects. These techniques will allow computation of the fractional contributions of stellar populations of different ages and metallicities to the integrated spectrum of the galaxies thus allowing one to further constraint the formation history. A long term observational program with the Southern African Large Telescope (SALT) is being carried out for such a detailed study. The analysis and results for a limited subset of S0s is presented in Chapters 9 and 10.

Part II

A Mid-IR Spitzer Study of the Bulges and Disks of S0 Galaxies

Chapter 5

The mid-IR RC3-Spitzer Sample of S0s, Data Reduction and 2-d Decomposition

Two key concepts were introduced in Chapter 1 concerning the assembly and evolution of galaxies. We discussed the definiton of S0 galaxies and their place in the overall scheme of formation and evolution of galaxies. As described in detail earlier, S0s were originally thought of as a mere transition class of objects but observational studies carried out by e.g. Barway et al. (2007, 2009, 2011, 2013); Laurikainen et al. (2005, 2010) demonstrate that this is not entirely true. S0 galaxies in fact comprise distinct sub-populations with vastly different formation histories with luminosity playing the primary role in the dominant formation mechanism and environment playing a secondary role. The second important concept highlighted in the first chapter is that of bulge morphology. A bulge can be defined as a morphological component, which manifests as an excess of light in the central region of the galaxy over the value predicted by an inward extrapolation of the outer disk described by an exponential function. Bulges come in two distinct flavors and in current literature, they are commonly referred to as classical and pseudo-bulges. Studies carried out by e.g. Fisher and Drory (2008, 2010); Gadotti (2009) adopt a common approach where surface brightness profiles of all galaxies with a bulge and disk component are decomposed to extract the bulge parameters which are used to classify them. The global morphology of the galaxy is not considered i.e. classical bulges and pseudobulges are compared independent of whether the galaxies in which they reside are S0s or spirals.

We know that S0s are a unique class of objects with some bearing closer resemblance to elliptical galaxies and others bearing closer resemblance to spiral galaxies. Hence it is important to consider a study of quantitative morphology of S0 galaxies

aimed at identifying the nature of the bulges and performing due comparison with ellipticals and spirals. The study described in this and following two chapters has been done with these goals in mind.

5.1 Considerations in Sample Construction

Construction of a sample of S0s often begins with a catalogue which provides detailed visual classification of galaxies done by expert astronomers. Examples of such catalogues include the Uppsala General Catalogue (UGC) (Nilson, 1973) and the Third Revised Catalogue of Galaxies (RC3) (de Vaucouleurs et al., 1991). Both catalogues are complete with respect to various criteria but the UGC however is constrained largely to the northern celestial hemisphere while the RC3 catalog is an all-sky catalogue. Thus we use the RC3 catalogue as a starting point to construct the sample of S0 galaxies needed in the current study.

The next important consideration is that of the source of imaging data. Our eventual goal is to use the technique of 2-d image decomposition to extract parameters describing the bulge, disk and/or bar of a galaxy by fitting well known parametric models to describe each component. In the ultraviolet and optical wavebands, one encounters various issues that render imaging data at these wavebands not ideal for the intended analysis. In case of the ultraviolet wavelengths, the light is a probe of recent or ongoing star formation and has little contribution from lower mass stars which by being present in large numbers, dictate the global morphology of the galaxy. Light at optical wavelengths as well as ultraviolet are subject to dust effects - dust both within the galaxy of interest as well as in our Milky Way. The former is referred to as intrinsic extinction while latter is commonly referred to as foreground extinction. This problem can be circumvented by choosing galaxies at high galactic latitudes (where foreground extinction is minimal) and by demanding the sample to consist of only face-on or near face-on galaxies (this reduces effects of intrinsic extinction). However, such a sample is bound to contain a lesser number of objects. Given that the numbers will further reduce during the process of searching for high quality archival data and the prior expectation that the fraction of pseudobulge hosts in S0 galaxies is low[1], such a constrained sample is not suitable to meet the goals of the current study.

Light coming from near- and mid-infrared is most suitable for studying the morphology of galaxies quantitatively. The light is little affected by both intrinsic and foreground extinction and takes into account the contribution of the numerous low mass stars present in a galaxy. Well known imaging surveys that cover these wave-

[1]In general, it is known that the fraction of pseudobulges tends to rise towards the later Hubble types. By extrapolation, one expects a lower fraction of pseudobulges in the S0 galaxies.

lengths include the Sloan Digitial Sky Survey (SDSS), the 2 Micron All Sky Survey (2MASS) and data obtained by the Spitzer Space Telescope. While not being a survey telescope, the Spitzer telescope has been used by several observers to study galaxies of different morphological types. The SDSS is constrained largely to the northern skies. The 2MASS has no such restriction but being a ground based survey with an exposure time $\sim 7.8s$, it does not produce high signal-to-noise ratio (SNR) imaging except for the brightest and nearest galaxies. Apart from the low exposure time, another major cause of the very low SNR is the brightness of the sky at infrared wavelengths. The Spitzer Space Telescope overcomes this disadvantage as it operates outside of the Earth's atmosphere and also has the benefit of not being constrained to certain regions of the sky as is the case with SDSS.

The Spitzer Space Telescope has three instruments on board. One of them is the Infrared Array Camera (IRAC) which takes images at four mid-IR wavebands namely 3.6, 4.5, 5.8 and 8 microns. We chose to use the 3.6 micron imaging data from the IRAC onboard the Spitzer Telescope for the current study. The process of sample construction is described in the next section.

5.2 Sample Construction

For reasons described in the earlier section, the RC3 catalogue was used as a starting point in the construction of the sample. The catalogue can be accessed with ease using the *Vizier* service[2]. This service has been developed by CDS, Strasbourg, France and offers a convenient way to astronomers for accessing more than 10,000 catalogues made available as a result of several decades of research. It has an easy-to-use web interface which allows one to download a catalogue in its entirety or a subset satisfying certain criteria. For the current study, only those 3657 galaxies having a Hubble stage parameter $-3 \leq T \leq 0$ were selected[3]. This way one selects S0 and S0/a galaxies, the latter being a transition class of objects believed to be galaxies transforming from spirals to S0s. Traditionally, these galaxies have been considered as lenticular galaxies and thus have been included in the present sample.

Next, a magnitude cut on the total B-band apparent magnitude of $B_T < 14.0$ is imposed. This assures a high signal-to-noise ratio for the imaging data, needed for the intended 2-d decomposition analysis. At this point, the sample is reduced to 1031 galaxies, which was then cross-matched with archival data from the Spitzer Space Telescope using the Spitzer Heritage Archive (SHA)[4]. Only imaging data taken

[2]http://vizier.u-strasbg.fr/viz-bin/VizieR

[3]The Hubble stage parameter is used to denote the class of a galaxy and was assigned by de Vaucouleur to all the galaxies in his catalogue viz. RC3. The value ranges from -6 to +10, from elliptical to late-type spirals.

[4]The Spitzer Heritage Archive is maintained by the Spitzer Science Centre and is a public inter-

using the IRAC at 3.6 micron wavelength was used for this cross-match. The SHA contains imaging data obtained through various observation programs executed over the lifetime of the Spitzer telescope. In some cases, the observations were aimed at obtaining imaging data for the object in question while in other cases, the objects were observed serendipitiously. Imaging data were found for 247 galaxies and were divided into two groups - "primary" referring to imaging obtained for an object directly and "secondary" in which case the object was observed serendipitiously. The motivation behind such a division was to exercise extra caution with the data in the latter case and check for quality as the object was not the intended target and thus the data may not be optimized for it.

Next, a thorough examination of the imaging data was conducted for all the 247 galaxies and several images had to be discarded due to one or more of the following reasons:

- Poor signal-to-noise ratio - the morphological parameters recovered using 2-d decomposition technique as implemented in the program GALFIT (Peng et al., 2002) are reliable only if the image has sufficient signal-to-noise ratio. So, images not satisfying this condition were discarded. The occurrence of such images was more in the "secondary" group, as expected.

- Galaxies with disturbed morphologies due to recent interactions or mergers. The 2-d image decomposition technique assumes that various components of the galaxies obey certain simple analytical profiles. This assumption breaks down for galaxies that have been disturbed by interactions and it is therefore not meaningful to analyze such objects.

- Galaxies for which "meaningful" fits were not obtainable. For some galaxies, the decomposition analysis did not find any meaningful model or solution and such galaxies had to be discarded as well[5].

The final sample used to obtain the results described in Chapters 6 and 7 contains 185 galaxies. The Hubble stage T distribution for this sample is shown in Figure 5.1. The distribution of K-band absolute magnitudes in AB system is shown in Figure 5.2. This figure also shows the line used in Barway et al. (2007) to divide S0 galaxies into bright and faint luminosity bins. The sample is biased towards fainter S0 galaxies compared to the sample described in Chapters 3 and 4. The K-band absolute magnitudes were obtained using the following procedure.

face to all archival data taken using the three instruments on board the Spitzer Space Telescope. (http://irsa.ipac.caltech.edu/applications/Spitzer/SHA/)

[5]The detailed analysis technique is described in the subsequent sections but for convenience of presentation, the data discarded post analysis is being described here.

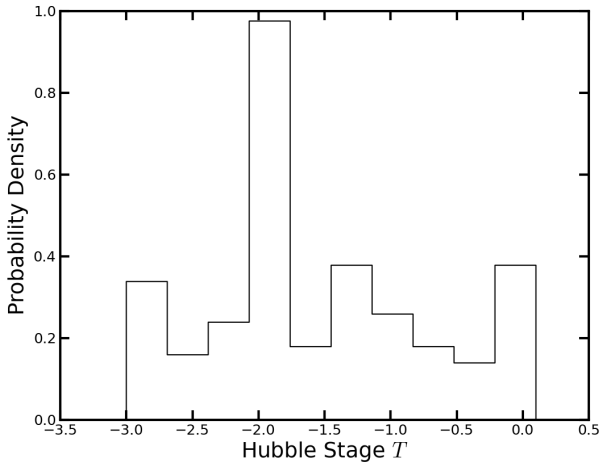

Figure 5.1: Distribution of the Hubble Stage Parameter T for the final sample of galaxies.

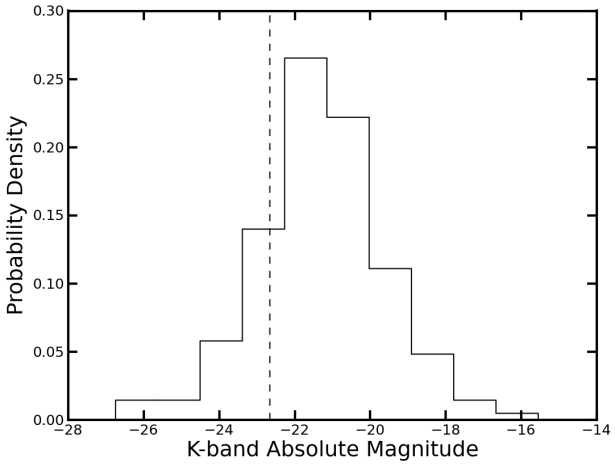

Figure 5.2: Distribution of the absolute K-band magnitudes for the final sample of galaxies, in the AB system. The dashed line indicates the division between the bright and faint galaxies used by Barway et al. (2007).

- The sample of 185 galaxies was cross-matched with the 2MASS Extended Source Catalogue to obtain the integrated K-band magnitudes for all galaxies.

- These magnitudes are reported in the Vega system and were thus transformed to the AB system (Oke and Gunn, 1983) by adding 1.84 to the Vega magnitude as suggested by Muñoz-Mateos et al. (2009).

- The redshifts for these galaxies were obtained from the NASA Extragalactic Database (NED)[6].

- The redshifts were used to obtain the distance moduli using the Python implementation of Ned Wright's cosmology calculator[7] written by James Schombert. For this purpose, the standard concordance cosmology was assumed where $H_0 = 70\,\mathrm{km\ s^{-1}\,Mpc^{-1}}$, $\Omega_\mathrm{m} = 0.3$ and $\Omega_\Lambda = 0.7$.

- The original divison line of -24.5 was transformed in a similar manner by adding 1.84.

The median redshift of the sample is $\sim$ 0.005 with a standard deviation of $\sim$ 0.002. Thus the sample, while not being complete, is a representative sample of S0 galaxies in the nearby Universe. The 2-d decomposition technique applied on this sample is described in the next section.

5.3 2-d Image Decomposition

The technique of decomposing the surface brightness profile of a galaxy into its components was briefly touched upon in Chapter 2. This section covers some details with emphasis on how the code GALFIT was used in the current study.

Given an image of a galaxy, there are a number of ways in which the 1-d surface brightness profile can be constructed. The simplest method is to take a slice along the major axis of the galaxy (Burstein, 1979) and measure the surface brightness at different points on the galaxy. However, one could then argue as to why such a slice cannot be taken along the minor axis of the galaxy. In fact, it has been observationally shown that the profiles of galaxies along the two axes can be significantly different (Ferrarese et al., 1994). Another method in which the complete image of the galaxy is utilized involves fitting ellipses to the isophotes of the galaxy. One then gets an azimuthally averaged surface brightness as a function of the semi-major axis of the galaxy. However, there are a few disadvantages of working with a 1-d profile.

[6] http://ned.ipac.caltech.edu/
[7] http://www.astro.ucla.edu/ wright/CosmoCalc.html

- By obtaining an azimuthally averaged profile, one is inherently assuming the axial asymmetries in the distribution of light in a galaxy can be ignored. This need not hold true in many cases - for example, in the case of barred galaxies.

- The use of azimuthally averaged profiles also ignores changes in the position angles (isophotal twists) and the ellipticities of the isophotes.

- Several studies have also demonstrated the existence of strongly degenerate solutions to the brightness profile when fitting with more than one component i.e. more than one combination of the two models being summed can explain the observed profile thus leading to an ambiguity of which combination is a better representation of the true profile.

- The residual obtained by subtracting the best-fit profile from the observed profile does not reveal much about the unaccounted structure within the galaxy.

- In case of galaxies where the bulge and disk do not share a common centre, the use of a 1-d profile is not correct.

If one is able to fit a 2-d analytical model over the observed image of the galaxy, many of the above limitations of the 1-d analysis can be overcome. The price one pays is an increase in the number of free parameters that need to be optimized to get the best-fit model. For a 2-d analytical profile, the X-centre, Y-centre, position angle, ellipticity/axis ratio are additional free parameters that need to be optimized. Apart from an increase in computational costs, this also means that parameter space is more complex and thus obtaining the best-fit solution becomes trickier. However, with modern computational power, the pros of the 2-d technique easily outweigh the cons. A 2-d analysis therefore offers far more reliable and richer information than its 1-d counterpart.

At the simplest conceptual level, the process of fitting a model on a galaxy image is about defining a merit function which can be minimized to obtain the best-fit parameters. A χ^2 function is most often used, with

$$\chi^2 = \sum_x \sum_y \left(\frac{O(x,y) - M(x,y)}{\sigma(x,y)} \right)^2 , \tag{5.1}$$

where

$$O(x,y) \rightarrow \text{Observed Image},$$

$$M(x,y) \rightarrow \text{Model},$$

$$\sigma(x,y) \rightarrow \text{Uncertainties}.$$

But the process becomes rather involved due to a number of factors such as

- Which model is best suited to describe the given galaxy? How many components are needed? There are no straightforward answers to these questions. One generally starts by fitting a single component for an elliptical galaxy, usually described by a Sérsic profile or two components in case of late-type galaxies - a bulge and a disk, described by a Sérsic profile and an exponential profile respectively. Other components such as a nuclear source or a bar may be added depending on the science goal, available resolution etc.

- Estimation of uncertainties. Incomplete estimation of uncertainties may still allow a best-fit model to be obtained using χ^2 but it is then not possible to use the statistical properties of χ^2 to measure the goodness-of-fit.

- Instrumental signatures in the observed image. For example, if there are severe optical distortions in the image, it may not make sense to use it for decomposition. Leakage of current from neighbouring pixels due to a very bright star can render the whole image unusable. If the flat-fielding of the image has not been done correctly, inter-pixel variations in detection efficiency can lead to incorrect representation of the distribution of light in the galaxy.

- If the galaxy is being modelled in a crowded field, the model is bound to be biased due to contamination by light from the neighbours. In such cases it is essential to construct suitable 'masks' to flag the pixels that should not be used when fitting an image. Masks are also needed to flag pixels that are damaged or contain signatures as described earlier.

- A given galaxy can have slightly different distribution of light depending on the telescope - detector combination used to image it. This is because no instrument ever produces a point image of a point source owing to diffraction and other effects. Thus one needs to know the Point Spread Function (PSF) in order to correct for the effect of the instrument on the actual distribution of light of the galaxy. For space based observations, the broadening effects due to Earth's atmosphere are not important.

As will be shown eventually, each of the above practical difficulty requires significant amount of preprocessing to be carried out on the observed images from the Spitzer Space Telescope before they can be used for modelling the distribution of light. This is described in the next section.

The code used in this study for 2-d decomposition of the galaxy image is GALFIT (Peng et al., 2002). GALFIT is a very flexible program which can fit a variety of functions including Sérsic, exponential, Moffat, Gaussian, Ferrer etc. The user can

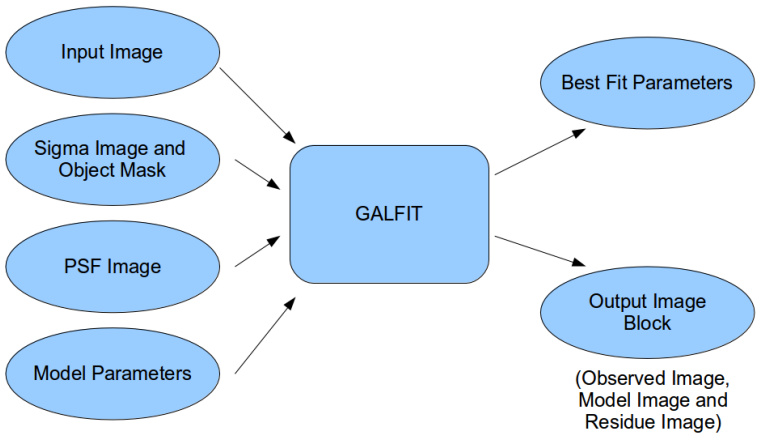

Figure 5.3: A diagram illustrating the use of GALFIT.

construct any combination of these profiles and also has flexibility in keeping any subset of parameters frozen or free. The user can also specify constraints which can be used to couple the parameters of the model or restrict their parameter range as required.

As input, GALFIT needs the following:

- The observed image on which the fit has to be performed.
- A mask file which flags the pixels that should not be used in the process of fitting.
- A PSF image file which it uses to account for the seeing of the instrument. The PSF image is allowed to have smaller pixel scale than the image itself which is important in case of space-based telescopes where the PSF is generally undersampled (see Section 5.6).
- An input configuration file which specifies details such as the models to be fitted and the starting guess parameters along with a constraints file, if any constraints need to be applied.

GALFIT uses the fast Levenberg-Marquardt algorithm for finding the best-fit parameters by minimizing χ^2. A key limitation of this algorithm is that it can easily get stuck in a local minima and thus the solutions have to be checked manually for correctness and physical meaningfulness. To account for the seeing effects of the instrument, GALFIT first convolves the model image constructed using the current set of parameters, with the PSF using a Fast Fourier Transform (FFT) routine

before subtracting it from the observed image. If the PSF is sampled more finely than the observed image, it constructs a model with a pixel scale matching the PSF and then bins it to match the observed image. The process of convolution is the most computationally expensive step carried out by GALFIT and can be turned off by appropriately tweaking the configuration file.

As output, GALFIT provides the following data

- A fit.log file which summarizes the final set of best-fit parameters found by GALFIT.
- A GALFIT compatible input file which contains the same information as above but can be used as a starting point for further fitting.
- An output image cube which contains a cut-out of the observed image, the final model and the residual image. Using appropriate command line options, GALFIT can be made to output model images of individual components as well.

The overall working of the GALFIT program is captured in the Figure 5.3.

5.4 Spitzer and Its Data

This section describes the Spitzer Space Telescope, the nature of data collected by it and its suitabiltity for 2-d decomposition.

The Spitzer Space Telescope has three instruments onboard:

- The Infrared Array Camera (IRAC), which takes imaging data in four mid-infrared wavebands - 3.6, 4.5, 5.8 and 8 microns - referred to in Spitzer parlance as channels.
- The Multiband Imaging Photometer (MIPS), which works at far-infrared wavelengths.
- The Infrared Spectrograph (IRS), which is used to obtain spectroscopic data at mid- and far-infrared wavelengths.

A large fraction of the light coming from a galaxy at 3.6 micron is stellar with little contribution from polycyclic aromatic hydrocarbons. But this dominance of stellar light drops significantly at 4.5 micron and higher wavelengths (Leitherer et al., 1999). Hence, for the intended analysis, we choose to work with the 3.6 micron imaging data taken using the IRAC.

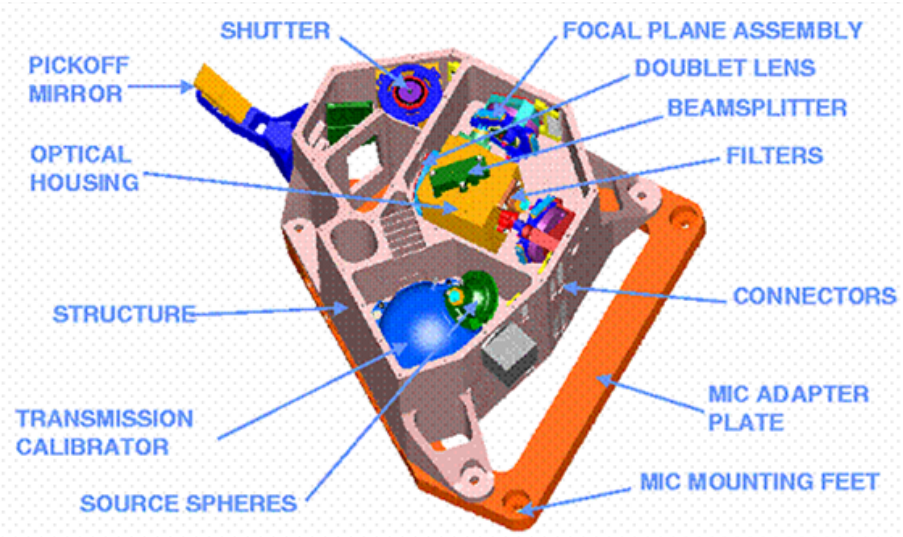

Figure 5.4: IRAC Cryogenic Assembly model, with the top cover removed to show the inner components. (Courtesy: The IRAC Instrument Handbook)

5.4.1 Brief Description of IRAC

Figure 5.4 sketches the layout of the IRAC instrument. IRAC contains four detectors or channels which can take images at 3.6, 4.5, 5.8 and 8 microns. The two lower wavelength detectors are made of InSb while the two higher wavelength detectors are made of SiAs. Each detector is an array of 256 $\times$ 256 pixels, each pixel capturing $\sim 1.22'' \times 1.22''$ of the sky. Thus each detector captures a field of view of $\sim 5.22' \times 5.22'$.

The light from the source hitting the telescope is split into a higher and lower wavelength component through a beam splitter and reaches the four detectors. The arrangement of the optics is such that the channels 1 and 3 have the same field of view which is different from the field of view common to channels 2 and 4 at any given time. The two fields of view are separated by a gap of 1.52 arcmin.

The IRAC is placed off-axis relative to the Spitzer focal plane as a result of which images captured by IRAC have optical distortions - these distortions can be as severe as 2.2 pixels relative to a regular undistorted grid. The use of beam splitters in turn implies the existence of a lateral chromatic abberation which is generally less than a pixel. Any resultant astrometry errors are recorded in the form of header keywords in all data obtained following the prescription of Shupe et al. (2005).

There are various read-out modes for the IRAC detectors such as

- A full array read-out mode - data obtained in this mode is the most used in the current study
- A stellar photometry mode - this uses shorter exposures for channels 1 and 2 while longer exposures for channels 3 and 4 to account for differences in flux as well as efficiency levels. This mode is not used for extended objects like

galaxies.

- A sub-array mode - where only a 32×32 sub-array is read out. This is again useful only for bright star photometry.
- A High Dynamic Range mode, few imaging data in the current study were observed using this mode.

In the next subsection, details on basic data obtaind from IRAC are described and their suitability for the intended analyis is explored.

5.4.2 Description of IRAC Data

The Spitzer Science Centre, through the SHA, offers three types of data products.

- Level 0 data. This is the raw imaging data which contains several instrumental signatures. These data are seldom used for scientific analysis.
- Level 1 data. These are raw data extensively processed by various pipelines to free them of various instrumental signatures. These are also called Basic Calibrated Data (BCD). The basic pipelines do not however correct for various specific effects such as leaked currents, ghost images etc. These are corrected by running a separate set of software tools by the Spitzer Science Centre and such data are referred to as Corrected BCDs or CBCDs.
- Level 2 data. These are constructed by coadding all the BCDs captured in a single observation request. These are also referred to as Post-BCDs or PBCDs and are meant to serve as quick preview data.

When the software pipeline processes Level 0 data to construct Level 1 data, it performs several operations such as data sanity checks, header keywords population, bit conversion, data inversion, Fowler sampling, response linearization, wrap-around corrections, mirror image effects, bandwidth corrections, background estimation etc. The entire process is captured in Figure 5.5, taken from the IRAC instrument handbook. A detailed discussion of all these corrections is beyond the scope of this thesis and can be found in the IRAC instrumemt handbook. The current discussion will focus on features of Level 1 data to check for their suitability for the intended analysis.

In order to determine the amount of dark current to be subtracted from the image, the telescope is pointed to the ecliptic pole and several exposures are obtained. These exposures are then combined and contribution from stars and other sources is removed. The remainder is then subtracted from all science images. As a result, in the process of removing dark current and bias a fraction of the celestial background

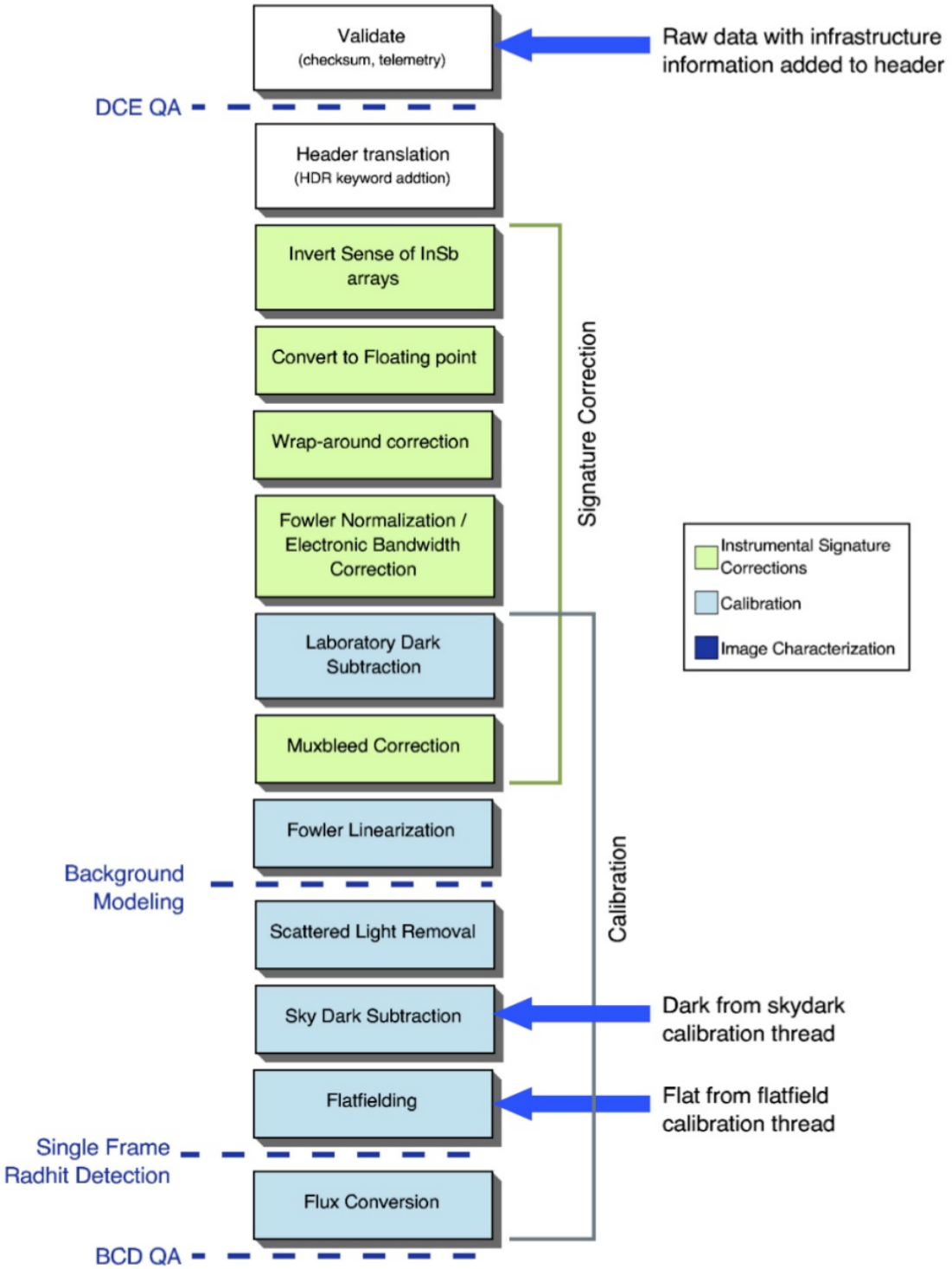

Figure 5.5: Overview of RAW image processing to construct Basics Calibrated Data (BCDs), taken from the IRAC instrument handbook.

is also removed. To compensate for this, the processing pipeline uses a *COsmic Background Explorer / Diffuse Infrared Background Experiment* (COBE/DIRBE) estimation of the background and adds it to the header. As a result, the true celestial background can never be determined in IRAC data. This, however is not a major problem for our analysis since any residual background and the galaxy model can be fitted simultaneously by GALFIT.

In order to perform flat-fielding, the telescope takes dithered images of well defined regions of the zodiacal background, 22 in number. The uncertainty of the flat-fielding is found to be 2.4% in Channel 1. However, the flat-field response over several observational cycles was found to be very stable and hence a super-flat was constructed which has an improved uncertainty of 0.4%. Since the Level 1 pipeline uses these flats, the inter-pixel response variation is not a problem. It is interesting to note that since the zodiacal background used for flat-fielding is a rather *red* source, the accuracy of the flat-field will degrade to as much as 10% should a source be observed that peaks in far infrared.

As mentioned earlier, IRAC is placed off-axis relative to the focal plane of the telescope. This results in optical distortions which can manifest as three different effects in the images:

- The pixel size in arcseconds changes across the image.
- The pixel scale in vertical and horizontal directions can be different.
- The axes of the image may not remain perpendicular.

As can be seen, these problems render an image unusable for a 2-d decomposition code like GALFIT which assumes a distortion free image. The variations in the solid angle subtended by a pixel can be as high as 1.5%. For this reason, the BCD images are not presented in the usual units of ADUs (analog-digital units) but calibrated directly in units of MJy/str. If one needs to perform aperture photometry, a suitable software can reconvert into pixel units by multiplying the solid angle and obtain accurate photometry. But this still does not help the case for image's usability for a tool such as GALFIT.

Solutions to Problems with Level 1 images: While optical distortions do exist in BCDs, they can be quantified and represented using suitable header keywords as described in Shupe et al. (2005). These corrections are generally upto second order but can also be as high as third order corrections. A software tool capable of understanding the header keywords which represent optical distortions can suitably reproject the images using an equal area projection scheme (TAN-TAN). This involves construction of a grid or a frame of equal area elements and projecting the BCD images onto it, correcting for optical distortions when doing so.

The Spitzer Science Center provides a tool called MOsaicking and Point EXtraction (MOPEX) which can perform this operation. In fact, this is exactly what is done by the pipeline responsible for constructing Level 2 data or PBCDs. The process of constructing Level 2 data this way has not only the advantage of providing a final image free of optical distortions i.e. images where every pixel subtends the same solid angle but also provides other collateral benefits -

- Instead of reprojecting a single image, several exposures can be coadded to give a higher signal-noise ratio final image.
- The Spitzer data analysis team has found that if dithered exposures are obtained for any object and combined this way, the flat-fielding accuracy increases.
- By extracting point sources in the image and cross-matching them with a catalogue such as the 2MASS point source catalogue, the overall astrometry can be made more accurate. This is called pointing refinement but since our science goals do not require very accurate astrometry, this is just an added bonus and not a critical improvement.

Ready-made Level 2 Data from SHA At the time when the analysis described here was conducted, the Level 2 products made available by SHA, which were prepared by the version S18.14 of their pipeline, were more *quick-look* images than *science-ready*. These images particularly suffered of an artifact as can be seen in the upper panel of Figure 5.6. This is a Level 2 image of the galaxy NGC 4374 and clearly there is something severely wrong with this image. For reference, a better image of the galaxy taken using the SDSS is shown in the lower panel of Figure 5.6. The *Spitzer Help Desk*, in private communication, explained that the pipeline being used at that time, had an inbuilt mechanism to detect a near-saturated source and replace it with an image of the PSF, thus producing images as shown in Figure 5.6. Further, the interpolation scheme and several other important settings are also not ideal for obtaining good quality level 2 data.

In summary,

- Level 1 products have several artificacts which do not allow their use for image decomposition.
- Level 2 products circumvent these problems but those made available by the version S18.14 of their pipeline have other issues which render them unusable.

Thus, the final strategy adopted for this study involves obtaining Level 1 data from the SHA and using the MOPEX tool to construct custom Level 2 data free from artifacts.

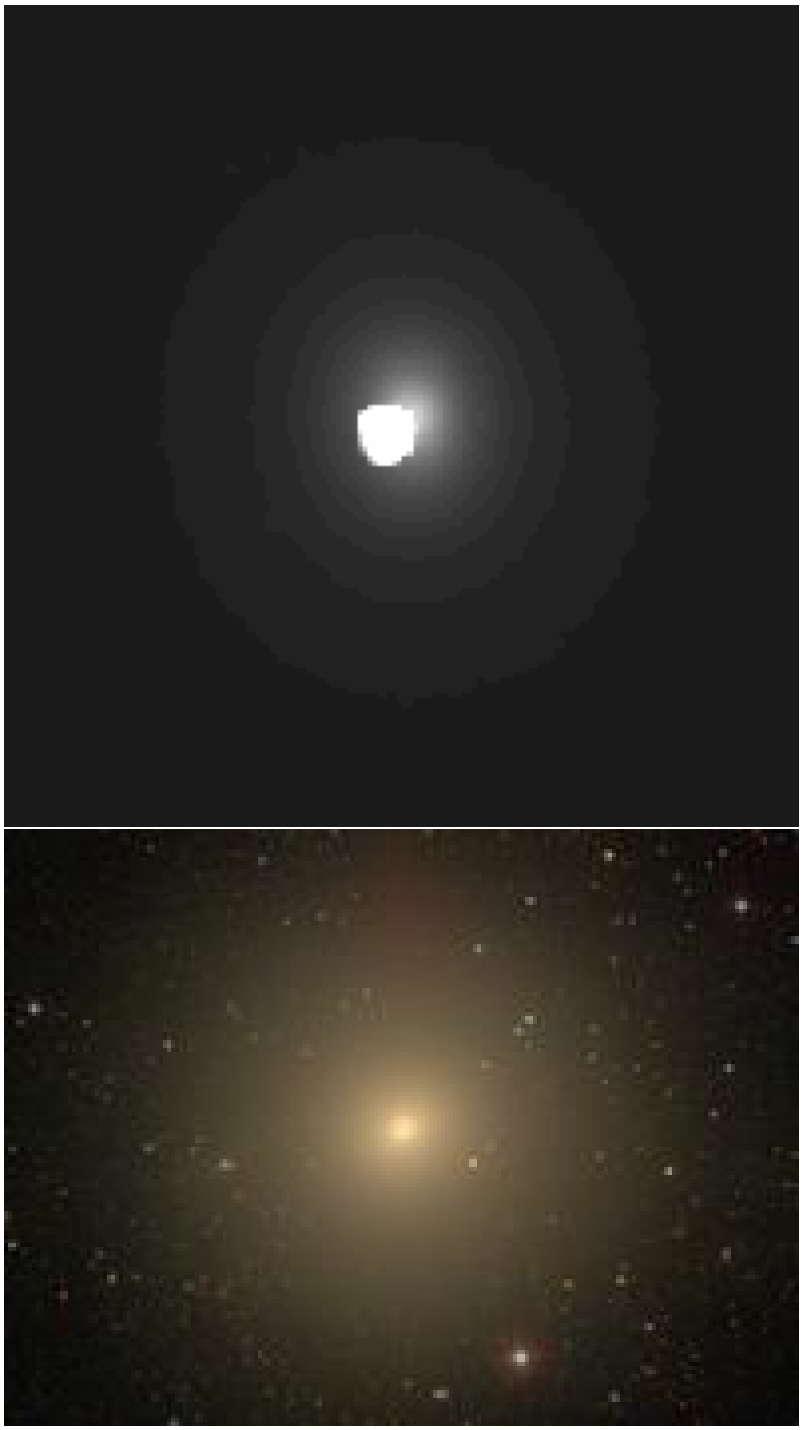

Figure 5.6: Top: Level 2 or PBCD image of the galaxy NGC 4374 made available on the SHA, showing a strong artifact in the image. Bottom: The image of the same galaxy taken by SDSS for comparison.

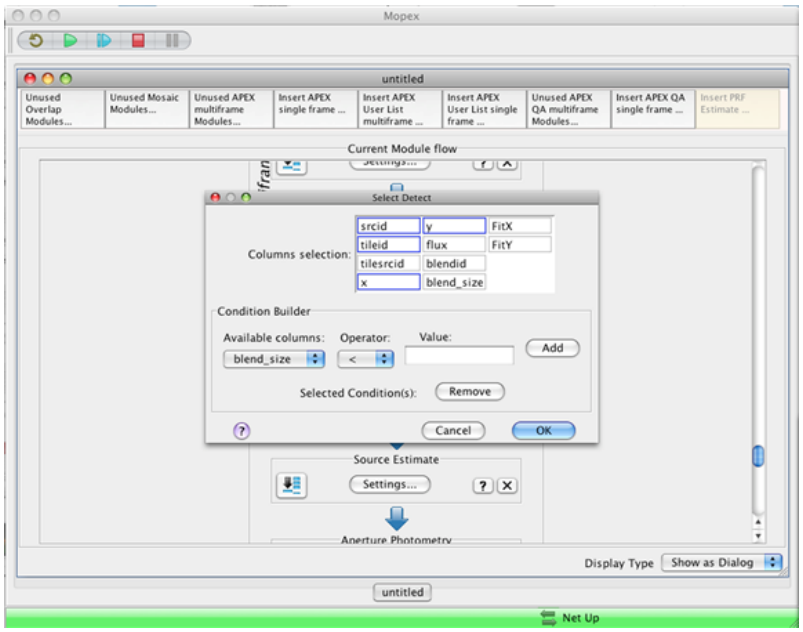

Figure 5.7: A screenshot of the MOPEX software's Graphical User Interface.

5.5 Construction of Custom Level 2 Data

In the earlier section, the need for constructing custom Level 2 data using (C)BCDs downloaded from the SHA, was discussed. The current section explains the working and use of MOPEX in achieving this.

MOPEX stands for MOsaicking and Point EXtraction. It is a tool provided by the Spitzer Science Centre and is specifically designed for use with data obtained from the Spitzer Space Telescope. Compared to the standard set of tools provided by the Image Reduction and Analysis Facility (IRAF), often used in optical and infrared astronomical image analysis, MOPEX can handle the keywords representing optical distortions and images calibrated in units of MJy/str with ease.

MOPEX can be run using both a graphical user-interface mode as well as a command line mode. In the former, the user can specify the files to be processed and the processes to be performed by using a simple system of menus. In the latter case, the user is expected to provide all the input in the form of a file known as a *namelist* and run the pipelines which are presented as Perl scripts. The namelist not only specifies the input files but also the sub-modules which should be executed within the pipeline and the various configuration parameters governing their behavior.

A screenshot of the graphical user interface to MOPEX is shown in Figure 5.7. Any pipeline may be added to the workflow by simply clicking it. For every pipeline, there is a dialog box marking all the sub-modules within it that are currently in the workflow. This can be used to easily add or remove the sub-modules. Each sub-module performs a specific task - for example, one submodule can be used to detect cosmic rays, another to detect spatial and temporal outliers etc. To aid the pro-

cess of selecting the pipelines, their submodules and the configuration parameters, MOPEX comes with built-in templates. There is one template for each pipeline for a given channel of a given instrument. The default parameters provided for Channel 1 of IRAC were sufficient to obtain usable, high quality mosaics/PBCDs in the current study.

5.5.1 Brief Description of Pipelines and Their Modules

There are three principal pipelines that are available in MOPEX

- Overlap Pipeline: This pipeline is used to match the background levels in all the (C)BCDs being combined. Without this matching, the resultant mosaic will be patchy due to unequal background levels.
- Mosaic Pipeline: This executes the actual process of constructing the final grid of pixels and projecting/coadding all images to produce the final mosaic.
- APEX Pipeline(s): This pipeline and its variants deal with point source detection and photometry. This was not used in the current study.

Any pipeline in MOPEX requires a set of input files which include:

- Image Stack File - this contains a list of input files that should be combined in order to produce the final mosaic.
- Sigma List File - this contains a list of uncertainty images for each file and allows MOPEX to construct an uncertainty mosaic which represents an approximate estimate of the uncertainty on each pixel.
- Mask files - there are various types which serve the general purpose of marking those pixels which, owing to various reasons, do not have reliable data.

The Overlap Pipeline: This pipeline works by running the following modules in order-

- Fiducial Image Frame (FIF) maker - this is used to construct the final grid of pixels onto which the (C)BCDs are projected. The grid is constructed to provide a sufficient edge padding so that all images may be combined suitably.
- MedFilter - Performs an estimate of the background level in the image to allow for the object detector module to work correctly.
- Detect - this attempts to detect the bright sources within an image which allows to mark those pixels which cannot be used reliably for background estimation.

- Interpolate - performs the actual projection of the images onto the fiducial image frame generated previously using a specified interpolation scheme. Available schemes include coarse gridding, linear, bicubic and drizzle.

- Compute Overlap Correction - computes the additive constant to be added to each image in order to equalize their background.

- Quick Look Mosaic - constructs a crude mosaic whose sole purpose is to allow a user to verify whether overlap corrections have been performed correctly. If overlap correction is not correct, the mosaic will look patchy due to unequal backgrounds in the combined images.

The Mosaic Pipeline: The main modules in order of how they appear in the workflow are described below.

- Fiducial Image Frame Maker - see above

- Mosaic Geometry - use the FIF generated above to determine how and which (C)BCDs to combine.

- MedFilter - creates temporary background subtracted versions of the images to enable subsequent modules to attempt cosmic ray and other outlier detections.

- Radhit - search for cosmic radiation hits using concentration of flux within pixels as a criterion

- Mosaic interpolate - perform the projection of images onto the FIF using a suitable interpolation scheme.

- Outlier Detection - this is actually a collection of four modules, which in tandem perform outlier detection using various schemes or methods.

- Mosaic RMask - Constructs a final mask based on the outliers detected using the previous set of modules.

- Reinterpolate - use the information of bad pixels and reinterpolate only the bad pixels using a suitable interpolation scheme.

- Mosaic Coadder - combine information for a pixel using contributions from all overlapping (C)BCDs.

- Mosaic Combine - construct the final output mosaic using the combined information from individual frames

For the purpose of this study, a handful of images were manually reduced using the GUI and were checked for image quality. Having established that the default template parameters for Channel 1 were producing high quality final data, the default parameters were exported to a namelist which was then used in testing MOPEX in command line mode. A bash script was then written which given a directory containing .zip files downloaded from the SHA, containing BCDs, performs the following steps:

- Decompress or unzip the data.
- Scan and identify actual images, masks and uncertainty images to construct file lists.
- Invoke the Outlier and Mosaic Perl scripts with suitable name lists to construct the final mosaic.

Using the above script, one can generate the required level 2 data for the downloaded images of all galaxies in an automated fashion. The process required approximately $\sim$ 48 hours to process all 247 galaxies' imaging data. At this point, two basic inputs required by GALFIT become available - the observed image and the uncertainty/sigma image. The next section discusses construction of the PSF, which is an important input required by GALFIT.

5.6 Determining the Point Spread Function for Spitzer IRAC

As described earlier, a point source appears to be extended, when imaged, due to the effects of the *telescope-detector* system on the incoming light. The spreading of the light from a point source is often termed as *seeing* and the complete effect is described using a Point Spread Function (PSF). The process of constructing the final image of an astronomical object using a telescope can then be mathematically described as a convolution of two functions, one representing the intrinsic light distribution of the source and the second being the PSF. The image of a galaxy represents the distribution of light in the galaxy but convolved with a PSF. Thus, one needs to first deconvolve the image and then study the light distribution. However, deconvolution tends to add noise to the image and is thus not a feasible solution especially for images which already have a low SNR (Peng et al., 2002). An alternate solution adopted by GALFIT is to convolve the model image with the PSF before subtracting it from the observed image, when computing the χ^2. Without a PSF, the parameters determined by GALFIT will be biased by any systematics specific

to the given telescope-detector combination and the bias becomes more acute for galaxies whose sizes are comparable to the Full Width at Half Maximum (FWHM) of the seeing. The PSF can be supplied as a 2-d FITS image to GALFIT. This feature of GALFIT is important since it takes away the need to approximate the PSF as some analytical function.

There are a number of methods by which the PSF can be determined. Some of these methods are highlighted below.

- **Coadding images of stars**. As explained earlier, the image of a star is the PSF itself. Thus, the simplest method of determining the PSF is to take cut-outs of isolated & bright foreground stars and coadd them to produce a high signal-noise ratio image of a star. The final image needs to be subtracted of any background and should be centered properly. If the sky background subtraction or centering is not done correctly, there will be artifacts which can affect the model fitting.

- **Assuming an analytical profile.** For ground based telescopes, the PSF can be approximated using a profile such as a Gaussian or Moffat function. One way to understand why a Gaussian is a good approximation is to invoke the central limit theorem. In the ideal scenario, the photon from a point source will travel along a perfectly straight path towards the detector. However, in realistic cases, the photons undergo random changes in their path due to various effects including those due to the atmospheric turbulence, due to their bouncing off the telescope walls, due to the optical elements, the filters and detectors. As such the probability distribution of paths taken by the photons from a source is a sum of several distribution functions, each describing the scatter of the photon due to a given effect - by the central limit theorem, one can approximate this using a Gaussian. Using, for example, the *imexamine* task in IRAF, it is possible to determine the FWHM of a Gaussian fit to a star. This information can then be used to construct a 2d Gaussian of a given width. If GALFIT is provided no input image but just an input configuration file with some model parameters, it constructs a model image and does no fitting. This feature can be used to construct the PSF given an analytical representation.

- **Semi-analytic approach.** The above method works well only if any extended non-Gaussian features in the PSF are small enough that they can be ignored and there are no optical distortions introduced by the telescope-detector system which can introduce asymmetries in the Gaussian. When an analytic function is not adequate, another more involved method can be adopted, which

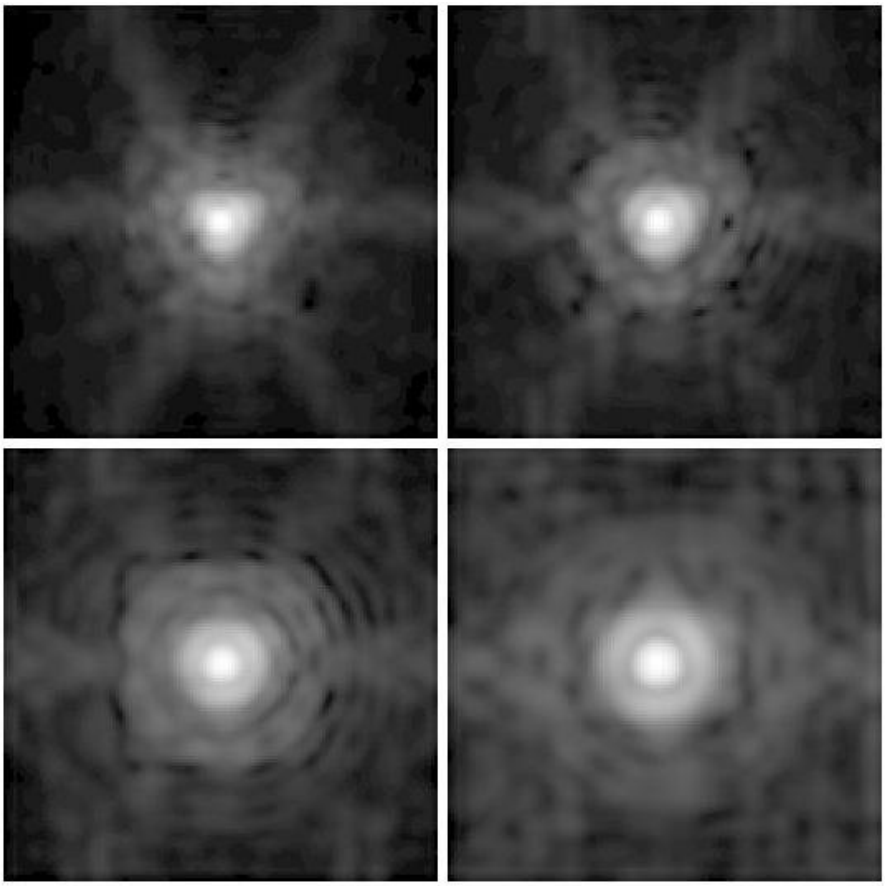

Figure 5.8: The core regions of the PSFs determined by the Spitzer Science Centre from in-flight calibration data, for the four channels of IRAC. The images are shown in logarithmic scaling. (Image Courtesy: Spitzer Science Centre)

involves identifying several bright foreground stars in the image and simultaneously fitting an analytical profile, such as a Gaussian or Moffat, to them. The average parameters needed to describe the stars are determined. The best-fit function is subtracted from the stellar profiles to determine the residuals. Any residuals due to non-symmetric or extended structures thus determined are added to the best-fit model. A PSF obtained this way thus takes into account both a smooth component of the PSF as well as any irregularities. Such a method can be implemented using the DAOPHOT package within IRAF.

The first two of the three methods can be used only if the PSF is sufficiently sampled i.e. the FWHM of the PSF should not be less than three pixels theoretically though in practice, a FWHM of atleast 4-5 pixels is needed. In other words, the PSF cannot be undersampled. If the PSF is undersampled, the first method does not work since for a given set of images of stars, the centroid of the PSF is difficult to constrain. This makes the process of aligning the images of the stars before coadding unreliable. In case of the second method, the number of data points available to reliably fit any profile to the stars to determine their FWHM is very low. The

third method *may* be used in case of undersampled PSFs by adopting a resampling method. The end result however can be strongly dependent on the interpolation scheme adopted etc. If the core of the PSF is quite asymmetric, the third method cannot be used anyway.

The typical FWHM of the PSF for the 3.6 micron IRAC data is $\sim 1.6 - 1.7$ pixels. Thus the PSF is severely undersampled. The detailed, simulated instrumental PSFs for the four channels of IRAC are shown in Figure 5.8. A close look at these also shows a highly asymmetric core that cannot easily be described using Gaussian/Moffat functions which generally work well for ground-based telescopes. Thus, none of the conventional methods apply to the Spitzer IRAC data.

In such cases, one has to rely on the simulated PSFs, a library of which is provided by the Spitzer Science Centre. There are 25 PSFs provided for each IRAC channel corresponding to 25 evenly spaced positions on the CCD. As described earlier, the BCD data of Spitzer is plagued with optical distortions, which cause the PSF to change across the CCD. Thus instead of a single PSF, a library of PSFs is provided. These PSFs have a pixel scale which is five times finer than the pixel scale of a BCD image. However, we do not use individual BCD images for our analysis here. Instead we coadd several dithered exposures of the galaxy to construct a mosaic. In such cases, the PSFs get scrambled and thus an important question to address is - which PSF does one use?

Any PSF can be described as having two main components, the central core which dominates its FWHM and the extended features. From the point of view of 2-d image decomposition, the FWHM of the PSF is of primary importance while accurate knowledge of the extended features is secondary especially if the galaxies are big and bright (Peng, in private communication). The PSFs do not vary in terms of the core structure across the CCD but largely in terms of extended structure. Thus, it was felt reasonable to use the PSF corresponding to the centre of the CCD as a decent approximation to the PSF usable with the final mosaic image i.e the PBCDs.

The simplest method for verifying how well the PSF works is to fit it to bright foreground stars in the image. This can be achieved using GALFIT. The only free parameters GALFIT optimizes in such a case are the centroids, the normalization and a constant sky background. It should be remembered that the PSF provided by Spitzer Science Centre is five times finer sampled than the final constructed mosaic. This information needs to be conveyed to GALFIT by setting the *fine sampling factor* to 5. GALFIT constructs a model image at a finer scale and then intregrates the flux in neighbouring pixels to degrade the model to match the pixel scale of the observed image. Only then the model image is subtracted from the observed image to carry out the optimization of the parameters.

The typical residual obtained when the central PSF is fitted to the stars in a

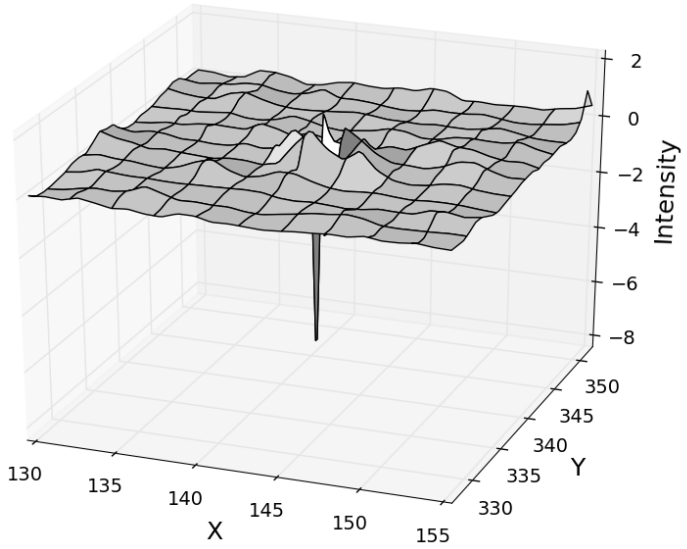

Figure 5.9: A surface plot of the residue of a star. As can be seen clearly, the centre has a negative residue while the wings have a positive residue.

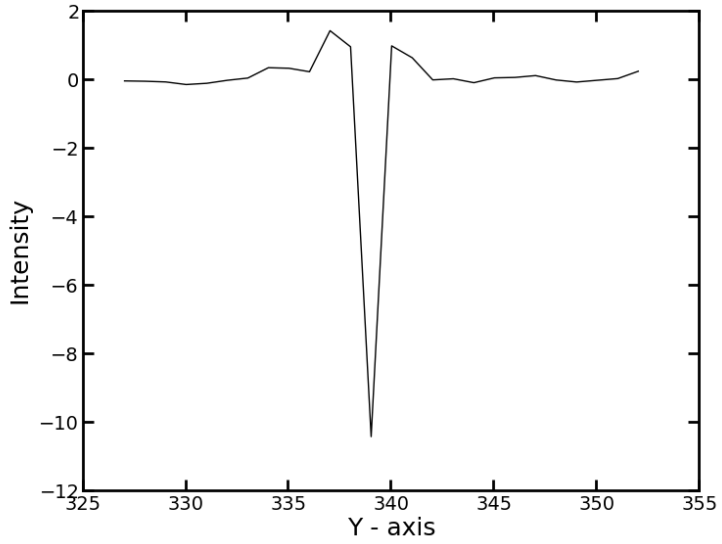

Figure 5.10: A plot along the central column of the residue described in Figure 5.9.

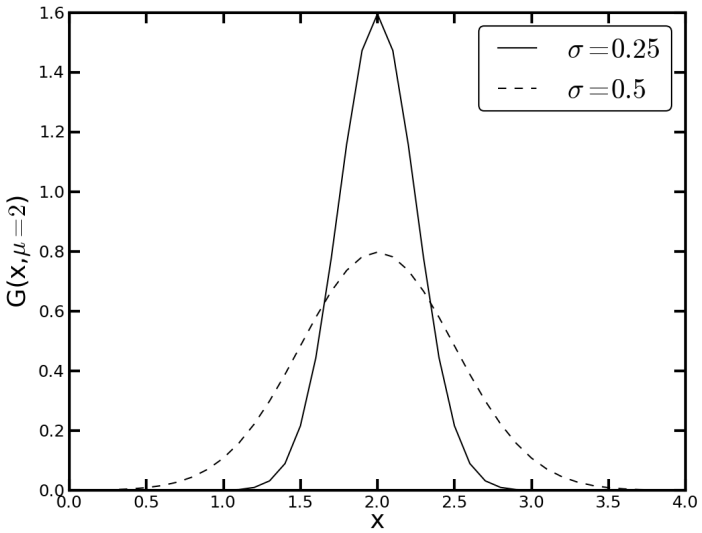

Figure 5.11: Gaussians representing the library PSF (solid line) and the mosaic PSF (dotted line). The Gaussians have a common centre and normalisation but different width.

mosaic is shown in Figure 5.9. As can be seen the PSF is unable to account for the general structure of the observed stars. There is a strong negative residual at the centre while the wings show a positive residual. This can be seen in a clearer fashion if a slice is taken along the surface plot through the centre as shown in Figure 5.10. A careful measurement of the amplitude of the residuals shows that within background noise levels, the total central negative residual ($\sim 6-15\%$) is equal to the positive residual found in the wings. This result can be explained as follows.

Consider that one is dealing with imaging data where the PSF can be described by a Gaussian. We use a given method to determine the FWHM of the PSF but due to some systematic error in the process of measurement, the FWHM is underestimated. So, the FWHM of the PSF being used for fitting is less than the actual FWHM for a given image. In other words, we are trying to fit a Gaussian of lower FWHM to a Gaussian of a higher FWHM. The best one can do is to adjust the centroids and the normalizations - the widths cannot be altered. In such a case, after the best-fit has been obtained the observed and fitted profiles appear as shown in Figure 5.11. Subtracting the fitted Gaussian from the observed profile results in a residual as shown in Figure 5.12. This residual is similar to what is observed when fitting the central PSF to a star in a mosaic. Thus it can be concluded that the overall width of the central PSF is lesser than that of the mosaic.

Why are the FWHMs different? Now that the incompatibility between the central PSF applicable to a BCD image and that valid for a mosaic has been explained as a difference in widths, one needs to understand the process responsible

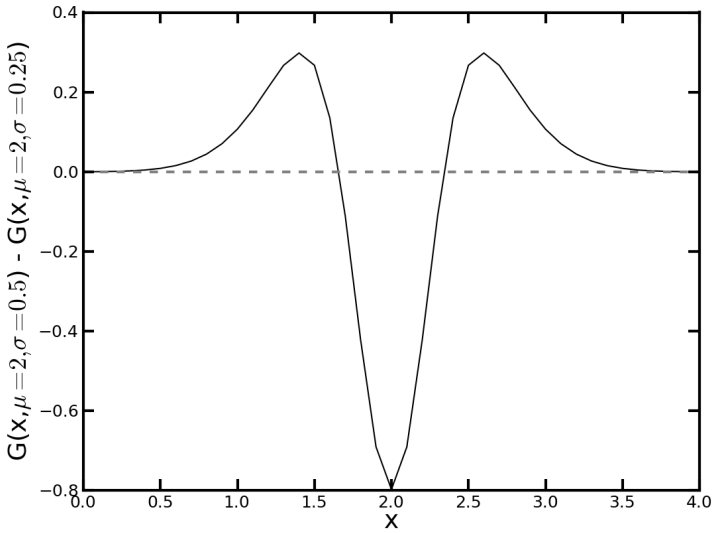

Figure 5.12: The difference obtained by subtracting the two Gaussian curves, as explained in the text. The central part shows a negative residue while positive residue is seen in the outer parts.

for the increased width in case of mosaics. The answer lies in the method by which mosaics are constructed. First, a grid of desired pixel size is constructed, known as the fiducial image frame. Individual BCDs are then projected onto this grid taking into account the distortions. Seldom will a pixel of the BCD align with a pixel of the final grid and thus one needs an interpolation scheme to redistribute the flux within a pixel among the pixels of the final grid onto which a given pixel is projected. The side-effect of this projection and interpolation is an increase in the width of the PSF in the final image.

Modifying instrumental PSF. As shown above, it is clear that the FWHM of the library PSF has a lower width. It is essential that FWHMs match since this has a first order effect on the final parameters of the galaxy. To make the central PSF suitable for use with a mosaic, its width must be increased i.e. it must be broadened. This can be achieved by convolving the PSF with a Gaussian of suitable parameters. The parameters needed to describe a Gaussian are its FWHM, position angle and axis ratio. To determine these, we ask GALFIT to fit a Gaussian convolved with the central PSF on bright but unsaturated field stars simultaneously. Further, a constraints file is provided to GALFIT requiring the FWHM, position angle and axis ratio must be equal for all the stars. This way, one obtains the best-fit parameters for a Gaussian averaged over all the stars used in this fit. An example of such an input file is shown in Figure 5.13 and the corresponding constraints file is shown in Figure 5.14.

When performing the above process, a border mask image is needed to avoid

```
# IMAGE and GALFIT CONTROL PARAMETERS
A) mosaic.fits         # Input data image (FITS file)
B) composite_out1.fits      # Output data image block
C) mosaic_unc.fits      # Sigma image name (made from data if blank)
D) Central_PSF.fits          # Input PSF image and (optional) diffusion
kernel
E) 5                   # PSF fine sampling factor relative to data
F) Border_Mask.fits           # Bad pixel mask (FITS image or ASCII coord
list)
G) Constraints        # File with parameter constraints (ASCII file)
H) 1    450     1  1103  # Image region to fit (xmin xmax ymin ymax)
I) 50     50           # Size of the convolution box (x y)
J) 20.472              # Magnitude photometric zeropoint
K) 1.223  1.223        # Plate scale (dx dy)   [arcsec per pixel]
O) regular               # Display type (regular, curses, both)
P) 0                   # Choose: 0=optimize, 1=model, 2=imgblock, 3=subcomps

# Component number: 1
0) gaussian               #  Component type
1) 189 607.5    1       1  #  Position x, y
3) 16.2115     1          #  Integrated magnitude
4) 0.7670      1          #     FWHM       [pix]
9) 0.8897      1          #  Axis ratio (b/a)
10) 4.1940      1          #  Position angle (PA) [deg: Up=0, Left=90]
Z) 0                       #  Skip this model in output image?  (yes=1, no=0)


# Component number: 2
0) gaussian               #  Component type
1) 216.5 617    1       1  #  Position x, y
3) 16.2115     1          #  Integrated magnitude
4) 0.7670      1          #     FWHM       [pix]
9) 0.8897      1          #  Axis ratio (b/a)
10) 4.1940      1          #  Position angle (PA) [deg: Up=0, Left=90]
Z) 0                       #  Skip this model in output image?  (yes=1, no=0)


# Component number: 3
0) gaussian               #  Component type
1) 277 577.5    1       1  #  Position x, y
3) 16.2115     1          #  Integrated magnitude
4) 0.7670      1          #     FWHM       [pix]
9) 0.8897      1          #  Axis ratio (b/a)
10) 4.1940      1          #  Position angle (PA) [deg: Up=0, Left=90]
Z) 0                       #  Skip this model in output image?  (yes=1, no=0)

# sky
0) sky
1) 0.08       1       # sky background       [ADU counts]
2) 0.000      0       # dsky/dx (sky gradient in x)
3) 0.000      0       # dsky/dy (sky gradient in y)
Z) 0                  #  Skip this model in output image?  (yes=1, no=0)
```

Figure 5.13: An example GALFIT input file used to determine the parameters of the Gaussian needed to broaden the library PSF.

```
1_2_3_4_5_6_7_8_9_10_11_12_13_14_15     re      offset
1_2_3_4_5_6_7_8_9_10_11_12_13_14_15     q       offset
1_2_3_4_5_6_7_8_9_10_11_12_13_14_15     pa      offset
```

Figure 5.14: An example GALFIT constraints file used to determine the parameters of the Gaussian needed to broaden the library PSF.

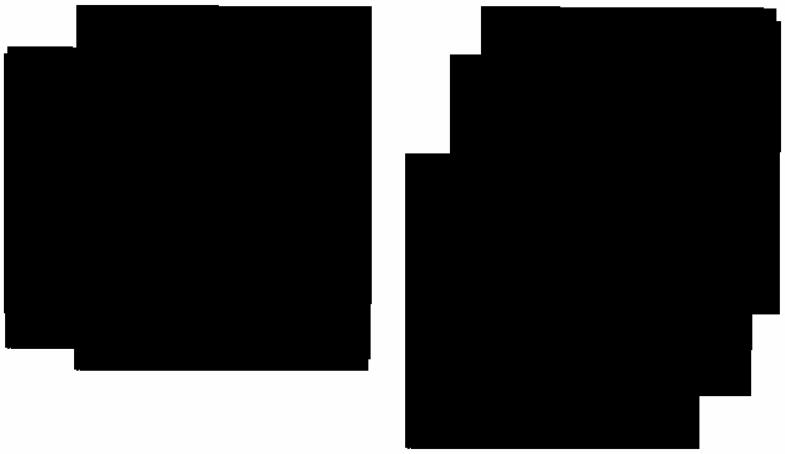

Figure 5.15: An example of a border mask image needed for the process of constructing a modified PSF.

segmentation faults when running GALFIT. In the process of fitting, GALFIT may utilize pixels that have been assigned a NaN value by MOPEX since the corresponding region of the sky was not observed in any BCD image. This leads to a segmentation fault and can be circumvented by providing a border mask. The border mask is an image of the same size as the mosaic but marks as 0 all the pixels with valid flux values while all pixels lying outside coverage area are marked as 1 or any other non-zero value. To construct this, the *imreplace* task in IRAF is used. First, this task is run with the following parameters -

```
images=Border_Mask.fits
value=max_value + 1000
lower=0
upper=0
```

This basically means that all pixels with value zero will be replaced with a value significantly larger than largest value in the science image (the largest value can be determined using *imstatistics* tool in IRAF). This works because *imreplace* treats NaN values as zeros. Thus an image is constructed where all pixels outside coverage area are given a very large value. Next, the imreplace task is rerun with following parameters -

```
images=Border_Mask.fits
value=0
lower=min_value
upper=max_value
```

This takes all pixels with values encompassing the range of all possible values in the

```
# IMAGE and GALFIT CONTROL PARAMETERS
A) none         # Input data image (FITS file)
B) NGC3990_PSF.fits      # Output data image block
C) none      # Sigma image name (made from data if blank)
D) Central_PSF.fits          # Input PSF image and (optional) diffusion
kernel
E) 1                   # PSF fine sampling factor relative to data
F) none           # Bad pixel mask (FITS image or ASCII coord list)
G) none        # File with parameter constraints (ASCII file)
H) 1    128     1  128  # Image region to fit (xmin xmax ymin ymax)
I) 128     128           # Size of the convolution box (x y)
J) 20.472             # Magnitude photometric zeropoint
K) 1.223  1.223        # Plate scale (dx dy)   [arcsec per pixel]
O) regular               # Display type (regular, curses, both)
P) 0                   # Choose: 0=optimize, 1=model, 2=imgblock, 3=subcomps


# Component number: 1
0) gaussian               #  Component type
1) 65.0 65.0    1       1  #  Position x, y
3) 11.0000     1          #  Integrated magnitude
4) 4.988      1          #     FWHM       [pix]
9) 0.8832      1          #  Axis ratio (b/a)
10) 5.9882      1          #  Position angle (PA) [deg: Up=0, Left=90]
Z) 0                      #  Skip this model in output image?  (yes=1, no=0)
```

Figure 5.16: Example of the GALFIT input configuration file needed for constructing the final PSF using the parameters of the Gaussian determined from the field stars.

science image and sets them to zero. The final image thus obtained is the border mask and is shown in Figure 5.15.

Once GALFIT is executed by supplying the required input file, constraints file, science image, uncertainty image and border mask, the best-fit parameters of the Gaussian are obtained. Note that these parameters, particularly the FWHM is reported in terms of the units of the science image i.e. if the best-fit FWHM is, say 1.2 pixels, the pixels here refer to the pixel in the science image. We now want to construct a final PSF which is the convolution of the library PSF with the Gaussian. But the width obtained is not in terms of the pixels of the PSF and thus should be multipled by 5 to take this into account. As mentioned earlier, when GALFIT is not provided any input image, it exits by constructing the model image. Thus, a final PSF can be constructed by using the obtained parameters of the Gaussian. A typical configuration file for this step is shown in Figure 5.16.

Testing the Final PSF To test whether the final PSF truly represents a point source as present in the mosaic, we again ask GALFIT to fit it onto a selection of stars. The average residual obtained using the modified PSF is shown in Figure 5.17. The residuals are well within the typical noise level in the image.

5.6.1 Modules for PSF Construction

The parameters of the Gaussian may vary depending on a number of factors such as the coverage level (the number of images contributing to a pixel in the final image),

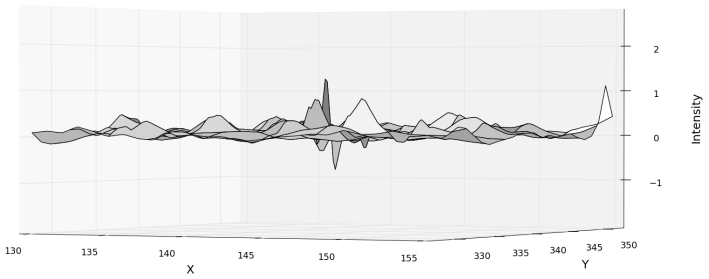

Figure 5.17: A surface plot of the residue of the star as in Figure 5.9 but now fitted with a modified PSF. Notice how the systematic feature found earlier is now replaced with noise like fluctuation.

the dithering pattern etc. Thus the process of constructing a modified PSF must be performed for all science images. To ease this process, a set of modules were developed in *Python* and *bash* which do the following:

- The image is opened in ds9. The user is required to mark the stars required for the estimation of the Gaussian parameters by clicking on them. This causes circles to appear on the stars, called *regions* in ds9 terminology. These regions are saved by the user as a file called *ds9.reg*, the default file name used by ds9.

- The ds9.reg file is parsed by a Python module to construct the required input and constraints file.

- A script is invoked to construct the border mask needed by GALFIT.

- GALFIT then performs the best-fit using these inputs.

- The output of GALFIT is parsed by another program which generates the required final file needed to construct the modified PSF.

- GALFIT is executed with the final input file.

At this point, the following information needed for running GALFIT is available to us - science/observed image, uncertainty image and the PSF. The next section deals with the construction of the final mask needed during the process of fitting the galaxy and the basic input file needed for performing the preliminary fit.

5.7 Final Masks and Preliminary Fit Input Configuration

5.7.1 Final Masks

The process of modelling the light distribution in a galaxy, as described in detail earlier, requires minimizing a χ^2:

$$\chi^2 = \sum_x \sum_y \left(\frac{O(x,y) - M(x,y)}{\sigma(x,y)} \right)^2$$

The data points $O(x, y)$ in the above equation refer to the pixels of the image but all pixels do not *belong to the galaxy*. What is meant is that the flux recorded in a given pixel may not be dominated by the light from the galaxy but by light from other astrophysical sources in its vicinity. Such pixels can affect the reliability with which the best-fit parameters are recovered. Thus, it is essential to construct a mask image, an image where all pixels that should be considered for fitting have a value 0 and those which should not be considered while fitting, have a non-zero value.

The simplest method to construct such an image is to use the *ellipse* task in IRAF which is used to fit ellipses to the isophotes of a galaxy. It allows users to interactively mask out pixels by simply pointing the cursor to a pixel and pressing the *m* key. The information about the masked pixels is stored in a .pl file which can be renamed as .fits with pixel data type changed to *real* and made compatible with GALFIT. However, the process of manually masking out the pixels in this manner is cumbersome and is not feasible when dealing with a sample of a few hundred galaxies. A more efficient method is described below.

SExtractor (Bertin and Arnouts, 1996) is a powerful astronomical software tool which uses neural networks to analyze images to auto-detect the sources in them. The software requires an input configuration file which determines various parameters used to distinguish a true source from noise spikes and estimate a probability for the source to be a star or a galaxy. The tool is also capable of providing various measures of flux for the sources it detects. In its typical usage, the tool's eventual goal is to produce a catalogue of all sources detected by it in an image with various quantities measured for each source. However, the tool also allows for the generation of a *segmentation image*. This is an image with the same dimensions as that of the input image with the value of the pixels indicating the object identifier, as assigned by SExtractor, to which the pixel belongs. For example, if a galaxy has been assigned the identifier 1 in the generated catalogue, all the pixels dominated by light coming from the galaxy have a value 1. If the identifier is 2, then pixels belonging to this source have a value 2, and so on. The pixels dominated by background flux

and not by any source have a value zero.

Thus, the following steps can be adopted to construct a mask:

- Run SExtractor on the observed / science image with suitable configuration input requesting for a segmentation image.
- Identify the galaxy that needs to be modelled in the catalog and note its object identifier.
- Replace all pixels in the segmentation image having the same value as the above identifier with zero using *imreplace* task.

The above steps only represent a general approach applicable for any image. To deal with IRAC 3.6 micron data, a few changes need to be adopted. The primary difference between IRAC final data and data typically used with SExtractor is that the former is in units of MJy/str while latter is in counts. Thus, the default SExtractor configuration cannot efficiently detect sources in IRAC images owing to the low range of values in MJy/str. One way to overcome this problem is to modify the SExtractor default configuration to make it suitable for IRAC images or to convert the IRAC images to approximate counts or counts/sec units. The latter can be easily achieved by creating a temporary copy of the image where each value is divided by the FLUXCONV parameter that can be found in the image header. In the present work, the latter method was adopted. So, before executing the above steps, the entire image is divided by FLUXCONV.

A few points worth noting here -

- SExtractor's output photometry with the above method may not be reliable. But the objective here is to detect the sources and construct the segmentation image and not perform accurate photometry of every source detected.
- The BCD images for which the original FLUXCONV parameter is computed by the software pipeline responsible for constructing BCDs from RAW data undergo significant amount of processing when they are coadded to construct the final mosaic. As a result, it does not make much sense to be actually dividing the image by FLUXCONV - it will not yield a true estimate of counts/sec. But for the purpose of letting the default SExtractor configuration detect sources efficiently, this is sufficient.

At this point, the modified segmentation image masks all pixels that do not belong to the galaxy or the background. But this image still does not mask out all the pixels lying outside the coverage area. The border mask used in the process of constructing the modified PSF, described in the earlier section, however masks

all pixels lying outside coverage area but not the pixels belonging to other objects. The final mask needed for use with GALFIT must mask both varieties of pixels. The simplest way to construct this mask is to perform an image addition of the border mask and the modified SExtractor segmentation image. This is referred to as a *master mask* and is supplied to GALFIT when performing the decomposition analysis.

5.7.2 Final Input File

A typical example of an input file aimed at fitting a bulge+disk model to a galaxy image is shown in Figure 5.18. At this stage, the observed image, the PSF image and the mask image have all been constructed. We need to specify the initial guesses to the Sérsic and exponential profiles used to model the bulge and the disk respectively. The most important of these are the centroids. Without a proper initial guess of the centroid, GALFIT is unlikely to recover good model parameters. To determine the centroid, the catalogue generated by SExtractor, described in the previous subsection, is used. Knowing the object identifier of the galaxy, its centroid as determined by SExtractor and made available in the generated catalogue is supplied as the guess centroid.

Based on quick look study of all the images, it was found that a common image cut-out of 300×300 pixels was sufficient to be able to model the galaxy. Thus the coordinates $(x_{gc}, y_{gc}) - (150, 150)$ and $(x_{gc}, y_{gc}) + (150, 150)$ were supplied as image cut out regions to GALFIT where (x_{gc}, y_{gc}) represent the x- and y-coordinate of the guessed centroid. The convolution box was chosen to be 150×150 based on experience. A smaller convolution box could potentially affect recovered parameters while a larger convolution box would increase computational overhead without significant improvement in the accuracy of the recovered parameters. Other initial parameters were kept common to all galaxies as well, based on experience. It should be noted that the key goal here was to perform an initial decomposition on all galaxies in an automated fashion followed by a manual case-by-case inspection. Thus no special attention was paid in performing tests to intelligently guess the other initial parameters for each galaxy. Such estimates are however possible - read Vikram et al. (2010) for more details.

The details of how the zero point magnitude, one of the parameters required by GALFIT, is computed are provided in the following section.

```
# IMAGE and GALFIT CONTROL PARAMETERS
A) mosaic.fits         # Input data image (FITS file)
B) BD1.in_out.fits      # Output data image block
C) mosaic_unc.fits      # Sigma image name (made from data if blank)
D) NGC3990_PSF.fits          # Input PSF image and (optional) diffusion
kernel
E) 5                   # PSF fine sampling factor relative to data
F) Master_Mask.fits           # Bad pixel mask (FITS image or ASCII coord
list)
G) none        # File with parameter constraints (ASCII file)
H) 385 685 136 436  # Image region to fit (xmin xmax ymin ymax)
I) 150     150           # Size of the convolution box (x y)
J) 20.472              # Magnitude photometric zeropoint
K) 1.223  1.223        # Plate scale (dx dy)   [arcsec per pixel]
O) regular               # Display type (regular, curses, both)
P) 0                   # Choose: 0=optimize, 1=model, 2=imgblock, 3=subcomps



# Adding a Sersic representing a bulge.

 0) sersic                 #  Component type
 1) 535 286 1 1  #  Position x, y
 3) 13.5459     1          #  Integrated magnitude
 4) 9.4520     1          #  R_e (effective radius)   [pix]
 5) 3.4525      1          #  Sersic index n (de Vaucouleurs n=4)
 9) 0.75475      1          #  Axis ratio (b/a)
10) -45.5484    1          #  Position angle (PA) [deg: Up=0, Left=90]
 Z) 0                      #  Skip this model in output image?  (yes=1, no=0)



# Adding an expdisk representing a disk.

 0) expdisk                #  Component type
 1) 535 286 1 1  #  Position x, y
 3) 14.5452     1          #  Integrated magnitude
 4) 32.5414     1          #  R_s (disk scale-length)   [pix]
 9) 0.8455      1          #  Axis ratio (b/a)
10) -47.2540    1          #  Position angle (PA) [deg: Up=0, Left=90]
 Z) 0                      #  Skip this model in output image?  (yes=1, no=0)

# Adding a variable sky pedestal.

0) sky                    #  Component type
 1) 9.123e-02      1       #  Sky background at center of fitting region
[ADUs]
 2) 0.000e+00      0       #  dsky/dx (sky gradient in x)     [ADUs/pix]
 3) 0.000e+00      0       #  dsky/dy (sky gradient in y)     [ADUs/pix]
 Z) 0                      #  Skip this model in output image?  (yes=1, no=0)
```

Figure 5.18: A typical configuration file used to perform a preliminary bulge+disk decomposition using GALFIT.

5.8 Zero Point Magnitude

GALFIT requires a zero point magnitude in order to compute the integrated magnitude of the components fitted by it. Given a model with total integrated flux F_{tot}, the corresponding integrated magnitude is computed by GALFIT using the following standard equation.

$$m = -2.5 \ \log\left(\frac{F_{tot}}{t_{exp}}\right) + \text{zero point} \tag{5.2}$$

IRAC images are calibrated in units of MJy/str. Strictly speaking, these are units of surface brightness and it is not an additive quantity. But from the point of view GALFIT, the numbers in a pixel are scaled versions of counts and hence can be treated as additive provided that an adjustment is made to the zero point to reflect this scaling. As opposed to the Vega magnitude system which computes magnitudes by using the flux received from Vega as a reference, the AB magnitude system (Oke and Gunn, 1983) uses absolute flux measurements. Given the calibration of IRAC images in absolute flux units, the AB system is a natural choice in the present study. The zero point magnitude can be derived as follows.

The equation defining the AB magnitude system is -

$$m_{AB} = -2.5 \ \log(F) - 48.60 \tag{5.3}$$

Here, F is in the units of ergs^{-1}cm^{-2}Hz^{-1}. Transforming the units of flux in the above equation, we can arrive at a zero point that can be provided to GALFIT.

$$\begin{aligned} m_{AB} &= -2.5 \ \log(F_{Jy}10^{-23}) - 48.60 \\ &= -2.5 \ \log(F_{Jy}) + 8.9 \\ &= -2.5 \ \log(F_{MJy/str} \times 10^6 \times \Omega_{pixel}(str)) + 8.9 \end{aligned}$$

The $\Omega_{pixel}(str)$ can be computed given the pixel scale of the mosaic is 1.22 arcsec as 3.5×10^{-11} str. Substituting this in the above equation, we get

$$m_{AB} = -2.5 \ \log(F_{MJy/str}) + 20.039 \tag{5.4}$$

Comparing equations 5.2 and 5.4, we get the zero point magnitude as 20.039. This is supplied to GALFIT through the input file.

The 1-d surface brightness profile of a galaxy or a model is a plot of the surface brightness in magnitudes per square arcsecond as a function of the semi-major axis of the galaxy, usually represented in kiloparsec units, though sometimes arcseconds

are also used. To determine the surface brightness profile, the *ellipse* task in IRAF is used. This task fits ellipses to the isophotes of the galaxy by expanding the intensity about the ellipse in terms of a Fourier series. The details can be found in Jedrzejewski et al. (1987). This task also needs to be supplied with a zero point in order to obtain the surface brightness profile. The above zero point is not valid if one needs a profile in magnitudes per square arcsecond. To obtain this, one modifies the above equation as follows. For convenience of notation as well as understanding, the $F_{MJy/str}$ is simply represented as C, which is some unit associated with the image, which from the point of view of the *ellipse* task is functionally same as counts.

$$\begin{aligned} \mu_{AB} \quad [\mathrm{mag/arcsec^{-2}}] &= -2.5\ \log(C/(1.22'')^2) + 20.039 \\ &= -2.5\ \log(C) + 20.470 \\ &= -2.5\ \log(F_{\mathrm{MJy/str}}) + 20.470 \end{aligned} \tag{5.5}$$

Note that the above equation is valid not only for an image bearing a 1.22 arcsec pixel scale but for any pixel scale so long as the image is calibrated in units of MJy/str.

5.9 Summary of Workflow

In the last several sections, details of how various input images / quantities, required by GALFIT to perform 2-d decomposition, are processed, have been presented. This section summarizes all the steps involved in the complete workflow. The next section discusses how the quality of fits was inspected and the addition of a bar component.

- All BCDs of each galaxy are downloaded from SHA as .zip files. A bash script, given a path where all .zip files are stored runs the overlap.pl and mosaic.pl MOPEX pipelines to construct the final mosaic images along with their uncertainty images.
- Next, the user is shown all mosaic images in a sequence. For each image, user marks the stars needed for determining the PSF as ds9 regions. Once this is done, the pipeline constructs the border mask, required GALFIT input and constraint files to determine the parameters of the Gaussian that should be convolved with the library PSF to make it compatible with a mosaic. A sub-module reads the determined FWHM, scales it appropriately, and uses it to make a GALFIT configuration file to construct the PSF.
- A new pipeline is executed which runs SExtractor on all constructed mosaics in order to generate the segmentation image. The user is shown the science

mosaic and the segmentation image as a blink sequence and asked to enter the object identifier of the galaxy to be fitted. The final mask is constructed by adding a border mask to the segmentation image. Using the SExtractor catalog to determine centroids, a GALFIT input file for a bulge+disk model is prepared.

- A module is run which allows GALFIT to sequentially perform the initial bulge+disk decomposition, logging any encountered errors and flagging them for manual inspection.
- Finally, a new module applies the *ellipse* task to construct surface brightness profiles for observed and model images. The module also constructs position angle and ellipticity profiles. The need for this is explained in the next section.

At this point, a bulge+disk model has been fitted to all the galaxies. The subsequent steps involve a manual inspection of the fits, any necessary refitting and the addition of a bar component.

5.10 Quality of Fits, Adding a Bar Component

5.10.1 Evaluating Quality of Fits

The ideal method of evaluating the quality of fits is to examine the χ^2_{red} i.e. the minimum χ^2 normalized by the number of degrees of freedom. For a model that describes the data well, we know that the expectation value of $\chi^2_{red} \sim 1$. This can be inferred from the properties of χ^2 (see for example Chapter 15 on data modelling - Press et al. (1992)). However, the use of χ^2 in judging the goodness-of-fit assumes that the estimation of the uncertainties, which go into the denominator part of χ^2 are accurate. Wrong estimation of the uncertainty will nullify the usefulness of χ^2 to gauge goodness of fit. For example, if one underestimates the error, even for a good model, $\chi^2_{red} \gg 1$. Blind use of χ^2 will reject this model as bad despite it being a good fit.

In the case of Spitzer IRAC data, we start with BCDs and build mosaics by projection and interpolation onto a grid. Even if the uncertainties in the BCDs are known, the method by which the final uncertainty mosaic is constructed does not guarantee a true representation of the final uncertainties. MOPEX constructs the final uncertainty image by simply mosaicking the individual uncertainty images in exactly the same manner as the science images. Further, consider a single pixel in a BCD with a well known noise. When it is projected onto a grid, its flux will most likely be distributed between four pixels of the final image through interpolation. This will lead to the noise in adjacent pixels being correlated. Thus noise will be

likely underestimated for a given mosaic pixel. In brief, determinining the uncertainties of the final pixels in the mosaic is non-trivial. As a result χ^2 is not useful for judging the goodness of fit. However, its utility as a merit function which can be optimized to determine the best-fit parameters in a model still persists.

In such a situation, the goodness of the parameters obtained has to be assessed through other diagnostic methods as described in Vikram et al. (2010). Some of these and other diagnostics used in the current study, are summarized below.

- Physical meaningfulness of parameters: The Sérsic index n in GALFIT is not allowed to exceed 20. However, in practice, it is rare to find bulges $n > 8.0$. So any model where this value is unreasonably large raises a warning flag that the fit is unlikely to be reliable. This argument is not only valid for just the Sérsic index but also for other quantities. For example, an effective radius or disk scale length larger than the image itself or the size of a galaxy as estimated visually in an image viewer like ds9. Or, a bar with length far exceeding that of the disk. With experience, an observer can reject or flag solutions with such strong discrepancies.

- Local Minima: The specific algorithm used in GALFIT for minimization of χ^2 - the Marquardt Levenberg method - is known for its speed but since it partly uses a downhill gradient method, it is prone to finding or getting stuck in local minima on the χ^2 surface. This can lead GALFIT to yield a solution which is not truly optimum. Thus, it is essential that for every fit, the best-fit parameters are perturbed reasonably and the fit rerun, to ensure that the same fit is obtained again. If the solution changes, the values of χ^2 can be compared to judge whether the earlier or the later solution was/is a local minima.

- Background Flux: Some observers prefer to find an independent estimate of the background flux and freeze its value in the GALFIT input file. In the current study, the background flux was left as a free parameter but during the inspection of the fit, it was ensured that the best-fit background value matches an independent estimate, which can be obtained by computing statistics such as mean or median of the pixels in regions of images unoccupied by any source. In most cases, GALFIT's estimate of the background and the independent estimate agreed and there was no need to rerun the fit with a fixed sky. This test is important since an underestimation or overestimation of the background can lead to systematically incorrect estimations of other parameters of the model.

- Examination of the residue: GALFIT provides, in its output image block, a residual image obtained by subtracting the model image from the observed

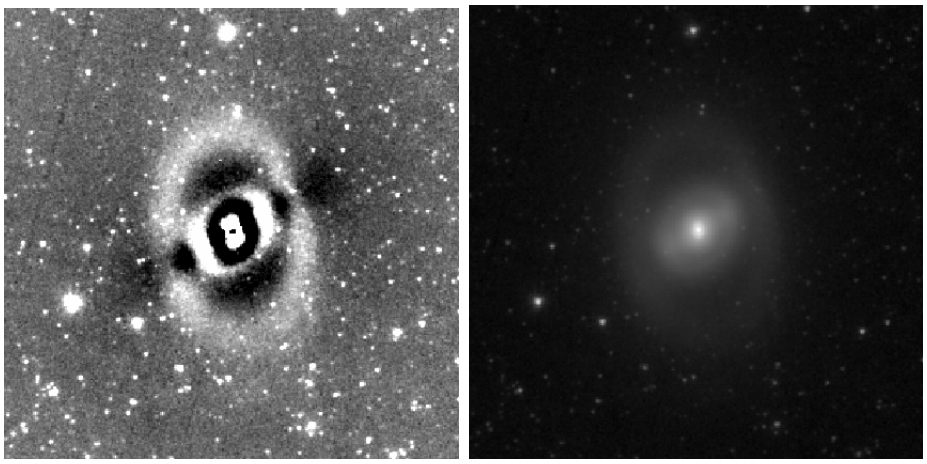

Figure 5.19: On the left, the residual image obtained when a bulge+disk model is fitted to a barred galaxy. On the right, the observed galaxy showing clearly the bar structure.

image. Ideally, the residual should be perfect noise. But this is seldom the case. The high signal-to-noise ratio images of the Spitzer IRAC probe several structures in the galaxy which otherwise get washed out in noise. In most cases, such structures contribute weakly and one can ignore their presence. However, it is possible that such structures contribute too much flux to be ignored. This is true in the case of bars which can account for as high as 20% of the total flux in some cases. In such a case, an additional component needs to be added to account for it.

- Comparison of 1-d surface brightness profiles: Using a routine like the ellipse task in IRAF, it is possible to determine the azimuthally averaged surface brightness as a function of the semi-major axis for both the observed image and the model image constructed by GALFIT. One can then plot them together to make a comparison. A good agreement as judged visually is a good discriminator especially against solutions obtained when GALFIT hits a local minimum.

Employing the diagnostics outlined above, it is possible to qualitatively evaluate the model fitted by GALFIT. In the course of the above process, it may be found that many galaxies have an unaccounted bar component. The identification, the need to account for a bar and the modelling process are described in the next subsection.

5.10.2 Fitting Bars

Is there a bar? There are a few methods by which the presence of bars can be detected. The easiest in this study is the examination of the residual images. An example of a residual image obtained when bulge+disk model is fitted to a barred

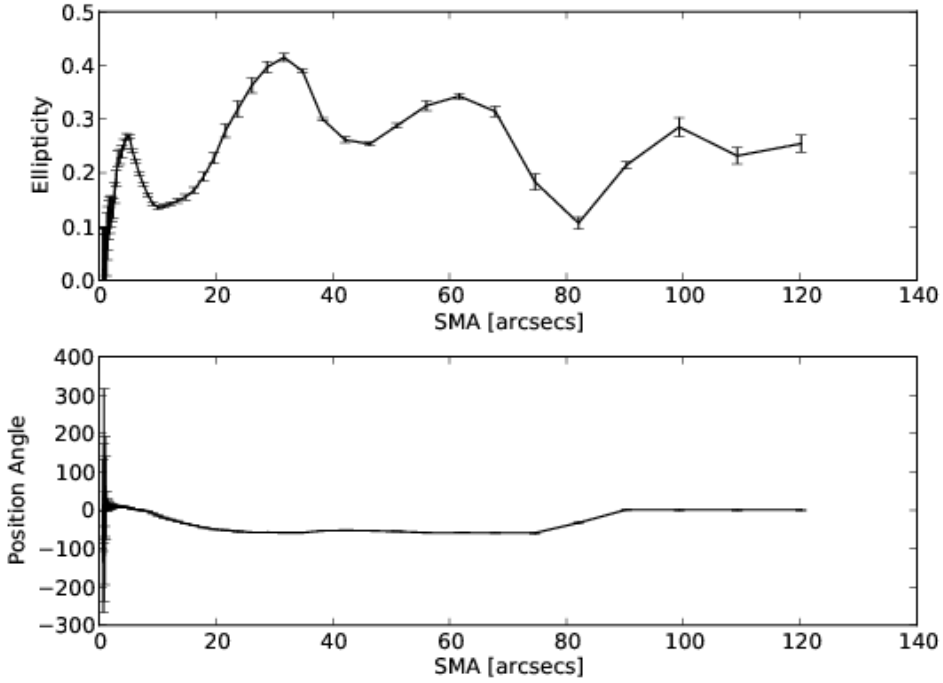

Figure 5.20: The position angle and ellipticity profile for the galaxy illustrated in Figure 5.19

galaxy is shown in Figure 5.19. It is clear that there is a large non-axisymmetric structure in the galaxy which has not been accounted for, by the fitted model. This can be seen in the observed image shown on the right panel of the same figure. But it is not always straightforward to detect a bar in this way. When a bulge+disk model is fitted, the Sérsic profile which is used to fit the bulge *does not know* it has to fit only the bulge. It fits the bulge and bar partly and thus the clear presence of a barred structure in the residue is not assured. In such a case, one can independently verify the existence of a bar by studying the position angle and ellipticity profiles.

These profiles can be obtained from the output of the ellipse task in IRAF. In the region dominated by the bulge, the isophotes will be of low ellipticity but as one leaves this region and moves to a bar dominated region, the bar being an elongated structure with a specific position angle, the isophotes become more and more elongated i.e. have higher ellipticity, while the position angle remains the same. As one moves further outwards, one leaves the bar dominated region and enters the disk dominated region. Here, the isophotes lower their ellipticity and change their position angle to match that of the disk. This results in a peak in the ellipticity profile at a specific semi-major axis (SMA). Around the same SMA, the position angle profile shows an abrupt jump. In this way, these profiles can be used to establish or verify the existence of a bar in a galaxy. An example of such a profile, for the galaxy shown in Figure 5.19, is shown in Figure 5.20. The profiles shown in

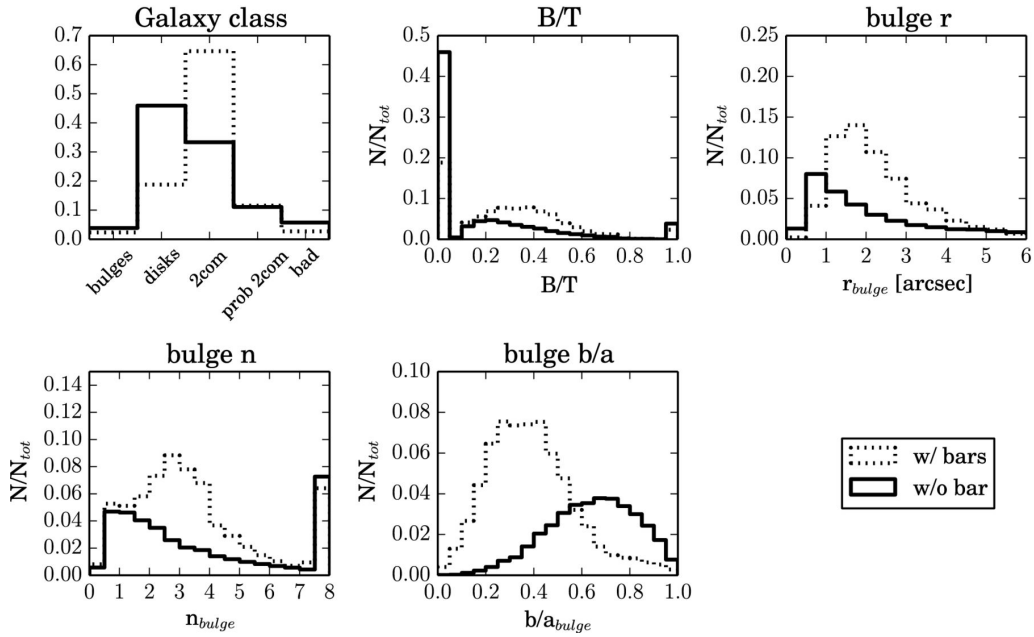

Figure 5.21: Figure 24 from the Meert et al. (2015) paper. The Figure illustrates the systematic effects in the measurement of bulge parameters due to an unaccounted bar.

this figure are however more complicated because the galaxy also contains a ring-like structure in the outer disk. The study of both the position angle and ellipticity profiles as well as the initial residual image can help identify barred galaxies.

Can bars be ignored? As mentioned earlier, the Sérsic profile used to model the bulge does not necessarily model only the bulge component. It can partly account for the bulge as well as the bar. In such a case, the parameters of this profile get systematically affected by the presence of the bar but the observer treats them as bulge properties. This effect has been systematically studied in Laurikainen et al. (2005); Gadotti (2008); Meert et al. (2015). Figure 26 from Meert et al. (2015) is reproduced in Figure 5.21 and shows the distribution of various properties of the 'bulge' for bulge+disk model fits to both barred and unbarred galaxies. The differences in these distributions are not a result of some real physical effect of the bar but a result of systematic effects of bar flux not being accounted for correctly. The figure shows that not accounting for bars can systematically overestimate the bulge-total ratio, the bulge effective radius, the Sérsic index and underestimate the bulge axis ratio. Thus, to recover reliable bulge parameters, bars need to be modelled simultaneously.

How can bars be modelled? Bars have a flat distribution of flux with an almost abrupt cut-off at outer radii. There are two profiles preferred for modelling such a flux distribution. One is to use the Ferrer's profile, shown below.

$$\Sigma(r) = \Sigma_0 \left(1 - (r/r_{out})^{2-\beta}\right)^{\alpha} \tag{5.6}$$

Here, α governs the sharpness of the truncation, β denotes the central slope and r_{out}, the truncation radius. The other method involves using a Sérsic profile with a low value of the n and a high ellipticity (low axis ratio). In an initial test by us, when using the Ferrer's profile, it was found that the overall computational time taken by GALFIT was higher and also in many cases, GALFIT encountered numerical singularities and crashed. This was however not the case with the Sérsic profile which gave reliable results in all test cases. Further, it is also not necessary for bars to have a perfectly flat profile like the one Ferrer's provides. Bars can be cuspy at the centre and thus a more flexible function like Sérsic works better. Moreover, the key purpose here in modelling a bar is not to get the most perfect parameters that can describe the bar, but to be able to take into account the flux contribution and prevent or minimize any systematics affecting the bulge parameters. Thus, it was decided to model the bars using a Sérsic profile. The isophotes of a bar are not only elongated but are also boxy. GALFIT allows for fitting a boxiness parameter to account for non-elliptical isophote shapes. However, the effect of introducing boxiness as an additional free parameter is minor from the point of view of recovering accurate values of other parameters but major from the point of view of computation time. Thus, boxiness was not included in a bar.

A modified version of the pipeline was used for performing the initial bulge+disk fits to the galaxies was used to add a bar component to those galaxies, which during the course of inspection were found to contain bars. These fits were again inspected manually and any necessary refitting was carried out to obtain the final parameters.

5.11 Final Parameters

Of the 247 galaxies for which 3.6 micron images were found in the SHA, the final sample comprises 185 galaxies. The reasons for this reduction of the sample size are highlighted in the sections dealing with the sample construction. One of the reasons for the reduction in the sample size is that GALFIT was unable to find any meaningful solution for some galaxies. By that we mean that the final fit could not satisfy many of the criteria laid down in the previous section expected from a good fit.

For the final 185 galaxies, GALFIT provides the following sets of parameters.

- For bulges - The bulge integrated magnitude, the bulge effective radius (along semi-major axis) in pixels, the Sérsic index, the position angle and the axis ratio.

- For disks - the integrated magnitude, the scale length, position angle and axis ratio.

- For bars - the same as bulges.

From these parameters output by GALFIT, various derived quantities were obtained. This section summarizes all the quantities contained in the final table of parameters and how they were computed.

- Redshift: Obtained from the NASA Extragalactic database.

- Age, Distance, kpc/arcsec conversion factor and Distance Modulus: The redshift obtained from NED was input to a modified version of the Python script written by Schombert that implements Ned Wright's cosmology calculator. These quantities are all output by this program. The standard concordance cosmology model was adopted for these calculations.

- Effective Radii and Scale Lengths: The pixel scale used to construct the final mosaics allows for the conversion of the radii and scale lengths output by GALFIT in pixels into arcseconds. These can then be converted into kiloparsec units using the conversion factor obtained from the cosmological calculator as explained above.

- Average Surface Brightness within Effective Radius: Using the summary of the mathematical properties of the Sérsic profile from Graham and Driver (2005), we can obtain the formula for computing this as

$$\langle \mu_e(< r_e) \rangle = m_{bul} + 2.5 \log(2\pi r^2_{e(arcsec)}) \tag{5.7}$$

  In the above equation $r_{e(arcsec)}$ is r_e output by GALFIT multiplied by the square root of the axis ratio. This correction is needed since GALFIT's r_e is measured along semi-major axis. The units for this quantity is magnitude arcsec^{-2}

- Disk Central Surface Brightness: The exponential profile used for modelling the disk is a Sérsic profile with $n = 1$. Thus again using the mathematical properties of this profile from Graham and Driver (2005), we can obtain the formula for the central surface brightness in magnitude arcsec^{-2}.

$$\mu_0 = m_{disk} - 1.123 + 2.5 \log(2\pi(1.678 * r_{d^2(arcsec)})) \tag{5.8}$$

  Here again, $r_{d(arcsec)}$ is r_d output by GALFIT corrected by multiplying the square root of the axis ratio.

- B/T, D/T and Bar/T Ratios: The total integrated magnitudes of all components were converted into fluxes using the standard equation

$$F = 10^{-0.4(m+zpt)}. \tag{5.9}$$

  The B/T, D/T and Bar/T ratios are the respective fluxes divided by the sum of all fluxes.

A table of all the relevant parameters for the final sample of 185 galaxies is shown in the Table 5.1. The data from this table have been used for the study of S0 galaxies presented in chapters 6 and 7.

5.12 Chapter Summary

This chapter covers the motivation behind the methods used in assembling the RC3-Spitzer sample of S0 galaxies. The primary motivation is that we need high SNR imaging data where effects from both intrinsic and foreground extinction can be ignored with the light representing well the underlying stellar mass of the galaxy. The technique of 2-d decomposition and the subtleties involved in its practical execution have been explained in detail as well. We have seen that there are several inputs required by a program like GALFIT used for performing the 2-d decomposition.

Discussed in this chapter are the characteristics of the Spitzer imaging data in the context of the intended analysis and the need for constructing custom PBCDs or mosaics and the method used. A detailed treatment of the PSF, its importance to 2-d decomposition, the challenge in finding it for the Spitzer IRAC Level 2 data and the solution, and the methods for determining quality of fits, checking for presence of bars, the need to fit for the bars and the fitting method. A snapshot of the total workflow involved in 2-d decomposition of Spitzer images has been presented along with the final parameters derived for the sample of 185 S0s.

In the next chapter, the demographics of pseudobulges in S0 galaxies have been discussed along with a study of possible signatures imprinted onto the correlations between the structural parameters, by the processes responsible for forming these systems.

Name	T	Bulge Type	L_K	Bulge parameters			Disk parameters		Bar Parameters			B/T	Bar/T
				$< \mu_e >$	r_e	n	μ_{0d}	r_d	m_{bar}	n_{bar}	$r_{e(bar)}$		
ESO079-007	4.0	1	-18.73	21.72	0.87	0.53	20.95	1.72	0.00	0.00	0.00	0.04	0.00
ESO085-030	-0.4	1	-18.76	20.23	0.86	1.41	19.25	0.78	0.00	0.00	0.00	0.64	0.00
ESO358-025	-2.6	1	-19.04	19.84	0.73	0.74	21.08	1.59	0.00	0.00	0.00	0.41	0.00
ESO420-013	-1.1	0	-22.21	13.94	0.29	1.91	18.49	1.52	0.00	0.00	0.00	0.60	0.00
ESO506-033	-2.0	0	-20.12	16.11	0.46	1.81	20.14	1.16	0.00	0.00	0.00	0.71	0.00
IC0051	-2.0	1	-19.85	18.80	1.00	1.20	20.28	1.34	0.00	0.00	0.00	0.56	0.00
IC0335	-2.1	0	-20.82	22.17	5.59	5.45	17.43	1.69	0.00	0.00	0.00	0.48	0.00
IC0719	-1.9	0	-20.61	18.08	1.49	1.35	24.67	4.20	0.00	0.00	0.00	0.94	0.00
IC2035	-2.6	0	-20.92	14.29	0.13	3.41	17.14	0.52	0.00	0.00	0.00	0.34	0.00
IC2040	-0.8	1	-18.70	19.99	0.98	0.83	21.60	1.44	0.00	0.00	0.00	0.68	0.00
IC2085	-1.2	1	-18.48	18.86	0.53	0.88	20.16	1.24	0.00	0.00	0.00	0.41	0.00
IC2569	-1.1	0	-23.43	17.30	2.40	1.97	19.42	14.68	0.00	0.00	0.00	0.28	0.00
IC5267	-2.9	0	-16.76	17.80	1.06	2.15	19.64	3.89	0.00	0.00	0.00	0.31	0.00
NGC0059	-2.0	0	-19.25	20.94	0.27	2.89	20.98	0.57	0.00	0.00	0.00	0.26	0.00
NGC0148	-3.3	0	-19.73	17.89	0.78	6.93	18.81	1.44	0.00	0.00	0.00	0.65	0.00
NGC0507	-1.2	0	-23.35	18.19	2.89	3.54	20.69	14.05	0.00	0.00	0.00	0.31	0.00
NGC0524	-1.7	0	-22.51	19.06	4.74	4.09	19.98	3.86	0.00	0.00	0.00	0.79	0.00
NGC0695	-1.1	0	-26.75	17.43	2.54	1.64	18.05	2.53	0.00	0.00	0.00	0.67	0.00
NGC0838	-2.6	0	-21.61	17.97	1.57	4.94	15.73	0.60	0.00	0.00	0.00	0.52	0.00
NGC1023	-2.4	0	-18.20	17.09	0.67	3.16	19.12	2.80	0.00	0.00	0.00	0.47	0.00
NGC1167	-2.5	0	-26.18	19.27	4.53	4.55	20.50	8.99	0.00	0.00	0.00	0.46	0.00

NGC1297	-2.2	0	-21.28	19.15	0.96	4.23	20.50	2.43	0.00	0.00	0.00	0.37	0.00
NGC1366	-3.0	0	-20.44	16.42	0.26	4.55	18.76	1.11	0.00	0.00	0.00	0.55	0.00
NGC1411	-2.0	0	-19.88	16.44	0.26	2.76	19.31	1.28	0.00	0.00	0.00	0.41	0.00
NGC1461	-0.8	0	-21.60	17.39	0.64	2.31	19.21	2.71	0.00	0.00	0.00	0.45	0.00
NGC1482	-1.6	0	-22.00	15.06	0.61	1.20	19.51	2.20	0.00	0.00	0.00	0.74	0.00
NGC1510	-1.8	1	-20.24	18.93	0.24	1.18	21.19	0.82	0.00	0.00	0.00	0.40	0.00
NGC1522	-2.3	1	-18.33	19.85	0.36	0.44	21.51	0.81	0.00	0.00	0.00	0.37	0.00
NGC1553	-2.0	0	-17.71	16.08	0.37	1.07	17.47	1.77	0.00	0.00	0.00	0.14	0.00
NGC1596	-2.0	0	-23.54	17.16	0.65	1.70	18.53	2.41	0.00	0.00	0.00	0.45	0.00
NGC2549	-2.2	0	-20.95	18.56	2.04	4.76	17.79	0.28	0.00	0.00	0.00	0.94	0.00
NGC2563	-2.2	0	-24.15	18.48	3.17	3.38	21.99	15.06	0.00	0.00	0.00	0.62	0.00
NGC2695	-1.1	0	-21.24	18.54	1.62	5.16	21.16	2.31	0.00	0.00	0.00	0.84	0.00
NGC2698	-2.0	0	-21.41	18.00	0.91	3.70	23.76	8.44	0.00	0.00	0.00	0.75	0.00
NGC2732	-2.0	0	-21.54	18.16	1.15	8.82	17.98	1.75	0.00	0.00	0.00	0.54	0.00
NGC3065	-2.9	0	-21.49	16.68	0.40	2.22	20.27	2.39	0.00	0.00	0.00	0.44	0.00
NGC3115	-2.1	0	-19.04	17.38	1.93	4.81	20.42	2.76	0.00	0.00	0.00	0.82	0.00
NGC3245	-1.5	0	-23.63	15.79	0.33	2.54	18.80	1.89	0.00	0.00	0.00	0.37	0.00
NGC3413	-2.0	1	-20.10	19.45	0.23	0.70	19.97	0.54	0.00	0.00	0.00	0.29	0.00
NGC3414	-0.4	0	-18.95	18.85	1.98	5.91	20.84	2.69	0.00	0.00	0.00	0.77	0.00
NGC3593	-3.2	0	-19.93	16.62	0.46	0.89	19.13	1.42	0.00	0.00	0.00	0.47	0.00
NGC3607	-0.9	0	-21.41	17.38	0.87	2.82	20.23	2.54	0.00	0.00	0.00	0.57	0.00
NGC3626	-0.1	0	-22.80	15.41	0.26	2.74	18.81	1.88	0.00	0.00	0.00	0.34	0.00
NGC3682	0.4	0	-21.67	17.53	0.68	1.48	21.17	2.79	0.00	0.00	0.00	0.60	0.00
NGC3730	-2.0	0	-23.34	17.71	2.04	1.37	18.75	2.53	0.00	0.00	0.00	0.48	0.00

NGC3773	-1.7	1	-18.70	18.31	0.22	1.06	20.55	0.79	0.00	0.00	0.00	0.29	0.00
NGC3801	-1.9	0	-20.84	20.49	7.01	6.88	20.06	4.33	0.00	0.00	0.00	0.82	0.00
NGC3870	0.6	1	-19.43	18.35	0.29	1.31	20.58	0.53	0.00	0.00	0.00	0.54	0.00
NGC3884	-0.2	0	-22.37	16.61	0.79	2.27	19.91	8.04	0.00	0.00	0.00	0.19	0.00
NGC3900	-0.1	0	-20.79	18.32	0.77	4.80	19.38	2.62	0.00	0.00	0.00	0.28	0.00
NGC3922	-2.8	0	-20.00	20.56	1.23	5.88	19.99	0.94	0.00	0.00	0.00	0.66	0.00
NGC3990	-2.1	1	-18.13	16.48	0.12	1.38	18.30	0.34	0.00	0.00	0.00	0.41	0.00
NGC3998	-1.8	0	-19.46	15.47	0.29	2.68	19.08	1.56	0.00	0.00	0.00	0.49	0.00
NGC4026	-2.1	0	-21.40	17.03	0.55	3.04	18.63	2.11	0.00	0.00	0.00	0.54	0.00
NGC4104	-1.3	0	-26.01	18.74	5.57	1.78	21.04	22.64	0.00	0.00	0.00	0.39	0.00
NGC4111	-2.1	0	-19.31	15.84	0.39	2.97	18.39	1.55	0.00	0.00	0.00	0.69	0.00
NGC4150	-1.8	0	-18.13	15.89	0.04	2.97	19.14	0.23	0.00	0.00	0.00	0.37	0.00
NGC4251	-0.9	0	-20.08	18.23	1.30	4.63	18.36	1.22	0.00	0.00	0.00	0.80	0.00
NGC4324	-0.1	0	-22.31	15.82	0.19	1.17	18.08	1.44	0.00	0.00	0.00	0.13	0.00
NGC4336	-0.6	1	-20.50	19.72	0.45	1.74	19.88	1.09	0.00	0.00	0.00	0.13	0.00
NGC4425	-0.9	0	-20.32	20.30	2.56	4.70	18.96	2.57	0.00	0.00	0.00	0.45	0.00
NGC4460	-2.0	1	-20.10	18.90	0.39	0.75	19.55	0.91	0.00	0.00	0.00	0.26	0.00
NGC4528	1.5	0	-20.50	16.56	0.23	1.95	18.08	0.81	0.00	0.00	0.00	0.34	0.00
NGC4544	-2.0	1	-20.26	18.73	0.91	0.49	19.26	1.04	0.00	0.00	0.00	0.34	0.00
NGC4578	0.4	0	-22.02	17.69	1.03	2.67	20.45	4.68	0.00	0.00	0.00	0.38	0.00
NGC4599	-2.7	0	-21.84	18.65	0.96	4.27	19.00	1.54	0.00	0.00	0.00	0.60	0.00
NGC4638	0.0	0	-19.57	16.67	0.70	1.78	20.15	1.77	0.00	0.00	0.00	0.60	0.00
NGC4659	-2.0	0	-19.11	17.77	0.14	2.22	20.36	0.73	0.00	0.00	0.00	0.32	0.00
NGC4694	-0.9	0	-19.98	21.26	4.82	5.38	19.66	1.07	0.00	0.00	0.00	0.91	0.00

NGC4710	-2.1	0	-20.22	17.17	0.42	0.93	18.00	2.48	0.00	0.00	0.00	0.17	0.00
NGC4802	-0.1	0	-21.22	19.84	1.53	4.00	19.85	0.88	0.00	0.00	0.00	0.73	0.00
NGC4866	-1.4	0	-21.92	17.76	1.02	3.77	18.92	5.22	0.00	0.00	0.00	0.30	0.00
NGC4880	-1.9	1	-21.70	20.82	1.72	1.94	21.03	2.78	0.00	0.00	0.00	0.27	0.00
NGC4958	-1.9	0	-20.66	16.04	0.47	1.72	18.02	1.97	0.00	0.00	0.00	0.41	0.00
NGC5273	-2.1	0	-21.45	16.71	0.19	5.55	19.81	1.54	0.00	0.00	0.00	0.21	0.00
NGC5308	-0.1	0	-21.81	16.95	0.67	3.25	17.85	2.60	0.00	0.00	0.00	0.39	0.00
NGC5311	-1.4	0	-22.72	18.53	1.83	3.76	21.97	6.37	0.00	0.00	0.00	0.64	0.00
NGC5422	-0.1	0	-20.98	17.39	0.72	3.07	19.16	3.31	0.00	0.00	0.00	0.50	0.00
NGC5587	-1.9	0	-21.98	16.77	0.23	3.31	18.63	1.99	0.00	0.00	0.00	0.12	0.00
NGC5631	0.4	0	-20.72	19.58	3.38	6.49	22.00	4.74	0.00	0.00	0.00	0.86	0.00
NGC5689	-1.7	0	-22.13	16.06	0.87	1.12	20.10	10.88	10.43	0.68	4.24	0.21	0.40
NGC5734	-2.7	0	-23.61	17.11	1.79	1.69	22.21	10.16	0.00	0.00	0.00	0.78	0.00
NGC5838	-1.1	0	-20.45	16.50	0.54	2.48	19.40	3.30	0.00	0.00	0.00	0.46	0.00
NGC5854	-1.7	0	-22.54	17.87	0.68	1.40	19.06	2.36	0.00	0.00	0.00	0.36	0.00
NGC5864	-1.2	0	-21.49	18.81	1.11	3.48	18.56	2.35	0.00	0.00	0.00	0.28	0.00
NGC5866	-1.8	0	-19.34	18.52	1.83	3.50	17.22	0.81	0.00	0.00	0.00	0.87	0.00
NGC6014	-1.9	0	-24.04	19.75	1.97	7.49	20.44	2.40	0.00	0.00	0.00	0.47	0.00
NGC6278	-2.8	0	-21.36	16.53	0.58	1.73	19.40	3.04	0.00	0.00	0.00	0.38	0.00
NGC6703	-2.6	0	-21.89	18.72	2.74	4.57	21.82	8.67	0.00	0.00	0.00	0.65	0.00
NGC7180	-1.9	0	-21.14	18.95	0.87	2.79	18.88	0.76	0.00	0.00	0.00	0.62	0.00
NGC7252	-1.9	0	-22.73	16.70	1.11	2.57	20.61	5.58	0.00	0.00	0.00	0.60	0.00
NGC7332	0.1	0	-19.95	17.06	0.59	6.49	18.08	1.69	0.00	0.00	0.00	0.53	0.00
NGC7371	-1.6	1	-23.06	18.21	0.55	1.52	19.68	3.00	0.00	0.00	0.00	0.10	0.00

NGC7709	-1.9	1	-20.92	19.16	0.72	0.41	19.58	1.70	0.00	0.00	0.00	0.20	0.00
UGC04551	-2.2	0	-19.47	16.91	0.41	1.47	20.17	2.48	0.00	0.00	0.00	0.65	0.00
ESO507-045	-3.0	0	-23.05	18.57	4.32	4.39	22.01	12.45	0.00	0.00	0.00	0.72	0.00
NGC0193	-2.9	0	-23.27	18.44	2.19	2.73	21.06	9.20	0.00	0.00	0.00	0.45	0.00
NGC0383	-3.7	0	-23.27	17.82	2.54	2.44	20.98	14.15	0.00	0.00	0.00	0.38	0.00
NGC0385	-2.0	0	-23.95	19.00	2.92	5.58	21.48	5.68	0.00	0.00	0.00	0.73	0.00
NGC0474	-3.6	0	-20.84	17.15	0.66	2.22	20.38	3.74	0.00	0.00	0.00	0.37	0.00
NGC0541	-2.8	0	-24.06	18.00	1.76	2.67	20.93	9.85	0.00	0.00	0.00	0.39	0.00
NGC0545	-1.2	0	-23.29	18.04	2.28	3.84	20.18	9.69	0.00	0.00	0.00	0.30	0.00
NGC0839	0.4	0	-23.39	15.53	0.81	5.57	22.36	5.28	0.00	0.00	0.00	0.92	0.00
NGC1032	-3.4	0	-21.25	17.98	1.98	3.56	19.58	5.63	0.00	0.00	0.00	0.64	0.00
NGC2300	-3.0	0	-21.95	18.45	2.43	3.58	21.91	14.01	0.00	0.00	0.00	0.49	0.00
NGC2329	-0.2	0	-25.14	19.94	7.94	5.42	22.24	7.71	0.00	0.00	0.00	0.90	0.00
NGC2562	-2.0	0	-23.04	17.77	2.52	1.70	22.02	6.91	0.00	0.00	0.00	0.78	0.00
NGC4169	-0.3	0	-22.28	18.18	2.80	4.14	20.88	4.11	0.00	0.00	0.00	0.92	0.00
NGC4268	-2.0	0	-21.72	18.46	1.05	5.72	19.08	1.99	0.00	0.00	0.00	0.51	0.00
NGC4270	-3.3	0	-21.32	20.17	3.24	7.87	18.84	2.25	0.00	0.00	0.00	0.51	0.00
NGC4342	-1.8	0	-19.25	14.80	0.09	6.54	16.55	0.28	0.00	0.00	0.00	0.53	0.00
NGC4350	-1.3	0	-20.29	15.53	0.22	1.45	17.33	1.25	0.00	0.00	0.00	0.30	0.00
NGC4382	-1.4	0	-15.55	17.43	0.66	3.20	19.03	2.44	0.00	0.00	0.00	0.26	0.00
NGC4459	-1.9	0	-21.52	18.79	2.45	5.38	21.60	7.03	0.00	0.00	0.00	0.72	0.00
NGC4570	-1.6	0	-23.97	16.63	0.83	3.67	18.23	2.92	0.00	0.00	0.00	0.53	0.00
NGC4761	-2.0	0	-25.02	17.95	1.73	2.52	20.10	7.04	0.00	0.00	0.00	0.31	0.00
NGC5047	-2.0	0	-22.61	18.79	1.12	4.22	18.90	2.69	0.00	0.00	0.00	0.49	0.00

NGC5532	-1.7	0	-23.89	18.73	6.23	3.56	21.71	17.27	0.00	0.00	0.00	0.62	0.00
NGC0693	0.2	0	-20.67	17.36	1.10	0.80	19.52	1.62	0.00	0.00	0.00	0.62	0.00
NGC5820	-1.0	0	-22.41	17.75	2.09	1.96	22.56	7.03	0.00	0.00	0.00	0.78	0.00
NGC6501	-2.8	0	-22.22	18.18	1.71	7.14	20.79	4.31	0.00	0.00	0.00	0.67	0.00
UGC02836	-1.3	0	-23.34	17.26	1.50	1.22	20.88	5.27	0.00	0.00	0.00	0.68	0.00
IC0676	-1.2	1	-20.02	19.27	1.14	1.13	20.61	1.71	14.07	0.05	0.29	0.30	0.16
NGC0254	-0.3	0	-20.28	16.52	0.34	2.08	20.57	3.21	13.07	0.29	2.29	0.29	0.18
NGC0473	-1.2	0	-21.84	18.52	0.71	3.75	19.87	2.14	13.90	0.22	1.32	0.26	0.18
NGC0936	0.6	0	-20.14	18.22	1.90	3.03	22.40	5.66	10.58	0.34	7.44	0.52	0.39
NGC1079	0.1	0	-22.82	17.31	0.41	2.36	19.58	2.28	13.35	0.10	2.70	0.22	0.11
NGC1291	0.1	0	-20.19	15.60	0.17	0.99	16.13	0.49	9.17	0.54	4.02	0.08	0.57
NGC1302	-1.8	0	-24.43	19.63	3.12	5.74	21.46	6.23	13.49	0.22	2.73	0.53	0.04
NGC1316	-0.7	0	-22.32	18.11	4.90	4.74	20.44	11.39	10.59	0.46	4.25	0.51	0.08
NGC1326	0.0	0	-24.00	16.13	0.39	0.88	18.41	1.47	11.48	0.28	7.77	0.29	0.26
NGC1358	-0.7	0	-24.51	16.53	0.56	1.49	20.58	7.72	13.74	0.44	2.74	0.19	0.10
NGC1386	0.9	0	-19.66	15.76	0.19	5.28	18.37	0.34	11.12	1.12	2.41	0.42	0.56
NGC1438	-2.5	0	-21.82	21.34	2.70	7.02	23.11	6.00	12.58	0.32	3.22	0.29	0.54
NGC1533	0.1	1	-18.79	16.67	0.22	0.95	19.68	1.58	12.94	0.50	0.89	0.22	0.07
NGC2655	0.4	0	-22.03	17.55	0.98	6.01	20.79	6.02	10.80	1.57	2.15	0.22	0.23
NGC2681	-1.0	0	-21.17	14.53	0.08	1.74	19.92	1.49	11.78	0.73	0.56	0.23	0.19
NGC2787	-1.2	0	-20.68	17.78	0.61	3.20	19.31	1.46	12.26	0.55	0.42	0.41	0.10
NGC2859	0.3	0	-22.80	16.54	0.46	1.48	19.12	1.83	15.56	0.01	1.87	0.40	0.01
NGC2893	0.0	0	-22.04	15.05	0.12	3.89	21.12	1.40	13.91	0.58	0.96	0.39	0.29
NGC3081	-0.3	0	-20.51	15.85	0.41	4.26	20.09	3.50	14.58	0.05	5.17	0.40	0.05

NGC3301	-2.0	0	-20.62	15.76	0.28	3.08	19.11	1.56	12.24	1.43	3.24	0.37	0.33
NGC3412	-1.2	0	-20.02	15.36	0.13	1.78	19.06	1.56	12.70	0.44	0.60	0.19	0.10
NGC3489	0.2	0	-20.40	15.32	0.14	2.58	18.32	0.92	12.43	0.29	0.36	0.29	0.11
NGC3896	-2.0	1	-21.33	21.23	0.53	0.66	22.14	1.65	16.65	0.01	0.34	0.23	0.05
NGC3941	-1.2	0	-17.11	15.57	0.19	1.72	18.59	1.42	12.23	0.32	0.95	0.23	0.12
NGC3945	-1.2	0	-22.11	16.67	0.49	0.97	21.58	7.19	11.24	0.59	2.04	0.23	0.27
NGC4106	-2.7	0	-23.06	17.11	0.92	2.47	20.67	4.35	12.96	0.33	2.83	0.45	0.12
NGC4203	0.1	0	-21.69	16.42	0.39	3.18	19.78	2.38	14.08	0.04	0.91	0.36	0.02
NGC4245	-2.7	1	-20.34	17.13	0.24	1.23	20.04	1.58	12.86	0.35	1.66	0.22	0.14
NGC4262	-1.3	0	-21.23	15.55	0.21	1.06	19.27	1.25	13.26	0.45	0.79	0.41	0.12
NGC4371	-0.5	0	-21.07	17.74	0.63	1.93	18.96	1.06	11.38	0.35	5.80	0.31	0.34
NGC4385	-0.3	0	-20.80	16.51	0.34	2.93	19.80	1.86	13.09	0.32	4.75	0.30	0.44
NGC4421	-1.9	1	-21.15	17.02	0.24	1.74	20.24	3.03	13.12	0.64	1.77	0.10	0.15
NGC4442	0.0	0	-20.25	17.03	0.32	3.16	17.78	0.35	10.97	0.82	2.45	0.42	0.37
NGC4454	0.4	0	-21.79	18.14	0.63	4.21	20.30	3.78	14.21	0.25	4.02	0.16	0.07
NGC4457	-0.8	0	-20.87	15.89	0.24	2.70	21.22	3.19	11.66	0.44	1.68	0.33	0.20
NGC4461	-1.9	0	-22.34	17.40	1.00	3.99	23.00	9.92	11.56	0.84	5.83	0.50	0.40
NGC4477	0.0	0	-22.23	16.77	0.44	1.77	19.64	3.23	12.06	0.45	1.71	0.18	0.11
NGC4488	-1.9	1	-19.45	18.95	0.36	1.36	22.46	5.48	12.58	0.75	2.50	0.12	0.43
NGC4526	-0.9	0	-20.70	15.63	0.16	1.26	19.09	1.70	10.31	0.88	0.60	0.16	0.31
NGC4596	-2.0	0	-22.82	17.47	0.97	2.69	20.68	8.09	11.56	0.45	4.68	0.20	0.15
NGC4612	-0.6	0	-21.62	16.35	0.28	1.68	21.72	6.14	11.83	0.87	2.21	0.15	0.37
NGC4643	0.0	0	-22.14	17.20	0.68	2.53	18.01	1.50	10.96	0.33	7.23	0.30	0.36
NGC4722	-0.7	0	-22.70	17.48	1.02	2.79	19.03	4.43	15.67	0.03	1.32	0.25	0.03

NGC4856	-0.8	0	-22.11	16.67	0.51	2.29	19.27	3.46	12.18	0.56	1.37	0.28	0.13
NGC4984	5.0	0	-21.71	15.52	0.24	1.08	18.74	1.57	12.54	0.67	0.57	0.26	0.12
NGC5105	-2.7	0	-20.56	17.68	1.66	3.67	18.54	4.36	10.79	0.19	21.93	0.25	0.37
NGC5473	0.4	0	-22.10	16.14	0.31	1.15	19.26	2.39	13.13	0.52	1.15	0.22	0.13
NGC5750	-2.0	1	-21.62	17.57	0.32	0.98	19.35	2.56	13.64	0.20	2.23	0.09	0.09
NGC5770	-1.9	0	-20.60	16.65	0.25	3.93	20.44	1.74	13.48	0.66	1.36	0.33	0.19
NGC6684	-1.8	0	-21.60	16.17	0.21	2.14	19.47	2.15	11.64	0.80	0.99	0.14	0.17
NGC7079	-1.3	0	-22.50	16.51	0.47	1.37	19.12	3.09	14.28	0.22	2.59	0.23	0.05
NGC7280	-1.8	0	-21.19	15.29	0.14	1.83	19.90	2.44	13.80	0.54	0.86	0.19	0.13
NGC7465	-1.3	0	-20.85	15.53	0.27	2.53	20.83	1.93	13.70	0.76	1.21	0.56	0.19
NGC7679	-0.9	0	-22.48	17.75	0.76	1.97	20.95	5.74	14.11	0.54	4.33	0.20	0.21
NGC7743	0.6	0	-21.67	17.95	0.84	6.64	20.41	3.43	13.74	0.23	4.44	0.33	0.07
UGC01385	-2.0	0	-22.05	14.25	0.35	2.45	19.81	2.42	15.00	0.35	2.36	0.49	0.14
NGC2950	-2.0	0	-21.67	15.42	0.26	1.55	20.32	2.84	11.93	0.63	1.52	0.36	0.24
NGC4143	-2.7	0	-20.97	16.42	0.22	0.73	18.05	0.96	14.06	0.19	0.86	0.26	0.04
NGC4267	-2.0	0	-21.10	16.20	0.22	1.60	20.07	2.12	13.00	0.72	0.66	0.25	0.08
NGC4386	-2.0	0	-21.55	16.78	0.46	2.24	20.08	2.77	13.12	0.33	2.21	0.33	0.14
NGC4435	-2.4	0	-21.14	16.34	0.24	1.20	19.17	1.16	12.27	0.41	1.06	0.31	0.16
NGC4754	-2.8	0	-22.16	16.47	0.47	2.73	20.16	4.46	11.90	0.48	1.50	0.28	0.16
NGC5574	-2.0	0	-20.48	18.71	1.15	2.76	22.18	3.98	13.93	0.28	1.95	0.60	0.15

Table 5.1: Important parameters for the sample of 185 S0 galaxies.

Notes: Column 1 - The common name of a galaxy; Column 2 - Hubble stage parameter T, Column 3 - Type of Bulge, CB=Classical

Bulge and PB = Pseudo-bulge, Column 4 - K-band absolute magnitude (AB system), Column 5 - the average surface brightness of the bulge within its effective radius, in mag per arcsec^2, Column 6 - bulge effective radius in kpc, Column 7 - the bulge Sérsic index, Column 8 - disk central brightness in mag per arcsec^2, Column 9 - disk scale length in kpc, Column 10 - integrated apparent magnitude of the bar, Column 11 - Sérsic index of bar, Column 12 - Bar effective radius in kpc, Column 13 - Bulge-Total ratio, Column 14 - Bar-Total ratio.

Chapter 6

Pseudobulges in S0 Galaxies - Secular Evolution of Disks?

The present chapter describes the first systematic study of pseudobulges in S0 galaxies, published in the Astrophysical Journal Letters in 2013 (**ApJ 2013 767L 33V**).

As discussed already, S0 galaxies are an interesting class of objects known to contain diverse types with different formation histories. When the bulges of all types of galaxies are considered, a similar trend is seen i.e. there are two types of bulges - classical and pseudo. Prior studies on S0 galaxies (Barway et al., 2007, 2009, 2011; Laurikainen et al., 2005, 2010) have focussed on the differences exhibited by bright and faint S0 galaxies with respect to various well known correlations between the structural parameters of the galaxy. These studies however considered the galaxy as a whole and did not attempt at classifying the bulges and constraining their formation mechanisms. Studies dealing with bulge dichotomy such as Fisher and Drory (2008, 2010), and Gadotti (2009) have dealt with bulges and their properties with no emphasis on the global morphology of the galaxy hosting the bulges. Samples used in Fisher and Drory (2008) and Fisher and Drory (2010) were small and it was not possible to divide them into morphological bins without losing statistical significance. The sample used in Gadotti (2009), while being large, did not have any visual classification information available. The present study aims at overcoming the limitations of the previous studies on S0 galaxies and bulge dichotomy. The chapter is organized as follows. The first section, for the convenience of the reader, summarizes the sample which has been described in detail in the earlier chapter, the second section focusses on the methods for bulge classification and the rationale behind the final method adopted for this study; the third section focusses on bulge demographics in S0 galaxies and differences in the disk properties of S0s as a function of the bulge type hosted by them.

6.1 Summary of Sample and Data Analysis

The sample was constructed so as to have a statistically significant number of S0 galaxies using the RC3 catalogue (de Vaucouleurs et al., 1991) as a starting point. The catalogue contains 3751 galaxies classified as S0 i.e. having a Hubble stage parameter $-3 \leq T \leq 0$. A total B-band magnitude cut of $B_T < 14.0$ brings down the sample size to 1031 galaxies.

The goal of this study is to employ the technique of 2-d bulge-disk-bar decomposition and recover the structural parameters. For this, we choose to work in mid-infrared waveband covered by the 3.6 micron channel of the infrared array camera (IRAC) on board the Spitzer Space Telescope to minimize high sky background and extinction and to maximize light from low mass stars which contribute the most to the total mass of the galaxy.

The parent sample of 1031 galaxies was cross-matched with the Spitzer Heritage Archive and imaging data for 247 galaxies were found. Filtering images based on data quality, disturbed morphologies of target galaxies and failure in modelling the components of the galaxies meaningully brought down the number to 185.

The 2-d image decomposition was carried out using GALFIT (Peng et al., 2002) employing the Sérsic profile to fit the bulge and bar components while employing the exponential profile to model the disk. The bar component was modelled to prevent systematic uncertainties from affecting the recovered bulge parameters if bars actually present are not taken into account, as demonstrated by Laurikainen et al. (2005) and Gadotti (2008).

6.2 Identification of Pseudobulges

In the introductory chapter, the classification of bulges into classical and pseudo was discussed. Several methods that can be used to distinguish between the two bulges were also outlined. This section revisits these methods with emphasis on convenience of application and reliability.

Fisher and Drory (2008) used V-band images obtained using the Hubble Space Telescope's (HST) to classify the bulges in their sample. The images obtained by HST offer a high resolution, close-up view of the structure of the central bulge region. If the bulge exhibited structure such as the presence of nuclear spiral arms, bars or rings it was classified as a pseudobulge, while any bulge that appeared smooth even at the high resolution of the HST, as a classical bulge. Classical bulges are virialized pressure supported systems likely built by merger events and are thus expected to be featureless. Pseudobulges, on the other hand, may be considered to be inner disks formed by rearrangement of gas and stars, what is termed in the literature

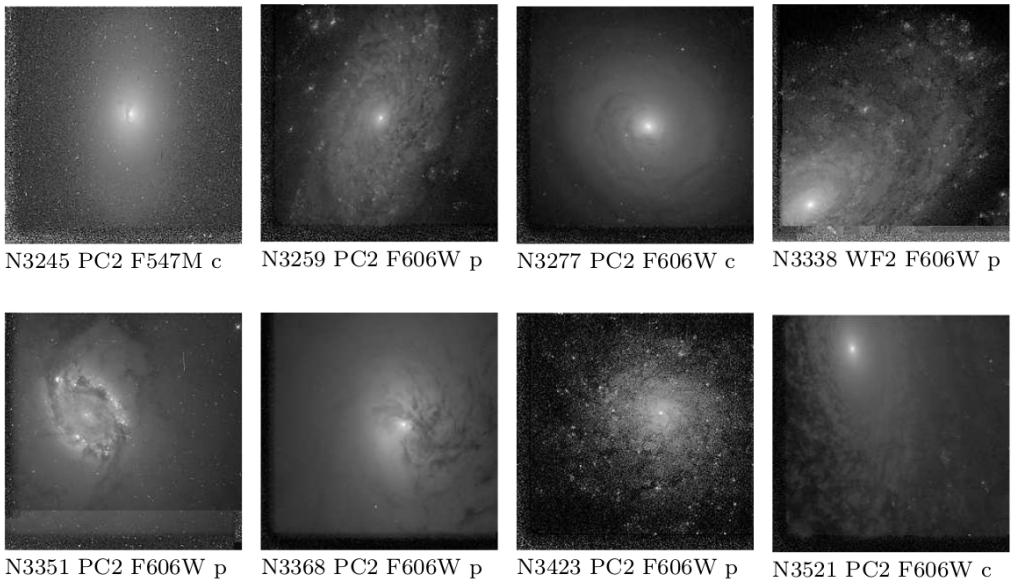

Figure 6.1: Examples of HST images used by Fisher and Drory (2008) to classify bulges. For each image, the name of the galaxy, the HST filter used and the type of bulge is denoted(p = pseudo, c = classical). The images cover the central regions of the galaxy having a size of a few hundred parsecs.

as secular evolution of galaxies. Such disks, being unstable structures in general, produce features used by Fisher and Drory (2008) in the classification. Example images from the study by Fisher and Drory (2008) for classical and pseudobulges are show in Figure 6.1. Note that only the central regions having a size of a few hundred parsecs are being shown in this image.

Having classified bulges into classical and pseudo types, Fisher and Drory (2008) go on to study various properties. Apart from finding that the classical bulges behave like elliptical galaxies with respect to the usual correlations and pseudobulges deviating from them, they found that most classical bulges have Sérsic index $n > 2$ while most pseudobulges have $n < 2$. They therefore suggested that the Sérsic index n alone, obtained from the surface brightness profile fits could be used to classify bulges with $n = 2$ being treated as the boundary between the two types.

Adopting this criterion, we find that of the 185 galaxies in our sample 111(60%) host classical bulges and 74 (40%) host pseudobulges. Of the 74 pseudobulge hosts, only 13 belong to the bright luminosity class while the remaining 61 belong to the faint luminosity class, as defined by Barway et al. (2007)[1]. There are however important reasons to not rely wholly on using n classify bulges.

- Physical motivation. There is no clear physical motivation as to why $n = 2$ is a reliable boundary to distinguish the bulges built from different physical

[1]The division of S0 galaxies into bright and faint luminosity classes is done by adopting a division line of -24.5 Vega magnitude (or -22.66 AB magnitude) in the K-band.

processes at work. This method is empirical and in fact comes from an observational study by Fisher and Drory (2008). This of course does not discount the fact the pseudobulges are indeed expected to have relatively lower values of n.

- The value of n is not easy to determine. The typical error bars are large relative to the complete range of values found in case of observed bulges (typically 0.5 - 8). Our own experience shows that the error bar on n can be as large as 20%. Gadotti (2008) reports error bars as large as 0.5. So, if one is given a bulge with a $n = 2.2 \pm 0.3$, for example, can it be securely classified as a pseudo- or a classical bulge? This picture is further complicated by the presence of a degeneracy between n and the effective radius r_e (Trujillo et al., 2001). What is meant by this is an over or under-estimation of one of the parameters leads to a systematic error in the estimation of the other, since the errors on these parameters are coupled. For example, an over-estimation of n implies an over-estimation of the concentration of light towards the centre and since r_e is defined as the radius containing half the total integrated flux of the bulge, this naturally gets underestimated.

Thus classifying bulges using n *alone* is not the most reliable method of bulge classification.

It is more reliable to adopt the original method used by Fisher and Drory (2008). Following their method, the Hubble Legacy Archive, a web interface to all publicly available observations made by the HST, was searched for high resolution imaging data of all the 185 galaxies in our sample - this was available for only 110 galaxies. In the absence of homogeneous availability of HST data for our sample, it was not possible to classify bulges of our sample based on this method.

An approach used by Gadotti (2009) helps overcome the difficulties associated with the method of using n alone to classify the bulges. Pseudobulges are kinematically cold and rotationally supported systems formed likely through secular evolution while classical bulges are dynamically hot and pressure supported systems, similar to elliptical galaxies. Elliptical galaxies are known to obey a well known relationship between the effective radius r_e and the average surface brightness within it $\langle \mu_b(< r_e) \rangle$, known as the Kormendy relation (Kormendy, 1977). This relation is a projection of a higher dimensional relationship known as the fundamental plane (Dressler et al., 1987; Djorgovski and Davis, 1987),between these two quantities and the central velocity dispersion of the galaxy. Classical bulges, like ellipticals, are expected to be virialized and pressure supported systems and hence must obey the Kormendy relation. On the other hand, disks are not expected to obey this correlation and observational studies have confirmed this (Pierini et al.,

2002). As explained earlier, pseudobulges are in fact inner disks. It should therefore be possible to distinguish bulges based on their position on the Kormendy relation.

Gadotti (2009) uses bulge-disk-bar decomposition for a sample of $\sim$ 1000 galaxies from SDSS containing ellipticals, classical bulges and pseudobulges. A straight line is fitted to the ellipticals on the Kormendy relation, the *rms scatter* about the best-fit line is computed and 3σ boundaries are marked on the diagram. All bulges lying below this boundary are classified as pseudobulges. The the efficiency of this method is discussed in Gadotti (2009).

To employ this method, we need a sample of elliptical galaxies for which Sérsic profiles have been fitted to the 2-d surface brightness distribution of the galaxy. These decomposition data were taken from a K-band study of elliptical galaxies in the Coma cluster, by Khosroshahi et al. (2000). To make the data compatible with those used in the current study, the magnitudes were transformed from K-band to 3.6 micron using $K - m_{3.6} = 0.1$ (Toloba et al., 2012; Falcón-Barroso et al., 2011) and then to the AB magnitude system by adding 1.84 following Muñoz-Mateos et al. (2009). The best-fit line for these ellipticals on the Kormendy relation is then obtained as

$$\langle \mu_{\rm b}(< {\rm r_e}) \rangle = (2.567 \pm 0.511)\ \log\ r_{\rm e} + 16.595 \pm 0.296. \tag{6.1}$$

The *rms scatter* in $\langle \mu_{\rm b}(< {\rm r_e}) \rangle$ for the Coma cluster ellipticals is 0.592. The best-fit line is shown as a solid line in Figure 6.2 while the dashed lines in the diagram enclose a region where all the points three times within the rms catter can be found. Following Gadotti (2009), galaxies corresponding to points below this region can be classified as pseudobulge hosts and there are 50 such points. Of these 50 points, only three of the 37 bright galaxies in the present sample can be found while the rest are all faint. This reinforces the finding of Barway et al. (2007, 2009) that bright S0 galaxies share more in common with the ellipticals while the faint S0s do not. The statistical robustness of this result can be verified as follows.

We know that 32% of the S0 galaxies, taken as whole, have pseudobulges in them, as classified using the Kormendy relation. Let us assume that this fraction is valid for both the bright and faint S0 galaxies. Using a binomial distribution we can then compute the probability of finding only three bright galaxies having pseudobulges. This probability is found to be $\sim 10^{-4}$ suggesting that it is highly unlikely for bright and faint galaxies to have the same chance of hosting a pseudobulge.

Several criteria for identification of pseudobulges are listed in the review by Kormendy and Kennicutt (2004). The more criteria the bulges satisfy, the more secure the classification becomes. For example, instead of using the structural parameters and high resolution images, it is also possible to measure the $D_n(4000)$ index, intro-

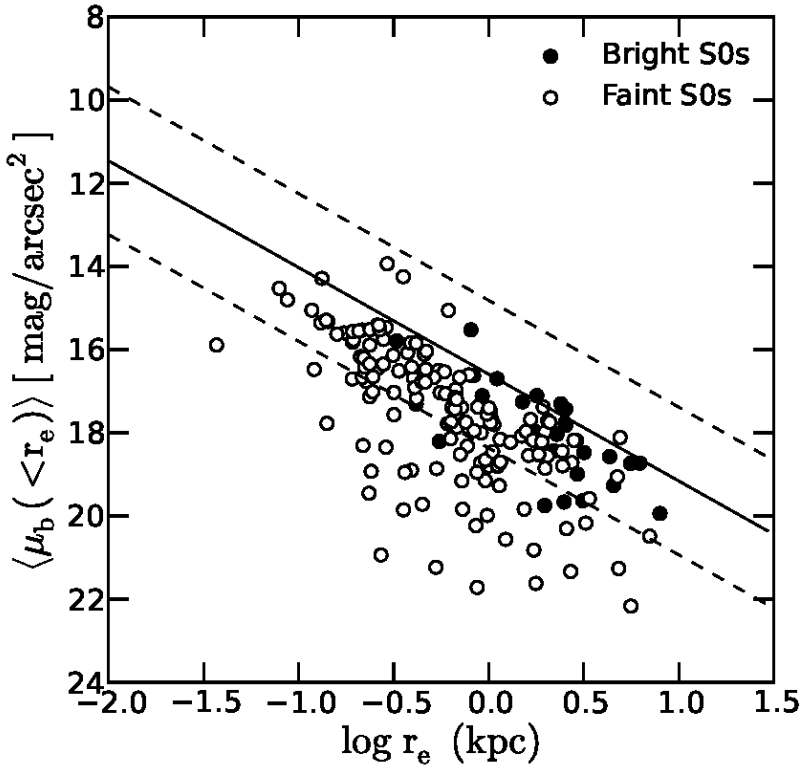

Figure 6.2: Kormendy relation with filled and open circles representing bright and faint S0s respectively. The solid line is the best-fit line to Coma cluster ellipticals while the dashed lines mark the 3σ limits of the scatter of the elliptical galaxies around the best fit line.

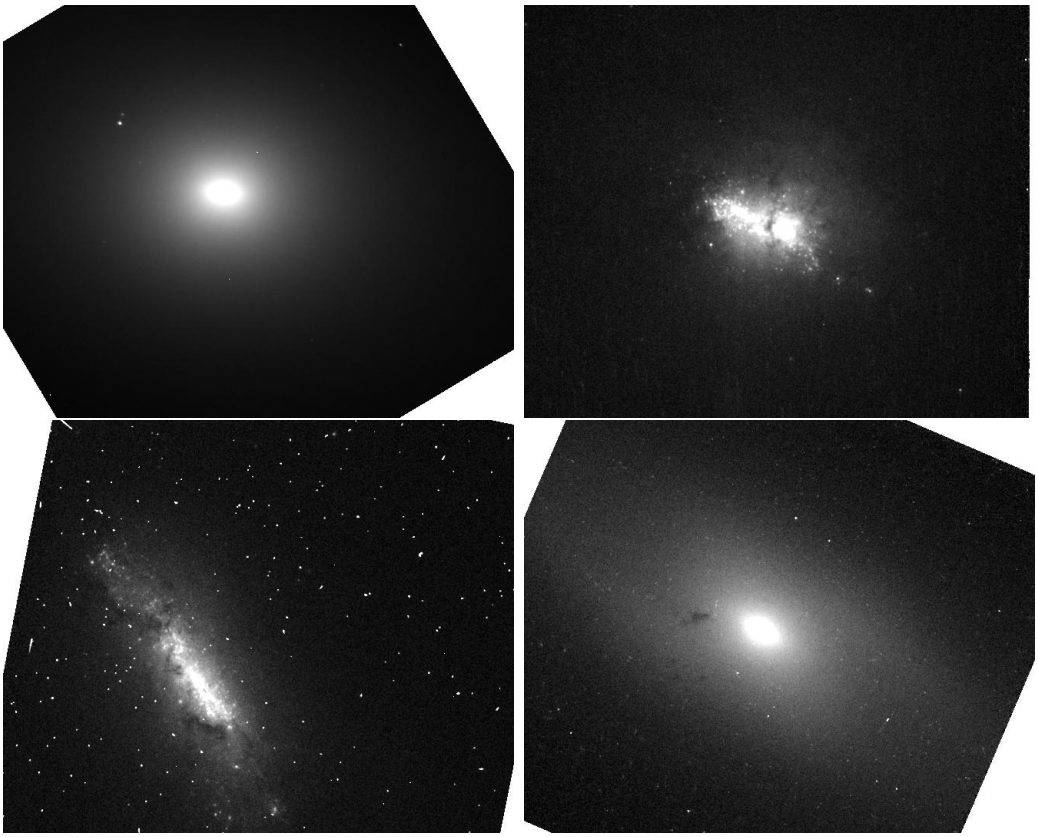

Figure 6.3: Examples of HST images from the present RC3 based sample of S0 galaxies. In the order of left-right, top-bottom, the images show the central regions of NGC 1023 (classical), NGC 3773 (pseudo), NGC 3870 (pseudo) and NGC 5854 (classical).

duced in Chapter 3. The pseudobulges are expected to have a younger and a more complicated mixture of stellar populations than classical bulges. A good estimator of whether a population of stars is extremely old is the $D_n(4000)$ index which can thus can be used to differentiate the two bulges to some extent. However, this requires the availability of homogeneous spectral data. The SDSS software pipelines automatically measure the $D_n(4000)$ index for all galaxies for which it obtains spectra, but since the SDSS is constrained to the northern hemisphere, such data were not available for most of our galaxies. Another method involves measuring the ratio of rotational velocity and velocity dispersion to comment on whether a system is rotationally supported or pressure supported. This too requires spectral data and thus none of these indicators could be employed for the current sample.

In absence of other indicators, but with the intent of making the classification more secure, we decided to impose the requirement that $n < 2$ on all bulges classified as pseudobulges based on their position on the Kormendy relation. Therefore, all bulges having *both* $n < 2$ and lying 3σ below the Kormendy relation are classified as pseudobulges. This reduces the final sample of pseudobulges to 27 (of which two are bright). All other bulges are classified as "classical". In order to verify the

efficiency of our adopted classification method, we took all pseudobulges for which HST data were available and examined the central structure. All these galaxies exhibit a disturbed morphology. Similarly, wherever possible, the HST data for classical bulges were checked and most of these galaxies were found to exhibit a smooth central morphology. Example images for four galaxies (two with classical and two with pseudobulges) are shown in Figure 6.3. This leads us to firmly believe that our classification method is secure. With this classification our sample contains 27 pseudobulges and 158 classical bulges.

6.3 Disk Correlations as a Function of Bulge Type

In a scenario where mergers play a dominant role in forming a galaxy, the bulge and disk parameters are not expected to be correlated (Laurikainen et al., 2010). In such scenarios, the bulge forms during the merger and after it has relaxed, the surrounding gas is accreted and it forms a disk. Thus the process responsible for forming the disk and the process responsible for forming the bulge are independent - thus the parameters are not expected to be coupled. But as we have seen, Courteau et al. (1996) found that the bulge effective radius (r_e) and the disk scale length (r_d) are well correlated for most late-type galaxies. This famous relation, referred to as $r_e - r_d$ correlation is often cited as a case against mergers playing a dominant role in formation of late-type galaxies. In case of pseudobulges, where the bulge is but an inner disk formed through secular evolution, this relation is naturally expected to hold good. Since the secular evolution involves the disk, it is expected that some signature or imprint may be left on the disk parameters.

In Figure 6.4, we plot r_e against r_d with filled and empty circles respectively denoting classical bulge hosting S0s and pseudobulge hosting S0s. Examination of this figure shows that the empty circles are shifted towards the left relative to the filled circles. In other words, the average disk scale length for pseudobulge hosting S0s is shorter relative to that of classical bulge hosts. To clearly bring this out, a histogram of disk scale lengths for the two populations is shown in Figure 6.5. The mean scale length of pseudobulge hosting disks is 1.6 kpc while that of the classical bulge hosts is 4 kpc. We find from a Student's t-test that the difference in the mean values is significant at > 99.9 % confidence level.

This indicates that pseudobulges preferentially occur in disks with low scale length.

The nature of the bulge largely depends on the formation history, in particular whether the bulge has grown as a result of mergers or whether the bulge has evolved through secular processes within the disk. If we assume that there is no reason to believe that only disks with larger scale length should undergo mergers while those

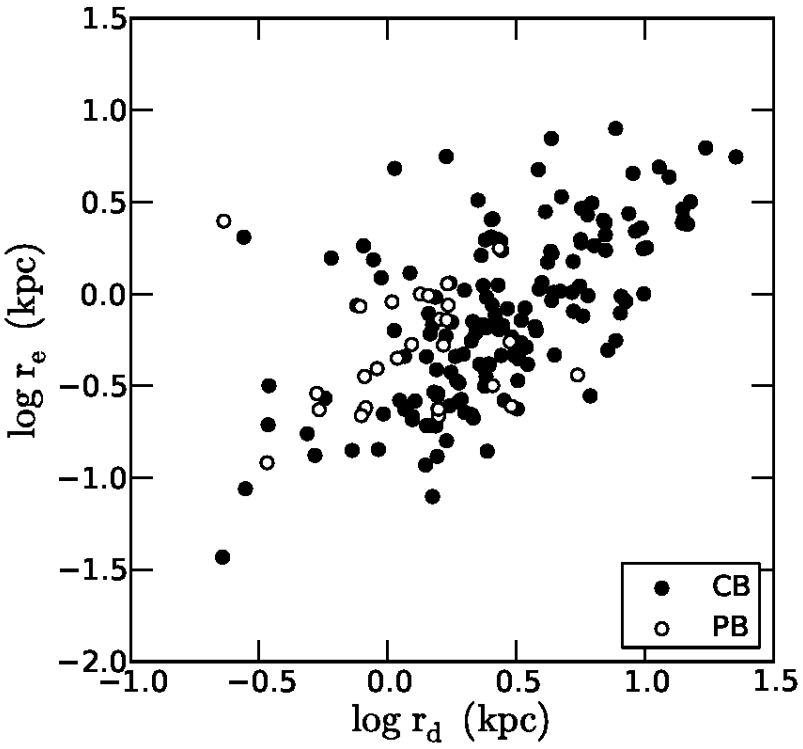

Figure 6.4: Plot of $r_{\rm e}$ vs $r_{\rm d}$ with filled and empty circles denoting classical bulges (CB) and pseudobulges (PB), respectively.

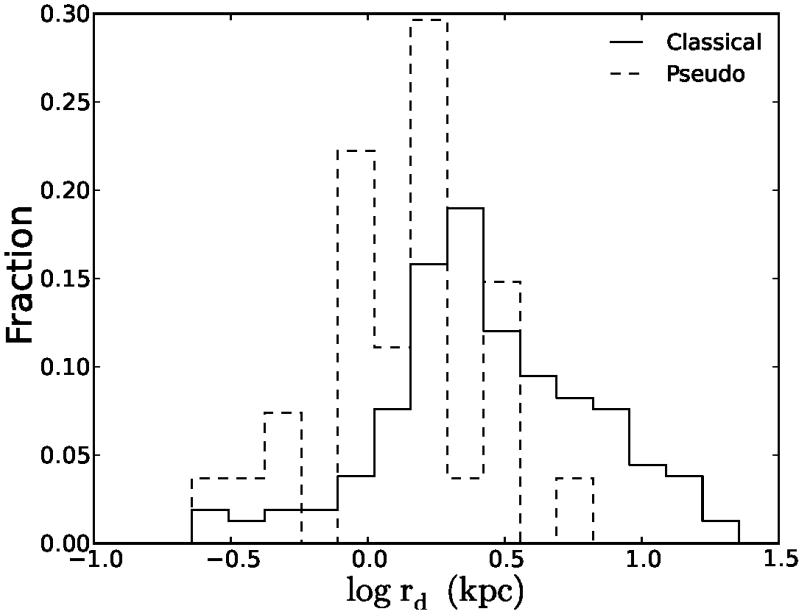

Figure 6.5: Scaled histogram showing the distribution of $\log r_{\rm d}$. The solid and dotted lines represent distributions for classical and pseudobulges, respectively.

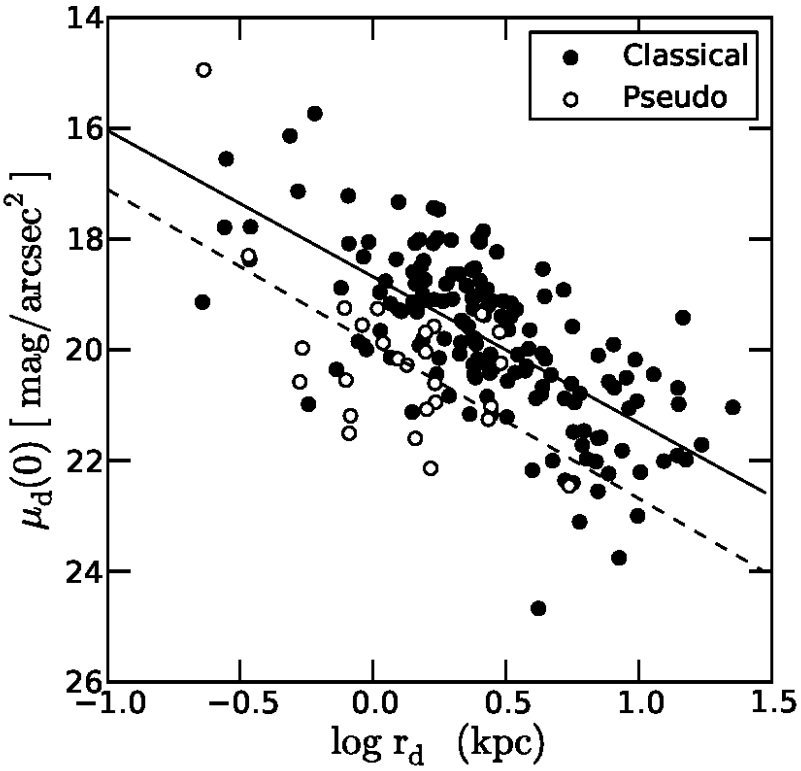

Figure 6.6: Plot of disk central surface brightness as a function its scale length. The filled and empty circles represent the classical and pseudobulges, respectively. The best-fit straight lines to them are the solid and the dashed lines.

with smaller scale length must evolve secularly, it is required that the formation process is responsible for the lowered scale length.

In order to search for further imprints of the processes that might be responsible for bulge formation, we plot another well known correlation between the central surface brightness of the disk $\mu_d(0)$ and its scale length r_d. This plot is shown in Figure 6.6. The central surface brightness being used in this plot is derived from the structural parameters obtained from GALFIT and therefore this quantity is corrected for seeing since the effects of PSF have been taken into account. The Figure 6.6 shows that overall there is a correlation between the two quantities with fainter central surface brightness corresponding to a large disk scale length but there is a clear offset between the disks of pseudobulge hosts and classical bulge hosts. For a given r_d, the disks hosting a pseudobulge are on the average fainter at the centre than disks hosting a classical bulge.

To verify that the disks hosting the two types of bulges could not have been drawn from the same parent populations, we perform Kolmogorov-Smirnov tests on a) disk scale length, b) central surface brightness and c) total disk luminosity. These tests rule out a single parent population at greater than 99.9% confidence level.

In his study, Gadotti (2009) finds that the disks of pseudobulge hosts are more extended and have a fainter surface brightness compared to those of classical bulge

hosts but the overlap between the two kinds of galaxies is significant. Our result differs from his in two ways.

- The trend is partly opposite i.e. disks of pseudobulge hosts in our sample are less extended but as found by Gadotti (2009), are fainter.
- The probability of these disks belonging to different parent populations is also higher.

These differences in the results obtained by us and Gadotti (2009) are most likely due to the differences between the samples used. Our sample comprises S0 galaxies while Gadotti (2009) focusses on bulge dichotomy using a sample comprising a mixture of different morphological types.

6.4 Conclusions and Summary

The present study is the first systematic study of pseudobulges in S0 galaxies aimed at searching for signatures of the evolutionary processes on their progenitor disks. The sample of S0s used in the current study is based on the RC3 catalogue and the structural parameters have been obtained using the technique of 2-d image decomposition, employed on 3.6 micron imaging data obtained using the Spitzer IRAC.

The position of the bulges on the Kormendy diagram has been used as an initial classification criterion for determining the nature of the bulge. To make the classification more secure, the criterion proposed by Fisher and Drory (2008) has also been used, which involves using the $n = 2$ division line on Sérsic index. We find that among the 185 S0 galaxies, 27 are pseudobulge hosts while 158 are classical. Of these 27 pseudobulge hosts, only two belong to the bright luminosity class ($M_K < -22.66$, AB system) while rest belong to the faint luminosity class ($M_K > -22.66$, AB system).

The disks of pseudobulge hosting S0s have on average smaller scale lengths, a lower central surface brightness and luminosity. There are two possible interpretations for these main results. One may claim that disks in the Universe fall in at least two distinct populations and that pseudobulges preferentially form in those possessing lower scale length and central surface brightness. The other interpretation is that the processes responsible for their formation result in the different disk properties. Is it possible that secular evolution alone can cause the disk to fade at the cost of bulge growth? If yes, is it possible to explain the numbers obtained in this study? One of the problems with the interpretation of observational results is that of a one-one correspondence between simulations and quantities measured from

observations. The evolution of the quantities derivable from observational studies is not fully predicted though a few recent studies such as Eliche-Moral et al. (2012) have been taking steps in this direction. We could not find in the literature a direct prediction of whether and by how much disk scale lengths are expected to change when the material within the disk (both gas and stars) rearranges to give rise to a pseudobulge. Only detailed hydrodynamical simulations may be able to say whether secular evolution can bring about such changes.

A possibility is that these pseudobulge hosting S0 galaxies were originally spiral galaxies which transformed into S0s through gas stripping or other environmentally driven processes. This is discussed in the next chapter.

Chapter 7

Spiral Galaxies as Progenitors of Pseudobulge Hosting S0s

The present chapter describes a study comparing the disk properties of pseudobulge hosting S0 and spiral galaxies, published in the Monthly Notices of the Royal Astronomical Society (**2015 MNRAS 450 873V**).

In the study presented in the previous chapter, it was found that disks of S0 galaxies which host pseudobulges have a lower scale length than the disks of S0s with classical bulges. This result has been interpreted to imply either that disks with lower scale lengths preferentially host pseudobulges OR that the lowered scale length is a consequence of the process responsible for the formation of the bulge or the galaxy as a whole. Whether pure internal secular evolution can explain these differences in the disk properties is something more likely to be verifiable in a simulation study - which is beyond the scope of this thesis. However, whether these differences can arise due to processes responsible for the transformation of spirals to S0s can be verified using a suitable comparison sample. This is one of the goals of the study presented in this chapter, the primary goal being to constrain formation mechanisms for pseudobulge hosting S0 galaxies.

The details of the sample of S0s and the technique of 2-d decomposition have been provided in the earlier chapters and the present chapter focusses on the propeties of the sample of spirals and its suitability to serve as a comparison sample of S0 galaxies. The first section covers sample description while the subsequent sections discuss the results and their implications.

7.1 The Comparison Sample of Spirals

The sample of spirals used in the present study was part of another independent multiwavelength study (Ghosh et al., 2008a,b; Mathur et al., 2010) and possesses

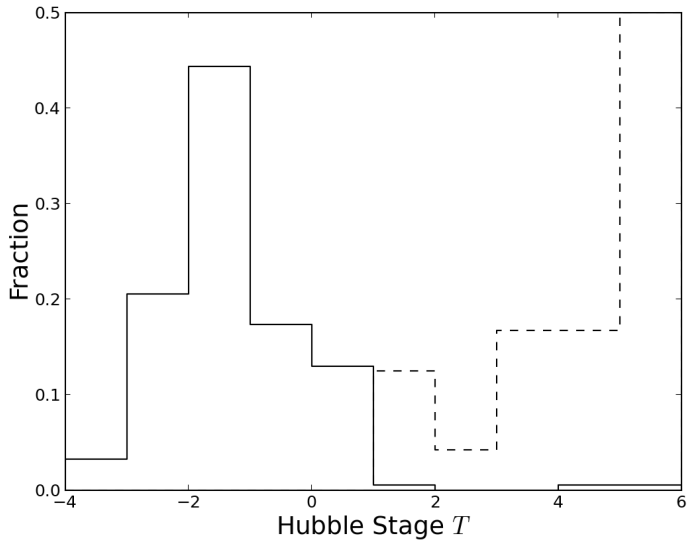

Figure 7.1: Distribution of the Hubble parameter T for the sample of S0s (solid line) and the spirals (dashed line). The Hubble parameter was determined from the Hyperleda database and does not always agree with the Hubble stage for the galaxy in RC3.

properties that make it a suitable comparison sample. This sample was constructed from the Nearby Galaxy Catalog (Tully and Fisher, 1988). as a quasi-volume-limited sample by taking all galaxies within 20Mpc with following filters: (1) close to face-on with inclination less than 35°, to ensure minimum obscuration by the disk of the target galaxy, (2) Galactic latitude $|b| > 30°$ to avoid obscuration and contamination from our own Galaxy, and (3) no known starburst or AGN activity. E and S0 galaxies brighter than $M_B = -18.50$ as well as galaxies with types later than Sdm were avoided. The final sample consists of 56 galaxies; this sample was used in Ghosh et al. (2008a,b) and Mathur et al. (2010) to look for nuclear AGNs with X-ray observations. For this sample, $3.6\mu m$ imaging data were available for 35 early and late-type spiral galaxies.

Among these 35 galaxies, there were four S0/a galaxies ($T \sim 0$) which are already a part of our sample of 185 S0 galaxies. These galaxies were chosen to be treated as S0 as has commonly been done in other studies such as Laurikainen et al. (2010). They have therefore been removed from the sample of spiral galaxies. Our sample of spiral galaxies therefore has 31 objects.

The distribution of the Hubble stage parameter T for the sample of 185 S0 galaxies as well as the sample of 31 spirals is shown in Figure 7.1. As can be seen from this figure, the sample of spirals contains both early- and late-type spiral galaxies and reasonably spans the complete range of Hubble stages. Note that the values of the T parameter used to plot this figure have been obtained from the

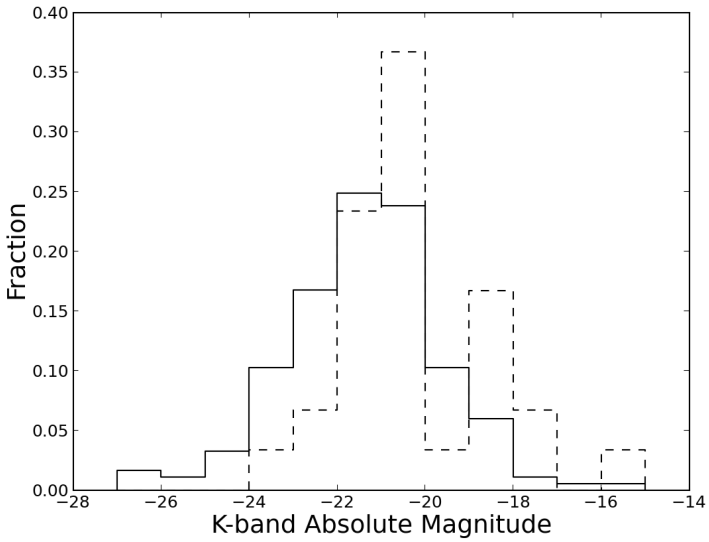

Figure 7.2: Distribution of the absolute K-band magnitudes for the sample of S0s (solid line) and the spirals (dotted line).

HyperLeda database[1] and thus need not agree with the Hubble stage as given in the RC3 catalogue, in case of S0 galaxies. Note that the four S0/a galaxies found common to both the samples, on visual inspection, are found to contain evidence of faint spiral arms. This is expected in the case of objects classified as such. These objects are speculated to be a transition class between S0s and the spirals.

It is clear that the criteria employed to obtain the sample of S0 galaxies and the sample of spirals are different. This leads one to question whether it is meaningful to make a comparison between the two samples. However, there are enough similarities in the properties of these samples that make them suitable for a comparitive study. As already mentioned, the sample of spirals contains both early- and late-type spirals in almost equal proportions. Figure 7.2 shows the distribution of the K-band absolute magnitudes of both the samples (in the AB magnitude system). The data used for plotting this diagram has been obtained from the 2MASS Extended Sources Catalog, as described in Chapter 5. The near-IR luminosity is known to be a good tracer of the stellar mass and hence the similarity in K-band luminosity indicated by the figure implies that the masses of the galaxies in the two samples are comparable. In Figure 7.3, the distribution of total B-band magnitudes is also shown. Without specifically imposing a B-band cutoff, the sample of spirals nonetheless obeys the criterion $B_T < 14.0$ originally employed for assembling the sample of S0s. Further, as is shown in the following section, the fraction of pseudobulges in the sample of spirals is comparable with the known fractions in literature and the total number of pseudobulges is comparable with that found in the case of S0s. These similarities

[1] http://leda.univ-lyon1.fr

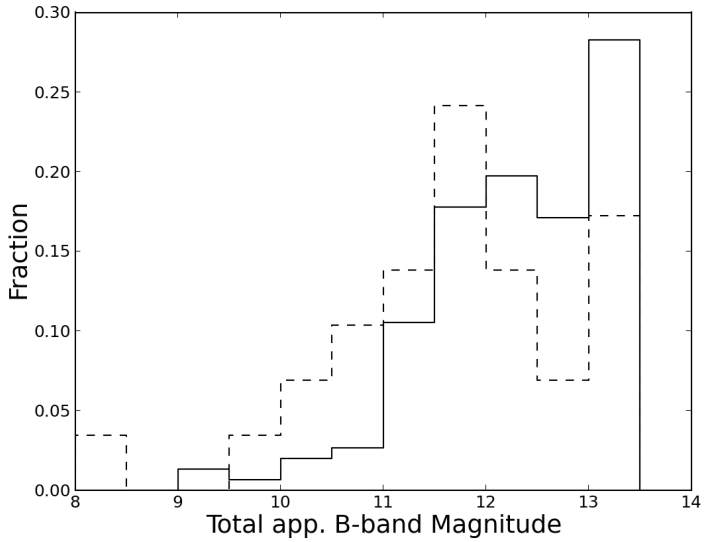

Figure 7.3: Distribution of the apparent B-band magnitudes for the sample of S0s (solid line) and the spirals (dotted line).

motivate us to use the sample of spirals for comparison. It should be noted that neither sample is complete but is a fair representation of S0s and spirals respectively in the nearby Universe.

For all the galaxies, the bulge-disk-bar decomposition has been carried out as explained in Chapter 5. A note on decomposition of spiral galaxies - it is possible to model spiral arms using the latest version of GALFIT (v3.0 and later) by using Fourier modes. However, the spirals are not known to have any systematic effects in determining the bulge properties. This is because unlike a bar which occupies the same physical space as a bulge and can thus skew the parameters of a Sérsic profile used to model the bulge, the spirals contribute less to the total light budget and also dominate only in the outer parts of the disk. Therefore the spirals arms have not been modelled and allowed to be a part of the residuals.

The final parameters for the sample of 31 spirals are presented in Table 7.2, at the end of the chapter.

7.2 Bulge Classification

We have shown in Figure 7.4 the Kormendy diagram for the bulges of S0s (filled circles) and spiral galaxies (empty circles). The solid line is the best fit for the Coma cluster ellipticals as in Figure 6.2, with the points representing the ellipticals left out for clarity. The dashed line represented the 3σ boundaries, where σ is the root mean square scatter of the ellipticals around the best-fit straight line. One notices an offset between bulges of S0s and the best-fit line to the ellipticals, which

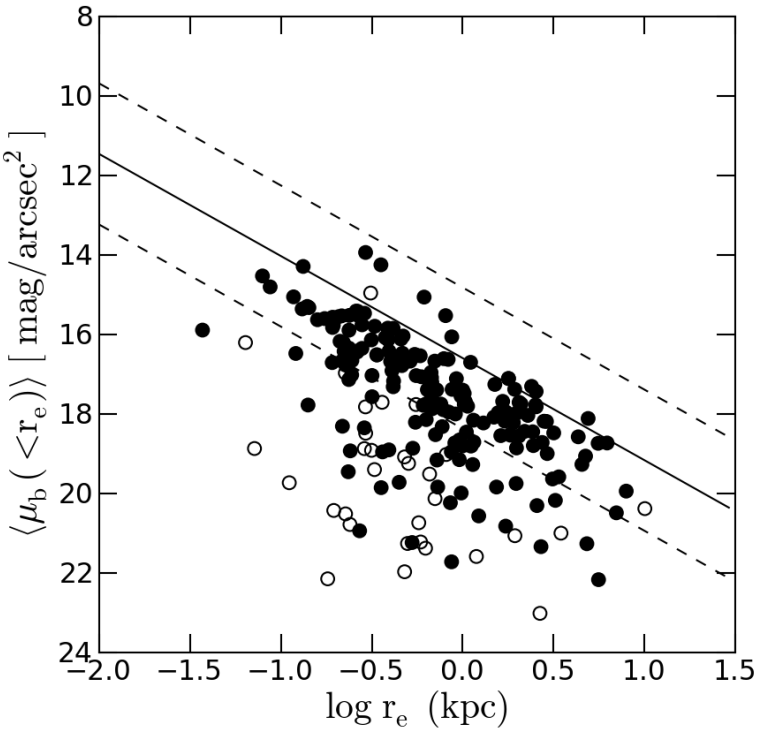

Figure 7.4: The Kormendy diagram showing the position of the bulges of S0 galaxies (filled circles) relative to the bulges of our sample of spiral galaxies (empty circles). The solid line is the best-fit to ellipticals while the dashed lines mark the 3σ boundaries. Points representing elliptical galaxies have been left out for clarity.

is consistent with the findings of Barway et al. (2009). The bulges of spiral galaxies exhibit a greater offset, which is consistent with studies such as Ravikumar et al. (2006) and Laurikainen et al. (2010)

Among 185 S0 galaxies, 25 are classified as pseudobulge hosts using the above criterion. For the same data set, in Vaghmare et al. (2013), explained in the Chapter 6, a different number (27) galaxies is reported as the number of pseudobulge hosts. During the course of study from the time when the pseudobulges were systematically investigated to the point in time of this study, we updated the structural parameters and found that two of these were no longer classified as pseudobulges. This change in number of pseudobulges does not affect the essential findings reported in Vaghmare et al. (2013) and in Chapter 6. In case of spiral galaxies, we find 24 of 31 to be pseudobulges. In Table 7.1, we summarize, for comparison, the distribution of the bulge types in the two samples as found using various criteria described in Chapter 6. For the remainder of the chapter, we use the bulge classification based on both Sérsic index and the Kormendy relation to identify bulge type.

Table 7.1: Distribution of the bulge types in the two samples according to various criteria.

Criterion Used	Bulges	S0's	Spirals
Kormendy only	Classical	137	2
	Pseudo	48	29
Sérsic only	Classical	111	6
	Pseudo	74	29
Both	Classical	160	7
	Pseudo	25	24

7.3 Results

Our primary motivation in this study is to try and systematically compare the pseudobulges in S0s with those in spirals and find clues to the origin of pseudobulges. In Figure 7.5, we replot the Kormendy diagram showing only the pseudobulges of both samples. This plot reveals an interesting feature. Along the effective radius axis, one does not find any appreciable difference in the distribution between the pseudobulges of the two morphological classes. Along the average brightness axis though, one finds that pseudobulges of spiral galaxies tend to be fainter on average. The difference in the mean surface brightness is ~ 0.9 mag/arcsec^2 with a significance of more than 95% as determined using a *t-test*.

We discussed the correlation between the bulge effective radius r_e and the disk scale length r_d (Courteau et al., 1996) in the previous chapter. As already mentioned, models or simulations where the bulge forms via a major merger and the disk forms later via gas accretion do not predict a strong correlation between these parameters. However, such a correlation is expected in a scenario where the disks form first and internal processes then build up the bulge by rearranging disk material. Barway et al. (2007) found that bright S0s show a weak anticorrelation while the fainter S0s show a strong positive correlation between r_e and r_d. The authors concluded that fainter S0s likely evolve through secular processes. In the previous chapter we saw that classical bulge and pseudobulge hosting S0s obey different correlations with a significant offset along the disk scale length axis.

In Figure 7.6, we plot the $r_e - r_d$ diagram for the pseudobulge hosts of the two samples to find that both samples show a correlation but with an offset. For a given r_e, one sees that on average the disk scale length r_d in the case of S0s is smaller than in case of the spiral galaxies. The mean disk scale length for S0 galaxies is 1.6 kpc while for spirals it is 2.8 kpc. The significance level of this difference as per the t-test is greater than 99.9%.

It is seen that there are outliers on either side i.e. there are S0s which possess

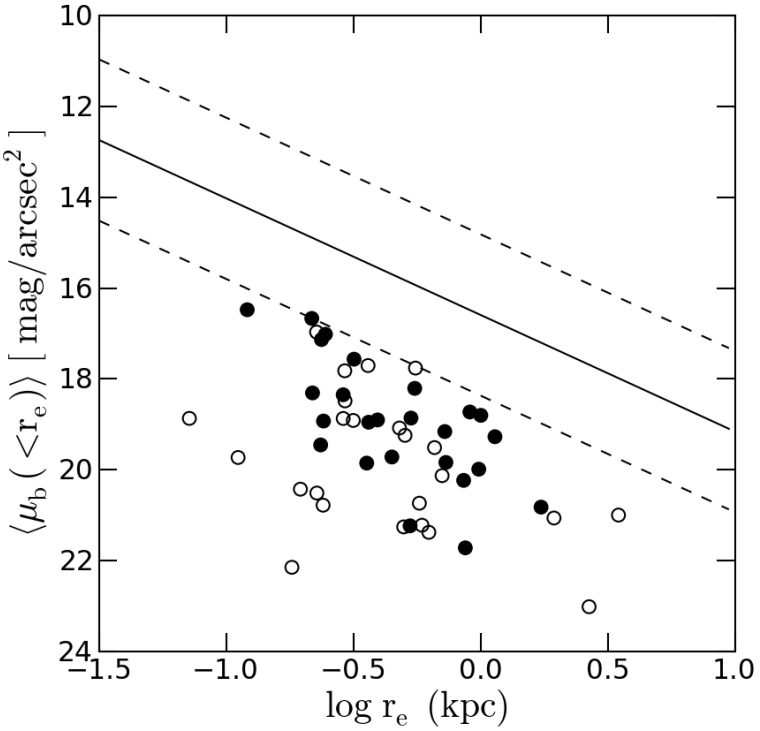

Figure 7.5: Same as Fig. 7.4, but plotting only the psuedobulges identified using both the criteria discussed in the text, for S0s (filled circles) and spirals (open circles).

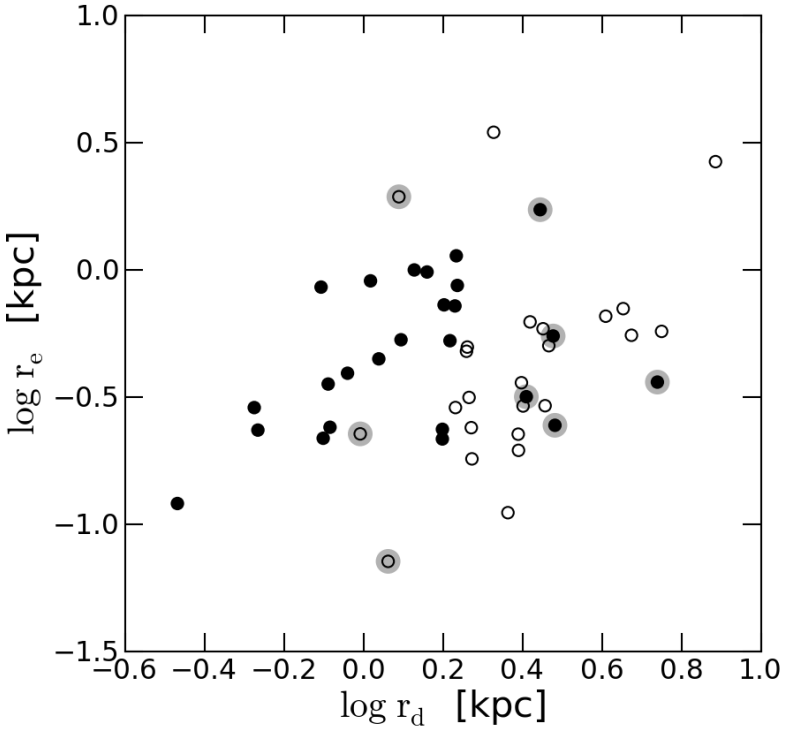

Figure 7.6: A plot of bulge effective radius against the disk scale length for the pseudobulges in our sample of S0 galaxies (filled circles) and spiral galaxies (empty circles). The outliers in both the samples are higlighted in grey.

a scale length typical of spirals and vice versa. We now comment on these outliers, which have been shaded in grey in Figure 7.6. *The same outliers have also been marked in Figures 7.7 and 7.9.* The five S0 galaxies found "amidst" the spiral galaxies on the $r_e - r_d$ diagram are NGC 4488, NGC 4421, NGC 7371, NGC4880 and NGC 5750. Of these NGC 4488 and NGC 4421 are classified as S0/a galaxies with $T \sim 0$ and are known to reside in the Virgo cluster. NGC 7371 and NGC 5750 are also classified as S0/a galaxies, with NGC 5750 known to be a part of a rich group environment while reliable environment information for NGC 7371 is not available. Together, these four objects are the same objects in our sample which were initially found to be common to the sample of S0s and spirals but were chosen to be kept as a part of the sample of S0s, as described in Section 7.1. The remaining galaxy is NGC 4880 which is classified as SA0 $\wedge$ +(r). Its SDSS color composite image suggests that this galaxy may have had a spiral structure which is now nearly lost. All these five objects can be thought of as having started as spirals which are now in transition and may eventually acquire the morphology of a typical S0 galaxy.

The three spiral galaxies NGC 1341, NGC 4571 and NGC 4136 lying "amidst" S0s in the $r_e - r_d$ diagram, also share an interesting commonality. NGC 1341 is an SAab galaxy residing in the Fornax cluster, NGC 4571 is an SAd galaxy in the Virgo cluster and NGC 4136 is an SAc galaxy, known to be a member of a group. Apart from being in rich environments, these three galaxies are observed to have anaemic spiral arms and have been speculated to be transition objects between S0s and spirals (van den Bergh, 1976; Kormendy and Bender, 2012).

Another correlation that was discussed in the previous chapter was that between the central surface brightness of the disk and its scale length. In Figure 7.7 we plot this diagram for the pseudobulge hosts of the two samples. As was the case with Figure 7.6, a separation is seen only along the disk scale length axis while no separation is found on the disk central brightness axis. In other words, the disk central brightness is the same on average for disks in both populations. The difference is largely seen in disk scale length.

7.4 Discussion

The study presented in this chapter is the first known systematic comparison between S0s and spiral galaxies hosting pseudobulges. In the previous section, we compared these two populations and found that the disk scale length of S0s is lesser on average than that of spirals, for a given bulge effective radius. We further find that there is no significant difference between these two populations with respect to disk central brightness. A difference is seen in average surface brightness within r_e. In this section, a discussion of these results and possible explanations within

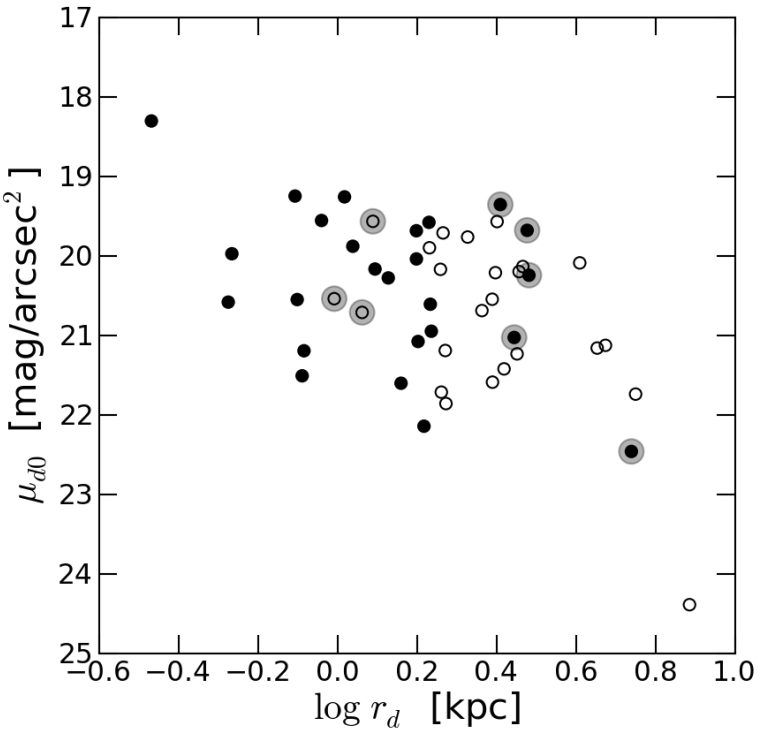

Figure 7.7: A plot of disk central surface brightness against the disk scale length for the pseudobulges in our sample of S0 galaxies (filled circles) and spiral galaxies (empty circles). The outliers described in Section 4 are shaded in grey.

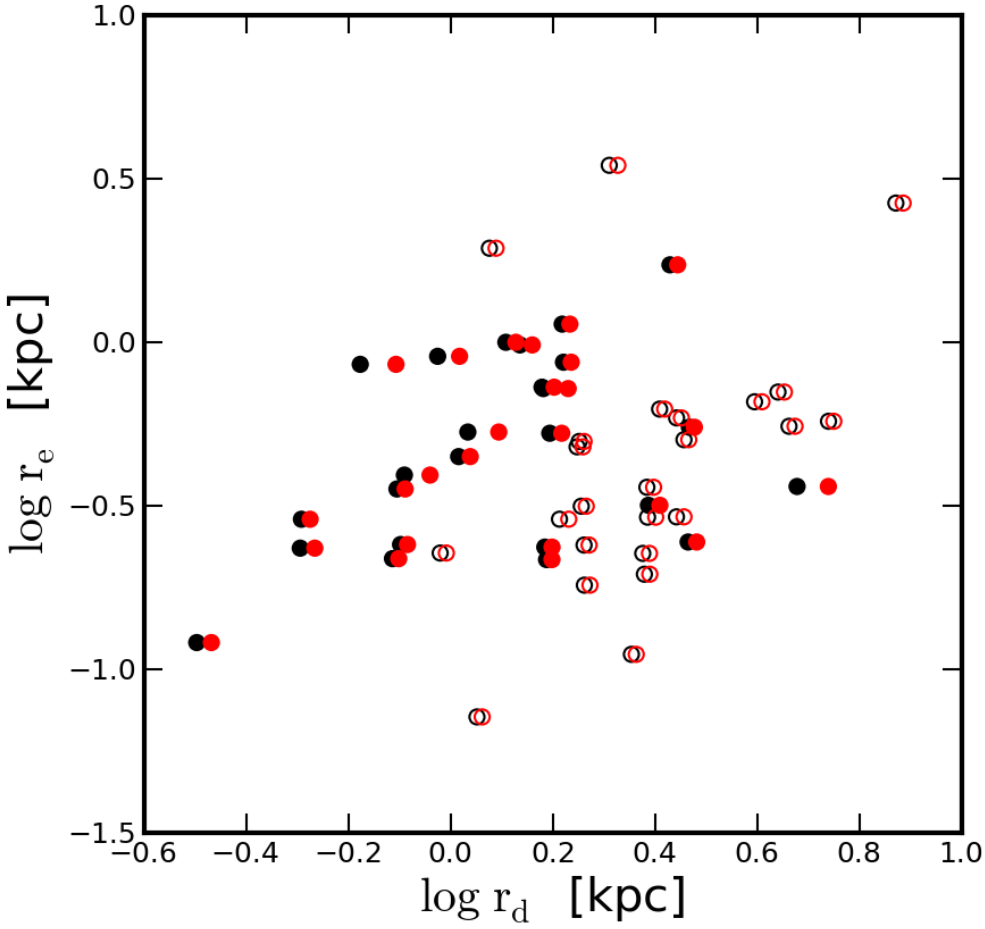

Figure 7.8: A plot as in Figure 7.6 but with counterpart red points indicating the change in disk scale length if inclination corrections, valid for the K-band, are taken into account. As can be seen, the shift in the points is not sufficient to explain the key result of the thesis as an inclination effect.

the context of various formation scenarios of both pseudobulges and S0 galaxies is presented.

Before we discuss the results, we need to consider an important question concerning the robustness of the results. While the samples have a similar K-band luminosity (and hence mass) range and represent well the galaxies in the nearby universe, the sample of S0s has no cut-off on inclination while the sample of spirals does have such a cut-off. One is thus led to question whether this can explain the difference in scale lengths of disks of pseudobulge hosts, which is the major result in this study. There is no literature examining inclination corrections to scale lengths and other quantities at 3.6 micron wavelength. So, the corrections for K-band used by Laurikainen et al. (2010) which in turn are based on studies by Graham and Worley (2008) and Driver et al. (2008), were used and it was ensured that the differences in scalelengths cannot be explained as a projection effect as the corrections

are too small relative to the difference found. The mean correction in the disk scale length is $\sim$ 0.02 dex and as can be discerned from Figure 7.6, is not sufficient to account for the observed differences in the disk scale lengths. To visualize how small the corrections are, the Figure 7.8 shows the positions of the points on the $r_e - r_d$ diagram before and after employing corrections in black and red color respectively. As can be seen, the result that the scalelengths are different, is unaffected.

The differences in corrections for 3.6 micron and K-band (2.2 micron) are expected to be fairly small. Note that the parameters listed in the tables and those used for plotting are not corrected for inclination effects as it is not strictly correct to use K-band corrections on 3.6 micron images. Even the bulge parameters are subject to projection effects, but determing these is difficult and involves performing detailed simulations with prior assumptions about the three dimensional structure of the bulge. An example of such a study is the one carried out by Pastrav et al. (2013). The key result in the current thesis is however based on the differences in the disk parameters and further, based on experience, it is unlikely that the corrections in the bulge parameters will be significant though this needs to be proved through simulations.

7.4.1 Pseudobulge Fraction in Spiral Galaxies

In the present study, a sample of 31 spiral galaxies was used of which 24 have been classified as pseudobulge hosts. This fraction (77%) is consistent with that found by Weinzirl et al. (2009), for example, who use optical imaging while we use mid-infrared imaging. Lorenzo et al. (2014) used a sample of 189 isolated spiral galaxies and found that 94% of the bulges in their sample are pseudobulges. A major reason for such a high fraction is due to their adopted criterion - they classify all bulges with $n < 2.5$ as pseudobulges, while we use a more conservative classifcation scheme. We have discussed at length, the possible misclassification of bulges and pseudobulges if the value of n is used as the sole criterion. Fisher and Drory (2011) find that classical bulges only account for 12% of the total population of disk galaxies with the rest being pseudobulges or galaxies with very low B/T ratios. This high fraction in turn implies that a large number of spiral galaxies have likely not experienced evolution driven by external influences and that their evolution is largely secular, with possibly some aid provided by minor mergers. As pointed out by studies such as the one by Fisher and Drory (2011), this poses a challenge to the currently accepted paradigm of galaxy formation where most galaxies form through hierarchical clustering, through a series of merger events.

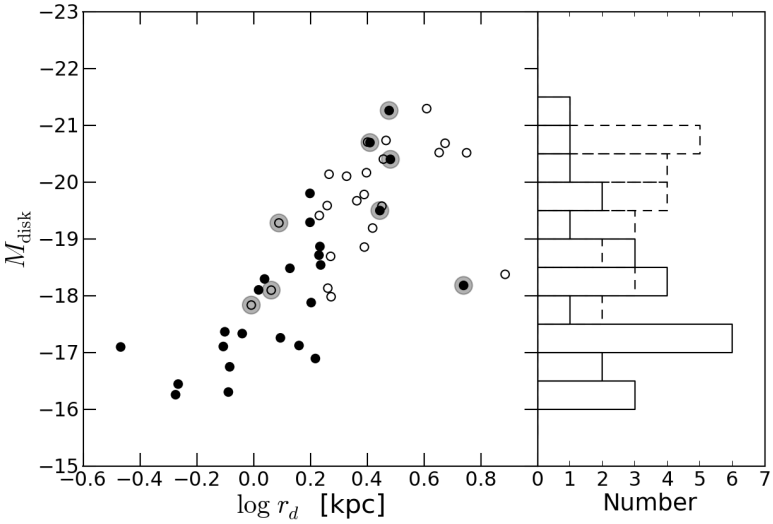

Figure 7.9: A plot of disk absolute magnitude against the disk scale length for the pseudobulges in our sample of S0 galaxies (filled circles) and spiral galaxies (empty circles). Shown in the right panel is the distribution of disk absolute magnitudes with solid lines representing S0s and dashed lines representing spirals. The outliers described in Section 7.4 are shaded in grey in the left panel.

7.4.2 Lowered Scale Length - Role of Gas Stripping

A common explanation invoked to explain the formation of S0 galaxies is that they form as a result of spirals losing their spiral arms due to gas stripping. The density-morphology relation (Dressler, 1980) has often been interpreted as evidence for this. However, Burstein et al. (2005) carefully measured total K-band absolute magnitudes of a sample containing both S0s and spirals (both early- and late-type) and found that S0s are more but not less luminous than spirals. This, according to the authors, rules out gas stripping as a viable mechanism as a difference of ~ 0.75 magnitudes, with S0s being fainter, is expected. When the difference in the mean total magnitude for two populations of pseudobulge hosts was computed, it was found that pseudobulge hosting S0s are indeed brighter by ~ 0.24 magnitudes. But if we divide our pseudobulge hosting spirals into early-type ($T < 5$, 12 galaxies) and late-type($T \geq 5$, 19 galaxies), we find that pseudobulge hosting S0s are fainter by ~ 1 magnitude than pseudobulge hosting early-type spirals while brighter by ~ 1 magnitude than pseudobulge hosting late-type spirals. Thus pseudobulge hosting early-type spirals transforming to pseudobulge hosting S0s via gas stripping cannot be ruled out based on the arguments of Burstein et al. (2005).

Thus we see that we should not treat spiral galaxies as a single population; early-type and late-type spirals have different properties and the PB hosting early type spirals may in fact transform into PB hosting S0s via gas stripping. It is also the case that we should not treat all the S0s as a single population; they have different

properties depending on luminosities as shown by Barway et al. (2007, 2009) and on the bulge-type found in them, as shown in Chapter 6.

The disk scale length is a free parameter of an exponential function which is used for describing the light distribution in a disk. The total flux received from a disk with central surface brightness μ_{0d} and a disk scale length r_d is given by $\sim 2\pi I_d(0) r_d^2$, where $I_d(0)$ is the central intensity of the disk corresponding to μ_{0d}. Thus a lowered scale length as in the case of S0s would imply a lowered disk luminosity if $I_d(0)$ remains the same. This relation between disk luminosity and scale length can be checked easily using Figure 7.9, which shows a plot of the disk absolute magnitude against disk scale length. Unlike previous plots involving disk scale length where trends were found only along the disk scale length axis, this plot shows trends along the disk absolute magnitude as well. Disks of pseudobulge hosting S0s tend to be less luminous than the disks in pseudobulge hosting spirals. The mean disk absolute magnitudes for pseudobulge hosting S0s and pseudobulge hosting spirals are ~ -18.16 and -19.57 respectively. This difference of 1.41 mangitudes is significant at a level better than 99.9%. This is expected in a scenario where S0s have spirals as their progenitors which undergo gas stripping to acquire a morphology resembling S0s.

We can see that early-type pseudobulge hosting spirals cannot be ruled out as progenitors of pseudobulge hosting S0s in the gas stripping scenario. The comparison of disk absolute magnitudes lends further support. Let us now consider the bulge absolute magnitudes to try and answer the question whether gas stripping alone is sufficient enough to bring about the transformation from early-type pseudobulge hosting spirals to S0s. If gas stripping is the only process at work, then one should not, for example, notice an increase in bulge luminosity. The mean bulge absolute magnitudes for pseudobulge hosts in S0s and spirals are respectively -17.16 and -16.45. If we treat the spirals separately as early- and late-type, the mean values are -18.19 and -15.41 respectively. So, pseudobulges of S0s are fainter than those of early-type spirals but brighter than those of late-type spirals.

If early-type spirals hosting pseudobulges undergo gas stripping, subsequent growth in the pseudobulge is also hindered - the lower luminosity of pseudobulges in S0s compared to those in early-type, is consistent with this. So, no additional process seems to be necessary to bring about this transformation. In the case of pseudobulge hosting late-type spirals though, this is not the case i.e. the S0 pseudobulges are more luminous. It is thus not possible for gas stripping alone to transform pseudobulge hosting late-type spirals into S0s unless an external process, such as a minor merger or an accretion of a nearby dwarf builds up the bulge luminosity. In general, it seems more viable for early-type pseudobulge hosting spirals to be the progenitors of pseudobulge hosting S0s.

7.4.3 Dynamical Formation Scenarios

By dynamical formation scenarios, we refer to any scenario for forming pseudobulge hosting galaxies which involves a mechanism other than (a) internal secular evolution and (b) evolution caused due to environmental effects such as gas stripping. One such formation scenario, as described in Guedes et al. (2013) and Okamoto (2013), is that pseudobulges formed as inner disks at $z \sim 2$ through a series of star bursts and evolved to their present day forms. However, it is difficult to verify whether such a formation mechanism is viable for pseudobulges in our sample mainly because there are no specific signatures predicted by these simulations. If any such simulations predict, say, a low disk luminosity, one may be able to comment on whether pseudobulges have formed in this manner.

Another possible dynamical evolution scenario is that a pseudobulge of lower than typical observed mass forms via secular processes and its eventual bulge growth is caused through minor mergers, as demonstrated in Eliche-Moral et al. (2012), who suggest that dry minor mergers can cause growth in the overall pseudobulge mass without really affecting scaling relations such as the $r_e - r_d$ correlation, provided such a correlation already exists. This opens the possibility for late type spirals to evolve into S0s too but that will still require some process to enable the removal of the spiral arms.

7.5 Summary

A comparison of pseudobulges in S0 and spiral galaxies is presented using structural parameters derived from 2-d decomposition of mid-infrared images taken at 3.6μm by Spitzer IRAC. We find that among spiral galaxies, 77% of the bulges are classified as pseudobulges. As pointed out by various studies, the presence of such a large fraction poses problems to our current picture of galaxy formation. However, our primary result is that the disk scale length of pseudobulge hosting S0s is significantly smaller on average than that of their spiral counterparts. This can be explained as a lowered disk luminosity which in turn implies that S0s have evolved from spiral progenitors. We also argue that early type spirals are more likely to be the progenitors based on total luminosity arguments. We speculate that if late type spirals hosting pseudobulges have to evolve into S0s, a mechanism other than gas stripping of spirals is needed.

We have also investigated the effect of environment on pseudobulges in the two samples. But no significant trends were found in the properties of the pseudobulges as a function of the various structural parameters. The study is made more difficult because of the low number statistics one deals with when the sample is

sub-divided based on whether it is in a field or group/cluster environment. The study of pseudobulges based on environment, however, is an interesting one and is something that can be considered for the future by carefully selecting a sample with statistically meaningful number of objects from diverse environments.

Name	T	Bulge Type	L_K	Bulge parameters			Disk parameters		Bar Parameters			B/T	Bar/T
				$< \mu_e >$	r_e	n	μ_{0d}	r_d	m_{bar}	n_{bar}	$r_{e(bar)}$		
ESO079-007	-2.0	PB	-18.73	23.25	0.87	0.53	21.23	1.72	0.00	0.00	0.00	0.04	0.00
ESO085-030	-0.4	PB	-18.76	20.50	0.86	1.41	20.94	0.78	0.00	0.00	0.00	0.64	0.00
ESO358-025	-2.6	PB	-19.04	20.42	0.73	0.74	21.72	1.59	0.00	0.00	0.00	0.41	0.00
IC0051	-2.0	PB	-19.85	19.85	1.00	1.20	20.74	1.34	0.00	0.00	0.00	0.56	0.00
IC2040	-0.8	PB	-18.70	20.58	0.98	0.83	22.26	1.44	0.00	0.00	0.00	0.68	0.00
IC2085	-1.2	PB	-18.48	20.37	0.53	0.88	21.79	1.24	0.00	0.00	0.00	0.41	0.00
NGC1510	-1.8	PB	-20.24	19.18	0.24	1.18	21.41	0.82	0.00	0.00	0.00	0.40	0.00
NGC1522	-2.3	PB	-18.33	20.63	0.36	0.44	21.83	0.81	0.00	0.00	0.00	0.37	0.00
NGC3413	-2.0	PB	-20.10	19.96	0.23	0.70	20.80	0.54	0.00	0.00	0.00	0.29	0.00
NGC3773	-1.7	PB	-18.70	18.87	0.22	1.06	20.71	0.79	0.00	0.00	0.00	0.29	0.00
NGC3870	0.6	PB	-19.43	19.44	0.29	1.31	20.94	0.53	0.00	0.00	0.00	0.54	0.00
NGC3990	-2.1	PB	-18.13	17.29	0.12	1.38	19.13	0.34	0.00	0.00	0.00	0.41	0.00
NGC4336	-0.6	PB	-20.50	20.64	0.45	1.74	20.48	1.09	0.00	0.00	0.00	0.13	0.00
NGC4460	-2.0	PB	-20.10	20.32	0.39	0.75	21.03	0.91	0.00	0.00	0.00	0.26	0.00
NGC4544	-2.0	PB	-20.26	20.98	0.91	0.49	20.57	1.04	0.00	0.00	0.00	0.34	0.00
NGC4880	-1.9	PB	-21.70	21.36	1.72	1.94	21.31	2.78	0.00	0.00	0.00	0.27	0.00
NGC7371	-1.6	PB	-23.06	18.46	0.55	1.52	19.73	3.00	0.00	0.00	0.00	0.10	0.00
NGC7709	-1.9	PB	-20.92	20.65	0.72	0.41	21.03	1.70	0.00	0.00	0.00	0.20	0.00
IC0676	-1.2	PB	-20.02	20.62	1.14	1.13	20.89	1.71	14.07	0.05	0.29	0.30	0.16
NGC1533	0.1	PB	-18.79	16.73	0.22	0.95	19.77	1.58	12.94	0.50	0.89	0.22	0.07
NGC3896	-2.0	PB	-21.33	21.54	0.53	0.66	22.77	1.65	16.65	0.01	0.34	0.23	0.05

NGC4245	-2.7	PB	-20.34	17.32	0.24	1.23	20.28	1.58	12.86	0.35	1.66	0.22	0.14
NGC4421	-1.9	PB	-21.15	17.35	0.24	1.74	20.59	3.03	13.12	0.64	1.77	0.10	0.15
NGC4488	-1.9	PB	-19.45	19.59	0.36	1.36	24.09	5.48	12.58	0.75	2.50	0.12	0.43
NGC5750	-2.0	PB	-21.62	17.84	0.32	0.98	19.94	2.56	13.64	0.20	2.23	0.09	0.09

Table 7.2: Important parameters for the sample of 31 spiral galaxies.

Notes: Column 1 - The common name of a galaxy; Column 2 - Hubble stage parameter T, Column 3 - Type of Bulge, CB=Classical Bulge and PB = Pseudo-bulge, Column 4 - K-band absolute magnitude (AB system), Column 5 - the average surface brightness of the bulge within its effective radius, in mag per arcsec^2, Column 6 - bulge effective radius in kpc, Column 7 - the bulge Sérsic index, Column 8 - disk central brightness in mag per arcsec^2, Column 9 - disk scale length in kpc, Column 10 - integrated apparent magnitude of the bar, Column 11 - Sérsic index of bar, Column 12 - Bar effective radius in kpc, Column 13 - Bulge-Total ratio, Column 14 - Bar-Total ratio.

Part III

A Spectroscopic Study of Stellar Populations in S0 Galaxies

Chapter 8

Spectroscopy as a Tool to Study Galaxies

In the first part of the thesis (Chapters 3 and 4), we have used broadband photometry at multiple wavelengths to construct various color-color diagrams and evaluate other diagnostic quantities to study the broad trends of stellar populations in S0 galaxies. From the point of view of finding statistical differences, these techniques are immensely useful and as already shown, reveal interesting trends among S0 galaxies. However, if we need to study the star formation history in detail for an individual object, we need to move from broad band imaging and photometry to very narrow band photometry i.e. spectroscopy. As we know, astronomers are severely handicapped. By that we mean that unlike other branches of science where scientists have the luxury of performing experiments in controlled conditions, astronomers can perform no experiments. Barring the exception of the nearby planets where probes can be sent, they cannot even touch the objects that they study. All they have access to is the light emenating from these astrophysical sources that reaches the Earth and everything that can be deduced about these objects has to be done through the study of this light. The technique of spectroscopy allows astronomers to study these objects in-depth and learn a lot about them despite their handicap.

The current chapter begins with a brief primer on the basic principles of spectroscopy and the steps involved in moving from a raw spectrum captured by a spectrograph on a CCD to a 'final spectrum', free from any artifacts added by the instrument. The next chapter i.e. Chapter 9 provides details of the Robert Stobie Spectrograph used on the Southern African Large Telescope (SALT) and the details of the analysis pipelines developed to perform basic data reduction on the data obtained from this instrument. The results obtained using these pipelines for a sample of S0 galaxies, identified as pseudobulge hosts using photometry based criteria are presented in Chapter 10.

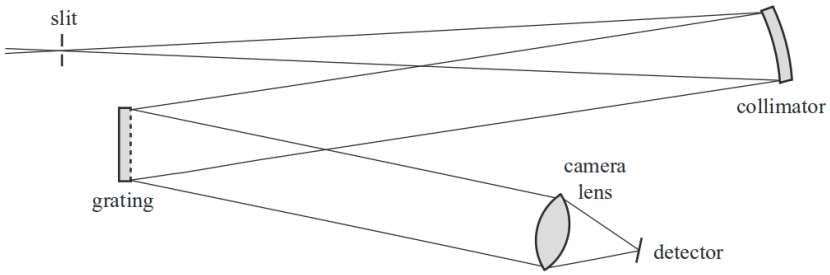

Figure 8.1: A basic schematic of a spectrograph. (Image from *Astronomical Spectroscopy* by Phil Massey.)

8.1 Basic Principles of Spectroscopy

Every spectrograph is designed in a different way motivated by the goals of the science team that designs it and the level of technology available to them. The technology used and the implementation can vary but a generic spectrograph can be described using a simple diagram as shown in Figure 8.1. As can be seen, a spectrograph consists of four essential components -

- A slit: It is placed on the focal plane of the telescope i.e. where the final image generated by the telescope optics is focussed. A slit is characterised by a width w. Generally, the slit can be oriented along the image in any direction. The choice of the width is governed by the desired resolution and detector sensitivity. If the width is too small, the signal-to-noise ratio (SNR) can be too low even for high exposure times, whereas a wide slit reduces the spectral resolution i.e. the ability to resolve spectral features along the wavelength axis.

- A collimator: The purpose of the collimator is to collect the light passing through the slit and render its rays parallel. This is necessary since we want the angle of incidence of the light falling on the grating (see below) to be equal for a given wavelength of the light in a narrow band $d\lambda$. Without this, a systematic wavelength dependent dispersion of the light cannot be obtained. The collimator is generally designed in accordance with the telescope optics so that the complete beam can just fill the collimator.

- Dispersion Element: Any device which, for light incident on it at a given angle of incidence, refracts it by an angle which depends on the wavelength, can be used as a dispersion element. This allows light to be split into its consitituent wavelengths. Typically, the dispersion element used in most spectrographs is a grating which is a glass slab with many grooves engraved on it. The behavior

of light wrt to the grating is governed by a *grating equation*, which is written as

$$m\lambda = \sigma(\sin i + \sin\theta) \tag{8.1}$$

The grating equation tells us what the angle of diffraction θ will be, for a given angle of incidence i, given a light of wavelength λ. m here can be any positive integer while σ is the number of grooves engraved per unit length. It is easy to see that wavelengths which are integral multiples of each other can have the same angle of diffraction. For example, 8000 angstrom light with $m = 1$ and a 4000 angstrom light with $m = 2$ can have the same angle of diffraction and thus will be incident at the same point on the detector. To prevent this mixing, suitable filters need to be used with the detector so that non-interesting wavelengths can be blocked.

- Detector: This records the light split by the grating. In modern instruments, a charge coupled devices unit (CCD) is used.

In principle, a spectrograph is just a suitable combination of the above four elements. The light captured by the telescope is cast in the form of a slit, the light from which is rendered parallel by a collimator, which in turn is split by a grating into its constituent wavelengths and recorded on a suitable detector. However, the final spectrum recorded by the CCD has in it several signatures of the insrument itself and the wavelength distribution is thus not the real distribution emitted by the source. The process of correcting for this is a rather involved one and the details can vary depending on the science goals and the nuances of the specific spectrograph used. A brief description of the process is given in the next section.

8.2 Basic Spectral Reduction

The present section briefly covers the important steps involved in the reduction of a typical spectrum obtained from a generic spectrograph containing the four essential elements described in the previous section.

- Bias Subtraction: A CCD contains an array of pixels, each converting the incident photons into a charge. The charge is read out by a suitable read-out circuit and converted into a digital number (DN) using an Analog-Digital Converter (ADC). The ADC is made of bit registers which represent the number in binary system as a series of 0s and 1s. So long as the number is guaranteed to be positive, the entire range of numbers accommodated by the bits can be

Figure 8.2: An example of a 'flat field' image from the Robert Stobie Spectrograph on the Southern African Large Telescope. Due to the non-uniformity of the pixel sensitivity as well as the transmission efficiency of the grating, the flat-field itself has a large scale illumination structure. To truly correct for intra-pixel variations, it is necessary to first model and remove the illumination.

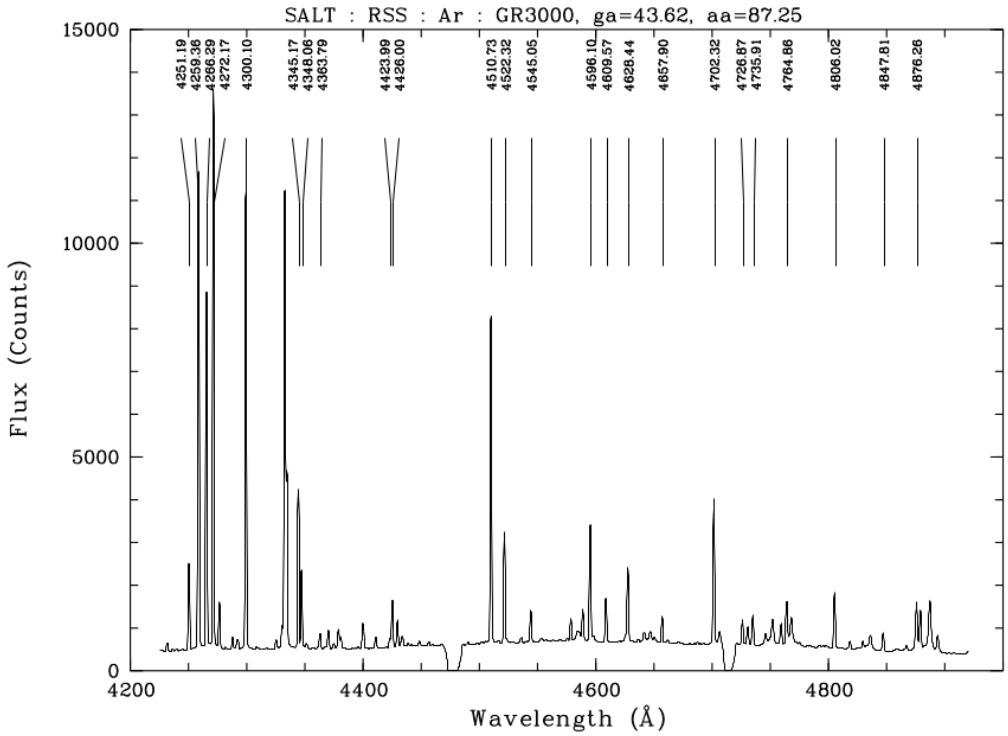

Figure 8.3: An example of an Argon lamp arc spectrum taken using SALT. Credit: *Atlas of Reference Spectra for RSS Observations* by Alexei Kniazev

used. However, if a charge of opposite polarity is read out, one of the bits will be used to represent the sign of the DN produced. To prevent this, an artificial level of charge is added to the CCD which needs to be subtracted before the data can be used for scientific analysis.

- Trimming: The image of the slit captured on the CCD does not cover the entire area of the detector and thus all other regions must be removed.

- Dark subtraction: As the instruments are at a non-zero temperature, there is a thermal current in the detector circuits which accumulates over the integration time of the detector. This needs to be removed and the process is refered to as *dark subtraction*.

- Flat fielding: This accounts for varying quantum efficiency in the pixels of the CCD. In imaging, this is achieved by taking an image of a bright region of the sky near the horizon around sunset or the image of a uniformly illuminated dome wall. However, the standard steps of flat-fielding assume that the source being captured is uniform. In case of a spectrograph, this can never be achieved because the different wavelengths of light fall on different parts of the CCD and the quantum efficiency of the pixels is a function of the wavelength. As a result, the flat-field spectrum has a large scale illumination structure as shown in the Figure 8.2. In this figure, the wavelength axis is along the horizontal and the bluer wavelengths towards the left. As a result of the combined effect of the grating transmission efficiency as well as the wavelength dependence of the quantum efficiency of the pixels, there is a large scale structure in the illumination. The astronomer thus needs to fit for this and remove it. One can then perform the usual steps of normalization and flat-field corrections. Sometimes the process of flat-fielding introduces noise and degrades the quality of the data. In such a case, this step is often skipped since the errors introduced by the correction process are larger than the corrections themselves.

- Wavelength Calibration: The spectrum captured on the CCD can be imagined to have two axes - a spatial axis which is aligned with the slit and a dispersion axis which represents the direction of changing wavelength. A plot of a series of pixel values along the dispersion axis gives a spectrum but the wavelength axis represents pixel numbers and not wavelengths. One therefore has to find a function $\lambda = f(x)$ where λ is the wavelength and x is the pixel number, in order to get the actual spectrum. To obtain such a function, a well known spectrum of a hot gas such as He, Ar etc. is obtained. The user then identifies well known emission lines in the spectrum and manually assigns a wavelength to them. These data are then used to determine the above function. Note

that this wavelength solution may be different along different positions on the spatial axis and may need to be adjusted for each poition. An example of an arc spectrum is shown in Figure 8.3.

- Background Subtraction: Along the spatial axis, there are regions filled with light from the background and those filled with the sources lying along the slit. The regions dominated by background light need to be marked and a suitable function needs to be found to describe it. This function can then be used to subtract the background from the spectrum.

- Spectral Extraction: This step is similar to the background subtraction except that one marks the regions occupied by the source and sums up all the pixel rows lying in that region to obtain a high SNR spectrum. However, the process of summing up the rows assumes that there is no tilt in the spectrum. But due to various instrument limitations and mechanical errors, a perfect alignment of the slit is not assured. This can cause the wavelength axis to be tilted relative to the CCD geometry. This can be checked by *tracing* the centroid of the spatial light distribution as a function of wavelength. Ideally it should be a constant but it seldom is. The behavior of the centroid can be modelled using a suitable function and a tilt correction can be performed.

- Flux Calibration: The spectrum obtained by this stage is usually free from most instrumental signatures but for one. The quantum efficiency of any given pixel on the CCD is a strong function of the wavelength. Even the dispersion element used in the spectrograph has a wavelength dependent transmission efficiency. In general, as a result of these two effects combined, the spectrograph is more sensitive to red light than blue. So, the spectrum at this stage under represents the blue light relative to the red. To correct for this, one observes a spectrophotometric standard star. This is a star whose spectrum is well known. Thus by comparing the spectrum recorded on the CCD with the known spectrum, one can determine a *sensitivity function* which can be used to correct for the wavelength dependent response of the spectrograph.

The above are common generic steps that need to be carried out to perform the basic reduction of a spectrum. Depending on the peculiarities of the data unique to a given instrument or on the eventual scientific goal for which the spectrum is being obtained, additional steps may be needed or the above steps may need to be performed in a different manner. As we will see in the next chapter, SALT is a unique telescope with peculiarities perhaps absent in many other telescopes. The data from SALT needs to be reduced in a somewhat different manner. Apart from this, the intended scientific analysis in this thesis is also complicated. Therefore

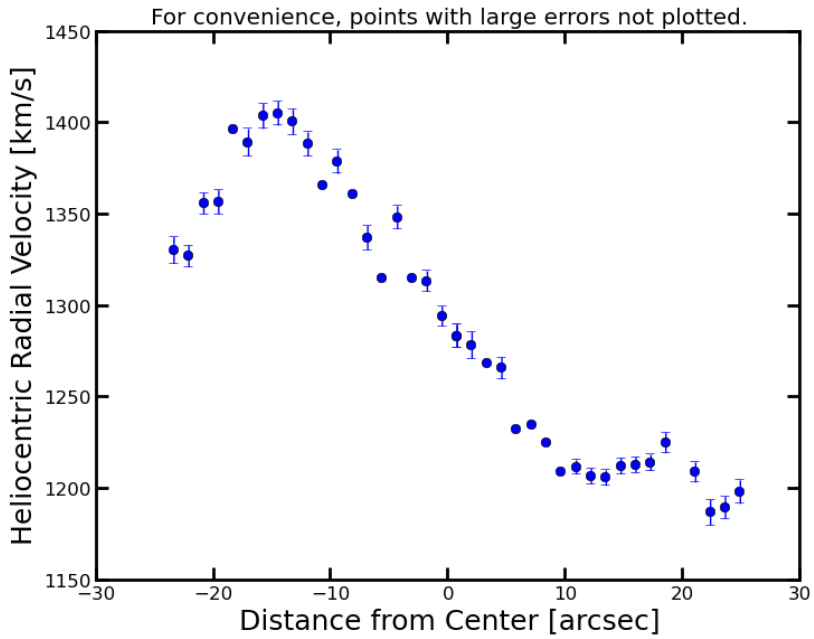

Figure 8.4: A rotation curve obtained using the H_α emission line for the galaxy ESO 085G-030 using SALT spectra. The Y-axis shows the heliocentric radial velocity while the X-axis shows the distance from the centre in arc seconds.

a few of the above steps have been modified and custom reduction pipelines have been written. The details of the instrument and the pipeline are provided in the next chapter. In the next section we will discuss the basic principles of how various aspects of galaxy formation can be studied using their spectra.

8.3 Probing Galaxies Using Spectra

We discussed in Chapter 2 how the images of galaxies can be used to study the physics responsible for their formation. Recall that the properties of a galaxy derived using the photometric analysis described in that chapter do not mean much for a single galaxy. Their usefulness lies in statistical studies where correlations can be studied to make general comments on a given class of objects. Spectroscopy in contrast allows astronomers to study in-depth a given object and study its properties and formation history. However, obtaining spectra is difficult and expensive in terms of telescope time and the detailed analysis involved in the reduction. Thus statistical studies with large samples are often difficult. In this section, we comment on a few aspects of the nature of information provided by a spectrum.

8.3.1 Redshifts, Kinematics

Owing to the expansion of the Universe, any given distant galaxy is moving away from us (after random and proper motions are subtracted) and thus the spectrum of this entire galaxy will be redshifted. The redshift of the galaxy can be obtained by comparing the spectrum obtained from the centre of the galaxy with a rest-frame template spectrum. The template can be fitted on top of the observed spectrum by adjusting the overall normalization of the flux and a shift along the wavelength axis. The shift allows one to determine the redshift of the galaxy and thus the velocity with which it is receeding away from us due to Hubble expansion. The process of template matching can be done using a number of methods. Tools such as *fxcor* use an advanced cross-correlation algorithm to determine these parameters while other tools may rely on a simple least squares approach.

Similar template cross-matching can be done for spectra obtained from regions away from the centre, say along the major axis of the galaxy to obtain the shifts for each part. One can then plot the velocities calculated from the shifts as a function of the distance from the centre. The contribution to these velocities from the Hubble flow can be subtracted from all the obtained velocities and this gives us the rotation curve. The rotation curve gives the rotation velocity V as a function of R, the distance from the centre. An example of a rotation curve is show in Figure 8.4. The rotation curves of galaxies were the first hints for astronomers to allow them to deduce the existence of *dark matter*. If we assume the gravitational potential of the galaxy to be governed only by the visible mass one expects a rotation curve with certain features. However, to explain the rotation curves of most galaxies including the one shown in Figure 8.4, one needs mass additional to the mass which can be deduced from the total light coming from the galaxy.

Another method to determine the rotation curve involves modelling of individual lines. Unlike in the previous method, where the whole spectrum is matched against a template, this method involves using specific emission and absorption lines and tracing their centroid as a function of the position along the spatial axis of the slit. This can be done by fitting the lines with a suitable profile such as a Gaussian or a Voigt profile. A major advantage of this approach is that it allows one to detect any differences in the rotation of the different components of the galaxy. For example, it is possible that the rotation curves from the emission lines and absorption lines are different. The emission lines are emitted by the hot gas present in the galaxy, heated by ongoing star formation while the absorption lines come from the stellar atmospheres. A difference in the rotation curves deduced by these indicates that the gas and the stars are not rotating in a similar manner i.e. they are kinematically decoupled. Examples of such galaxies and possible implications for their formation

can be found in Katkov et al. (2014). The difference generally indicates a recent disturbance in the galaxy, such as a merger, and can offer several insights into the nature of the formation mechanism of the galaxy.

One can also measure the velocity dispersion of the galaxy. This is a measure of the random motion of the stars about the centre of the galaxy. Such a random motion is found typically in elliptical galaxies and classical bulges and leads to the broadening of a spectral line. The width of the spectral lines can be measured by modelling them suitably to obtain the velocity dispersion of the stars. A higher velocity dispersion relative to rotational velocity often indicates a dynamically hot system which is pressure supported while a lower velocity dispersion indicates a rotationally supported system.

In the present study, rotational curves have been obtained for a sample of S0 galaxies by modelling individual lines. However, the use of these rotation curves for dark matter modelling etc is not the main objective of the present study, which is to study the stellar populations of the galaxies as a function of position to find clues about the star formation histories of the galaxies. However, in the process, the determination of the rotation curve is a crucial step as will be described in the next chapter.

8.3.2 Stellar Population Modelling

Consider an instantaneous burst of star formation at a given instant of time. This can happen due to a rapid collapse of a giant gas cloud or due to a wet merger event i.e. a merger involving gas-rich galaxies. The star formation history can be mathematically expressed as a suitable Dirac δ-function. This episode of star formation leads to a collection of a large number of stars of different masses and hence different spectral types[1]. To be able to see how the integrated spectrum of such a collection of stars looks like, one needs two basic pieces of information:

- The distribution of the different types of stars in such a collection.
- The spectrum of each type of star.

The distribution of the different types of stars is the same as the distribution of the mass of the stars, given a metallicity. This is described by an *initial mass function* (IMF). The knowledge of the spectrum of different types of stars can be obtained by observing the respective stars and recording their spectra. The spectrum can also be obtained theoretically by working out the models of radiative

[1]From basic theory of star formation, we know that the properties and the evolution of a star is largely a function of its mass with an additional role played by metallicity of the gas leading to the star formation.

transfer and atmospheric opacities for a given stellar type. Due to limitations in the understanding of the theory as well as limitations in computational power, in the past the agreement between the models and the actual spectra was not very good. However, with modern advances in the field, the two approaches today are almost equivalent. Given the distribution of the masses of stars and spectra of different types of stars the process of obtaining the integrated spectrum of such a collection of stars is straightforward. It is simply the weighted sum of all spectra, the weights being governed by the IMF.

All these stars of different masses start out on the main sequence of the Hertzspreng - Russell diagram but follow different evolutionary tracks depending on their masses. The nature of these evolutionary tracks is quite well known except for a few phases of stellar evolution that stars of specific types go through, such as the Asymptotic Giant Branch or the Thermally Pulsating phase. However, the overall difference made by stars in these phases to the optical spectrum of a galaxy is negligible. Using the evolutionary tracks, it is possible to say what the spectrum of the different stars looks like after a certain time has lapsed since the initial burst that created them. Once again, to obtain the integrated spectrum of the stars at this epoch, one simply finds the relevant spectra and obtains a weighted sum. Models today can also take into account the dying of the stars in supernovae and the chemical enrichment caused by it. The population of stars born in a single burst is referred to as a Simple Stellar Population (SSP).

In constructing the spectrum of a galaxy with a given star formation history, the SSP is the most fundamental building block. Any star formation history can be expanded or written as a series of instantaneous star bursts. This means that the spectrum of a galaxy at any instant of time can be written as a sum of spectra of SSPs. The spectrum of a galaxy at time t, with a star formation rate $\psi(t)$ and a metal enrichment law $\zeta(t)$ can be written as (Bruzual and Charlot, 2003):

$$F_\lambda = \int_0^t \psi(t-t')S_\lambda[t', \zeta(t-t')]dt' \tag{8.2}$$

Here $S_\lambda[t', \zeta(t-t')dt']$ is the flux per unit wavelength per initial mass of an SSP with age t' and a metallicity $\zeta(t-t')$.

In this manner, the integrated spectrum of the galaxy has embedded in it the star formation history of the galaxy. This history can be obtained by modelling the spectrum using a suitable combination of SSPs. This can be achieved using various tools such as the ULySS (University of Lyons Spectroscopic analysis Software) (Koleva et al., 2011), Starlight (Cid Fernandes et al., 2005) and NBursts (Chilingarian et al., 2007). The present thesis uses Starlight for stellar population modelling. The details of the working of this tool and the software pipelines written to interface

with Starlight are described in the next chapter.

Chapter 9

SALT RSS Spectroscopy - Basic Reduction, Kinematics and Stellar Modelling Pipelines

The previous chapter offered a quick overview of the basics of spectroscopy and basic spectroscopic data reduction. The chapter also covered briefly the different types of information that can be obtained from a spectrum. In this chapter, we will revisit these topics but stress on the implementation of the steps with respect to the data obtained from the Southern African Large Telescope (SALT) using its Robert Stobie Spectrograph (RSS). In the first section, we will briefly discuss the construction and features of the SALT and the RSS. The second section is a summary of the proposals submitted to the SALT over a period of several years and the type of observations carried out. In the third section, we discuss the basic data reduction pipeline written while in the fourth section we focus on the tools used for the determination of the rotation curve and population modelling using Starlight.

9.1 SALT and RSS

9.1.1 A brief description of SALT

The design of SALT is inspired by the Hobby Eberly Telescope (HET) at the McDonald Observatory in Texas, USA. The telescope is designed in such a way that it always has a fixed altitutde of 37 degrees[1]. The telescope is allowed a complete rotational freedom of 360 degrees along the azimuth. At the top end of the telescope is a tracker beam which can follow an object of interest for about 12 degrees. This

[1]The HET has a fixed altitude of 35 degrees. However, if SALT had been constructed with the same fixed altitude, a fraction of the Large Magellanic Cloud, a prime object of interest in the southern celestial hemisphere would not be easily observable. Hence SALT was fixed at a slightly different altitude of 37 degrees.

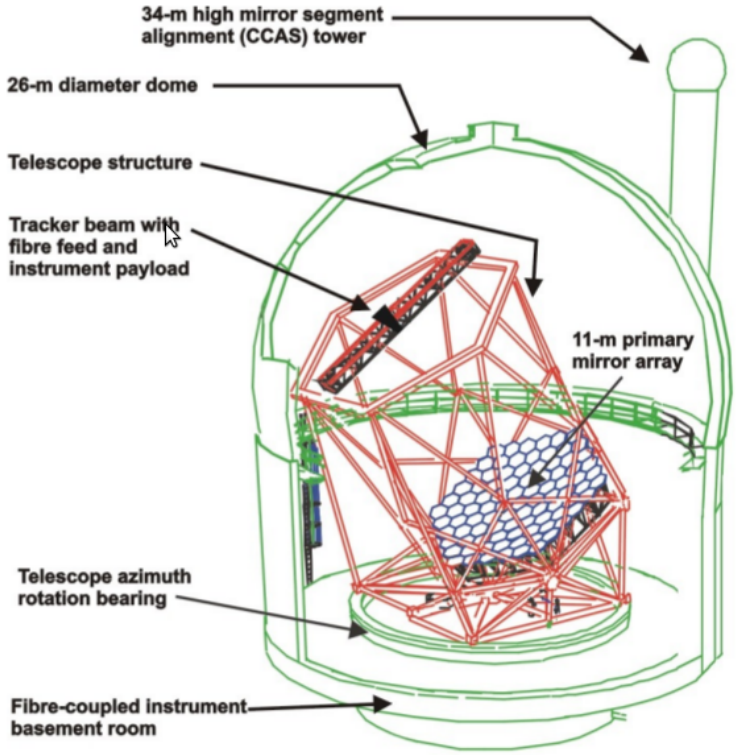

Figure 9.1: A schematic diagram showing the structure of SALT. Credit: Peter Martinez

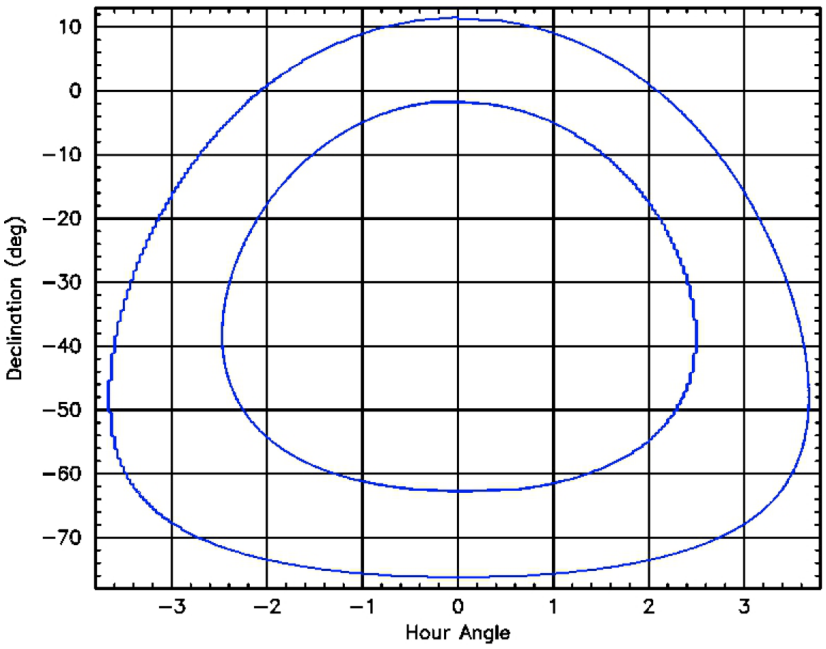

Figure 9.2: A plot of declination against the hour angle with an *annulus* showing the region visible to SALT. Humorously referred by many as the 'toilet seat' diagram. Credit: The South African Astronomical Observatory.

means that only those objects can be observed which are within a 12 degree annulus around the fixed altitude of 37 degrees. While this appears as a disadvantage, it must be noted that since the telescope remains at a fixed altitude, the overall requirements of the supporting structure are significantly reduced thus allowing the construction of a 11 metre class telescope at a significantly lowered cost. The overall construction of the SALT is illustrated in Figure 9.1 while the observable annulus is illustrated in Figure 9.2.

Taking into account the latitude of Sutherland where the telescope is located and the restrictions imposed by its design, the telescope is able to observe objects between a declination of -75d $22'$ and $+10$d $47'$. Objects close to the equator can at worst be observed for no more than 48 minutes including acquisition overheads[2] while objects further to south (< -58 degrees) can be observed upto a time of 90 minutes. As a result, all observations using SALT are done using a queue mode, where all programme objects observable in a night are queued to maximize telescope time utilization.

The spherical primary mirror has a maximum diameter of 11m and comprises 91 hexagonal mirror segements, each having an inscribed diameter of 1m and a radius of curvature 26.165m. In comparison to the HET, the SALT uses an improved design of the spherical abberation corrector which allows the total reflecting area of the primary mirror to be equivalent to that of a 9.96m telescope. An important aspect of the entire design is that the image pupil changes during the process of tracking / exposure. This means that the effective area of the telescope changes during an observation thereby not allowing absolute photometry or spectrophotometry. It is still possible to observe spectrophotometric standards in order to achieve a relative calibration i.e. it is possible to get a spectrum with the correct relative shape. The primary objective of the spectral study carried out in this thesis does not require absolute flux calibration as the tools used for spectral fitting can work by accepting an input spectrum with relative flux calibration. However, the spectra obtained cannot be used for measurement of stellar masses since this requires absolute photometric calibration.

The variation in the effective area of the telescope across single or multiple observations also has another important consequence. A general observation strategy is to divide a single long exposure into several frames of smaller exposures and then take a sum or a mean spectrum. Even though each frame is taken with the same exposure time, they have different levels of signal. Thus it may become necessary for the effective exposures to be equalized using a suitable technique before combining

[2] Acquisition overhead refers to the time taken for any telescope to physically move the structure to be able to observe an object and take the necessary images needed to be able to fine tune the pointing and the instrument configuration.

the spectra.

There are various instruments / payloads on SALT which allow for various types of data to be acquired. For completeness, we mention all of them but the current thesis solely uses the data acquired using the RSS.

- SALTICAM: This is an imaging and acquisition camera operating in the wavelength region of 320 - 900nm. It has capabilities of high time resolution imaging and also supports, in a limited way, tracking of non sidereal sources. Unless a secondary photometric standard occupies the same field of view as the source of interest, it is not possible to do any absolute photometry with this imager given the variable pupil. In the present thesis, images from SALTICAM were purely used for source acquisition and verification.

- RSS: The Robert Stobie Spectrograph is the main instrument of SALT and since it has been extensively used in the present study, a separate section is devoted to a detailed discussion of the instrument.

- HRS: The High Resolution Spectrograph is an Échelle spectrograph capable of achieving resolutions between 14000 and 65000. The HRS instrument has been only recently deployed on SALT (c. 2014).

- BVIT: The Berkeley Visible Imaging Tube camera is a photon counting camera capable of very high time resolution (from milli- to micro- arcseconds) photometry in the B, V, R and H-alpha bands.

9.1.2 A brief description of RSS

The RSS has been named after late Robert Stewart Stobie, a former director at the South African Astronomical Observatory and is the main instrument on board the SALT. The instrument is designed to be versatile and offers various modes to cater to a diverse range of scientific goals. It is sensitive in the wavelength range of 320 to 900 nm. Using slits of different widths and suitable gratings, a resolution over a wide range upto 9000 can be achieved across different wavelength regions.

The available modes of RSS include

- Long-slit spectroscopy - this is the mode used for all data presented in this thesis

- Narrow band imaging

- Multi-object spectrograph (MOS)

- Low resolution (LR) Fabry-Perot imaging spectroscopy and tunable filter (TF) narrow-band imaging

- Single-etalon medium resolution (MR) Fabry-Perot imaging spectroscopy for emission line studies

- High time-resolution spectroscopy

- (Future) A near infrared extension to the spectrograph is being developed and is scheduled to be deployed in 2016.

RSS has six transmission gratings of which five are *Volume Phase Holographic* (VPH) gratings while the sixth is a standard surface relief grating. An important characteristic of the VPH is that its transmission efficiency is a function of the angle of incidence. Thus the wavelength range to be covered with high efficiency can be tweaked by adjusting the angle between the collimated beam and the normal to the grating. Thus the grating angle is an important parameter to adjust when planning observations with the RSS. The SALT science website offers a Java based tool known as the RSS Simulator[3], which allows astronomers to determine the wavelength coverage, resolution and SNR as a function of wavelength and exposure time.

As mentioned in the previous chapter, the grating equation implies that wavelengths bearing an integral ratio can have the same angle of diffraction and thus overlap. To avoid this it is necessary to use a blocking filter, which blocks required wavelengths and prevents overlap. For this purpose, the RSS offers five common blocking filters namely PC00000 (clear), PC03200, PC03400, PC03850 (UV) and PC04600 (Blue).

The most commonly used mode in the RSS is the longslit spectroscopy mode. As mentioned earlier, a choice of slits is available allowing the user to choose the right combination of SNR and spectral resolution. Available widths include 0.6, 1, 1.25, 1.5, 2.0, 3.0 and 4.0 arc seconds, each offering a length of 8 arcmin. These slits are placed in a slit-mask magazine and can cover a wide range of requirements of spectral resolution.

The detector onto which the spectrum is recorded comprises an array of 3 CCDs. Each CCD has 2048×4096 pixels, each pixel 15 microns in size. The gap between each CCD is 225 microns wide (15 pixels) and the plate scale is 117 microns/arcsec. The presence of CCD gaps implies that certain wavelengths of the spectrum will not be captured. If an important feature of the spectrum lands in the gaps, the spectrum will not be usable for studying the given feature. However, the distribution of wavelengths can be adjusted by adjusting the grating angle as mentioned earlier.

[3]http://astronomers.salt.ac.za/software/rss-simulator/

Proposal ID	Proposal Code	Title	Total Obs. Time
758	2010-1-RSA-OTH-IUCAA-001	Star formation histories in Lenticular galaxies	15.3h
1447	2011-3-RSA-IUCAA-OTH-001	Star formation histories in Lenticular galaxies	8h
2136	2012-1-IUCAA-RSA-OTH-001	Star Formation Histories in Pseudobulges	8.7h
2624	2012-2-IUCAA-RSA-OTH-001	Star Formation Histories in Pseudobulges	6.7h
4619	2014-1-IUCAA-RSA-OTH-001	Pseudobulges in S0 Galaxies	18.7h

Table 9.1: Note: The 2010 proposal is a commissioning phase proposal.

9.2 Proposals and Data

Long-slit data for 50 objects were obtained through a series of proposals from 2010 to 2014. About 33 objects among these are S0 galaxies spanning a wide range of luminosities and bulge types while the remaining 17 are spirals known to host pseudobugles as established in Fisher and Drory (2010). The proposal codes, IDs and titles are given in the table 9.1. The present thesis does not aim at providing detailed analysis results for all objects for which data were obtained. Instead, the thesis aims at describing the detailed pipeline developed for the analysis and present stellar population analysis carried out on a subset of S0s known to host pseudobulges as established in the studies described in Chapters 6 and 7. Given the volume of the data, the entire process of analysis will be a long term study with the common scientific goal of learning as much as possible about the star formation histories of these objects.

The tentative[4] distribution of the bulge types and galaxies is captured in Figure 9.3. As mentioned earlier, the thesis focusses on a detailed analysis of pseudobulge hosting S0s.

We conclude this section with a quick summary of the technical specifications of the observational modes used in all the proposals.

- Slit used: 1 arcsec.
- Grating used: PG0900

[4]Based on prior information obtained from various studies and thus need not be a reflection of the actual nature of the objects.

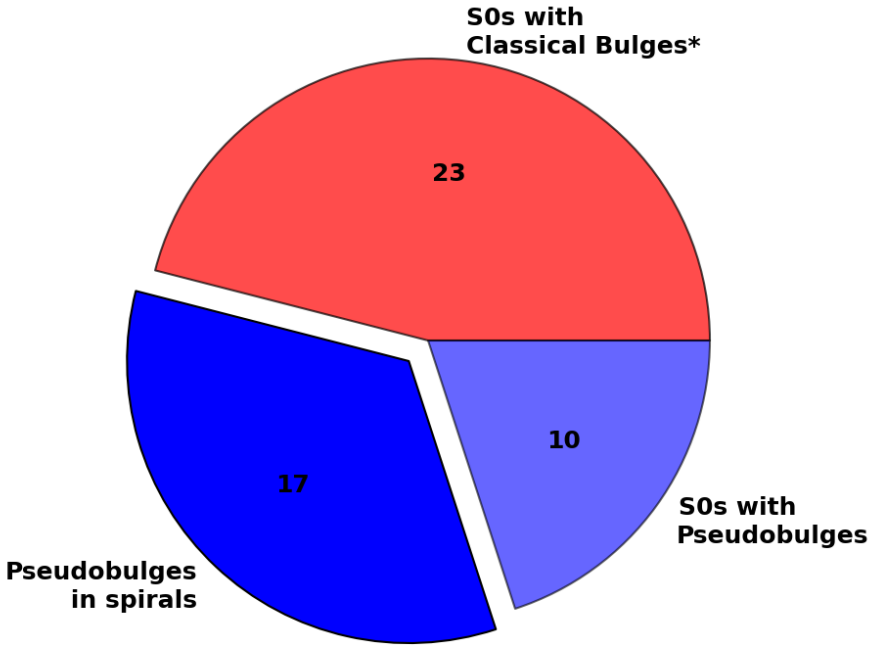

Figure 9.3: The distribution of the objects observed using SALT / RSS. *Since all these objects are not a part of the photometric studies described in the previous chapters, the exact nature of their bulges is unknown. They have tentatively been classified as classical for the purpose of making this chart.

- Resolution achieved: ~ 1500
- Wavelength coverage: $\sim 3640 - 6765$ Angstrom
- Pixel binning used for improving signal-noise ratio: 2×4 (wavelength and spatial axes)
- Calibration data: Flats, Argon arc lamps, and spectrophotometric standards.
- Typical grating angle: 13.25 - 14 degrees.
- Typical SNR: variable across the galaxy, but of the order of 20.

9.3 Basic Reduction Pipeline

This section explains the basic spectral reduction pipeline used for reducing the SALT / RSS spectra. The pipeline has been written by us using Python[5] and largely uses the PyRAF interface which allows IRAF tasks to be called as regular functions within Python. Each module performs one of the basic operations highlighted in

[5]Python is an freely distributed and open source high level programming language. It has become, in recent times, the preferred choice for coding astronomical data reduction tools and pipelines.

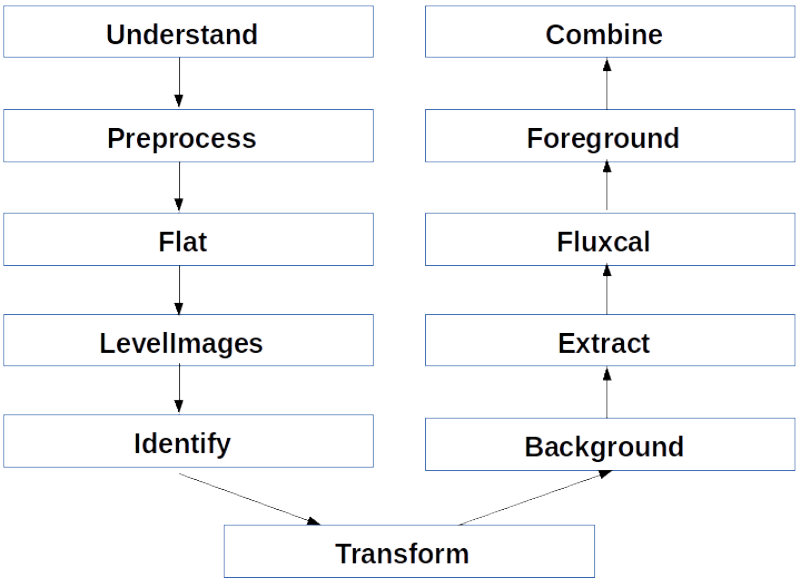

Figure 9.4: A flow chart illustrating the sequence in which the modules of the basic spectral reduction pipeline are executed.

the previous chapter. The order in which the modules are executed is captured in Figure 9.4.

Before a detailed description of all modules is presented, we will quickly summarize the preprocessing carried out by the SALT science team on the RAW data obtained using RSS. The preprocessing is done using a pipeline called PySALT (Crawford et al., 2010) and the end result is referred to as *product data*. The product data in most cases were of acceptable quality and did not require any custom preprocessing. The basic steps carried out by PySALT are:

- Data Preparation: This includes addition of necessary keywords in the headers to allow other modules including those in IRAF to identify the images, the observing conditions, noise etc.

- Gain Correction: Recall that the entire spectrum is captured by three CCDs. Each CCD has a different level of gain which will result in artificial jumps in the counts when moving from one chip to the other. To account for this, the gain of the read-out amplifiers for all CCDs needs to equalized.

- Cross-Talk correction: The read-out circuits for the three CCDs experience cross-talk which needs to be corrected.

- Bias Correction: This is a standard step involved in reduction of any CCD data.

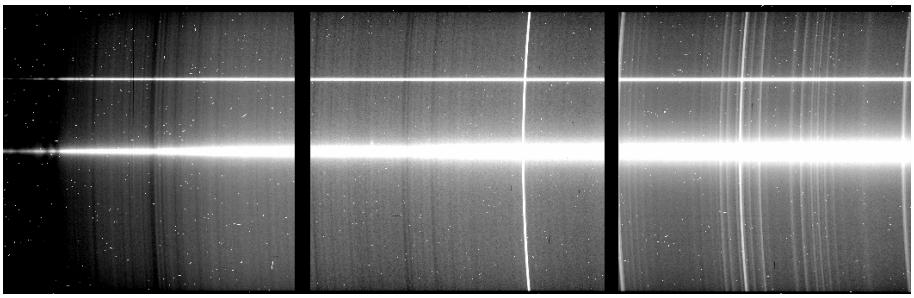

Figure 9.5: An example of the product data obtained from PySALT for the galaxy NGC 1533.

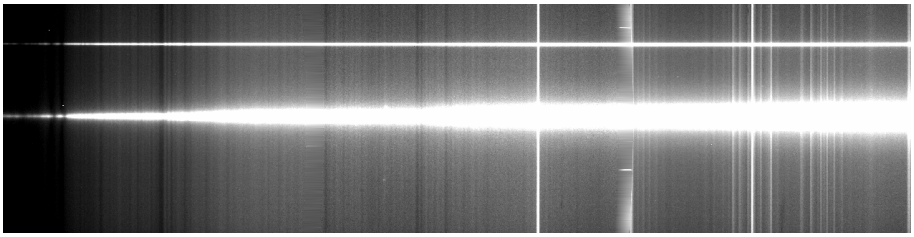

Figure 9.6: An example of the product data shown in Figure 9.5 after it has been transformed using the wavelength and coordinate transformation solutions obtained from the arc spectrum.

- SALT Mosaic: We eventually want to work with a single FITS file containing the entire spectrum as opposed to three pieces of the spectra stored as three individual files. For this, we use a suitable geometry configuration and mosaic all the CCDs onto a single frame.

The typical product data obtained at the end of these steps is shown in Figure 9.5. It is clear that there are several artifacts in these images which need to be corrected. For example, one can see spectral emission lines of the sky exhibiting a curvature due to a variation in the wavelength distribution along the vertical direction. One can also see several cosmic ray events captured in the spectrum. The corrections for these along with the standard spectral reduction procedures are carried out using the basic reduction pipeline. The basic modules in this pipeline are:

- Understand: By default, the science FITS image comes as a multi-extension FITS file. One extension contains basic observational information while the second extension contains detailed parameters describing the instrument modes / settings. Further, each file is named using an observation code made up of the date of observation and its queue ID for the given observation night. This step performs two basic operations - 1) Merging of the header information to obtain a simpler and easier-to-handle single extension FITS file, 2) Renaming of the files using object names. The module also creates files which contain

information identifying the flats, arc lamp and science frames. These files are used by subsequent modules to identify the different types of files. The module also offers the user to trim away any part of the data not relevant to the reduction by accepting the image coordinates.

- Preprocess: This module performs two important operations - 1) CCD gap filling and 2) Cosmic Ray correction. The CCD gaps represent an abrupt change in the intensity along the wavelength axis. In the flat-fielding step, a function is fitted to the large scale illumination structure. This process of fitting can get severely affected by the presence of discontinuities in the spectrum and so the gaps are filled using the gradient of flux across them. This step is also crucial for background subtraction as is explained below. The cosmic ray correction is carried out using the *L A Cosmic* routine (van Dokkum, 2001).

- Flat: As a first step, the module identifies the flat-field images as marked by the *Understand* routine and combines them to produce a high SNR flat frame. Using *mkillumflat* task of IRAF, the large scale illumination is fitted separately in the vertical and horizontal directions and removed. The flat obtained at this stage now purely represents the intra-pixel variations in efficiency, which is then normalized and applied to all the science frames (except the arc).

- LevelImages: Recall the issue of the moving pupil in case of SALT. As a result, individual frames though obtained using the same exposure time have different signal levels. After reducing all the frames we will need to combine them into a single frame of high SNR. During the combination, we will also construct a standard deviation frame which will be used to determine the error spectrum. For these steps to be meaningful, it is important to equalize the effective exposures of all the frames. This can be done by equalizing the median, the maximum or the mean flux level in the spectra. The module allows user to choose any of the options, preview the equalization and approve one that works best.

- Identify: The *Identify* module is an interface to the PyRAF tasks *identify* and *reidentify*. The *identify* task in IRAF presents the arc spectrum to the user who is required to identify the emission features interactively. A handful of features covering a broad wavelength range are identified and a prelimiary solution is obtained. This preliminary solution can be used to auto identify all the other features in the arc spectrum. At this stage it is important to ensure that this auto identification has been done correctly. It was found useful to delete some of the features near the CCD gaps since the curvature introduced

by optical distortion can cause these features to disappear into the gaps at some points along slit. A Chebyshev polynomial fit of high order was mostly used for obtaining a good solution with a root mean square scatter of 0.4 Angstroms.

At this stage, the solution is obtained only for the central part of the slit. As is clear from Figure 9.5, this solution changes across the slit. The task *reidentify* is thus invoked to adjust the solution as a function of the position along the slit. This information is stored in a database file by IRAF. The module then allows the user to preview the coordinate transformation that will be needed to remove this variation.

- Transform: As we move along the slit, the wavelength changes due to a combined effect of the telescope optics and grating response. For ease of reduction, it is imperative that the wavelength remain the same across the slit. For this, the entire frame has to be transformed. The information of this transformation is stored in the form of the varying wavelength solution along the slit, obtained in the previous step. The *Transform* module uses this information to reconstruct the entire frame. The spectrum now looks as shown in Figure 9.6.

- Background: At any given point along the slit, the spectrum obtained is a sum of the flux from the object as well as the sky. In order to remove the latter, regions along the slit unoccupied by any astrophysical source are identified. A polynomial is then fitted to the flux in these regions as a function of the position along the slit which is then used to subtract the background spectrum from the entire frame. Recall that we had filled the CCD gaps using gradient information. If this step had not been carried out, it would be difficult to determine the best-fit polynomial owing to the sudden flux jumps in the CCD gaps.

- Extract: When the science goal is to obtain a single 1-d spectrum of the object of interest, the process of extraction is simple. One adds all the rows occupied by the spectrum and produces a high SNR 1-d spectrum. However, the goal of the current study is to obtain a 2-d spectrum so that changes in the spectrum along the (major) axis of the galaxy can be studied. One might therefore simply "cut out" the relevant portion of the FITs file, however this assumes that the dispersion axis is perfectly aligned with the CCD. This is seldom the case and thus one needs to perform *trace correction* which involves tracing the centroid of the spatial axis as a function of wavelength and applying a transformation to remove this variation. The *apextract* task with *strip* mode

is used for this purpose.

- Fluxcal: This step extracts the spectrum of the spectrophotometric standard star and uses it to determine the variation of the sensitivity as a function of the wavelength. The sensitivity function is then applied to all object frames to equalize the wavelength response.

- Foreground: The dust in the Milky Way alters the spectrum of an object by attenuating the flux. The attenuation is a well known function of the wavelength as well as the position of the object relative to the Milky Way plane. This module communicates the object information to the NASA Extragalactic Database to determine the coefficient of reddening A_v and then uses then *deredden* task in IRAF to correct the spectrum for foreground extinction.

- Combine: At this point, every object frame is corrected for instrumental signatures as well as the effects of extinction due to Milky Way. This module combines all the frames into a common frame. Before combining, the module displays a blink sequence of all frames so that we can check for the presence of any shifts. During extraction, it is possible to specify the region of extraction in a way that the spectra are always aligned across the frames. Thus, normally no further corrections are needed and the frames can be combined directly. This step also produces a standard deviation frame along with the mean frame. The standard deviation frame is divided by the square root of the number of frames so that it reflects the error frame of the combined mean. Note that it is not meaningful to construct the standard deviation frame if the effective exposures are not equalized as done by the *LevelImages* module.

At this stage, one has a 2d spectrum of the galaxy corrected for all possible instrumental signatures and a corresponding 2d error spectrum which represents the uncertainty in the actual spectrum. This is the final reduced spectrum which can be used for scientific analysis.

9.4 Kinematics and Population Modelling

The primary goal of the analysis for which spectra were obtained is to study the formation history of these galaxies. For this, we need to model a spectrum as a suitable linear combination of SSPs as described in the previous chapter. Typical programs which are used to perform such modelling accept a 1-d input spectrum and output suitable parameters. As opposed to studies which aim at obtaining a spectrum from just the centre of the galaxy, we aim at obtaining spectra from multiple positions along the major axis and model each spectrum. This will allow

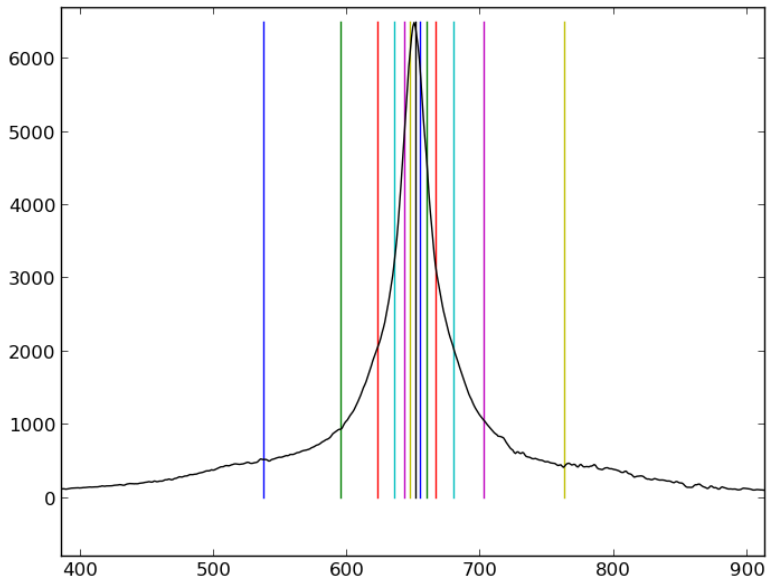

Figure 9.7: The intensity profile along the slit with a scheme of marking apertures to obtain high SNR 1d spectra from several points across the slit.

us to construct age and metallicity gradients as well as other diagnostics which will help us to infer how the galaxy assembled its stellar populations. For this, we need a method of obtaining spectra from multiple positions across the slit.

The simplest method by which this can be done is to simply take one row starting from the centre, treat it as one spectrum and model it. This way, one obtains as many spectra as there are rows. However, there are several problems associated with this approach. The SNR of a spectrum obtained from a single row may be sufficient near the centre of the galaxy. However, as one moves away from the centre, the SNR degrades rapidly so that one is not able to securely model the spectrum. A solution to this problem is to mark out equal apertures of N rows each along the slit and sum up the N rows to construct a high SNR spectrum representative of the light at a given position on the slit. However, this still does not alleviate us of the problem of degrading SNR. A more suitable approach will be to mark apertures of varying widths across the slit, with the width being inversely related to the total flux in that aperture. This way, one will mark out smaller apertures at the centre where the flux is high and larger apertures in the outer area. This is illustrated by the plot in Figure 9.7 which shows the intensity profile along the slit and a scheme of marking apertures as described.

Let us now assume that the apertures are marked and we know which rows need to be summed up in order to produce a 1-d spectrum for a specific position on the slit. However, it is not possible to directly add the rows due to the rotation

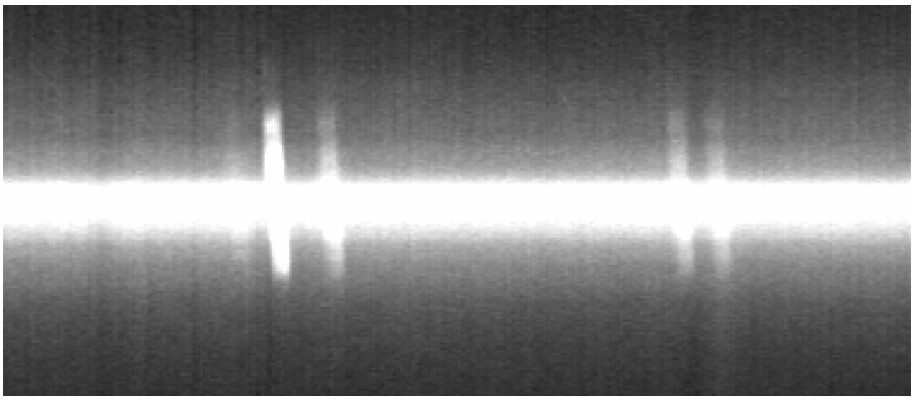

Figure 9.8: The H_α, NII and SII emission lines in the 2d spectrum for the galaxy IC 2085. The lines exhibit bending which is due to the rotation of the galaxy.

of the galaxy. The 2-d spectrum of the galaxy IC 2085 near the H_α, NII and SII emission lines is shown in Figure 9.8. As can be seen in this figure, the spectral lines are bending about the centre. This is due to the rotation of the galaxy - the spectrum on one side of the centre is redshifted due to the systematic motion of the stars away from us while the other side is blue-shifted due to the systematic motion towards us. A simple addition of rows will mix up the spectra and the final spectrum obtained this way will be unusable for modelling. For this reason, it is necessary to *derotate* the spectra before addition. This can be done by modelling the rotation curve of the galaxy. The details of the pipeline used for this (referred to as the *kinematics pipeline*.) are described in the following subsection while the modules used for population modelling are described in a later subsection.

9.4.1 Kinematics Pipeline

This pipeline is a collection of modules which allow one to determine the rotation curve of a galaxy, fit it using a suitable function and perform the spectral extraction. The pipeline is written by me largely in Python and uses PyRAF, a Python interface to the tasks in the IRAF package. A module by module description of the pipeline is provided below.

GetCurve.py: This program determines the intensity weighted centroid along the spatial axis and displays the central spectrum to the user. The user is allowed to provide an approximate redshift of the galaxy so that the spectrum can be displayed in a deredshifted form. The program is interactive and the user can mark the absorption or emission feature of interest using the mouse to locate the boundaries and pressing the 'm' key. Once the spectral feature is marked, the user is asked to provide the number of components that should be used to model it. For example, when modelling the Mg absorption lines at moderate resolution, two of its features appear blended while a third one appears as distinct. It was found that such a

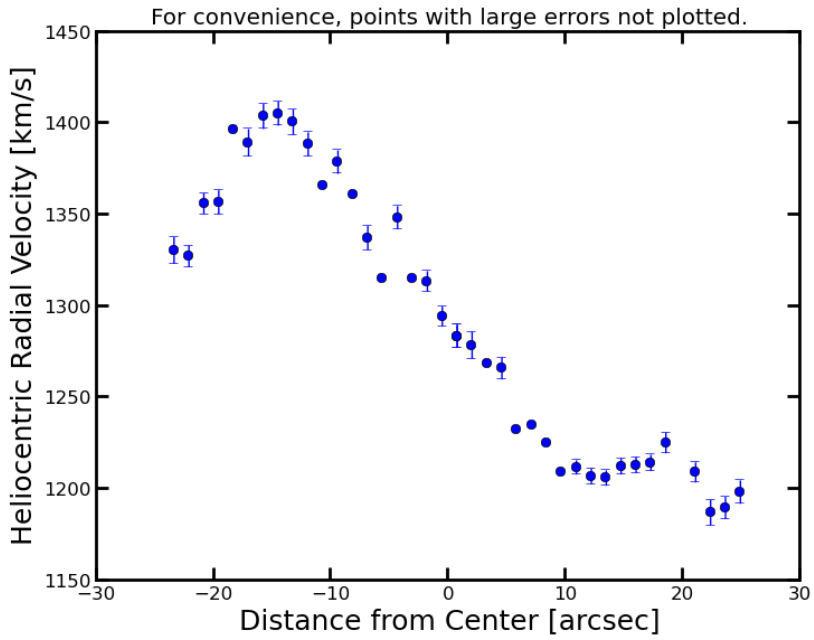

Figure 9.9: Example of a rotation curve produced by the GetCurve.py module. The example is that for the H_α emission in the galaxy ESO 085G 030.

feature is best modelled using a combination of two Gaussians.

The spectral feature is modelled using the following analytical function.

$$F(\lambda) = a + b\lambda + c\lambda^2 + \sum_{i=1}^{k} G_i(\lambda, \mu, \sigma) \tag{9.1}$$

G_i refers to a Gaussian function in λ characterized by a centroid (mean) and a width. The quadratic at the beginning of the equation is used to model the underlying continuum while the remaining terms represent individual spectral features. The fitting is done using the Marquardt Levenberg method implemented in the *lmfit* package in Python. The parameters of the Gaussians are not left entirely free. Instead a constraint, that the difference in the centroids remains a constant equal to the difference in the rest-frame wavelengths, is imposed. A further constraint is that the widths of the Gaussian are kept equal to each other. This is motivated by the reasonable assumption that both the spectral features are emitted by the same stellar system and thus cannot have varying separations in their centroids and different widths.

However, in order to achieve a sufficient SNR, a certain number of rows (customizable using a configuration file) are summed before the fitting is carried out. The routine then moves on either side of the central row in steps with a configurable step size, fitting the centroid in each case. This way, one can map the variation of the centroid of the spectral features along the spatial axis. The difference between

the centroid and the corresponding rest-frame wavelength can be converted into a velocity to which heliocentric corrections can be applied. The final rotation curve obtained in this manner looks as shown in Figure 9.9.

The routine runs in an infinite loop till the user wishes to exit, allowing them to model individual rotation curves. The advantage of this method, as mentioned earlier, is that it allows us to check for differences in curves obtained for emission and absorption lines which in turn indicate a kinematic decoupling between the gas and the stars. All rotation curves approved by the user are stored in the form of ASCII tables which can be read by other modules in the pipeline.

MakeMeanCurve.py This routine detects all rotation curves obtained and approved by the user and displays them on a common plot. This allows the user to verify if there is any significant difference between the rotation curves determined for various features. Having allowed a comparison of the rotation curves, the user can then select those curves which can be combined to construct a mean rotation curve. If the gas is found to be kinematically decoupled, the user may wish to use purely the stellar rotation curves else both emission and absorption line based curves can be combined. The module then constructs the mean curve and allows user to approve it or discard it.

EditCurve.py Sometimes, the quality of the data does not enable the determination of the data points on a rotation curve at all locations on the slit. In such cases, one can get highly unphysical outlier points that can affect the fitting of the rotation curve. For such cases, the user can run this simple utility which allows points to be either deleted or replaced by a value determined using suitable interpolation between the neighbouring points.

FitRotationCurve.py This program accepts a rotation curve table as an input and allows the user to fit it using a polynomial. It was found that the use of spline and regular polynomials was unsuitable for this purpoe. The spline fit is too flexible and overfits even outlier points while regular polynomials can be ill behaved for higher orders. It was thus decided to use Chebyshev polynomials to fit the rotation curve. The program sequentially fits the curve with increasing order and offers a preview of the fit each time. It also shows the change in the residual. The point at which the improvement in the residual is less than 1% is usually accepted as a *sufficiently high* order of the polynomial. Once the user approves this, the polynomial solution is saved to the disk.

DerotExtract.py At this point, we have a model of the rotation curve which allows to infer the redshift correction to be applied to each row before it can be added to form a 1-d spectrum at a given point on the slit. This program begins by displaying the intensity profile along the spatial axis and allows the user to mark regions to be used for spectral extraction. Having marked the region, the user is

then asked to choose the number of apertures to be extracted from this region. The algorithm used for deciding the apertures works by first marking a central aperture and calculating total flux enclosed. Then the number of rows in the outer aperture is increased iteratively till approximately the same amount of flux is obtained. The process continues until all the apertures have been marked.

The information about the apertures is determined using a separate routine which conveys the same to the main program. The main program then takes each aperture and performs the following operations on them:

- Copy each row into separate 1-d spectrum files.
- Determine redshift using the model of the rotation curve.
- Use IRAF task *dopcor* to perform the correction to each row spectrum.
- Use PySynphot, a Python package for handling spectra developed by STScI to resample the spectrum over a common grid of wavelengths.
- Find the mean spectrum.
- A similar operation is carried out for rows from error spectrum except that the addition is done in quadrature and a suitable normalization is carried out.

Each spectrum is stored as a table file containing the wavelength, the flux and the error on the flux. The sampling is done at integral steps of wavelength as this is required by Starlight, the program used for population synthesis modelling. At this stage, one has converted the entire 2-d spectrum into a collection of 1-d spectra, one for each position on the slit. The information of the one-one correspondence between these spectra and their positions on the slit is stored in a file referred to as an *aperture map*. These 1-d spectra are formatted in a form compatible with Starlight.

9.4.2 Population Synthesis Pipeline

Before describing the actual population synthesis pipeline, we will first discuss the program used for modelling the spectrum.

Starlight

The Starlight code was developed by Cid Fernandes et al. (2005) and is written in FORTRAN 77. The primary purpose of the code is to model the input spectrum as a linear combination of some base spectra which are generally SSPs of a suitable range of metallicities and age bins. The model spectrum can be written

as $M_\lambda(\vec{x}, A_V, A_V^Y, v_*, \sigma_*)$ where $\vec{x}$ is known as the population vector and is made of N_* components, with N_* being the total number of SSPs that constitute the base. A_V is the global extinction parameter while A_V^Y is the optional *selective extinction parameter*. V_* and σ_* represent the kinematical parameters - the overall velocity shift and the velocity dispersion respectively.

The model can be written as

$$M_\lambda = \sum_{j=1}^{N_*} L^0_{\lambda,j} * G(v_*, \sigma_*) 10^{-0.4 A_{\lambda,j}} \tag{9.2}$$

Here, $L^0_{\lambda,j}$ refers to the jth base spectrum without any extinction or kinematic filters applied, G refers to a Gaussian characterized by a centroid v_* and a width σ_*. The operation $*$ implies a convolution.

To determine these parameters, a χ^2 minimization is carried out using a mixture of simulated annealing plus Metropolis plus Markov Chain Monte Carlo techniques. Here, χ^2 is defined as,

$$\chi^2 = [w_\lambda (O_\lambda - M_\lambda)]^2 \tag{9.3}$$

O_λ refers to the observed spectrum while w_λ refers to the weights. The weights applied are generally the inverse of the error spectrum except for those points declared as bad using a mask in which case a zero weight is used.

The following inputs are required for the execution of Starlight:

- An input spectrum: This should be at minimum a two column ASCII table which contains wavelengths in the first column and the flux in the second column. Ideally, the error spectrum should be supplied as the third column and an optional weight can be supplied as the fourth column. Starlight demands the spectrum be sampled at integral wavelengths else it uses a crude resampling algorithm to achieve this. To prevent this from happening we use PySynphot's resampling features to construct a Starlight compatible spectrum in the spectral extraction step of the kinematics pipeline. If an error spectrum is not provided, Starlight computes a signal to noise ratio in a predefined range of wavelengths and uses an isoskedastic error bar on all flux values. While this might be helpful in getting a crude model spectrum, the overall results are not completely reliable.

- Mask file: All bad wavelength data points should be masked so that they do not contribute to the value of χ^2. Even emission lines should be masked. This is because emission lines originate from hot gas while Starlight is used to purely model the stellar spectrum. The mask file is a two column ASCII text

file marking the beginning and end of the wavelength regions to be masked.

- The base file: This file contains the total number of base spectra on the first line followed by a description of the actual base spectra. This information needs to be provided in the form of a table, the first column specifying a file name where the base spectrum is stored, the second column the age of the spectrum, followed by metallicity, a nick name, fraction of initial mass of stars still present, a flag specifying the nature of extinction modelling to be applied to the base spectrum and the [α/Fe] ratio. All the base spectra should be kept in a common directory.

- Configuration File: This file controls all the technical parameters used in the algorithm used to explore the parameter space to minimize the χ^2. The parameters set at their default values work best for most science cases and seldom need to be modified.

- The grid file: This file contains information about all the above inputs. It is used to specify the total number of fits, the input spectra, their path, the base spectra, their location, the configuration file, the redenning law, the guess kinematical parameters, the seed number used for generating the Markov chains and parameters for the resampling algorithm.

The output files produced by Starlight, one per each input spectrum fitted contain a huge amount of information including details of the various parameters used for the exploration of the parameter space. Below, we list the important parameters:

- The value of reduced χ^2 and the average deviation in percent.

- The kinematic parameters v_0 and σ_*.

- A_V extinction parameter.

- The population vector presented as a table with parameters describing the constituent spectra as specified by the user in the base file. The population vector represents the percentage contribution of light from a given base component to the input spectrum. An equivalent mass vector is also provided which provides mass contributions in percentage.

- The input and model spectra in the form of a table.

Using the above information, it is possible to derive further parameters namely

- Light weighted mean age.

- Light weighted mean metallicity.

- Mass weighted mean age.
- Mass weighted mean metallicity.
- Fraction of young stellar populations ($< 10^8$ years)
- Fraction of intermediate age stellar populations ($> 10^8 \& < 10^9$ years)
- Fraction of old stellar populations ($> 10^{10}$ years)

The above parameters represent summary versions of the information provided by the complete light and mass population vectors determined by Starlight. Note that the fractions of young, intermediate and old stellar populations are dervied using the light population vector.

Base Selection

As mentioned in the previous section, Starlight models the input spectrum as a linear combination of SSPs. The SSPs are selected by the user and input to Starlight. So naturally one is led to ask the question - what is the best method to choose these SSPs that constitute the base? Starlight comes equipped with a default base of 45 SSPs based on the stellar population libraries of Bruzual and Charlot (2003). This base comprises 15 spectra of different ages, each for three different metallicities. The spectra are hand picked and thus it is not guaranteed that they will prove to be adequate for representing a realistic spectrum through a suitable linear combination. A realistic galaxy will be a sum of SSPs picked from a continuum of ages and metallicities. A hand picked base does not assure a uniform sampling of the age and metallicity parameter space.

However, it is not feasible to model the galaxy spectrum using an infinite number of base spectra. Thus it seems reasonable to choose a large base with as much coverage of parameter space as possible. Asari et al. (2007), for example, use a base of 150 spectra. But the computational overhead in the fitting process scales as N_*^2 i.e. as the square of the number of base spectra. Thus the computational time needed when such a large base is used will be very high. Also, many of the spectra of such a large base look sufficiently similar i.e. there is an inherent degeneracy which makes the solutions unstable.

An ideal strategy, one which alleviates all these problems, is to devise a suitable method to automatically select base spectra for which degeneracies are minimum and the sampling of the parameters is as even as possible so as to mimic a smooth continuum. In order to do this, the prescription by Richards et al. (2009) is followed. This method involves using the diffusion mapping technique which is used

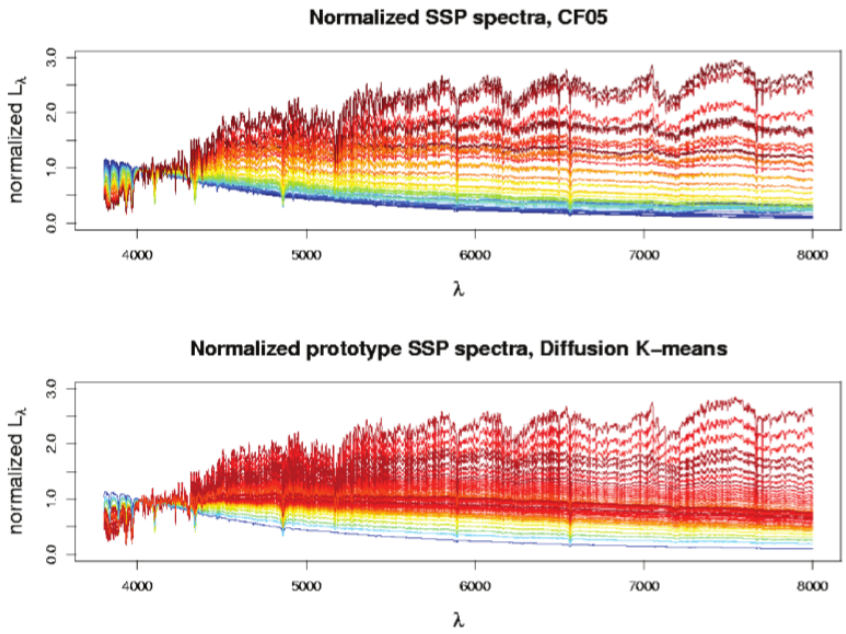

Figure 9.10: The top panel shows the spectra from the standard base of 45 spectra provided by Cid Fernandes et al. (2005) while the bottom panel shows the reconstructed base obtained from the algorithm of Richards et al. (2009).

for dimensionality reduction. The algorithm accepts a large number of base spectra and returns a reduced set of spectra which satisfy the above properties.

In the present study, we used the latest stellar libraries made available by MILES (Medium resolution Isaac Newton Library of Empirical Spectra) to construct a large base of 150 spectra spanning three bins of metallicities with 50 age steps for each metallicity. These are then cast into a form compatible with the MATLAB code provided by Richards et al. (2009) which is then executed to reduce the number of base spectra to 45. A base of 45 spectra is commonly accepted in literature as a compromise between having too many and too few base spectra. The effect of this technique of diffusion mapping is best illustrated using Figure 9.10. This shows spectra of various properties of a hand selected base in the top panel while the spectra reconstructed using this technique are shown in the bottom panel. This figure clearly shows the base spectra constructed using this algorithm offer a more uniform coverage and hence have lesser degeneracy. The authors also argue that this technique significantly reduces the *classic* age-metallicity degeneracy.

Stellar Modelling Pipeline

The following are the Python modules which constitute the stellar modelling pipeline-

Masker.py The spectrum from the intensity weighted centroid along the spatial direction is displayed to the user who is then expected to mark out those regions

on the spectrum that should not be used for fitting. As already explained, this largely consists of the emission lines from the hot gas in the galaxy. In case of SALT spectra, it is also important that the regions occupied by the CCD gaps be masked. Having marked all the regions, a preview is offered to the user who can then approve or reject the mask constructed. The mask, which at this point appears as regions marked on a plot is then translated into a form compatible with Starlight and stored with an appropriate file name.

PrepareStarlightInput.py As the name suggests, this module uses the information about the spectra extracted by DerotExtract.py module and prepares all the necessary input files needed for Starlight to run on the same. Once this module is done executing, the user has to invoke Starlight by passing the created grid file as input. For example, if the spectrum is named as NGC1553_2d.fits, then the grid file created is named as NGC1553_2d_grid.in. The user can run Starlight on this using the command -

```
starlight < NGC1553_grid.in
```

A general caveat to watch out for comes from a limitation of Starlight that it cannot handle file paths containing more than 100 characters. Thus it may become necessary to actually change the location of the directory where the analysis is being carried out so that the complete path is less than 100 characters.

StarlightOutput.py This module is not an executable but contains a Python class which constructs a Pythonic object representation of the output generated by Starlight. The output file is provided to the class constructor and the object generated has several attributes and methods which allow easy access to the different portions of the output. For example, the fraction of old, intermediate and young stars can be accessed by saying `s.young_fraction` where 's' is a Starlight output object. This class is utilized by other routines in the pipeline to parse the Starlight output but is designed in a general manner so that it can be used outside of the pipeline as well.

Starlight_Error.py, Parse_Errors.py Starlight does not provide any estimate of the errors on the various parameters output by it. However, without error bars, it is not possible to comment on whether a gradient of some property across the galaxy is statistically significant. In order to derive error bars, this module uses the error spectrum in order to construct several realizations (~ 100) of the input spectrum. For each realization, Starlight is executed, its output parsed and all derived parameters recalculated. The dispersion in the parameters obtained for these realizations is used as an estimate of error bar. The error estimates obtained this way are stored in suitable output tables.

CompleteSLOutput.py The final step in this pipeline is to generate the output of the complete analysis. This program generates three PDF files. The first PDF file contains the output, model and residual spectrum for each aperture along with some important parameters. The second PDF file contains summary plots of age, metallicity and population fraction gradients while the third PDF file contains histograms representing the formation history of various regions of the galaxy.

All the tools described in this chapter have been made available on a public GitHub[6] repository with the URL: https://github.com/kaustubhvaghmare/ksda_tools. Equipped with these tools it is possible to derive the rotation curves from 2-d spectra, perform aperture extraction using a suitable weighing scheme, perform population synthesis and derive the trends in populations along the slit. The results obtained from the application of these tools to the pseudobulge hosting S0s are described in the next chapter.

[6]GitHub is an online project code and repository management tool that is compatible with the *git* version control system.

Chapter 10

A Spectrosopic Study of Pseudobulge Hosting S0 Galaxies

In Chapter 8, a general overview of how a spectrum of a galaxy can be obtained and used for unravelling its star formation history was presented. Chapter 9 presented details of SALT and RSS along with a description of the working of the custom software tools constructed for the analysis of the data. A total of 50 objects were observed through a series of proposals of which the present thesis aims at studying those S0s which host pseudobulges, as determined from photometric studies described in Chapters 6 and 7. In this chapter, we present results obtained using the pipelines and techniques described in the previous chapter for a sample of pseudobulge hosting S0s. The first section describes the sample and the technical details of the observations carried out using SALT. The next section describes individual galaxies while the concluding section offers details of other techniques / analyses that can be carried out on this sample.

10.1 The Sample and Observations

The RC3 based sample of S0 galaxies was described in detail in Chapter 5. The final sample comprising of 185 S0 galaxies, for which 3.6 micron archival imaging data observed using Spitzer IRAC are available, were analyzed using the technique of 2-d image decomposition. Using the determined bulge properties, those bulges which had a Sérsic index $n < 2$ (Fisher and Drory, 2008) and found to deviate more than 3 σ below the best-fit line to ellipticals on the Kormendy relation (Gadotti, 2008), were classified as pseudobulges. These are 25 in number and the differences between them and the classical bulges based on their photometric properties, are discussed in Chapters 6 and 7.

Recall that the accepted formation mechanism for pseudobulges is through disk

Object Name	R.A. (J2000)	Dec (J2000)	Mag. (Filter)	Obs. Time
ESO079-007	00h 50m 04s	-66d 33m 10s	13.7 (B)	4500
ESO085-030	05h 01m 30s	-63d 17m 36s	13.8 (B)	4500
NGC1533	04h 09m 52s	-56d 07m 06s	11.8 (B)	3600
IC2085	04h 31m 24s	-54d 25m 01s	14.2 (B)	5000
NGC1522	04h 06m 08s	-52d 40m 06s	14.0 (B)	5000
NGC1510	04h 03m 33s	-43d 24m 01s	13.4 (B)	4500
NGC1326	03h 23m 56s	-36d 27m 53s	11.4 (B)	3600
NGC7709	23h 35m 27s	-16d 42m 18s	13.6 (B)	4500
NGC7371	22h 46m 04s	-11d 00m 04s	12.7 (B)	4500
NGC5750	14h 46m 11s	-00d 13m 23s	12.5 (B)	4500

Table 10.1: Targets observed in the SALT proposal *2014-1-IUCAA-RSA-OTH-001*.

instabilities such as a bar, which cause gas infall towards the centre, leading to the rise of an inner disk-like component. If this is true, one can expect certain signatures in the spectra of these galaxies. For example, if the pseudobulge indeed has formed through disk matter rearrangement, the stellar population at the centre of the galaxy dominated by the bulge, is expected to have a larger fraction of younger stars relative to the disk. Using the tools described in the previous chapter, we are in a position to derive such information and test various formation mechanisms for pseudobulges and their host galaxies.

Of the 25 pseudobulges identified in photometric studies of S0 galaxies, a subset of 15 were within the declination limits of SALT. A proposal was submitted to observe as many of these galaxies as possible and obtain RSS long-slit spectra. A total of 10 galaxies were observed through the proposal *2014-1-IUCAA-RSA-OTH-001*. Table 10.1 summarizes the list of objects along with some basic information.

In Chapter 9, we covered details concerning the observational limits imposed by the design of SALT. There is an annular region on the sky with a width of $\sim$ 12 degrees accessible to SALT. This means that there is an upper limit on the maximum exposure that can be achieved for a given object depending on its RA and Dec. In case of 7 of the 10 objects in this sample, the *track time* was not sufficient to achieve the required SNR. For these objects, two independent observations were carried out on different nights and later coadded to achieve the required SNR. However, the reduction of the spectra for these objects requires great care owing to the following factors.

- The effect of the variation in the pupil is even greater and thus significant corrections need to be applied to equalize the effective exposure of all the observations. While equalizing the mean flux levels generally works, the cosmic ray corrections sometimes not being perfect can render the use of mean as inefficient. In such cases, equalizing based on median of flux needed to be

carried out.

- The position of the object along the slit can significantly vary from one night to the other. To account for this, in the process of aperture extraction, the aperture widths were chosen in a manner such that the spatial centroids as well as the sizes of the final frames match. One can then combine the frames without any need for shift corrections.

The steps of flat-fielding, wavelength calibration and flux calibration need to done independently for both sets of observations. All observations were taken within a day or two of each other and in largely similar conditions. So, no systematic variations in wavelength or flux calibration solutions were observed.

10.2 Star Formation Histories

In this section, we will describe in detail every object in the sample of pseudobulge hosting S0 galaxies and comment on the overall consistency of the findings with currently accepted formation mechanisms for pseudobulge hosting galaxies. Figure 10.1 shows the optical images of the galaxies for which detailed comments are presented in the subsections that follow. These optical images have mostly been obtained from NED and are a part of the Digitized Sky Survey (DSS). The 2-d spectra can be found in Figure 10.2. In these figures the vertical direction represents the spatial position along the slit while the horizontal direction represents the wavelength axis. Each row in this image represents a spectrum corresponding to a specific position on the long slit.

In Figures 10.3, 10.4 and 10.5, are presented the formation histories of the galaxies whose images are shown in Figure 10.1 and 2-d spectra in Figure 10.2. The formation history is described by a histogram which is constructed using the population vector output by Starlight, as described in the previous chapter. Recall that the population vector is a collection of percentages representing the contribution of a particular base SSP (Simple Stellar Population) to the total flux in the observed spectrum. Each SSP is associated with a particular age and metallicity. To construct the formation histories represented in figures like 10.3, we divide the complete age range of the base SSPs into equal bins and measure the contributions in each age bin using the population vector. Knowing this information, a histogram is constructed, which shows the fraction of the total stars in a galaxy born at various epochs. For example, if the histogram has a large collection of peaks at $\log(\text{age}) = 9 - 10$, it means that most of the stars have formed at a very early epoch. On the contrary, if the histogram has a large collection of peaks around $\log(\text{age}) \sim 7$, most of the stars have formed relatively recently. According to the current theories of large scale

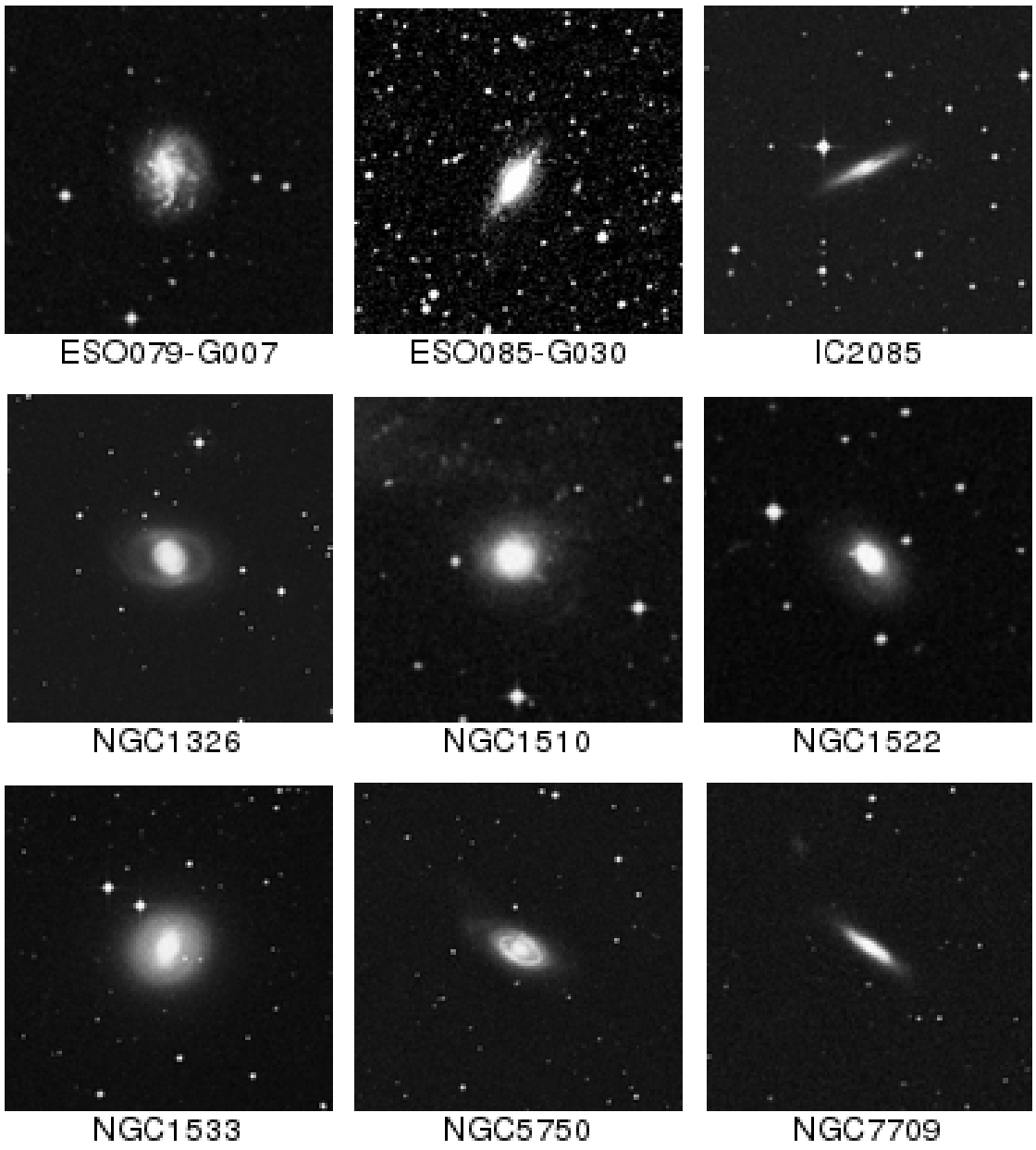

Figure 10.1: The optical images of the galaxies whose population histories are described in this chapter. Note that the data for the galaxy NGC 7371 were not of sufficient quality to present any analysis. This galaxy has not been included in this figure.

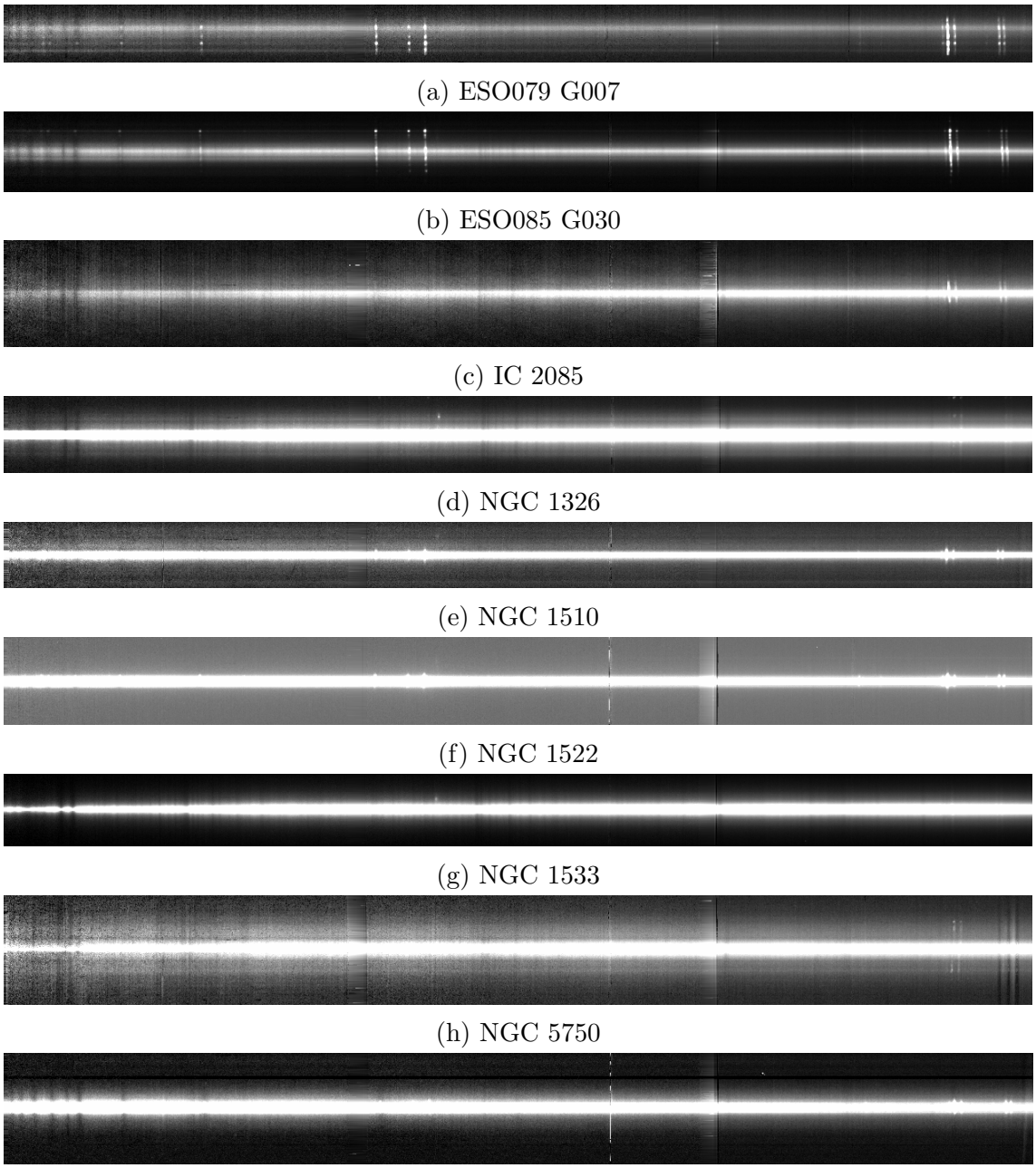

(a) ESO079 G007

(b) ESO085 G030

(c) IC 2085

(d) NGC 1326

(e) NGC 1510

(f) NGC 1522

(g) NGC 1533

(h) NGC 5750

(i) NGC 7709

Figure 10.2: The final 2-d reduced spectra for the galaxies described in this chapter. The vertical direction is the direction of the slit while the horizontal direction is that of the wavelength. Each row here is a spectrum corresponding to a particular position on the long slit.

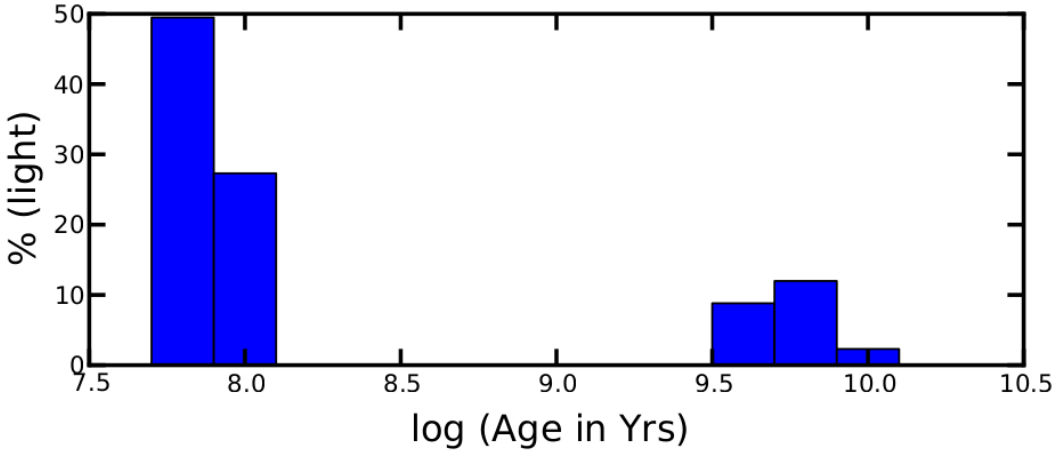

(a) ESO079 G007

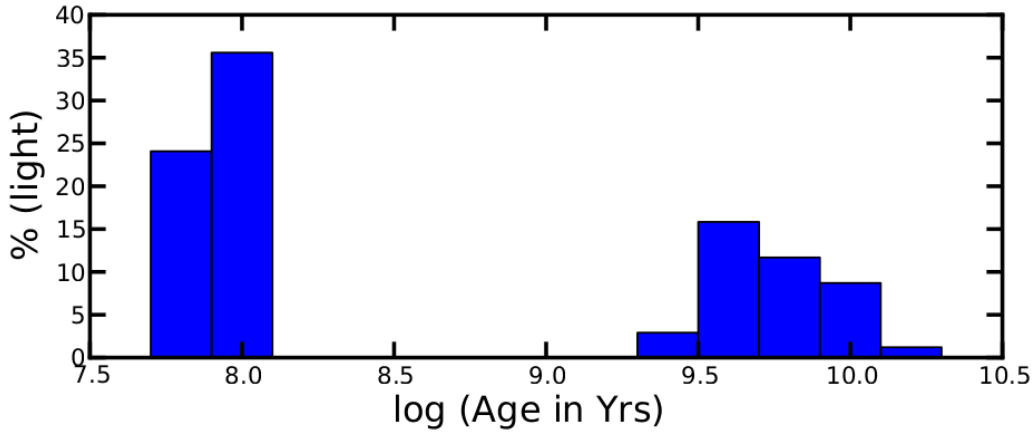

(b) ESO085 G030

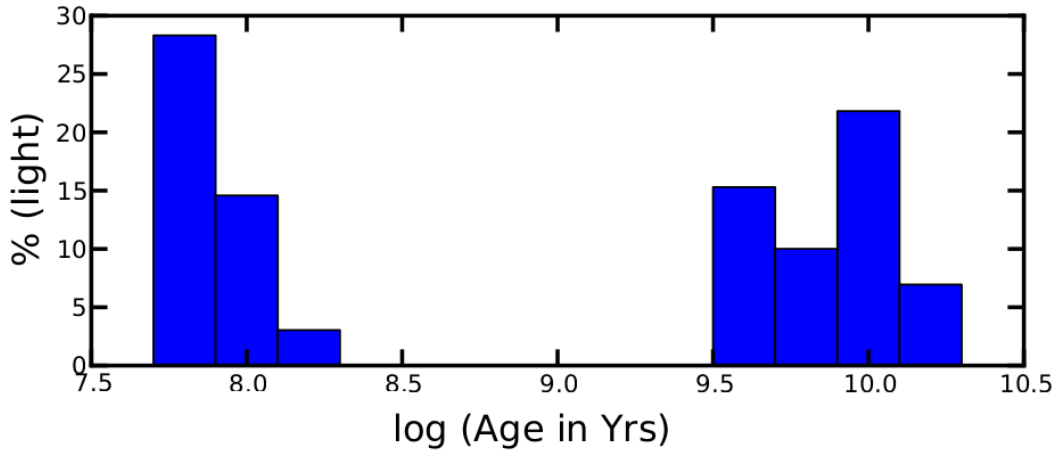

(c) IC 2085

Figure 10.3: Formation histories for the galaxies discussed in this chapter.

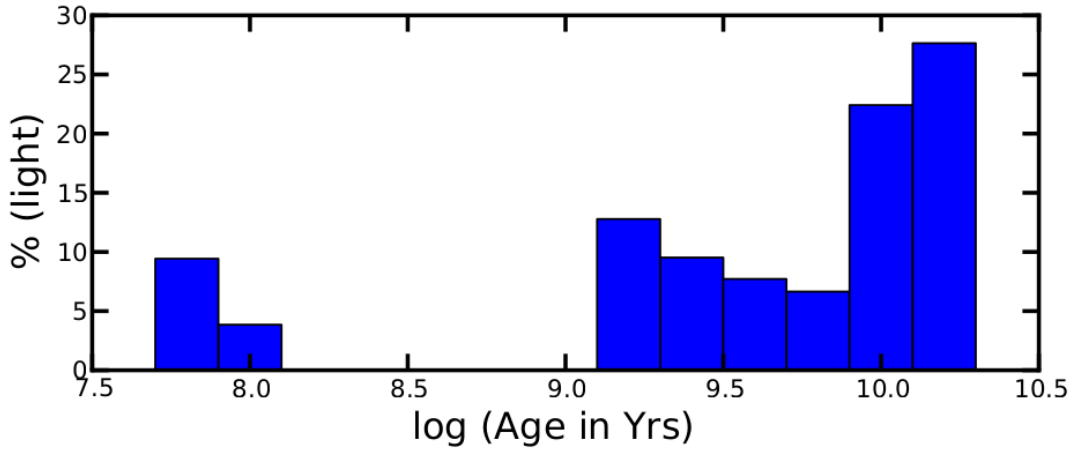

(a) NGC 1326

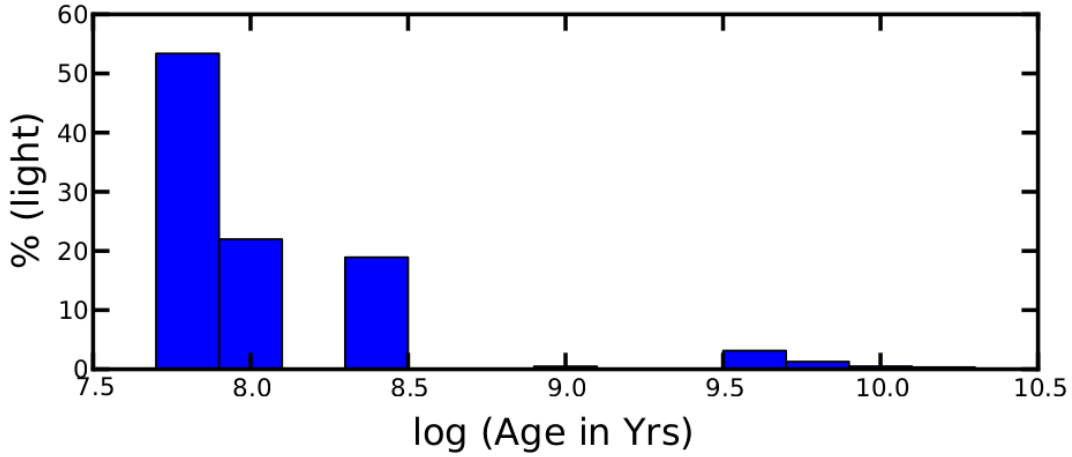

(b) NGC 1510

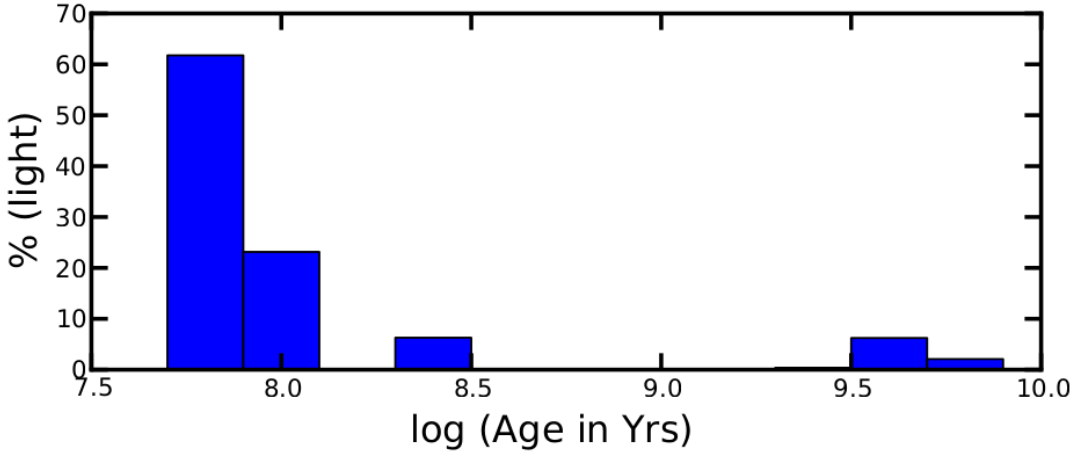

(c) NGC 1522

Figure 10.4: Formation histories for the galaxies discussed in this chapter.

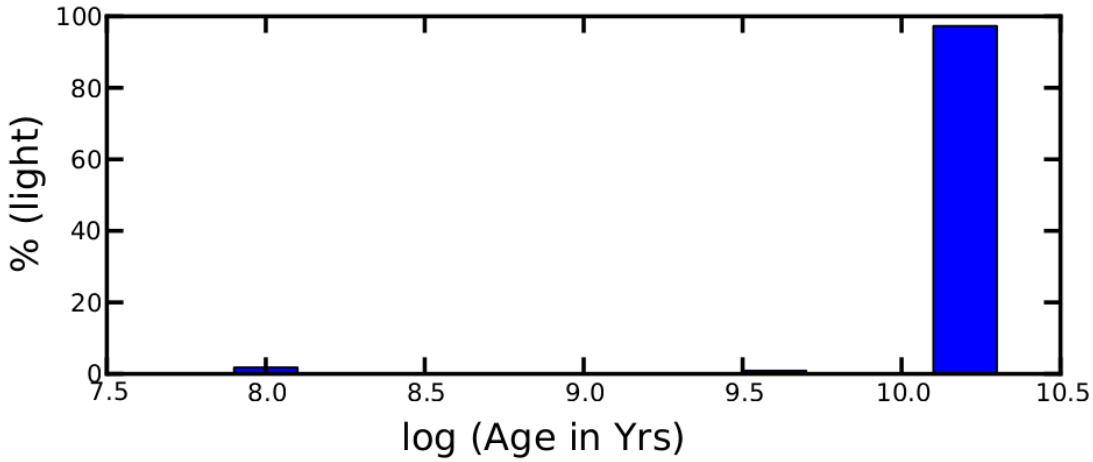

(a) NGC 1533

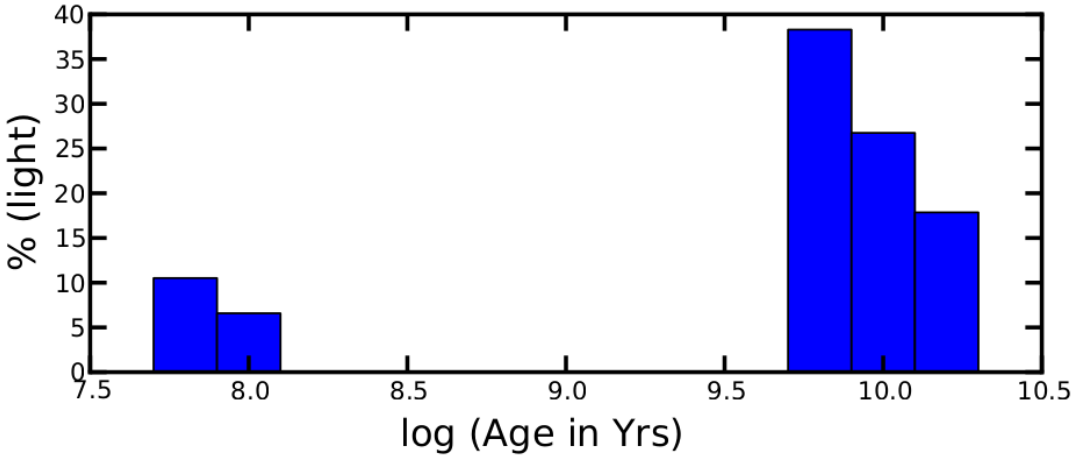

(b) NGC 5750

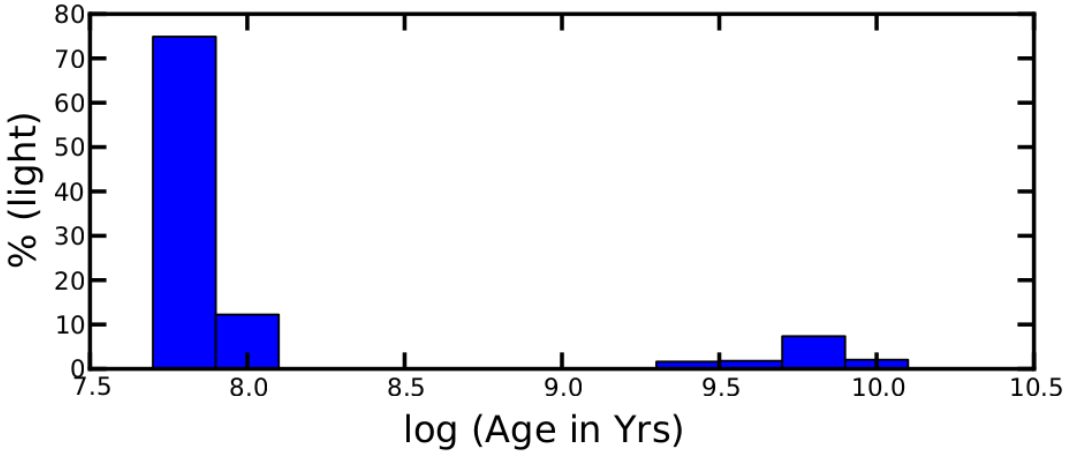

(c) NGC 7709

Figure 10.5: Formation histories for the galaxies discussed in this chapter.

structure formation, we know that such a young stellar population is unlikely to have formed through major mergers as those become less common at smaller redshifts. Please note that the pipeline described in the previous chapter generates as many formation history plots for a galaxy as the number of apertures extracted from a 2-d spectrum. If, for example, for a given galaxy, 20 apertures are marked and hence 20 spectra are extracted - for each spectrum, one formation history diagram can be plotted using the Starlight output for it. However, for the current study, we are showing only the formation history diagrams for the central region of the galaxy.

The parameters derived using 2-d image decomposition as well as the Hubble stage T, for the current sample of galaxies, have already been presented in the Table 5.1 presented at the end of Chapter 5. To illustrate the important spectral features produced by early-type and late-type galaxies and the differences in their spectra, we show in Figure 10.6 two spectra, one for an early-type galaxy and the other for a late-type galaxy with ongoing star formation. Familiarity with these spectra will aid the reader in understanding the following sections.

10.2.1 ESO079-007

According to the RC3, this galaxy is classified as an S0 galaxy with a Hubble stage $T = -2.0 \pm 0.8$. On NED, the galaxy is described as being peculiar owing to some non-axisymmetric structure atypical of S0 galaxies. There are no clear spiral arms discernable from the image taken by the Palomar 48-inch telescope shown in Figure 10.1. The reduced 2-d spectrum obtained from SALT for this galaxy reveals several strong emission lines (Figure 10.2a), likely to be hot gas emission from HII regions spread across the galaxy. The truly interesting feature of this galaxy is the asymmetry in the distribution of the emission lines about the continuum. To explain this asymmetry, a narrow portion of the spectrum near the H_α, NII and SII emission lines is shown in Figure 10.7. The stellar continuum has been marked in this region along with the emission lines. It can be clearly seen that there are more emission line regions below the continuum than there are above the continuum. This in turn implies an asymmetric star formation i.e. strong formation on one side of the galaxy as opposed to the other side of the galaxy.

The program used for extracting the rotation curve of a galaxy sums the spatial profile along the wavelength axis and then uses a centroiding algorithm to determine the spatial centre of the galaxy. When extracting the rotation curve of this galaxy, the centroiding algorithm always inferred a position away from the continuum due to the overall strength of the emission flux relative to the stellar continuum. To get a non-biased estimate of the centroid, a part of the spectrum was obtained free from emission lines and the centroiding algorithm was rerun. The central spectrum, the

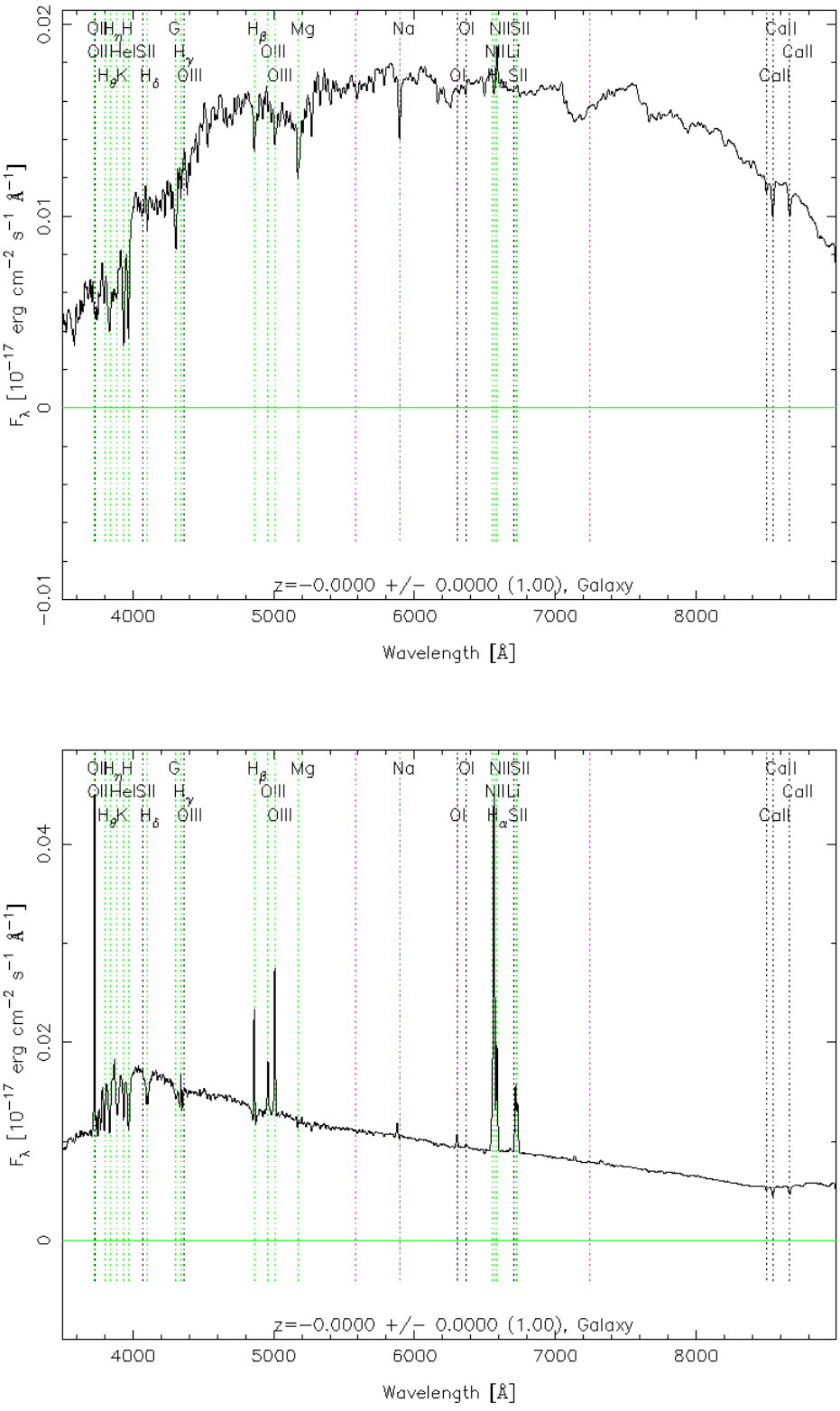

Figure 10.6: A template spectrum for an early-type galaxy (top panel) containing an old stellar population and a late-type galaxy (bottom panel) which is dominated by a younger stellar population and exhibits ongoing star formation. (Image Credit: SDSS)

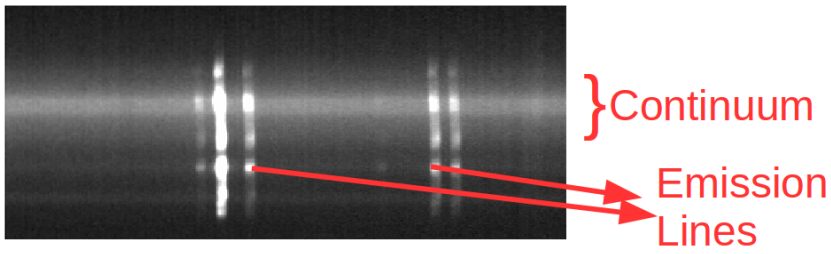

Figure 10.7: A narrow region of the 2-d spectrum of the galaxy ESO079-003, near the H_α, NII and SII emissions. The continuum has been marked along with the emission lines. As can be seen, the distribution of the emission lines about the continuum is asymmetric.

best-fit Starlight model and the residue obtained from subtracting the model from the observed spectrum are all shown in Figure 10.8.

The galaxy is a nearly face-on galaxy, thus the rotation curve obtained was fitted using a low order polynomial in order to extract the apertures along the slit. As can be seen in the spectrum, the absorption features of this galaxy are hard to model, so the H_α emission based rotation curve was used. Using the fits obtained for each aperture, an age gradient i.e. the variation of age as a function of distance from the centre, was derived. In the case of this galaxy, variation in light weighted average age from 8.1 to 8.4 Gyr was found. Such a small variation at this age range cannot be easily captured by stellar synthesis models. The difference such a small step in age has, on the overall shape of the optical spectrum, is small relative to the typical noise levels in the spectra. Therefore, it is better to rely on an alternate quantity which is more robust. In this study, we have defined the fraction of stars older than 10^9 yr, computed using Starlight and mapped its variation as a function of distance from the centre. Note that this fraction is derived using the light population vector output by Starlight which means the fraction here is terms of flux. As a binned statistic, this quantity is more reliable and is more easy to interpret from the point of view of understanding the star formation history. The variation in this quantity is captured in the lower left part of Figure 10.8.

A similar plot (not shown here), for intermediate age stars (between 10^8 and 10^9 yr) indicates that no such stars are found in this galaxy along the major axis, while a plot for young stars ($< 10^8$ yr) shows an opposite trend. The fraction of older stars increases towards the centre while that of younger stars decreases. If this galaxy indeed hosts a pseudobulge and if it is true that the pseudobulges form after disks through instabilities, one does not expect a rise in the fraction of older stellar population in the galaxy towards the centre, a region dominated by the bulge. One possible explanation could be that this is a reflection of the distribution of stellar population in the disk itself rather than that of a bulge. The bulge contributes

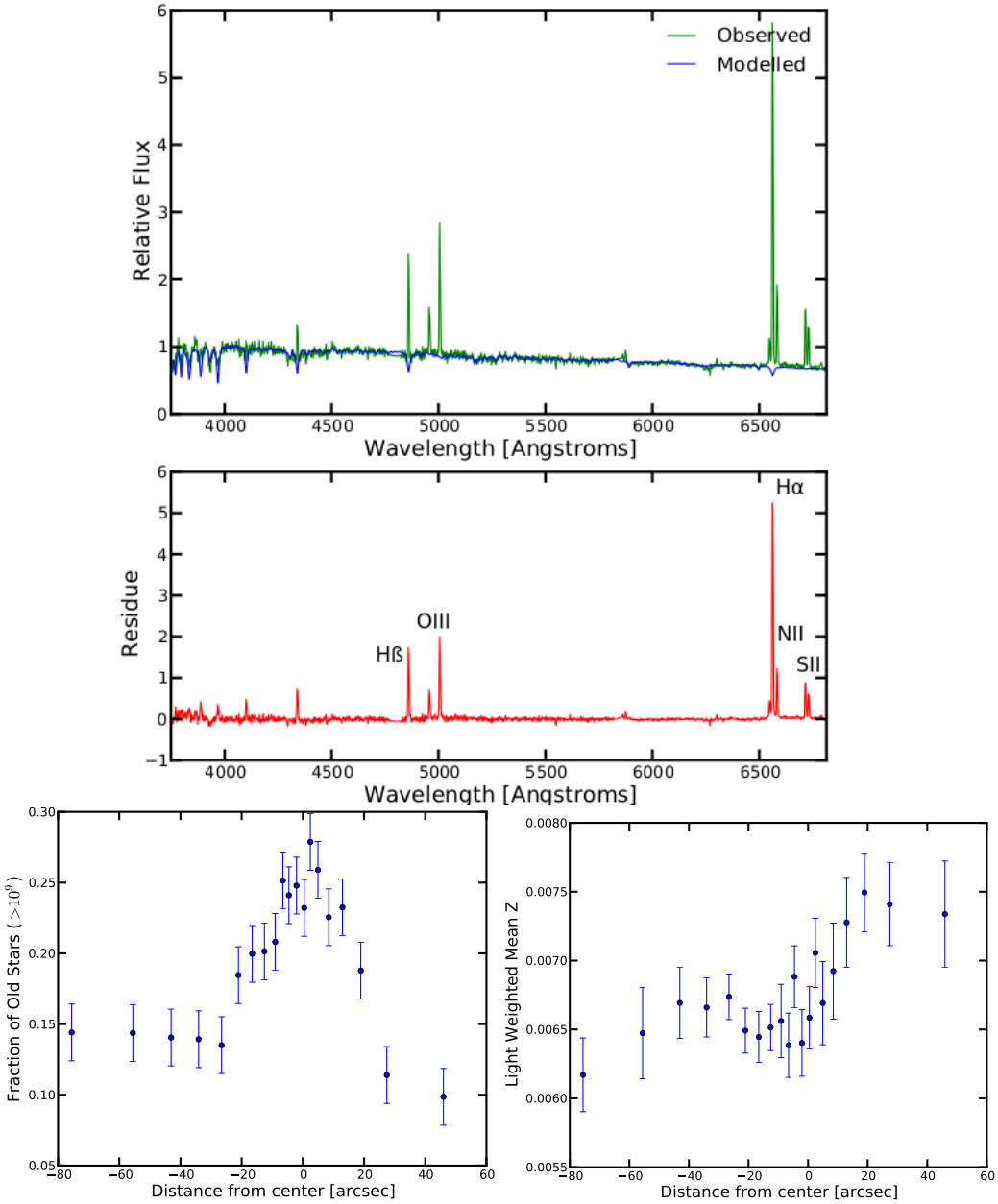

Figure 10.8: The observed spectrum from the centre of the galaxy ESO079-G007, along with the best-fit Starlight model are shown in the first panel while the second panel shows the residual. Important emission lines have been marked in the residual spectrum in this figure. The lower left and lower right plots are age and metallicity gradients respectively.

only $\sim 4\%$ to the total flux in 3.6 microns. Thus it is reasonable to assume that this observed gradient is more a reflection of the disk population rather than the bulge population. A caveat with this argument is the assumption that the B/T ratio determined at 3.6 microns can be used to make comments on the optical spectra. But the shallow rise in the age at the centre seems consistent with most disk formation scenarios which support an inside-out formation i.e. stars at the centre form first followed by formation outside.

The metallicity gradient is shown in the lower right plot of Figure 10.8. Two interesting features stand out. One is the overall asymmetry in the metallicity trend around the galaxy centre. This seems to reflect the overall asymmetry of the distribution of emission regions in the 2d spectra. The emission line regions in some way are affecting the metallicity gradients though the the exact mechanism is not known. The second feature of this plot is the sub-solar range of values of metallicity.

Overall, this object is quite interesting, exhibiting strong star formation, lack of a conspicious bulge, an asymmetric distribution of emission lines and an unconventional morphology. Further investigations will be needed to understand more about this object.

10.2.2 ESO085-030

ESO085-030 is the second galaxy in this sample and exhibits spectral features similar to that of ESO079-007 except for the distribution of emission lines being less asymmetric. Presence of strong emission regions with no easily discernable spiral arms has resulted in this galaxy being classified as a peculiar S0 with a Hubble stage $T = -1 \pm 1.7$ (note the large error bar indicating high ambiguity as to the nature of the galaxy). The spectrum, model and residue for the central region of the galaxy are shown in Figure 10.9. The spectrum reveals a dominant population of young and hot stars as can be judged by the 4000 angstrom break.

On studying the behavior of the fraction of old stars, as done for the previous galaxy, one finds that about 40% of the total light at the centre comes from old stars - this fraction falls to 15% as one moves outward. This can be seen in Figure 10.9. Also shown in this figure is the metallicity gradient. Note that this gradient is similar to the age gradient and thus rules out the effects of age-metallicity degeneracy. This is a common problem with fitting galaxy spectra - a similar spectrum can be obtained for two cases: 1) a younger population but with high metallicity, and 2) an older population with low metallicity. If we find opposite trends of age and metallicity, an alarm flag can be raised that the numbers obtained are unreliable and likely an effect of the degeneracy between these parameters. However, in this case, we find both quantities exhibiting a similar trend and thus it is safe to assume that this

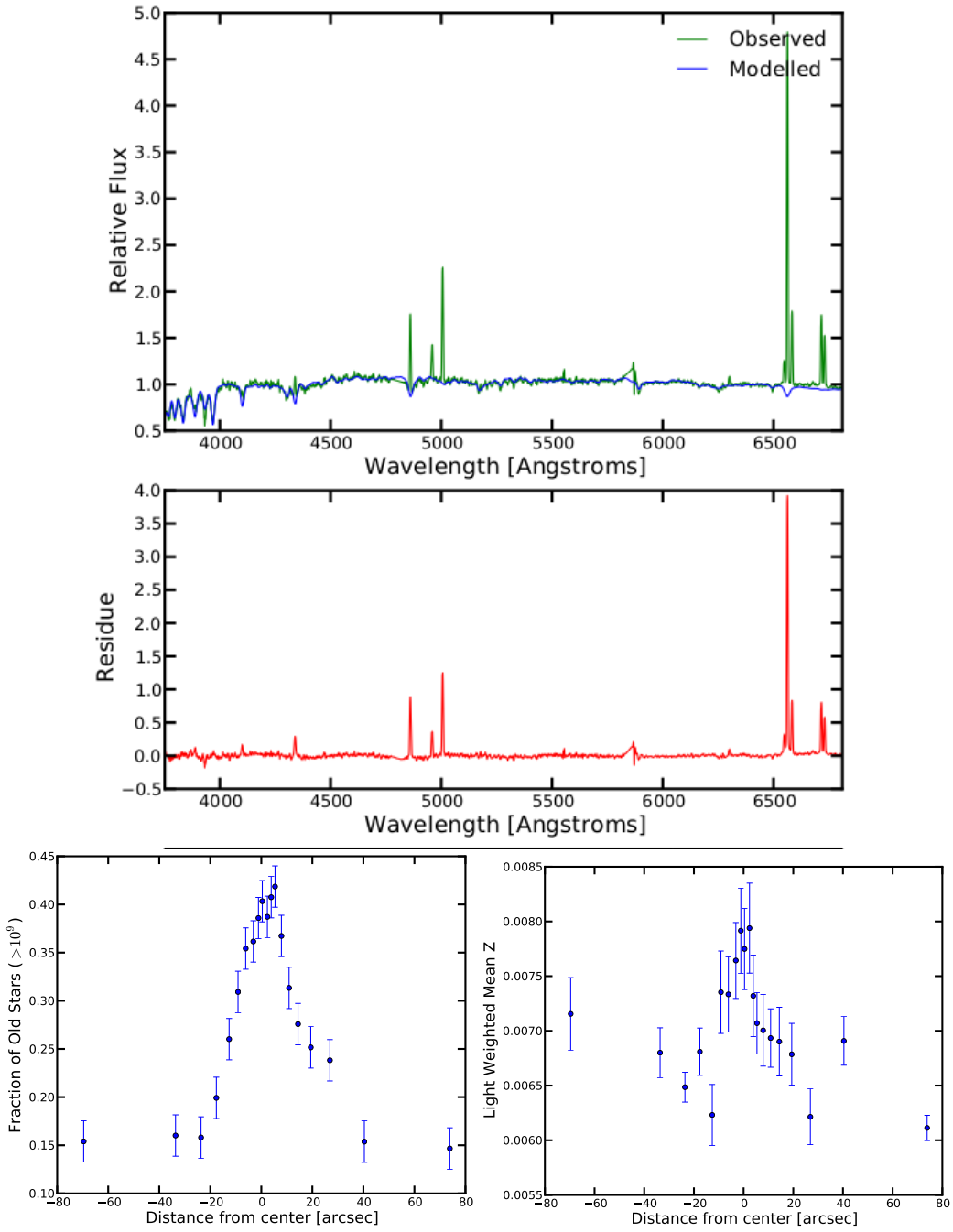

Figure 10.9: The observed spectrum from the centre of the galaxy ESO085-G030, along with the best-fit Starlight model are shown in the first panel while the second panel shows the residual. The lower left and lower right plots are age and metallicity gradients respectively.

degeneracy is not playing a role here.

The B/T ratio of this galaxy is quite high with almost 60% of the total light accounted by the bulge. Thus unlike in the previous case where one could argue that the trends were dominated by a disk, this is clearly a reflection of the underlying pseudobulge. The pseudobulge shows signs of an inside-out formation with stars towards the centre having an older age. This can perhaps be said to be consistent with gas infall. However, it is difficult to say how much of this gradient is due to the bulge and how much due to the disk. Further, to explain the higher B/T ratios in pseudobulges, we had argued that gas stripping could fade the disk. However, there is clear evidence for high star formation given the strength of the H_α emission line. Independent of whether this star formation is happening in the disk or the pseudobulge, it hints at an abundant supply of gas. These two arguments seem contradictory. One may resolve them by arguing that the bulge has acquired mass through a minor merger involving a gas rich dwarf. This can explain both the induced star formation as well as the increased B/T ratio. According to Eliche-Moral et al. (2012), a minor merger can increase B/T ratios without destroying the bulge-disk coupling typical of pseudobulges.

10.2.3 NGC 1533

NGC 1533 is a barred lenticular galaxy with a smooth and featureless morphology, atypical of a pseudobulge hosting S0. The spectrum too is indicative of an old and coeval stellar population. However, the bulge's effective radius and Sérsic index have led to its classification as a pseudobulge. The typical age of the stars is $\sim 10^{10}$ yr as expected, again exhibiting both a metallicity and age gradient showing a rise in the fraction of older stars towards the centre with more than 95% of the stellar light contribution coming from them. The bulge effective radius is about 16 arcsec and thus in these plots, we are not even probing the region dominated by the disk. It is thus not possible to compare the disk and bulge stellar populations in this case. The metallicity is more or less the same as solar metallicity which is expected given the other characteristics of this galaxy.

Overall, the results for this galaxy come as a clear surprise. Despite having selected pseudobulges using a highly conservative criterion, it is clear that this is not a pseudobulge host galaxy and shows all the tell tale signs of being a classical bulge formed at a very early epoch. This misclassification is unlikely to be due to the lack of accounting of a bar since the bar light has been taken into account when modelling the surface brightness profile. Other possible reasons could be the presence of a small unresolved pseudobulge within the classical bulge. Erwin et al. (2015) and others have studied such cases, known as composite bulges. However,

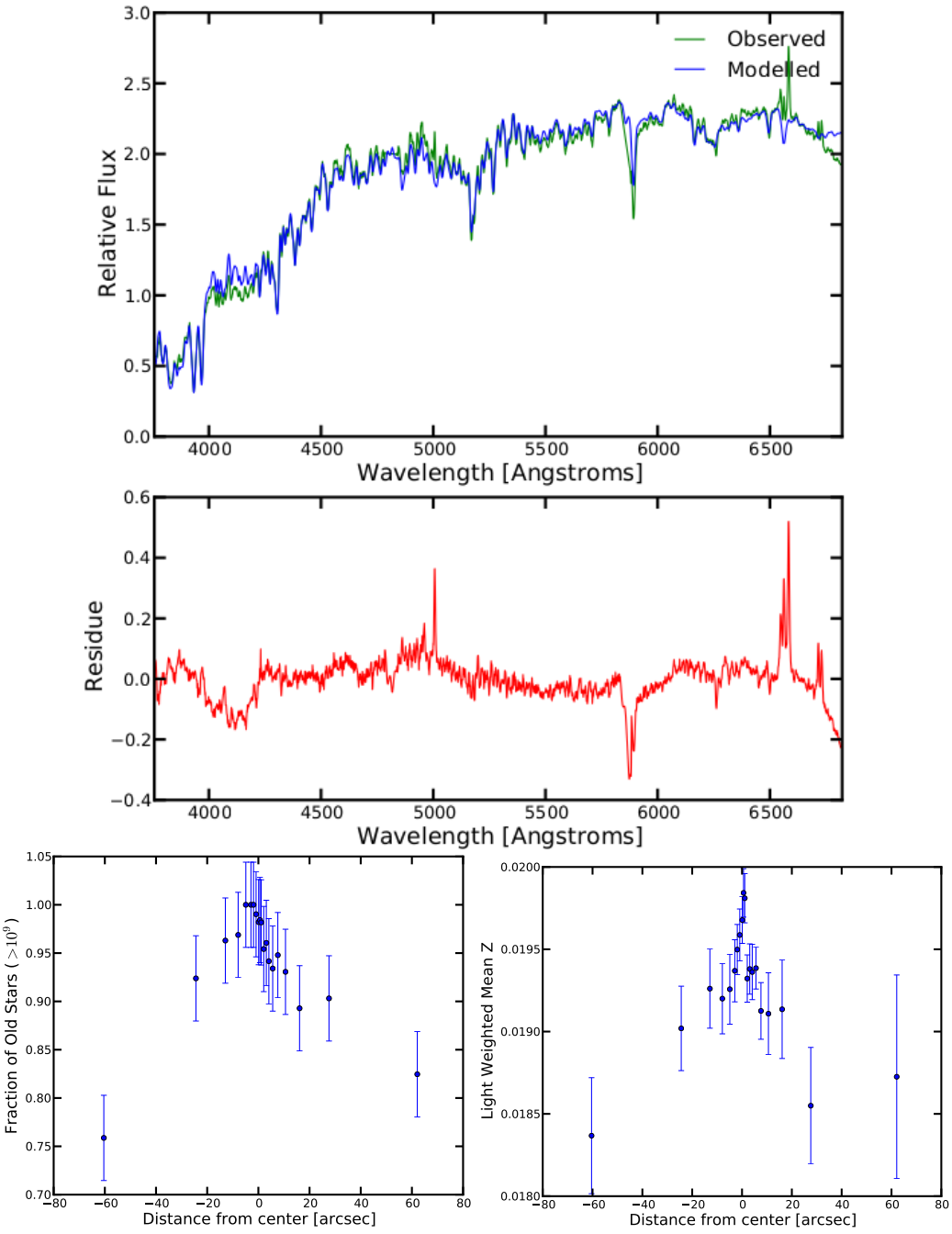

Figure 10.10: The observed spectrum from the centre of the galaxy NGC 1533, along with the best-fit Starlight model are shown in the first panel while the second panel shows the residual. The lower left and lower right plots are age and metallicity gradients respectively.

since the sample is small in size, statistical comments on the behavior of such systems cannot be made. Concerning the disk of this galaxy, the spectrum does not contain an adequate signal from it to comment on its contributions.

10.2.4 IC 2085

IC 2085 is a highly inclined S0 galaxy with Hubble stage $T = -2.0 \pm 0.8$ with no prior spectral studies carried out on it. The overall quality of the spectrum as can be judged from the 2-d image shown in Figure 10.2c, is not too high. But the SNR is sufficient for the intended analysis as can be seen from Figure 10.11. Its central spectrum shows a unique feature. The consecutive absorption features below 4000 Angstrom indicate a young population while the H_α, NII and SII emission lines indicate some level of star formation and hot gas. Along with these signs, seen in earlier galaxies, one also sees a substantial break at 4000 Angstrom, a feature of an older and evolved population.

Figure 10.11 captures the age and metallicity gradients. However, what is seen does not appear to make physical sense. The age on one side of the centre is higher than the other side, a trend not found in any of the previous galaxies. However, whether the trend is real, is open to debate because the metallicity gradient shows an opposite trend. It is well known that age and metallicity are degenerate quantities. In this case, it seems like the overall variation in the age captured by these plots is being produced as a result of degeneracy rather than being a real trend. What is perhaps the only reliable conclusion, which one expects from a simple visual inspection of the spectrum as shown in Figure 10.11, is that the population is an almost equal mixture of old and young stars.

In Figure 10.3c we plot the percentage of light contribution coming from populations of various ages. One can clearly see a bimodal distribution, a population of stars which is very old ($\sim 10^{9.5}$ yr) along with a younger population of stars ($\sim 10^7$ yr). A similar trend is seen in other galaxies as well though it is significantly pronounced in this case. Thus in the formation history of this galaxy, there seem to be two distinct epochs of star assembly, one at an early epoch and another at more recent times. It should be noted that this figure appears to indicate the youngest stellar population has age $\sim 10^7$ yr. This age obtained however could be a reflection of the fact that this is the youngest population of stars considered in the base used for fitting the spectrum. It might be worthwhile to try and use a base especially constructed to have more representative spectra of even younger SSPs. The current base was selected keeping in mind the expected range of ages for S0 galaxies. But independent of the base used, it is clear that this galaxy's formation history is not a simple one.

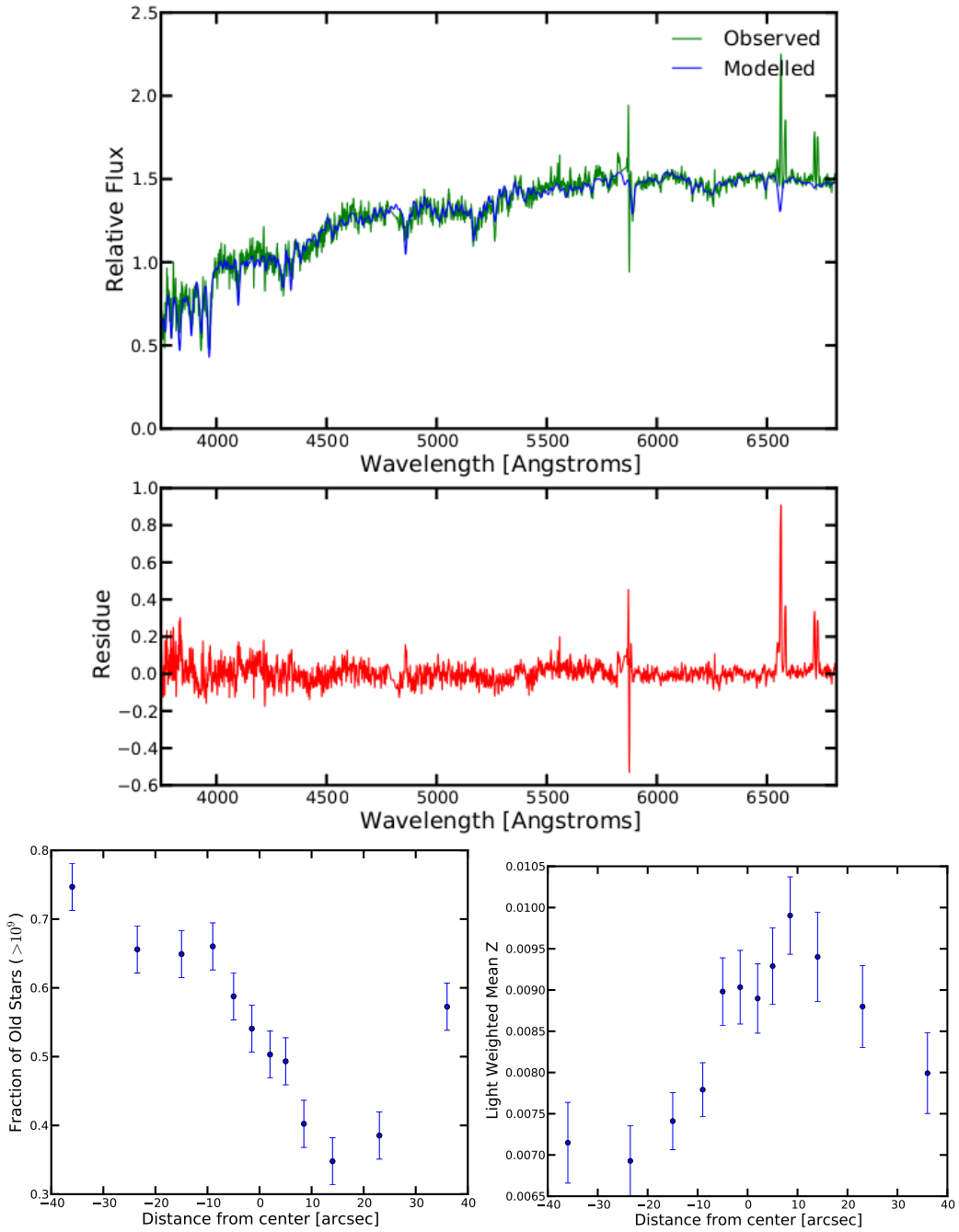

Figure 10.11: The observed spectrum from the centre of the galaxy IC 2085, along with the best-fit Starlight model are shown in the first panel while the second panel shows the residual. The lower left and lower right plots are age and metallicity gradients respectively.

The star formation in the central region of this galaxy seems consistent with an induced gas infall due to disk instabilities. However, to explain the presence of very old stars, not typical of a disk, one might imagine that there was an already formed classical bulge in place before the second episode of star formation took place. In other words, we could be looking at a composite bulge system - an inner disk growing through gas infall within an already existing classical bulge.

10.2.5 NGC 1522

NGC 1522 is classified as a peculiar S0 with $T = -2.3 \pm 0.7$. The spectrum of this galaxy (Figure 10.12) hints at a stellar population dominated by very young stars population with little to no sign of older stars. The age and metallicity gradients reveal hardly any consistent trend across the galaxy. Given that 95% of the total light budget comes from very young stars with a very low subsolar metallicity, it is clear this object is indeed special. This galaxy has a well defined bulge contributing $\sim 40\%$ of the total galaxy light but it is clear that the bulge has no signs of being a classical one. The high B/T ratio is also surprising for a galaxy with so many young stars, which has ongoing star formation and is metal poor. It could be that this high B/T is a manifestation of the faded disk. But the level of star formation seems to suggest presence of a lot of gas.

Okamoto (2013) used simulations to suggest an alternative mechanism for forming a pseudobulge hosting galaxy. In these simualations, what is defined as a pseudobulge by us manifests as an inner disk at $z \sim 2$. This inner disk forms at an early epoch but not through secular processes as is envisioned for most pseudobulges but through a series of star bursts possibly caused by minor merger events. In other words, the pseudobulge does not form through a secular process but a dynamical one. If one were to rule out the fading of the disk as an explanation for the high B/T ratio of a pseudobulge host and the unlikeliness of secular evolution building up such a high B/T, this mechanism seems to offer an alternate explanation. It must be remembered however that the B/T ratio used in all these arguments is derived using analysis of 3.6 micron imaging which especially probes the low mass stars while the spectral analysis is being done in the optical where younger and more massive stars dominate.

10.2.6 NGC 1510

NGC 1510 is an S0 galaxy termed as 'peculiar' and has a Hubble stage $T = -2.3 \pm 0.7$. This galaxy is known to be one of a pair of galaxies with the other member being NGC 1512. This system is famous for being a pair of starburst galaxies with a common HI envelope (Meurer et al., 2006). That it is a star burst galaxy requires

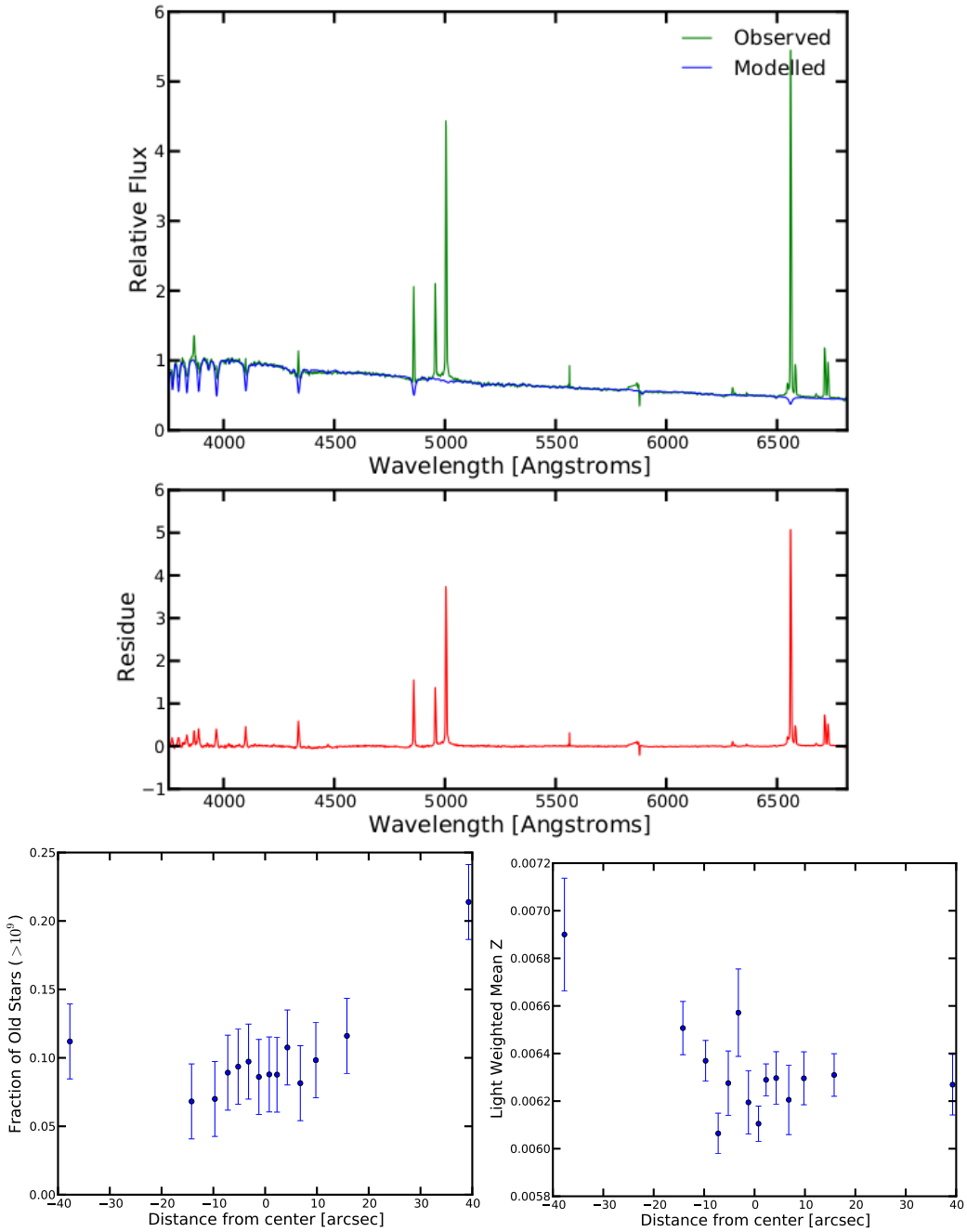

Figure 10.12: The observed spectrum from the centre of the galaxy NGC 1522, along with the best-fit Starlight model are shown in the first panel while the second panel shows the residual. The lower left and lower right plots are age and metallicity gradients respectively.

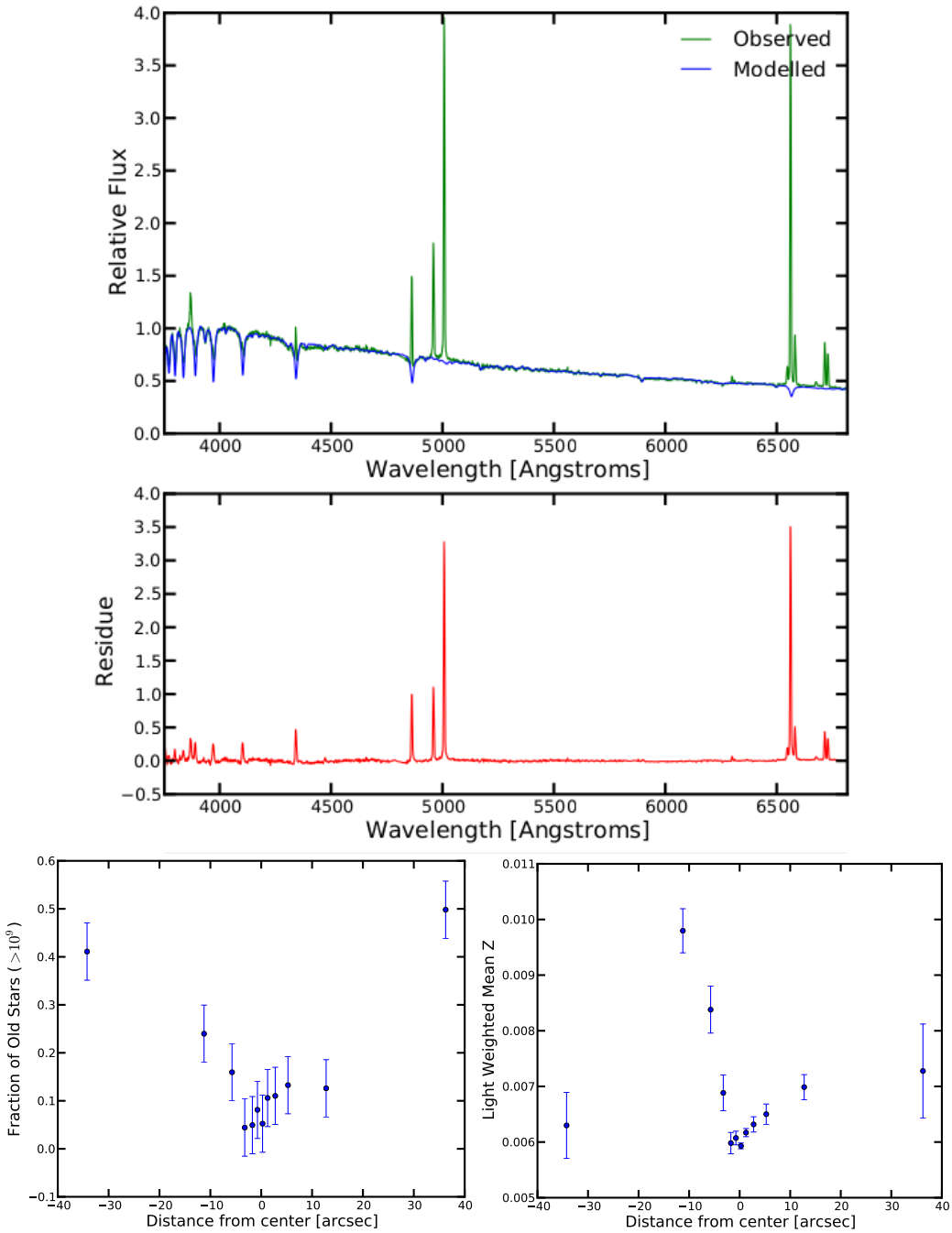

Figure 10.13: The observed spectrum from the centre of the galaxy NGC 1510, along with the best-fit Starlight model are shown in the first panel while the second panel shows the residual. The lower left and lower right plots are age and metallicity gradients respectively.

nothing more than a glimpse of its central spectrum as shown in Figure 10.13. The spectrum shows very strong H_α emission and the light is completely dominated by a young hot population.

The age and metallicity gradient show peculiar features as well with more than 95% of the light coming from young, hot stars. The average age of this population is $\sim 10^8$ yr. There is an asymmetry in the distribution of old stars - the regions dominated by these also being slightly metal rich. This could be explained by the known fact that this galaxy is a part of a pair. Some form of tidal interaction with the neighbor may cause star forming regions dominated by young stars to be distributed non-uniformly in this galaxy. The bulge-disk decomposition of this galaxy using 3.6 micron imaging data reveals a B/T ratio at this wavelength of ~ 0.4.

10.2.7 NGC 1326

NGC 1326 is a barred S0 galaxy which has a ring. It has Hubble stage $T = -1.0 \pm 0.3$. Overall, most of the features of this galaxy resemble those of NGC 1533. Almost 90% of the central flux can be accounted for by an old stellar population with a metallicity only slightly below solar metallicity. It is interesting to note that this is the second galaxy in our sample which despite a stringent criterion for selecting pseudobulges having been applied to it, the bulge clearly appears to be classical. What is also interesting is that both galaxies i.e. NGC 1326 and NGC 1533, are barred. With the usual caveat of over interpreting results for a very small sample, one is led to ask the question whether this criteria somehow fails for barred galaxies. There are several ways to understand this:

- We are fitting the bar using a Sérsic profile. However it is not necessary for all features of a bar to be completely accounted by it. This can lead to systematics in the estimation of bulge parameters leading to their classification as a pseudobulge when photometry based criteria are employed. This seems to be unlikely given studies such as Gadotti (2008); Laurikainen et al. (2005) which demostrate that once a bar has been accounted for, most systematics in the bulge parameters disappear.

- There is some effect that bars have on classical bulges which causes them to stray off the Kormendy relation and also acquire a lower Sérsic index. Again, if this is true, one should be noticing a general trend between barred and unbarred galaxies on the Kormendy relation. This is not the case as studies like Barway et al. (2009), Gadotti (2009) and Laurikainen et al. (2010) clearly show. Even with the sample of S0s described in Chapter 5, this has not been found.

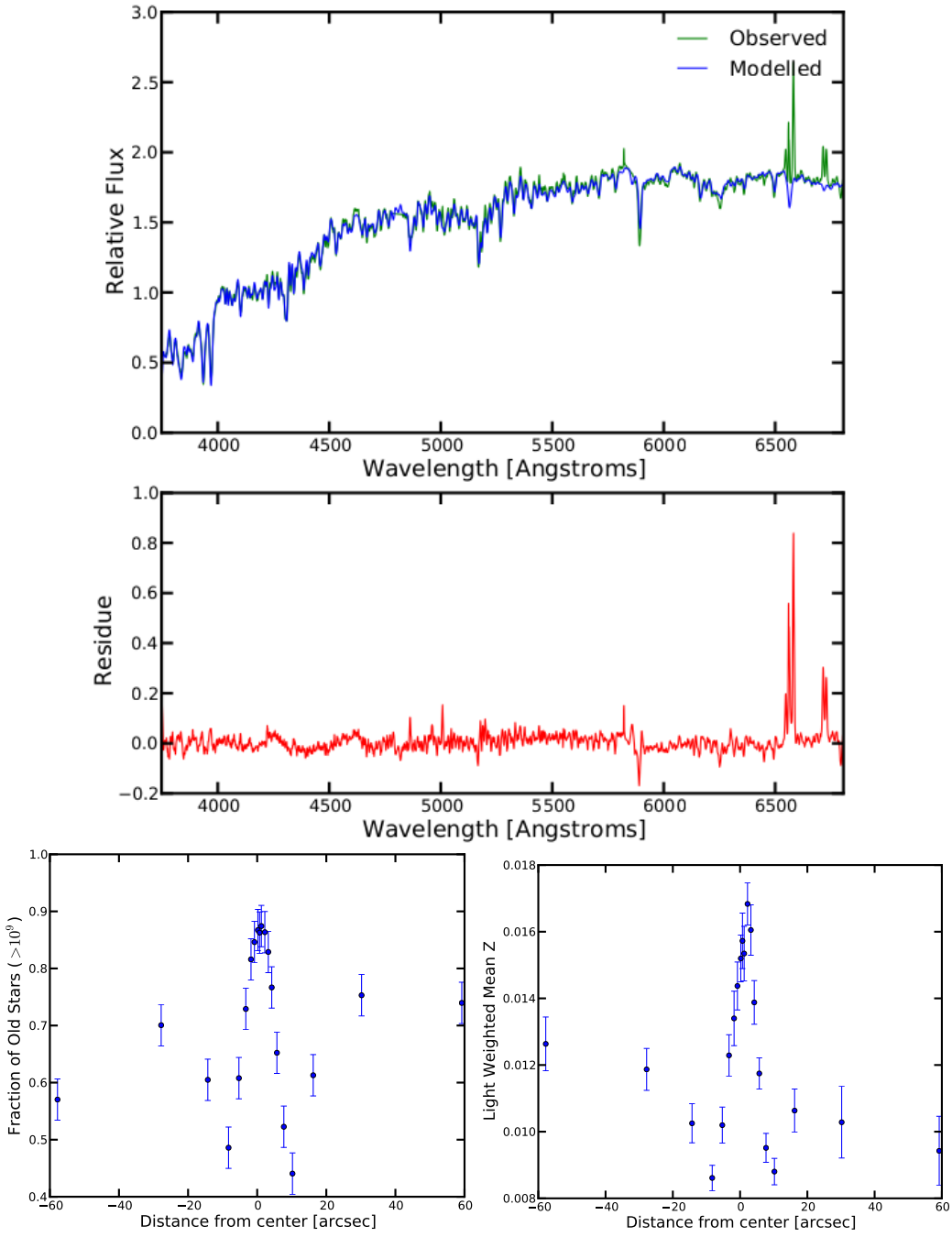

Figure 10.14: The observed spectrum from the centre of the galaxy NGC 1326, along with the best-fit Starlight model are shown in the first panel while the second panel shows the residual. The lower left and lower right plots are age and metallicity gradients respectively.

- Bars lead to the rise of an inner component within an existing classical bulge which when modelled using relatively low resolution imaging such as that of Spitzer IRAC, induces systematics in bulge parameters that lead to their classification as pseudobulges when using photometric criteria.

Please note that all this speculation is subject to the possibility of over-interpreting a sample with a low number of objects.

10.2.8 NGC 7709

NGC 7709 is a highly inclined galaxy classified by NED as a peculiar S0 galaxy with a Hubble stage $T = -2.0 \pm 0.8$. In terms of features, this galaxy resembles NGC 1522: strong ongoing star formation, very little contribution from old stars and a sub-solar metallicity. All conclusions about NGC 1522 should apply more or less to this galaxy as well.

10.2.9 NGC7371

This object is among the 7 targets for which two telescope visits were needed to get the required SNR as described at the beginning of this chapter. Unfortunately, during the second visit there were technical problems leading to a fluid spill over the optics of the telescope, rendering the data useless. The spectrum obtained by combining frames from the first visit did not have enough SNR to be able to even derive a rotation curve. As a result, the object could not be studied.

10.2.10 NGC5750

NGC 5750 is truly an interesting object. Classified as a barred S0/a galaxy with Hubble stage $T = 0.0 \pm 0.3$, it has what appears to be a ring like structure though in *The Carnegie Atlas of Galaxies*, Sandage speculates it to be two very tightly bound spiral structures emenating from the ends of the bar. The spectrum of the galaxy is similar to NGC 1326 and NGC 1533 - dominated by more old stars than young. This can be discerned from both the 2d spectrum shown in Figure 10.2h and the central spectrum shown in Figure 10.16.

The age and metallicity gradient shown in Figure 10.16 lend support to this. About 85% of the light comes from an old stellar population with slightly sub-solar metallicity. This galaxy becomes the third pseudobulge hosting galaxy in this sample to show an unusually high dominance of old stars and is also barred, thus reinforcing some of the speculations offered when discussing NGC 1326.

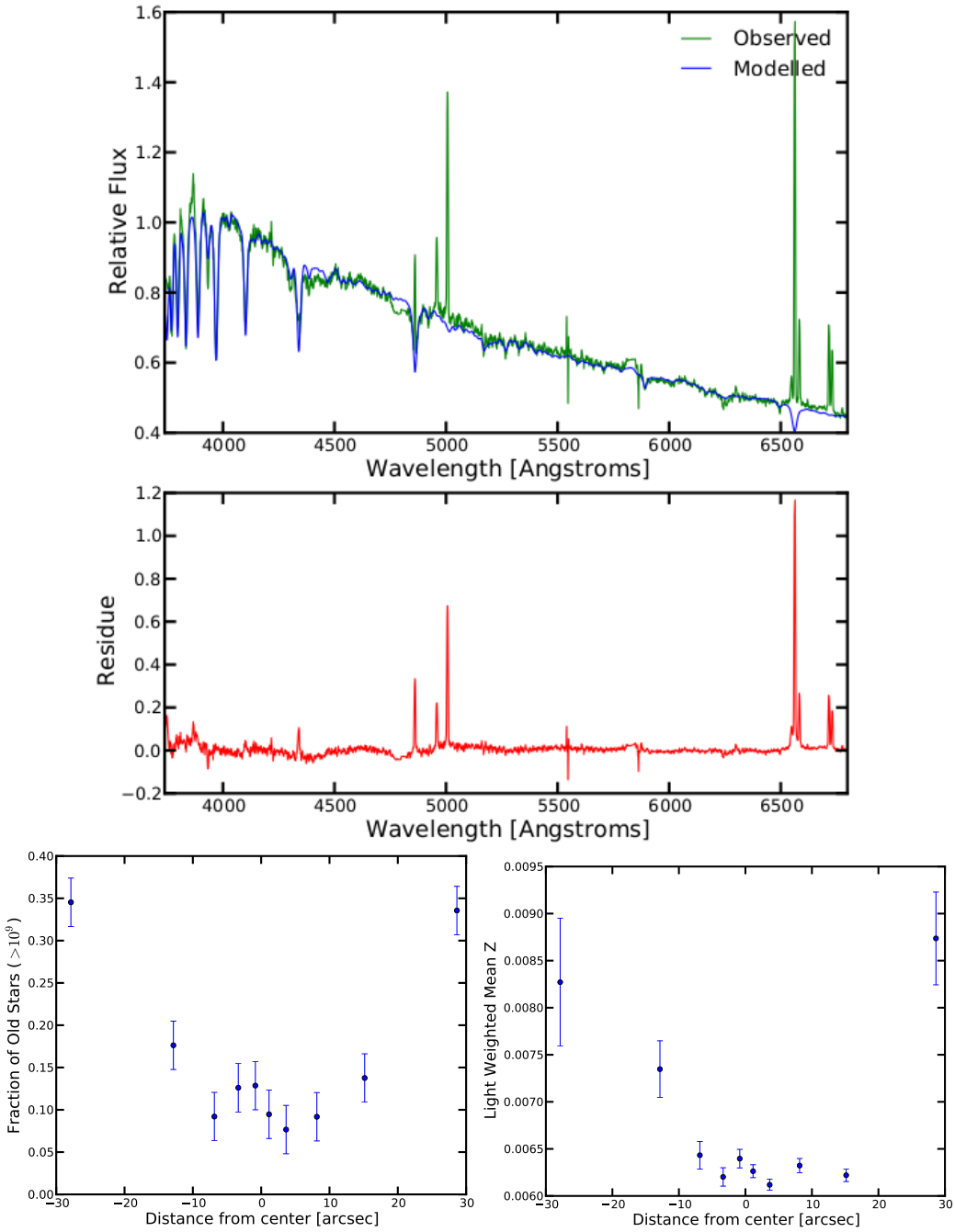

Figure 10.15: The observed spectrum from the centre of the galaxy NGC 7709, along with the best-fit Starlight model are shown in the first panel while the second panel shows the residual. The lower left and lower right plots are age and metallicity gradients respectively.

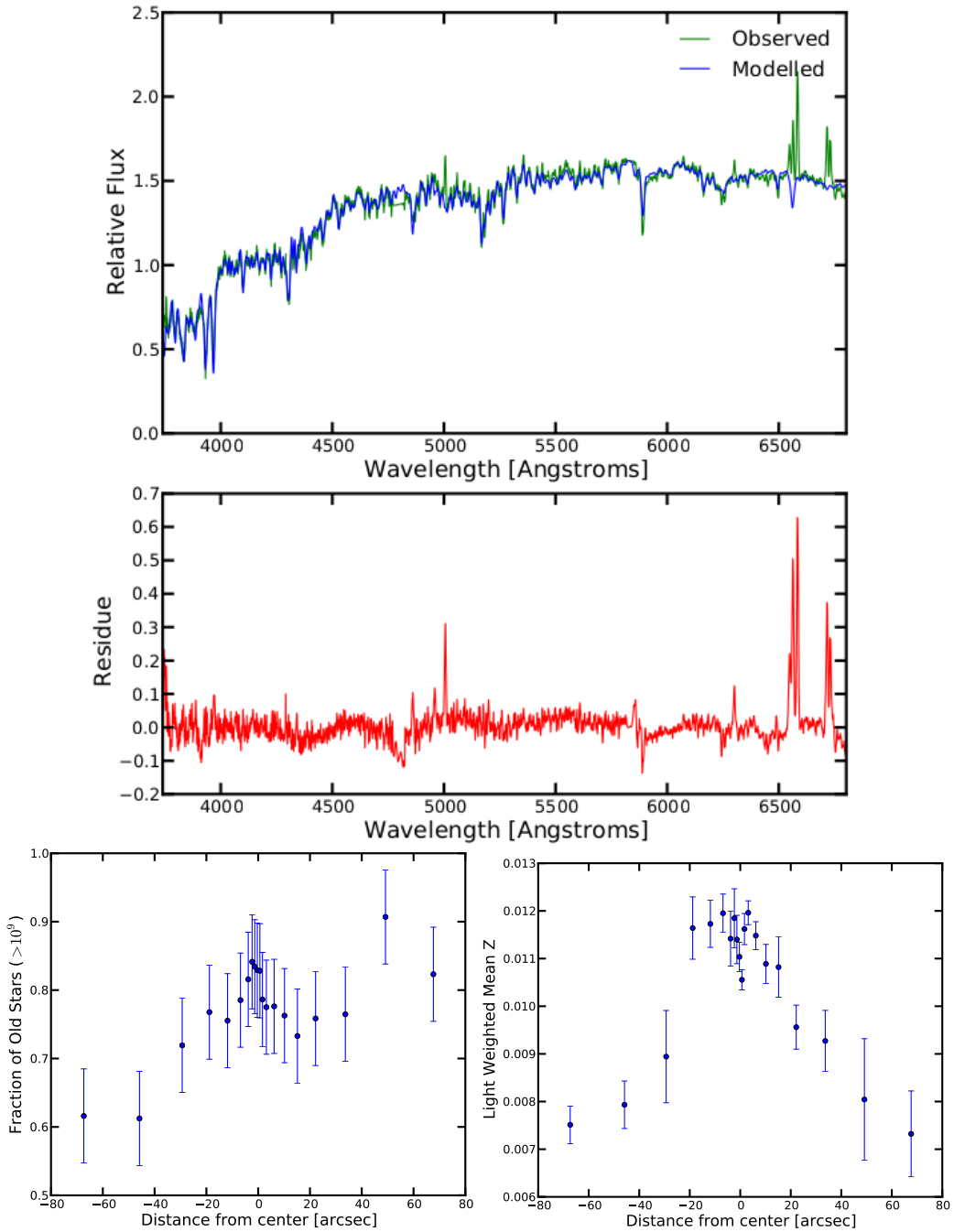

Figure 10.16: The observed spectrum from the centre of the galaxy NGC 5750, along with the best-fit Starlight model are shown in the first panel while the second panel shows the residual. The lower left and lower right plots are age and metallicity gradients respectively.

10.3 Conclusions

The previous section discussed the properties of each object based on their SALT spectra, the best-fit models found by Starlight and the age-metallicity gradients. Recall that all these objects have been classified as pseudobulge hosting galaxies, based on their photometric properties derived using 3.6 micron Spitzer IRAC imaging data.

Of the 10 galaxies considered, 6 show signs of very recent star / ongoing star formation. This is consistent with the expectation from pseudobulge hosting galaxies (Refer to Chapters 1 and 6 for more details on bulge dichotomy and properties of bulges). While the presence of a significant fraction of a young population of stars in these galaxies is consistent with these galaxies being pseudobulge hosts, it is not consistent with their being S0 galaxies. By this we mean that traditionally we do not expect S0 galaxies to exhibit ongoing star formation of the nature found in these galaxies. This is because S0 galaxies are either thought of as end products of (major) mergers likely to contain an old coeval population of stars like ellipticals, or are thought of as transformed spirals. For spirals to be progenitors of S0 galaxies, we often invoke the mechanism of gas stripping in order to explain the fading of the spirals arms of the progenitors. But if this is true, how can gas poor galaxies exhibit such activities of recent star formation, as made evident by the presence of intense H_α and other emission lines?

One possible way to circumvent this problem is to invoke minor mergers. A gas poor S0 with its lack of gas caused by it having undergone gas stripping, accretes a neighbouring dwarf which is gas rich. This gas rich satellite replenishes the gas supply in the S0 allowing star formation to be seen in these galaxies. Another possible explanation, one that seems more likely to the author personally, is that pseudobulge hosting S0s do not have a relationship with spirals at all. They are not transformed spirals through gas stripping and hence the presence of a very young population along with ongoing star formation is not a problem at all. However, as we have seen in Chapters 6 and 7, these pseudobulge hosting S0s have on average a lower scale length than their spiral counterparts and classical bulge hosting S0s. Earlier, this lower scale length was thought to be due to the fading of the disk, but if we imagine a scenario where these S0s formed without going through a spiral phase, we are left with an unexplained property for these objects.

Three objects were found which showed tell tale signs of being a classical bulge, formed at a very early epoch. However, the interesting commonality between all these objects is the presence of a bar. While lacking statistical significance, one can imagine these objects getting classified as pseudobulges as having much to do with the presence of a bar. An interesting speculation is that the classical bulges of

these galaxies host an inner pseudobulge grown as a result of the bar. The spatial resolution in SALT data is unlikely to allow one to investigate this possibility using spectra while a similar problem with Spitzer imaging does not allow investigating this using image analysis. It might be worthwhile to obtain spectroscopic or imaging data at higher resolutions to investigate these objects further. At the time of writing this thesis, the preparation of a manuscript describing these results has begun.

This chapter presents *first* results for this sample of objects. However, there are many more methods by which the spectra can be analyzed to allow one to study and explore further. We conclude this chapter with a list of further analyses that may be carried out using these data.

- Use of Lick indices: These are ratios of various emission and absorption lines which can be used as proxies for age and metallicity of an object. This method offers an independent way of verifying the trends revealed using Starlight. Programs such as *Lector* allow for the measurement of such indices. However, the measurement of some of these indices requires the emission part of the spectrum to be removed first. Tools are being developed to automate this process for all apertures along a galaxy and map the variation of these quantities along the slit.

- Usage of alternate bases: One of the caveats pointed out in the previous section was regarding the lower limit of the age of the stars in the galaxy. In Figure 10.3c, for example, we see a large fraction of stars with an age around $\sim 10^7$ yr. This does not rule of the presence of a younger population since the base itself has this lower limit of age. It might therefore be worthwhile to redo the analysis using a base which has a much lower age cut-off. Use of alternate bases will also allow us to unravel the dependence of the results of the choice of the base, if any.

- Accurate kinematics: In principle, Starlight will provide the value of velocity dispersion for a given spectrum. However, the value is systematically affected by the instrumental resolution, which may vary across wavelengths. This is one of the reasons why detailed kinematic analysis of these galaxies was not presented in the current study. If detailed kinematics can be obtained, the ratio of rotation velocity to dispersion velocity could be determined along the axis to study the overall nature of the dynamics of these objects. Even without the information about velocity dispersion, the rotation curve itself can be fitted to infer properties of dark matter distribution, for example.

- Spectral decomposition: There have been attempts in recent times to decompose a spectrum into bulge and disk components. It is worthwhile to

investigate if such a study is feasible with the available SALT data.

- Comparison with other objects: As explained in Chapter 9, data for a total of 50 objects have been obtained through SALT through various proposals. The complete analysis of the data is a part of a long term study which will eventually allow comparison of pseudobulge hosting S0s with pseudobulge hosting spirals and classical bulge hosting S0s.

Chapter 11

Summary and Future Directions

Real knowledge is to know the extent of one's ignorance.
- Confucius

11.1 Summary of the Thesis

The general goal of the study described in this thesis is to study the class of galaxies known as S0s or lenticulars. As already described, S0s are a very important piece of the puzzle concerning the formation and evolution of galaxies. While typically classified as a single class in the earlier classification schemes of galaxies, they encompass a wide variety of objects with diverse properties and formation histories.

Barway et al. (2007, 2009) find a dependence of structural parameters of S0 galaxies and their correlations on luminosity and environment. The inference drawn by these studies is that bright and faint S0 galaxies have different formation mechanisms. The aim of the first part of this thesis was to verify this using multiwavelength data ranging from ultraviolet to infrared wavelengths and studying various color-color relationships. The photometric data comes from GALEX, SDSS, 2MASS and WISE. Using various color based diagnostics, we find that the stellar population of most bright S0s is consistent with having formed in a single episodic burst. In case of faint S0s however, such a consistency is not found implying a more complex formation history with star formation taking place over extended periods of time. Environment is also found to play an important role in these differences.

In the second part of the thesis, we aimed at studying the bulges of S0 galaxies using the technique of 2-d image decomposition on 3.6 micron imaging data obtained by the Spitzer Space Telescope. Chapter 5 describes the pre-processing required to be able to use these data for 2-d image decomposition and the techniques developed to perform the analysis. Once the analysis was done the properties of the bulge, namely the Sérsic index, effective radius and the average surface brightness within it were used to classify the bulges as classical or pseudo. In Chapter 6 we showed

that the disk properties, mainly the disk scale length, is a function of the bulge type, with pseudobulge hosting S0s having a lower scale length on average, compared to the classical bulges. This can be interpreted as either a preference of pseudobulges to arise in disks of small scale length or a signature of the process responsible for bulge growth. Another alternative explanation is that this lowered scale length is a result of the processes capable of transforming spirals to S0s. In Chapter 7, we investigate this using a comparison sample of spiral galaxies. We conclude that early type spirals can transform into S0s, in the case of pseudobulge hosts, without any process except gas stripping. However, for late-type spirals, additional assistance via minor mergers, for example, is required.

While the study described in the first part of the thesis allows broad statistical trends of the stellar populations and formation histories, to be investigated, only detailed analysis of individual spectra can help constrain formation histories for individual objects. This is the goal of an ongoing study where long-slit spectroscopic data obtained using SALT-RSS are fitted using a linear combination of SSPs. The third part of the thesis presents such an analysis of pseudobulge hosting S0s, as identified using Spitzer IRAC photometry. Of the 10 objects studied, data for one were found to be of poor quality. Of the remaining nine, six were found to contain a dominantly young stellar population consistent with their being pseudobulges. For the remaining three, a surprisingly old stellar population was found. Interestingly, all these three galaxies are barred. This fact may have interesting consequences for the role played by bars in determining the photometric properties of classical bulges.

In the next section, we describe future studies that can be carried out on the basis of the findings and analysis carried out in this thesis.

11.2 Future Directions

Some S0 galaxies appear to be closely related to ellipticals in terms of their formation histories while others are closer to spirals. In some cases, it is possible that the objects are a stand-alone class of galaxies with a very different route of formation altogther. We have discovered these differences using photometric as well as spectral analysis. The differences found are in terms of structural parameters and their inter-correlations, their colors and spectra which in turn imply different stellar populations. Finding more such differences can provide further clues concerning the link between S0s and other elliptical galaxies. For example, differences in properties of dark matter haloes is not a well explored area. Using rotation curves obtained from long-slit spectra, it may be possible to model them as a sum of contributions from bulge, disk and the dark matter halo. Information about dark matter potentials in which these galaxies reside can provide important clues to help understand

galaxy formation in general.

Among the many conceptions developed about S0 galaxies, that they are relatively dust free is a common one. But it is clear from all the studies presented in this thesis that there should be many S0 galaxies with an abundance of dust. Using Spitzer data from higher wavelength bands i.e. mid- and far-infrared, it should be possible to study the dust emission properties of S0 galaxies. In particular, it would be interesting if the signatures of PAH emissions can be isolated and studied. This can be done using the 8 micron channel of IRAC as well as the data from MIPS at 24 micron and higher wavelengths.

Using the multiwavelength sample of S0 galaxies described in the first part of the thesis, one can move beyond simple color diagnostics and attempt detailed modelling of the complete UV-optical-IR-midIR spectral energy distribution. Further, performing a detailed 2-d decomposition analysis for this sample can help in exploration of correlations between the structural parameters and color information. Such a study will allow mass determination of individual stellar components of galaxies, providing further insights about them.

One of the missing pieces of information for many of the galaxies in all the samples used is that of the environment. By this we do not refer to the group/cluster and field classification used in the first part of the thesis. Instead we refer to a more physically motivated and quantitative description of the environment - for example, how strong is the influence of the group or cluster potential on the galaxy? A study that aims at obtaining such information will require sensitive surveys and detailed modelling techniques which take into account not just the apparent separation of the objects on the sky but the physical separation, by incorporating a third dimension of radial distance. Such a study will also require better models for the dark matter haloes of the galaxies.

A powerful technique used in study of galaxies using their images, not covered in detail in this thesis, is that of isophotal fitting. In this technique, the isophotes of the galaxies are fitted with ellipses using a Fourier series expansion. The higher order coefficients that remain after such a fit, represent deviations of isophotes from perfect ellipses. For example, the coefficient of $\cos 4\theta$ term allows such isophotes to be classified as either boxy or disky. In case of elliptical galaxies, significant differences have been found between galaxies that exhibit these deviations and those that do not. A similar analysis in case of S0s should be interesting.

It would not be an understatement to say that we have barely scratched the surface in terms of extracting information from the long-slit spectra described in the third part of the thesis. Chapter 10 describes in detail the kind of analysis that can be done with these data. Over and above what is described there, one of the projects being planned by us using SALT is to identify S0s with strong emission lines

and acquire Fabry - Perot imaging data. This will allow for detailed 3-d kinematical modelling of these galaxies.

A recent trend in the study of galaxies has been to move beyond conventional long-slit spectra and use either multi-object spectrographs or even better, Integrated Field Units. One can obtain 100s of spectra for a single galaxy, one from each point on the surface, analyze them and construct 2-d maps showing variation in age, metallicity and other properties. However, the process of data reduction for such instruments is very complicated and requires high performance computing. But the dividends in terms of the information that can be extracted are very high. One future direction would be to take advantage of future telescopes with such instruments to study S0s.

Despite decades of research, the study of S0s, especially their evolution is far from being complete. Nature is incomprehensibly complicated and vast. To be able to understand even the feeblest part of it is a privilege.

Bibliography

K. N. Abazajian, J. K. Adelman-McCarthy, M. A. Agüeros, S. S. Allam, C. Allende Prieto, D. An, K. S. J. Anderson, S. F. Anderson, J. Annis, N. A. Bahcall, and et al. The Seventh Data Release of the Sloan Digital Sky Survey. *ApJS*, 182:543, June 2009. doi: 10.1088/0067-0049/182/2/543.

C. P. Ahn, R. Alexandroff, C. Allende Prieto, S. F. Anderson, T. Anderton, B. H. Andrews, É. Aubourg, S. Bailey, E. Balbinot, R. Barnes, and et al. The Ninth Data Release of the Sloan Digital Sky Survey: First Spectroscopic Data from the SDSS-III Baryon Oscillation Spectroscopic Survey. *ApJS*, 203:21, December 2012. doi: 10.1088/0067-0049/203/2/21.

Y. C. Andredakis and R. H. Sanders. Exponential bulges in late-type spirals: an improved description of the light distribution. *MNRAS*, 267:283–296, March 1994.

N. V. Asari, R. Cid Fernandes, G. Stasińska, J. P. Torres-Papaqui, A. Mateus, L. Sodré, W. Schoenell, and J. M. Gomes. The history of star-forming galaxies in the Sloan Digital Sky Survey. *MNRAS*, 381:263–279, October 2007. doi: 10.1111/j.1365-2966.2007.12255.x.

E. Athanassoula. On the nature of bulges in general and of box/peanut bulges in particular: input from N-body simulations. *MNRAS*, 358:1477–1488, April 2005. doi: 10.1111/j.1365-2966.2005.08872.x.

M. L. Balogh, S. L. Morris, H. K. C. Yee, R. G. Carlberg, and E. Ellingson. Differential Galaxy Evolution in Cluster and Field Galaxies at z˜0.3. *ApJ*, 527:54–79, December 1999. doi: 10.1086/308056.

S. Barway, A. Kembhavi, Y. Wadadekar, C. D. Ravikumar, and Y. D. Mayya. Lenticular Galaxy Formation: Possible Luminosity Dependence. *ApJ*, 661:L37–L40, May 2007. doi: 10.1086/518422.

S. Barway, Y. Wadadekar, A. K. Kembhavi, and Y. D. Mayya. Near-infrared bulge-disc correlations of lenticular galaxies. *MNRAS*, 394:1991–2000, April 2009. doi: 10.1111/j.1365-2966.2009.14440.x.

S. Barway, Y. Wadadekar, and A. K. Kembhavi. Bar fraction in lenticular galaxies: dependence on luminosity and environment. *MNRAS*, 410:L18–L22, January 2011. doi: 10.1111/j.1745-3933.2010.00970.x.

S. Barway, Y. Wadadekar, K. Vaghmare, and A. K. Kembhavi. Luminosity-dependent star formation history of S0 galaxies: evidence from GALEX-SDSS-2MASS-WISE colours. *MNRAS*, 432:430–437, June 2013. doi: 10.1093/mnras/stt478.

E. Bertin and S. Arnouts. SExtractor: Software for source extraction. *A&AS*, 117: 393–404, June 1996.

G. Bruzual and S. Charlot. Stellar population synthesis at the resolution of 2003. *MNRAS*, 344:1000–1028, October 2003. doi: 10.1046/j.1365-8711.2003.06897.x.

D. Burstein. Structure and origin of S0 galaxies. III - The luminosity distribution perpendicular to the plane of the disks in S0's. *ApJ*, 234:829–836, December 1979. doi: 10.1086/157563.

D. Burstein, L. C. Ho, J. P. Huchra, and L. M. Macri. The K-Band Luminosities of Galaxies: Do S0s Come from Spiral Galaxies? *ApJ*, 621:246–255, March 2005. doi: 10.1086/427408.

M. Capaccioli. Photometry of early-type galaxies and the R exp 1/4 law. In H. G. Corwin, Jr. and L. Bottinelli, editors, *World of Galaxies (Le Monde des Galaxies)*, pages 208–227, 1989.

M. Cappellari, E. Emsellem, D. Krajnović, R. M. McDermid, N. Scott, G. A. Verdoes Kleijn, L. M. Young, K. Alatalo, R. Bacon, L. Blitz, M. Bois, F. Bournaud, M. Bureau, R. L. Davies, T. A. Davis, P. T. de Zeeuw, P.-A. Duc, S. Khochfar, H. Kuntschner, P.-Y. Lablanche, R. Morganti, T. Naab, T. Oosterloo, M. Sarzi, P. Serra, and A.-M. Weijmans. The ATLAS^{3D} project - I. A volume-limited sample of 260 nearby early-type galaxies: science goals and selection criteria. *MNRAS*, 413:813–836, May 2011. doi: 10.1111/j.1365-2966.2010.18174.x.

J. A. Cardelli, G. C. Clayton, and J. S. Mathis. The relationship between infrared, optical, and ultraviolet extinction. *ApJ*, 345:245–256, October 1989. doi: 10.1086/167900.

C. M. Carollo, M. Stiavelli, P. T. de Zeeuw, and J. Mack. Spiral Galaxies with WFPC2.I.Nuclear Morphology, Bulges, Star Clusters, and Surface Brightness Profiles. *AJ*, 114:2366, December 1997. doi: 10.1086/118654.

I. Chilingarian, P. Prugniel, O. Sil'Chenko, and M. Koleva. NBursts: Simultaneous Extraction of Internal Kinematics and Parametrized SFH from Integrated Light Spectra. In A. Vazdekis and R. Peletier, editors, *IAU Symposium*, volume 241 of *IAU Symposium*, pages 175–176, August 2007. doi: 10.1017/S1743921307007752.

R. Cid Fernandes, A. Mateus, L. Sodré, G. Stasińska, and J. M. Gomes. Semi-empirical analysis of Sloan Digital Sky Survey galaxies - I. Spectral synthesis method. *MNRAS*, 358:363–378, April 2005. doi: 10.1111/j.1365-2966.2005.08752.x.

M. Cohen, W. A. Wheaton, and S. T. Megeath. Spectral Irradiance Calibration in the Infrared. XIV. The Absolute Calibration of 2MASS. *AJ*, 126:1090–1096, August 2003. doi: 10.1086/376474.

C. Conroy, J. E. Gunn, and M. White. The Propagation of Uncertainties in Stellar Population Synthesis Modeling. I. The Relevance of Uncertain Aspects of Stellar Evolution and the Initial Mass Function to the Derived Physical Properties of Galaxies. *ApJ*, 699:486–506, July 2009. doi: 10.1088/0004-637X/699/1/486.

C. J. Conselice. The Relationship between Stellar Light Distributions of Galaxies and Their Formation Histories. *ApJS*, 147:1–28, July 2003. doi: 10.1086/375001.

S. Courteau, R. S. de Jong, and A. H. Broeils. Evidence for Secular Evolution in Late-Type Spirals. *ApJ*, 457:L73, February 1996. doi: 10.1086/309906.

S. M. Crawford, M. Still, P. Schellart, L. Balona, D. A. H. Buckley, G. Dugmore, A. A. S. Gulbis, A. Kniazev, M. Kotze, N. Loaring, K. H. Nordsieck, T. E. Pickering, S. Potter, E. Romero Colmenero, P. Vaisanen, T. Williams, and E. Zietsman. PySALT: the SALT science pipeline. In *Society of Photo-Optical Instrumentation Engineers (SPIE) Conference Series*, volume 7737 of *Society of Photo-Optical Instrumentation Engineers (SPIE) Conference Series*, page 25, July 2010. doi: 10.1117/12.857000.

G. de Vaucouleurs. Classification and Morphology of External Galaxies. *Handbuch der Physik*, 53:275, 1959.

G. de Vaucouleurs, A. de Vaucouleurs, H. G. Corwin, Jr., R. J. Buta, G. Paturel, and P. Fouqué. *Third Reference Catalogue of Bright Galaxies. Volume I: Explanations and references. Volume II: Data for galaxies between 0^h and 12^h. Volume III: Data for galaxies between 12^h and 24^h.* 1991.

V. P. Debattista, C. M. Carollo, L. Mayer, and B. Moore. Bulges or Bars from Secular Evolution? *ApJ*, 604:L93–L96, April 2004. doi: 10.1086/386332.

S. Djorgovski and M. Davis. Fundamental properties of elliptical galaxies. *ApJ*, 313: 59–68, February 1987. doi: 10.1086/164948.

J. Donas, J.-M. Deharveng, R. M. Rich, S. K. Yi, Y.-W. Lee, A. Boselli, A. Gil de Paz, S. Boissier, S. Charlot, S. Salim, L. Bianchi, T. A. Barlow, K. Forster, P. G. Friedman, T. M. Heckman, B. F. Madore, D. C. Martin, B. Milliard, P. Morrissey, S. G. Neff, D. Schiminovich, M. Seibert, T. Small, A. S. Szalay, B. Y. Welsh, and T. K. Wyder. GALEX UV Color Relations for Nearby Early-Type Galaxies. *ApJS*, 173:597–606, December 2007. doi: 10.1086/516643.

A. Dressler. Galaxy morphology in rich clusters - Implications for the formation and evolution of galaxies. *ApJ*, 236:351–365, March 1980. doi: 10.1086/157753.

A. Dressler, D. Lynden-Bell, D. Burstein, R. L. Davies, S. M. Faber, R. Terlevich, and G. Wegner. Spectroscopy and photometry of elliptical galaxies. I - A new distance estimator. *Astrophysical Journal*, 313:42–58, February 1987. doi: 10.1086/164947.

S. P. Driver, C. C. Popescu, R. J. Tuffs, A. W. Graham, J. Liske, and I. Baldry. The Energy Output of the Universe from 0.1 to 1000 μm. *ApJ*, 678:L101–L104, May 2008. doi: 10.1086/588582.

M. C. Eliche-Moral, A. C. González-García, J. A. L. Aguerri, J. Gallego, J. Zamorano, M. Balcells, and M. Prieto. Evolution along the sequence of S0 Hubble types induced by dry minor mergers. I. Global bulge-to-disk structural relations. *A&A*, 547:A48, November 2012. doi: 10.1051/0004-6361/201118711.

P. Erwin and L. S. Sparke. Double Bars, Inner Disks, and Nuclear Rings in Early-Type Disk Galaxies. *AJ*, 124:65–77, July 2002. doi: 10.1086/340803.

P. Erwin, R. P. Saglia, M. Fabricius, J. Thomas, N. Nowak, S. Rusli, R. Bender, J. C. Vega Beltrán, and J. E. Beckman. Composite bulges: the coexistence of classical bulges and discy pseudo-bulges in S0 and spiral galaxies. *MNRAS*, 446: 4039–4077, February 2015. doi: 10.1093/mnras/stu2376.

J. Falcón-Barroso, G. van de Ven, R. F. Peletier, M. Bureau, H. Jeong, R. Bacon, M. Cappellari, R. L. Davies, P. T. de Zeeuw, E. Emsellem, D. Krajnović, H. Kuntschner, R. M. McDermid, M. Sarzi, K. L. Shapiro, R. C. E. van den Bosch, G. van der Wolk, A. Weijmans, and S. Yi. The SAURON project - XIX. Optical and near-infrared scaling relations of nearby elliptical, lenticular and Sa galaxies. *MNRAS*, 417:1787–1816, November 2011. doi: 10.1111/j.1365-2966.2011.19372.x.

L. Ferrarese, F. C. van den Bosch, H. C. Ford, W. Jaffe, and R. W. O'Connell. Hubble Space Telescope photometry of the central regions of Virgo cluster elliptical galaxies. 3: Brightness profiles. *AJ*, 108:1598–1609, November 1994. doi: 10.1086/117180.

D. B. Fisher. Central Star Formation and PAH Profiles in Pseudobulges and Classical Bulges. *ApJ*, 642:L17–L20, May 2006. doi: 10.1086/504351.

D. B. Fisher and N. Drory. The Structure of Classical Bulges and Pseudobulges: the Link Between Pseudobulges and SÉRSIC Index. *AJ*, 136:773–839, August 2008. doi: 10.1088/0004-6256/136/2/773.

D. B. Fisher and N. Drory. Bulges of Nearby Galaxies with Spitzer: Scaling Relations in Pseudobulges and Classical Bulges. *ApJ*, 716:942–969, June 2010. doi: 10.1088/0004-637X/716/2/942.

D. B. Fisher and N. Drory. Demographics of Bulge Types within 11 Mpc and Implications for Galaxy Evolution. *ApJ*, 733:L47, June 2011. doi: 10.1088/2041-8205/733/2/L47.

K. C. Freeman. On the Disks of Spiral and so Galaxies. *ApJ*, 160:811, June 1970. doi: 10.1086/150474.

D. A. Gadotti. Image decomposition of barred galaxies and AGN hosts. *MNRAS*, 384:420–439, February 2008. doi: 10.1111/j.1365-2966.2007.12723.x.

D. A. Gadotti. Structural properties of pseudo-bulges, classical bulges and elliptical galaxies: a Sloan Digital Sky Survey perspective. *MNRAS*, 393:1531–1552, March 2009. doi: 10.1111/j.1365-2966.2008.14257.x.

H. Ghosh, S. Mathur, F. Fiore, and L. Ferrarese. Low-Level Nuclear Activity in Nearby Spiral Galaxies. *ApJ*, 687:216–229, November 2008a. doi: 10.1086/591508.

H. Ghosh, S. Mathur, F. Fiore, and L. Ferrarese. Detecting Low-Mass Supermassive Black Holes. In S. K. Chakrabarti and A. S. Majumdar, editors, *American Institute of Physics Conference Series*, volume 1053 of *American Institute of Physics Conference Series*, pages 39–42, October 2008b. doi: 10.1063/1.3009518.

A. W. Graham and S. P. Driver. A Concise Reference to (Projected) Sérsic $R^{1/n}$ Quantities, Including Concentration, Profile Slopes, Petrosian Indices, and Kron Magnitudes. , 22:118–127, 2005. doi: 10.1071/AS05001.

A. W. Graham and C. C. Worley. Inclination- and dust-corrected galaxy parameters: bulge-to-disc ratios and size-luminosity relations. *MNRAS*, 388:1708–1728, August 2008. doi: 10.1111/j.1365-2966.2008.13506.x.

J. Guedes, L. Mayer, M. Carollo, and P. Madau. Pseudobulge Formation as a Dynamical Rather than a Secular Process. *ApJ*, 772:36, July 2013. doi: 10.1088/0004-637X/772/1/36.

E. P. Hubble. *Realm of the Nebulae*. 1936.

R. I. Jedrzejewski, R. L. Davies, and G. D. Illingworth. CCD surface photometry of the bright elliptical galaxies NGC 720, NGC 1052, and NGC 4697. *AJ*, 94: 1508–1518, December 1987. doi: 10.1086/114584.

I. Jorgensen, M. Franx, and P. Kjaergaard. Spectroscopy for E and S0 galaxies in nine clusters. *MNRAS*, 276:1341–1364, October 1995.

I. Y. Katkov, O. K. Sil'chenko, and V. L. Afanasiev. Decoupled gas kinematics in isolated S0 galaxies. *MNRAS*, 438:2798–2803, March 2014. doi: 10.1093/mnras/stt2365.

H. G. Khosroshahi, Y. Wadadekar, and A. Kembhavi. Correlations among Global Photometric Properties of Disk Galaxies. *ApJ*, 533:162–171, April 2000. doi: 10.1086/308654.

M. Koleva, P. Prugniel, A. Bouchard, and Y. Wu. ULySS: A Full Spectrum Fitting Package. Astrophysics Source Code Library, April 2011.

J. Kormendy. Brightness distributions in compact and normal galaxies. II - Structure parameters of the spheroidal component. *ApJ*, 218:333–346, December 1977. doi: 10.1086/155687.

J. Kormendy. Kinematics of extragalactic bulges: evidence that some bulges are really disks. In H. Dejonghe and H. J. Habing, editors, *Galactic Bulges*, volume 153 of *IAU Symposium*, page 209, 1993.

J. Kormendy and R. Bender. A Revised Parallel-sequence Morphological Classification of Galaxies: Structure and Formation of S0 and Spheroidal Galaxies. *ApJS*, 198:2, January 2012. doi: 10.1088/0067-0049/198/1/2.

J. Kormendy and R. C. Kennicutt, Jr. Secular Evolution and the Formation of Pseudobulges in Disk Galaxies. *ARA&A*, 42:603–683, September 2004. doi: 10.1146/annurev.astro.42.053102.134024.

E. Laurikainen, H. Salo, and R. Buta. Multicomponent decompositions for a sample of S0 galaxies. *MNRAS*, 362:1319–1347, October 2005. doi: 10.1111/j.1365-2966.2005.09404.x.

E. Laurikainen, H. Salo, R. Buta, J. H. Knapen, and S. Comerón. Photometric scaling relations of lenticular and spiral galaxies. *MNRAS*, 405:1089–1118, June 2010. doi: 10.1111/j.1365-2966.2010.16521.x.

C. Leitherer, D. Schaerer, J. D. Goldader, R. M. G. Delgado, C. Robert, D. F. Kune, D. F. de Mello, D. Devost, and T. M. Heckman. Starburst99: Synthesis Models for Galaxies with Active Star Formation. *ApJS*, 123:3–40, July 1999. doi: 10.1086/313233.

G. B. Lima Neto, D. Gerbal, and I. Márquez. The specific entropy of elliptical galaxies: an explanation for profile-shape distance indicators? *MNRAS*, 309: 481–495, October 1999. doi: 10.1046/j.1365-8711.1999.02849.x.

T. Lisker, E. K. Grebel, and B. Binggeli. Virgo Cluster Early-Type Dwarf Galaxies with the Sloan Digital Sky Survey. I. On the Possible Disk Nature of Bright Early-Type Dwarfs. *AJ*, 132:497–513, August 2006. doi: 10.1086/505045.

R. Lopes de Oliveira, G. B. Lima Neto, C. Mendes de Oliveira, E. Janot-Pacheco, and C. Motch. Discovery of a cluster of galaxies behind the Milky Way: X-ray and optical observations. *A&A*, 459:415–422, November 2006. doi: 10.1051/0004-6361: 20065681.

M. Fernández Lorenzo, J. Sulentic, L. Verdes-Montenegro, J. Blasco-Herrera, M. Argudo-Fernández, J. Garrido, P. Ramírez-Moreta, J. E. Ruiz, S. Sánchez-Expósito, and J. D. Santander-Vela. Are (pseudo)bulges in isolated galaxies actually primordial relics? *The Astrophysical Journal Letters*, 788(2):L39, 2014. URL http://stacks.iop.org/2041-8205/788/i=2/a=L39.

J. M. Lotz, J. Primack, and P. Madau. A New Nonparametric Approach to Galaxy Morphological Classification. *AJ*, 128:163–182, July 2004. doi: 10.1086/421849.

C. L. Mancone and A. H. Gonzalez. EzGal: A Flexible Interface for Stellar Population Synthesis Models. *PASP*, 124:606–615, June 2012. doi: 10.1086/666502.

S. Mathur, H. Ghosh, F. Fiore, and L. Ferrarese. Discovery of supermassive black holes in normal galaxies. *X-ray Astronomy 2009; Present Status, Multi-Wavelength Approach and Future Perspectives*, 1248:241–242, July 2010. doi: 10.1063/1.3475222.

A. Meert, V. Vikram, and M. Bernardi. A catalogue of 2D photometric decompositions in the SDSS-DR7 spectroscopic main galaxy sample: preferred models and systematics. *MNRAS*, 446:3943–3974, February 2015. doi: 10.1093/mnras/stu2333.

G. R. Meurer, D. J. Hanish, H. C. Ferguson, P. M. Knezek, V. A. Kilborn, M. E. Putman, R. C. Smith, B. Koribalski, M. Meyer, M. S. Oey, E. V. Ryan-Weber, M. A. Zwaan, T. M. Heckman, R. C. Kennicutt, Jr., J. C. Lee, R. L. Webster, J. Bland-Hawthorn, M. A. Dopita, K. C. Freeman, M. T. Doyle, M. J. Drinkwater, L. Staveley-Smith, and J. Werk. The Survey for Ionization in Neutral Gas Galaxies. I. Description and Initial Results. *ApJS*, 165:307–337, July 2006. doi: 10.1086/504685.

J. C. Muñoz-Mateos, A. Gil de Paz, J. Zamorano, S. Boissier, D. A. Dale, P. G. Pérez-González, J. Gallego, B. F. Madore, G. Bendo, A. Boselli, V. Buat, D. Calzetti, J. Moustakas, and R. C. Kennicutt, Jr. Radial Distribution of Stars, Gas, and Dust in SINGS Galaxies. I. Surface Photometry and Morphology. *ApJ*, 703:1569, October 2009. doi: 10.1088/0004-637X/703/2/1569.

P. Nilson. *Uppsala general catalogue of galaxies*. 1973.

T. Okamoto. The origin of pseudo-bulges in cosmological simulations of galaxy formation. *MNRAS*, 428:718–728, January 2013. doi: 10.1093/mnras/sts067.

J. B. Oke and J. E. Gunn. Secondary standard stars for absolute spectrophotometry. *ApJ*, 266:713–717, March 1983. doi: 10.1086/160817.

B. A. Pastrav, C. C. Popescu, R. J. Tuffs, and A. E. Sansom. The effects of dust on the photometric parameters of decomposed disks and bulges. *A&A*, 557:A137, September 2013. doi: 10.1051/0004-6361/201322086.

C. Y. Peng, L. C. Ho, C. D. Impey, and H.-W. Rix. Detailed Structural Decomposition of Galaxy Images. *AJ*, 124:266–293, July 2002. doi: 10.1086/340952.

D. Pierini, G. Gavazzi, P. Franzetti, M. Scodeggio, and A. Boselli. 1.65-μm (H -band) surface photometry of galaxies - VIII. The near-IR κ space at z =0. *MNRAS*, 332:422–434, May 2002. doi: 10.1046/j.1365-8711.2002.05323.x.

William H. Press, Saul A. Teukolsky, William T. Vetterling, and Brian P. Flannery. Numerical recipes in c: The art of scientific computing. second edition, 1992.

C. D. Ravikumar, S. Barway, A. Kembhavi, B. Mobasher, and V. C. Kuriakose. Photometric scaling relations for bulges of galaxies. *A&A*, 446:827–838, February 2006. doi: 10.1051/0004-6361:20053547.

A. Renzini. Origin of Bulges. In C. M. Carollo, H. C. Ferguson, and R. F. G. Wyse, editors, *The Formation of Galactic Bulges*, page 9, 1999.

J. W. Richards, P. E. Freeman, A. B. Lee, and C. M. Schafer. Accurate parameter estimation for star formation history in galaxies using SDSS spectra. *MNRAS*, 399:1044–1057, October 2009. doi: 10.1111/j.1365-2966.2009.15349.x.

A. Sandage. *The Hubble atlas of galaxies*. 1961.

K. Schawinski, S. Khochfar, S. Kaviraj, S. K. Yi, A. Boselli, T. Barlow, T. Conrow, K. Forster, P. G. Friedman, D. C. Martin, P. Morrissey, S. Neff, D. Schiminovich, M. Seibert, T. Small, T. K. Wyder, L. Bianchi, J. Donas, T. Heckman, Y.-W. Lee, B. Madore, B. Milliard, R. M. Rich, and A. Szalay. Suppression of star formation in early-type galaxies by feedback from supermassive black holes. *Nature*, 442: 888–891, August 2006. doi: 10.1038/nature04934.

D. J. Schlegel, D. P. Finkbeiner, and M. Davis. Maps of Dust Infrared Emission for Use in Estimation of Reddening and Cosmic Microwave Background Radiation Foregrounds. *ApJ*, 500:525–553, June 1998. doi: 10.1086/305772.

J. L. Sersic. *Atlas de galaxias australes*. 1968.

D. L. Shupe, M. Moshir, J. Li, D. Makovoz, R. Narron, and R. N. Hook. The SIP Convention for Representing Distortion in FITS Image Headers. In P. Shopbell, M. Britton, and R. Ebert, editors, *Astronomical Data Analysis Software and Systems XIV*, volume 347 of *Astronomical Society of the Pacific Conference Series*, page 491, December 2005.

M. F. Skrutskie, R. M. Cutri, R. Stiening, M. D. Weinberg, S. Schneider, J. M. Carpenter, C. Beichman, R. Capps, T. Chester, J. Elias, J. Huchra, J. Liebert, C. Lonsdale, D. G. Monet, S. Price, P. Seitzer, T. Jarrett, J. D. Kirkpatrick, J. E. Gizis, E. Howard, T. Evans, J. Fowler, L. Fullmer, R. Hurt, R. Light, E. L. Kopan, K. A. Marsh, H. L. McCallon, R. Tam, S. Van Dyk, and S. Wheelock. The Two Micron All Sky Survey (2MASS). *AJ*, 131:1163–1183, February 2006. doi: 10.1086/498708.

E. Tago, E. Saar, E. Tempel, J. Einasto, M. Einasto, P. Nurmi, and P. Heinämäki. Groups of galaxies in the SDSS Data Release 7 . Flux- and volume-limited samples. *A&A*, 514:A102, May 2010. doi: 10.1051/0004-6361/200913687.

E. Toloba, A. Boselli, R. F. Peletier, J. Falcón-Barroso, G. van de Ven, and J. Gorgas. Formation and evolution of dwarf early-type galaxies in the Virgo cluster. II. Kinematic scaling relations. *A&A*, 548:A78, December 2012. doi: 10.1051/0004-6361/201218944.

I. Trujillo, A. W. Graham, and N. Caon. On the estimation of galaxy structural parameters: the Sérsic model. *MNRAS*, 326:869–876, September 2001. doi: 10.1046/j.1365-8711.2001.04471.x.

R. B. Tully and J. R. Fisher. *Catalog of Nearby Galaxies*. April 1988.

K. Vaghmare, S. Barway, and A. Kembhavi. A Spitzer Study of Pseudobulges in S0 Galaxies: Secular Evolution of Disks. *ApJ*, 767:L33, April 2013. doi: 10.1088/2041-8205/767/2/L33.

S. van den Bergh. A new classification system for galaxies. *ApJ*, 206:883–887, June 1976. doi: 10.1086/154452.

P. G. van Dokkum. Cosmic-Ray Rejection by Laplacian Edge Detection. *PASP*, 113:1420–1427, November 2001. doi: 10.1086/323894.

V. Vikram, Y. Wadadekar, A. K. Kembhavi, and G. V. Vijayagovindan. PYMORPH: automated galaxy structural parameter estimation using PYTHON. *MNRAS*, 409:1379–1392, December 2010. doi: 10.1111/j.1365-2966.2010.17426.x.

T. Weinzirl, S. Jogee, S. Khochfar, A. Burkert, and J. Kormendy. Bulge n and B/T in High-Mass Galaxies: Constraints on the Origin of Bulges in Hierarchical Models. *ApJ*, 696:411–447, May 2009. doi: 10.1088/0004-637X/696/1/411.

E. L. Wright, P. R. M. Eisenhardt, A. K. Mainzer, M. E. Ressler, R. M. Cutri, T. Jarrett, J. D. Kirkpatrick, D. Padgett, R. S. McMillan, M. Skrutskie, S. A. Stanford, M. Cohen, R. G. Walker, J. C. Mather, D. Leisawitz, T. N. Gautier, III, I. McLean, D. Benford, C. J. Lonsdale, A. Blain, B. Mendez, W. R. Irace, V. Duval, F. Liu, D. Royer, I. Heinrichsen, J. Howard, M. Shannon, M. Kendall, A. L. Walsh, M. Larsen, J. G. Cardon, S. Schick, M. Schwalm, M. Abid, B. Fabinsky, L. Naes, and C.-W. Tsai. The Wide-field Infrared Survey Explorer (WISE): Mission Description and Initial On-orbit Performance. *AJ*, 140:1868, December 2010. doi: 10.1088/0004-6256/140/6/1868.

T. K. Wyder, M. A. Treyer, B. Milliard, D. Schiminovich, S. Arnouts, T. Budavári, T. A. Barlow, L. Bianchi, Y.-I. Byun, J. Donas, K. Forster, P. G. Friedman, T. M. Heckman, P. N. Jelinsky, Y.-W. Lee, B. F. Madore, R. F. Malina, D. C. Martin, P. Morrissey, S. G. Neff, R. M. Rich, O. H. W. Siegmund, T. Small, A. S. Szalay, and B. Y. Welsh. The Ultraviolet Galaxy Luminosity Function in the Local Universe from GALEX Data. *ApJ*, 619:L15–L18, January 2005. doi: 10.1086/424735.